UNIVERSIDAD DE GRANADA

FACULTAD DE CIENCIAS

Departamento de Química Inorgánica

PROGRAMA DE DOCTORADO EN QUÍMICA

TESIS DOCTORAL

ELECTRODOS BASADOS EN CARBÓN, OBTENIDOS A PARTIR DE RESIDUOS AGRÍCOLAS Y GELES DE CARBONO, PARA SUPERCONDENSADORES Y ELECTRO-REDUCCIÓN DE OXÍGENO

ABDELHAKIM ELMOUWAHIDI

Granada, Julio 2017

Editor: Universidad de Granada. Tesis Doctorales
Autor: Abdelhakim Elmouwahidi
ISBN: 978-84-9163-631-1
URI: http://hdl.handle.net/10481/48617

ELECTRODOS BASADOS EN CARBÓN, OBTENIDOS A PARTIR DE RESIDUOS AGRÍCOLAS Y GELES DE CARBONO, PARA SUPERCONDENSADORES Y ELECTRO-REDUCCIÓN DE OXÍGENO

ABDELHAKIM ELMOUWAHIDI

Memoria presentada para optar al grado de Doctor

por la Universidad de Granada

Fdo.: **Abdelhakim Elmouwahidi**

Licenciado en Química

Los Directores de la Tesis

Prof. Dr. Francisco Carrasco Marín

Catedrático del Departamento de Química Inorgánica. Universidad de Granada.

Prof. Dr. Agustín Francisco Pérez Cadenas

Profesor Titular del Departamento de Química Inorgánica. Universidad de Granada.

Tesis presentada para aspirar al grado de Doctor en Química por

ABDELHAKIM ELMOUWAHIDI

Realizada bajo la dirección del Catedrático de Química Inorgánica Prof. Dr. Francisco Carrasco Marín y del Profesor Titular de Química Inorgánica Dr. Agustín Francisco Pérez Cadenas, en la Facultad de Ciencias de la Universidad de Granada, y juzgada el 24 de Julio de 2017, en dicha Facultad, por el siguiente Tribunal:

PRESIDENTE:

Prof. Dr. D. José Rivera Utrilla, Catedrático de Química Inorgánica, Universidad de Granada.

VOCALES:

Prof. Dr. D. Agustín Bueno López, Catedrático de Química Inorgánica, Universidad de Alicante.

Prof. Dra. Dª. María Pérez Cadenas, Profesora Ayudante Doctor de Química Inorgánica, Universidad Nacional de Educación a Distancia.

Dr. D. Sergio Morales Torres, Investigador Científico, Universidad de Oporto.

SECRETARIO:

Profa. Dra. Dª. María de los Ángeles Ferro García, Catedrática de Química Inorgánica, Universidad de Granada.

Francisco Carrasco Marín y Agustín Francisco Pérez Cadenas como directores de la presente Tesis Doctoral, y el doctorando Abdelhakim Elmouwahidi

GARANTIZAN QUE:

el trabajo ha sido realizado por el doctorando respetando los derechos de otros autores a ser citados cuando se han utilizado sus resultados o publicaciones.

Y para que conste a los efectos oportunos, en el cumplimiento de la legislación vigente, firmamos el presente certificado en Granada 14 de junio del 2017.

Fdo.: **Francisco Carrasco Marín**
Catedrático de Química Inorgánica de la Universidad de Granada.

Fdo.: **Agustín F. Pérez Cadenas**
Profesor Titular de Química Inorgánica de la Universidad de Granada.

Fdo.: **Abdelhakim Elmouwahidi**
Licenciado en Química.

“Soy de los que piensan que la ciencia tiene una gran belleza. Un científico en su laboratorio no es sólo un técnico: es también un niño colocado ante fenómenos naturales que le impresionan como un cuento de hadas”

Marie Curie

“A nadie pedí la vida. Me esfuerzo por aceptar, sin júbilo ni rabia, todo lo que la vida ofrece. Partiré sin preguntar al prójimo acerca de mi curiosa permanencia en este mundo.”

OMAR KHAYYAM

A la memoria de mi Madre Fouzia

Para ti mi madre querida que hoy descansas en paz

El destino quiso que te fueras rápido y no estuvieras a mi lado, me haces mucha falta, pero nada ni nadie podrá arrancarte de mi corazón, en donde estará para siempre tu recuerdo y memoria.

Jamás te olvidaré y siempre pienso en ti mamá.

A la Memoria de mi Abuela Elbatoul,

Gracias por cuidarme, educarme y enseñarme muchos valores

Por sacar lo mejor que había en mí.

Nunca te olvidaré...

A mi padre Abdallah

A mis hermanos y mis hermanas

AGRADECIMIENTOS

Deseo expresar mi más sincero y profundo agradecimiento a mis Directores de Tesis, Prof. Dr. Francisco Carrasco Marín y Prof. Dr. Agustín Francisco Pérez Cadenas, por vuestra dirección, preocupación y dedicación durante mi estancia a Granada, así como, por ser un gran apoyo no solo a nivel científico sino también a nivel personal, sobre todo, por la confianza depositada en mí en todo momento a lo largo de estos años predoctorales. No me cabe más que felicitarles por su talla científica y humana. Gracias también a sus maravillosas familias.

Al Prof. Dr. Carlos Moreno Castilla por darme la oportunidad de realizar esta Tesis en el Grupo de Investigación en Materiales de Carbón de la Universidad de Granada, por darme la primera oportunidad de descubrir este maravilloso grupo, y también por sus consejos y su calidad humana, sin olvidarme del resto de miembros de dicho grupo: José Rivera, Paco Pepe, Isa, Mª Ángeles, por permitir integrarme en el grupo fácilmente y por el ambiente formidable que tenemos en el grupo. Todos ellos me han confirmado la gran suerte que he tenido de poder realizar la presente Tesis Doctoral en este excelente grupo humano y científico.

También quiero dar las gracias a toda la gente que he conocido durante estos cuatro años de trabajo en el Laboratorio de Adsorción y Catálisis y que se han convertido en más que amigos. Y especialmente la gran "JEFA" Esther, también a mis compañeros de laboratorio Mary y Nelson, José, David, Jesica, Hesham, Zulamita, Sergio y Abdallah todos nos hemos convertido en la familia del carbón, apoyándonos siempre ante las dificultades y compartiendo grandes momentos. Por otro lado, están los compañeros de Química General: Mahmoud, Raúl, Valente, Ahmed, Alegría, Adil, Ihsan, Paulina, Fran y Said, grandes personas y científicos. No quiero olvidarme de todos los que han pasado de estancia en el laboratorio y que sin duda han dejado huellas: Norberto, Amra, Luis, Francesca, Karol (calabazaaa), Carmen, Fran, Chris, Damarys, Camilo, Stefania Jorge Medina Valtierra, Adriana, Safa, Filipa y Alex. A todos gracias por cada uno de los momentos especiales que me habéis regalado.

Agradecer a la Profesora Vanessa Fierro por permitirme realizar mis estancias predoctorales en Epinal, gracias por su calidad humana, por su generosidad y por ayudarme a hacerme la estancia realmente agradable. Agradezco también el Profesor Alain Celzard sus consejos y por ayudarme especialmente en la parte de tratamiento de las muestras con boro. Igualmente agradezco a todos los amigos que conocí en Epinal: Asma, Antonio, Clara, Philipe, Andrzej, Ángela, Ludmila, Flavia, Sébastien e Maxime.

Quiero agradecer también al Grupo de Carbones de la Universidad de Jaén: Vicky, Miguel Ángel, María, y Paco, por su amistad.

A los miembros del Centro de Investigación Científica de la Universidad de Granada, especialmente a María del Mar y Alicia (Técnicos especialistas de TEM y SEM), Domingo y Pablo.

Agradecer a todos mis compañeros de trabajo a Ouarzazate y especialmente Aicha Chahbi, gracias por su calidad humana y por recibirme como hijo, gracias también a toda su familia.

A todos mis amigos de diferentes países que conocí en Granada, por los buenos momentos que hemos pasado, Gertrudis, Edgar, Ibrahim, Meknassi, Suhail, Yasser, Nabil, Biba, Boubker, Omar, Oussama, Abouromane, Anas, Mouad, Diaa, Ahmed Salama, Elghanam, Mahmoud Hassan, Wael, Mahmoud, Tarik, Mustapha, Sedik, Ihab, Obid, Redwan, Hanane, Choumicha., Karim Amour y Rachid.

Quiero agradecer a todas las personas que, de una manera u otra, han contribuido a que este trabajo llegue a su fin.

A toda mi familia, en especial a mi padre Abdallah y a Naima, por su paciencia, por su apoyo incondicional y por muchas buenas cosas, soy la persona que soy gracias a vosotros. También a mis hermanas y hermanos. Gracias por vuestro amor y por todo, a mis sobrinos Yasser, Assia e Imran. A toda la familia Elmouwahidi y toda la familia El Khadari, especialmente a mis abuelos. Os quiero mucho.

Este Trabajo de Investigación ha sido financiado por la Junta de Andalucía, a través del Grupo de Investigación RNM-172 y del Proyecto de Excelencia P12-RNM-2892; y también por el Ministerio de Economía y Competitividad y fondos FEDER a través del Proyecto Retos CTQ2013-44789-R. Igualmente, Abdelhakim Elmouwahidi agradece al Programa ERASMUS MUNDUS la concesión de una beca Al Idrisi, Acción 2, Lote 1.

ÍNDICE

CAPÍTULO I: *INTRODUCCIÓN Y OBJETIVOS*

CONTENIDOS Y ESTRUCTURA DE LA TESIS

En la presente Tesis Doctoral se han preparado y caracterizado diferentes series de materiales basados en carbono, tanto carbones activados como materiales compuestos óxido metálico - xerogel de carbón. Estos materiales se obtuvieron mediante activación con KOH y H_3PO_4 de diferentes residuos agrícolas tales como maderas de olivo, higuera y chirimoya, además se ha empleado como material de partida un residuo de la industria oleícola, el alperujo, subproducto obtenido durante el sistema continuo de extracción de dos fases y que consiste de una mezcla de alpechín y orujo. Se trata de un residuo altamente contaminante que, según las actuales normativas medioambientales, debe ser separado antes de destinarlo a cualquier uso como la obtención de energía.

Por otra parte, se han sintetizado también materiales compuestos óxidos metálicos - xerogel de carbón, seleccionándose los óxidos: TiO_2, ZrO_2 y V_2O_5. Los materiales preparados han sido caracterizados química y texturalmente, y empleados como electrodos de condensadores electroquímicos para el almacenamiento de energía eléctrica en forma electrostática, y en la reacción de electro-reducción de O_2.

Esta Tesis Doctoral se enmarca dentro de los proyectos de investigación que se han desarrollado en el Grupo de Investigación en Materiales de Carbón de la Universidad de Granada. Estos proyectos han sido: “Transformado de desechos del olivar en materiales avanzados para la conversión electro-catalítica de CO_2 en hidrocarburos” Proyecto de Excelencia de la Junta de Andalucía, P12-RNM-2892, y “Reducción de emisiones de CO_2 y tecnologías de almacenamiento de energías renovables empleando materiales avanzados de carbón”, financiado por el Ministerio de Economía y Competitividad y fondos FEDER, CTQ2013-44789-R.

El trabajo desarrollado durante la realización de esta Tesis Doctoral se ha organizado en diferentes Capítulos cuyos contenidos son los siguientes:

Capítulo I: Introducción y Objetivos.

Se presenta una introducción y revisión bibliográfica sobre los distintos materiales de carbón y su aplicación para el almacenamiento de energía, así como, un estudio de los parámetros que influyen y que son determinantes en estas aplicaciones como la presencia de diferentes grupos superficiales y de óxidos de metales. Por otra parte, se presenta una revisión bibliografía sobre la electro-reducción del oxigeno y los tipos de materiales usados para esta aplicación junto con las características de los materiales usados.

Capítulo II: Métodos y técnicas de caracterización

Se describen métodos de preparación, caracterización textural y química de los diferentes materiales preparados y también las técnicas usadas en los procesos de las dos aplicaciones.

Capítulo III: Preparación de carbones activados a partir de residuos de la industria oleícola mediante activación con KOH y H_3PO_4. Estudio de su aplicación como electrodos de supercondensadores.

En este capítulo se lleva a cabo el estudio de la preparación de muestras de carbón activado a partir de alpechín mediante activación química con KOH y H_3PO_4. Se analiza el efecto del método de preparación sobre la características texturales y químicas de las muestras, La influencia de la porosidad y los grupos superficiales sobre el comportamiento de esos materiales como electrodos para almacenamiento de energía en medio acido H_2SO_4, 1M.

Capítulo IV: Electrocatalizadores libres de metal para la electro-reducción de oxígeno obtenidos a partir de los residuos de biomasa de la industria oleícola.

Se realiza el estudio del tratamiento superficial de muestras de carbón activado preparadas a partir del alpechín con acido tioglicólico para introducir grupos superficiales de azufre y su efecto sobre el comportamiento como electrocatalizadores para la reacción de reducción de oxígeno en KOH 0.1 M.

Capítulo V: Carbones activados preparados a partir de subproductos agrícolas, y dopados con azufre mediante tratamiento solvotermal, como electrodos de supercondensadores.

Se dedica al estudio del efecto del tratamiento de las muestras de alperujo con acido tioglicólico a diferentes porcentajes y su comportamiento como electrodos de condensadores de doble capa eléctrica en medio H_2SO_4 1M y KOH 6 M.

Capítulo VI: Preparación de carbones mediante activación química con H_3PO_4 y KOH de maderas para su uso como electrodos de condensadores electroquímicos.

En este capítulo se describe la preparación y caracterización de muestras de carbón activado a partir de tres tipos de maderas, olivo, higuera y chirimoya mediante el proceso de activación química con KOH y H_3PO_4 y el estudio de sus características texturales y químicas y su comportamiento como electrodos para almacenamiento de energía.

Capítulo VII: Influencia de la química superficial de carbones activados, preparados a partir de residuos de madera, en su comportamiento electroquímico.

A partir de muestras seleccionadas de carbón activado descritas en el capítulo anterior, se estudia el efecto de la modificación química mediante la introducción de grupos superficiales mediante tratamiento con 4 agentes, dos para la oxidación y dos otros para introducir grupos nitrogenados**.** Los agentes usados son ácido nítrico, peroxidisultato amónico, melamina y carbamato amónico. Finalmente se estudia el efecto de esos tratamientos sobre las características electroquímicas de esas muestras como electrodos para supercondensadores.

Capítulo VIII: Materiales compuestos carbón-óxido de titanio como electrodos de supercondensadores.

En este capítulo se describe la preparación y caracterización química y textural de materiales compuestos carbón-óxido de titanio y se realiza un estudio de sus aplicaciones como electrodos de doble capa eléctrica.

Capítulo IX: Comportamiento electroquímico de supercondensadores basados en materiales compuestos carbón-ZrO_2.

Se presentan los resultados obtenidos de la utilización de materiales compuestos de xerogeles de carbono y oxido de zirconio como electrodos para almacenamiento de energía y el efecto del contenido de zirconio sobre las características electroquímicas de los electrodos.

Capítulo X: Preparación de microesferas de carbón recubiertas de óxido de vanadio para su uso como electrodos de supercondensadores.

Se estudia la preparación y la caracterización de materiales compuestos de xerogeles de carbono y oxido de vanadio y sus aplicaciones como electrodos para el almacenamiento de energía.

Capítulo XI: Nuevos materiales compuestos carbón-óxido de vanadio como catalizadores para la electro-reducción de oxígeno.

Se presentan los resultados de la utilización de materiales compuestos de xerogeles de carbono con diferentes porcentajes de oxido de vanadio como catalizadores para la electro-reducción de oxigeno en medio alcalino KOH 0.1 M.

Capítulo XII: Conclusiones generales.

Parte de los resultados del trabajo de investigación realizado durante el desarrollo de esta Tesis se recogen en los siguientes artículos de difusión internacional:

1. **Abdelhakim Elmouwahidi**; Esther Bailón-García; Agustín F. Pérez-Cadenas; Francisco J. Maldonado-Hódar; Francisco Carrasco-Marín. Activated carbons from KOH and H_3PO_4 - activation of olive residues and its application as supercapacitor electrodes. Electrochimica Acta 2017, vol 229, 219-228.

2. **Abdelhakim Elmouwahidi**, Jose F. Vivo-Vilches, Agustín F. Pérez-Cadenas, Francisco J. Maldonado-Hódar, Francisco Carrasco-Marín. Free metal oxygen-reduction electro-catalysts obtained from biomass residue of the olive oil industry. Chemical Engineering Journal 2016, vol 306, 1109-1115.

3. **Abdelhakim Elmouwahidi**, Jose F. Vivo-Vilches, Agustín F. Pérez-Cadenas, Francisco J. Maldonado-Hódar, Francisco Carrasco-Marín. Activated carbons from agricultural waste hydrothermally doped with sulphur as electrodes for supercapacitors. In progress.

4. **Abdelhakim Elmouwahidi**, Esther Bailón-García, Agustín F. Pérez-Cadenas, Francisco J. Maldonado-Hódar, Francisco Carrasco-Marín. Electrochemical performances of new carbon-ZrO_2 composites. In progress.

5. **Abdelhakim Elmouwahidi**, Esther Bailón-García, Agustín F. Pérez-Cadenas, Francisco J. Maldonado-Hódar, Francisco Carrasco-Marín. Development and electrochemical performance of new vanadium coated microspheres for their application as electrodes for supercapacitors. In progress.

6. **Abdelhakim Elmouwahidi**, Esther Bailón-García, Agustín F. Pérez-Cadenas, Francisco J. Maldonado-Hódar, Francisco Carrasco-Marín. Carbon titanium oxide composites as electrochemical supercapacitors electrodes. In progress.

7. **Abdelhakim Elmouwahidi**, Esther Bailón-García, Agustín F. Pérez-Cadenas, Francisco J. Maldonado-Hódar, Francisco Carrasco-Marín. H_3PO_4 and KOH activated carbons from waste wood as electrodes for electrochemical capacitors. In progress.

8. **Abdelhakim Elmouwahidi**, Esther Bailón-García, Agustín F. Pérez-Cadenas, Francisco J. Maldonado-Hódar, Francisco Carrasco-Marín. Influence of surface chemistry on the electrochemical performance of electrode from waste wood activated carbons. In progress.

9. **Abdelhakim Elmouwahidi**, Esther Bailón-García, Agustín F. Pérez-Cadenas, Francisco J. Maldonado-Hódar, Francisco Carrasco-Marín. New carbon vanadium composites as catalyst for oxygen electro- reduction. In progress.

Otros trabajos llevados a cabo durante los años de estudios de Doctorado y en colaboración con otros miembros del Grupo de Investigación en Carbones de la Universidad de Granada son:

1. Esther Bailón-García**, Abdelhakim Elmouwahidi**, Francisco Carrasco-Marín, Agustín F. Pérez-Cadenas, Francisco J. Maldonado-Hódar: *Development of Carbon-ZrO2 composites with high performance as visible-light photocatalysts*. Applied Catalysis B Environmental (2017), Vol 217, 540-550.

2. Abdalla Abdelwahab, Jesica Castelo-Quibén, María Pérez-Cadenas, **Abdelhakim Elmouwahidi**, Francisco J. Maldonado-Hódar, Francisco Carrasco-Marín, Agustin F. Perez-Cadenas: *Cobalt-Doped Carbon Gels as Electro-Catalysts for the Reduction of CO2 to Hydrocarbons*. Catalysts (2017), Vol. 7(1), 1-13.

3. Esther Bailón-García, **Abdelhakim Elmouwahidi**, Miguel A. Álvarez, Francisco Carrasco-Marín, Agustín F. Pérez-Cadenas, Francisco J. Maldonado-Hódar: *New Carbon xerogel-TiO2 composites with high performance as visible-light photocatalysts for dye mineralization*. Applied Catalysis B Environmental (2017), Vol 201, 29-40.

4. **Abdelhakim Elmouwahidi**; Esther Bailón-García; Agustín F. Pérez-Cadenas; Francisco J. Maldonado-Hódar; Francisco Carrasco-Marín. Electrodes Supercapacitors from carbons obtained by a templating procedure from resorcinol, melamine, ammonium carbamate and formaldehyde. (en Preparación).

5. **Abdelhakim Elmouwahidi**; Esther Bailón-García; Agustín F. Pérez-Cadenas; Francisco J. Maldonado-Hódar; Francisco Carrasco-Marín**.** Manganese doping activated carbon and their application as electrochemical supercapacitors.(en Preparación)

6. **Abdelhakim Elmouwahidi**, Esther Bailón-García, Agustín F. Pérez-Cadenas, Vanessa Fierro, Francisco J. Maldonado-Hódar, Alain. Celzard,

Francisco Carrasco-Marín. Nitrogen doped Carbon sphere as electrode material for supercapacitors (en Preparación)

7. **Abdelhakim Elmouwahidi**, M. Helena Garcia Rosero, Esther Bailón-García, Agustín F. Pérez-Cadenas, Francisco J. Maldonado-Hódar, Francisco Carrasco-Marín. Doped N, S, P, B activated carbon as catalyst for electro reduction of oxygen. (en Preparación)

8. **Abdelhakim Elmouwahidi**, Esther Bailón-García, Agustín F. Pérez-Cadenas, Francisco J. Maldonado-Hódar, Francisco Carrasco-Marín. Synthesis and characterization of carbon from catalytic pirolisis of polypropylene and their application as catalysts for oxygen reduction. (en Preparación)

9. **Abdelhakim Elmouwahidi**, Esther Bailón-García, Agustín F. Pérez-Cadenas, Vanessa Fierro, Francisco J. Maldonado-Hódar, Alain. Celzard, Francisco Carrasco-Marín. B and N doped activated carbon as catalyst for electro-reduction of oxygen. (en Preparación)

10. **Abdelhakim Elmouwahidi**, Esther Bailón-García, Agustín F. Pérez-Cadenas, Francisco J. Maldonado-Hódar, Francisco Carrasco-Marín. Preparation of manganese doped carbon sphere and their application as supercapacitors. (en Preparación)

El doctorando también ha presentado las siguientes comunicaciones a congresos nacionales e internacionales:

1. **Abdelhakim Elmouwahidi**, Jesica Castelo-Quibén, Agustín F. Pérez-Cadenas, Francisco J. Maldonado-Hódar and Francisco Carrasco-Marín. Metal carbon composites prepared by catalytic pyrolysis of polyethylene as electro-catalysts for the reduction of CO_2 to hydrocarbons. Carbon 2016. Penn State Conference Center, State College, PA, USA. July 10-15.

2. J.F. Vivo-Vilches, **A. Elmouwahidi**, F. Carrasco-Marín, F.J. Maldonado-Hódar, A.F. Pérez-Cadenas. Fonctionalization of activated carbon for oxygen reduction reaction. Carbon 2016. Penn State Conference Center, State College, PA, USA. July 10-15.

3. **Abdelhakim Elmouwahidi**, Agustín F. Pérez-Cadenas, Francisco Carrasco-Marín, Francisco José Maldonado Hódar. Carbones activados dopados con oxido de manganeso. Estudio de su comportamiento como electrodos de supercondensadores. GEC2015, XIII Reunión del Grupo Español del Carbón. Del 18 al 21 de Octubre de 2015 - Alicante

4. **Abdelhakim Elmouwahidi**, Agustín F. Pérez-Cadenas, Francisco Carrasco-Marín, Francisco José Maldonado Hódar. Geles de carbón obtenidos mediante polimerización de resorcinol, carbamato de amonio y melamina con formaldehido como electrodos para supercondensadores. GEC2015, XIII Reunión del Grupo Español del Carbón. Del 18 al 21 de Octubre de 2015 - Alicante.

5. **Abdelhakim Elmouwahidi**, E. Bailón-García, Agustín F. Pérez-Cadenas, Francisco Carrasco-Marín, Francisco José Maldonado Hódar. Composites de carbón-óxido de titanio como electrodos de supercondensadores. . GEC2015, XIII Reunión del Grupo Español del Carbón. Del 18 al 21 de Octubre de 2015 - Alicante.

6. J.F. Vivo-Vilches, **A. Elmouwahidi**, F. Carrasco-Marín, F.J. Maldonado-Hódar, A.F. Pérez-Cadenas. Carbones activados funcionalizados con azufre como electrocatalizadores en la reacción de reducción del oxígeno. GEC2015, XIII Reunión del Grupo Español del Carbón. Del 18 al 21 de Octubre de 2015 - Alicante.

7. **Abdelhakim Elmouwahidi**, Agustín F. Pérez-Cadenas, Francisco Carrasco-Marín, Francisco José Maldonado Hódar. Hierarchical porous carbon from resorcinol formaldehyde as electrode for supercapacitors. XXXIX Reunión (39RIA) Ibérica de Adsorción. Baeza 14-17 septiembre 2014.

8. **Abdelhakim Elmouwahidi**, Agustín F. Pérez-Cadenas, Francisco Carrasco-Marín, Francisco José Maldonado Hódar. Activación química de alpechín, estudio del Comportamiento de los carbones activados como electrodos de supercondensadores. XXXIX Reunión (39RIA) Ibérica de Adsorción. Baeza 14-17 septiembre 2014.

9. **Abdelhakim Elmouwahidi**, Agustín F. Pérez-Cadenas, Francisco Carrasco-Marín, Francisco José Maldonado Hódar. Activación química de alpechín, carbones activados preparados mediante activación de madera de olivo con KOH y H_3PO_4. Aplicación como electrodos para supercondensadores. XXXIX Reunión (39RIA) Ibérica de Adsorción. Baeza 14-17 septiembre 2014.

10. **Abdelhakim Elmouwahidi**, Agustín F. Pérez-Cadenas, Francisco Carrasco-Marín. Pirólisis de polietileno de baja densidad catalizada por óxidos de hierro, cobalto y níquel. Estudio de los materiales de carbón como electrodos de supercondensadores. XII Reunión del Grupo Español del Carbón (GEC), 20 a 23 de Octubre 2013, Madrid.

11. **Abdelhakim Elmouwahidi**, Agustín F. Pérez-Cadenas, Francisco Carrasco-Marín. Obtención de carbones activados mediante activación química de residuos agrícolas. Caracterización química, textural y Estudio de su comportamiento como electrodos de supercondensadores. XII Reunión del grupo español del carbón (GEC), 20 a 23 de Octubre 2013, Madrid.

1. INTRODUCCIÓN

El consumo energético mundial aumenta sin cesar, impulsado tanto por el crecimiento socioeconómico de las naciones como por el aumento de la población mundial, que alcanzará los 9.100 millones en el año 2050, (Figura 1). Las abundantes reservas mundiales de combustibles fósiles hacen suponer que este recurso seguirá siendo utilizado durante muchos años. No obstante cada vez existe una mayor alarma y leyes más restrictivas que afectan a las emisiones de gases efecto invernadero y un creciente interés por la protección y cuidado del medio ambiente ante la amenaza del Calentamiento Global.

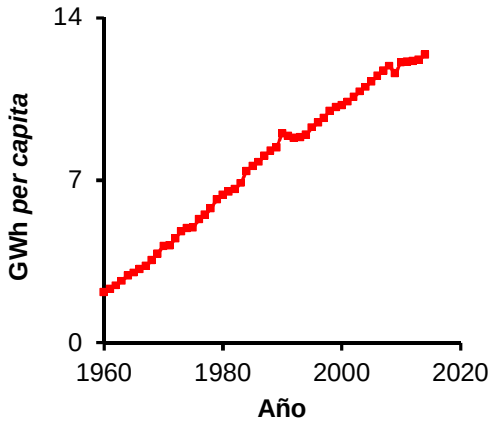

Figura 1. Consumo energético mundial per cápita entre los años 1960 y 2014. http://www.bancomundial.org/

La Agencia Internacional de Energía (IEA por sus siglas en inglés) en su informe del año 2016 [1] (Figura 2) puso de manifiesto la gran dependencia que aún hoy en día existe hacia las fuentes de energía de origen fósil y su variación desde el año 1973 al año 2014. La versatilidad y abundancia de reservas de combustibles fósiles en todo el mundo hace suponer que este recurso va a seguir siendo utilizado en los próximos años. La necesidad de generar energía eléctrica en el mismo momento en que se produce su demanda hace que el funcionamiento de los sistemas eléctricos sea complejo, esto es debido a la gran dificultad que actualmente existe para su almacenamiento.

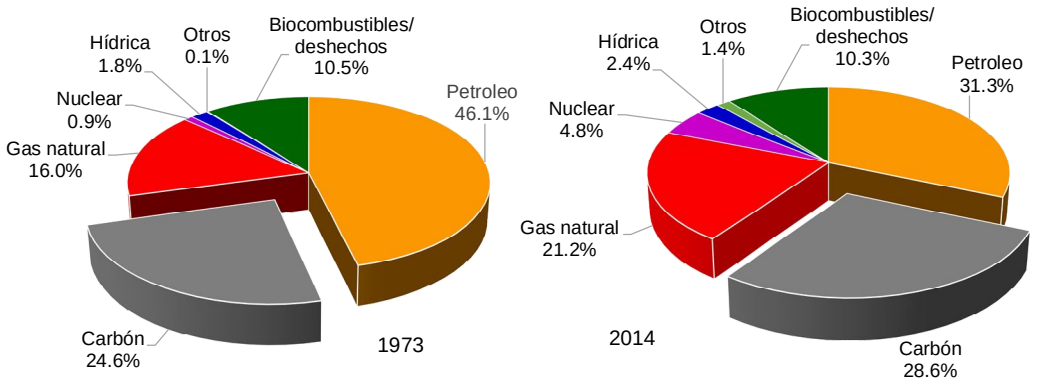

Figura 2. Origen de las fuentes primarias de energía empleadas en el mundo

Durante este periodo la producción de energía a partir de biomasa apenas ha sufrido variación debido a las problemáticas generadas por su implantación como son: sistemas de monocultivo y problemas de seguridad alimentaria debido al incorrecto uso del recurso suelo. El uso de productos agrícolas para la producción de biocombustibles provoca un incremento en los precios de productos alimenticios al ser estos usados en la producción de biocombustibles como la caña de azúcar, el arroz, el maíz y la palma de cera entre otros. Así, de acuerdo con el informe emitido por la Organización de las Naciones Unidas para la Alimentación y la Agricultura (FAO) (2013), se está generando un nuevo reto para mantener en equilibrio entre progreso y sostenibilidad.

Una de las principales limitaciones que presentan las energías renovables, especialmente eólica, solar y mareomotriz (entre otras), cuyo crecimiento en el mismo periodo correspondió a un 1,3 %, es que su producción fluctúa con las condiciones climatológicas. Con el fin de garantizar un uso eficiente y sostenible de las energías obtenidas a partir de fuentes renovables, se hace necesario el almacenamiento de estas energías durante los picos de producción, para posteriormente liberarlos en los sistemas de suministro eléctrico durante las horas de mayor demanda o cuando los niveles de producción sean bajos en relación con la demanda energética. Por esta razón, se ha intensificado la búsqueda de

sistemas más eficientes que permitan el almacenamiento y suministro de la energía con mayor durabilidad y mejores tiempos de respuesta durante los ciclos de carga y descarga.

Los dispositivos diseñados para el almacenamiento de energía eléctrica, se clasifican generalmente de acuerdo con el sistema de almacenamiento que utilizan; pudiendo ser este indirecto como en el caso de las baterías, en el que la energía es almacenada en forma de energía química potencialmente disponible donde en el proceso de oxidación - reducción de las especies electroquímicamente activas y los procesos directos, en estos la energía es almacenada a manera de cargas electrostáticas; como en el caso de los condensadores, en forma de cargas positivas y negativas en los electrodos.

Los sistemas de mayor interés para generar y almacenar energía eléctrica son las celdas de combustible, baterías recargables y supercondensadores, los cuales son una alternativa para mitigar el impacto ambiental, reduciendo la huella de carbono y el calentamiento global. Si se dispusiese de un almacenamiento eficiente, las energías renovables no tendrían límites técnicos, y estarían sometidas tan solo a límites económicos marcados por los precios de mercado. Estas técnicas de almacenamiento de energía eléctrica (Electric Energy Storage – EES) también pueden aplicarse en otros sectores tales como el de la automoción y el industrial.

La selección del tipo de EES, para una aplicación específica con un adecuado funcionamiento y un mínimo consumo de energía, dependerá de la carga que acepte el dispositivo a un voltaje fijo, tiempo de almacenamiento y número de ciclos de carga-descarga a un voltaje determinado [2,3].

Las baterías y los condensadores electroquímicos o supercondensadores (SCs) se consideran como las tecnologías más destacadas para un EES eficiente. En la Figura 3 se presenta el diagrama de Ragone [4], en el cual se compara la energía específica con la potencia específica de diversos sistemas de almacenamiento de energía. En esta figura se observa como los supercondensadores cubren el espacio de necesidades energéticas existente

entre los condensadores convencionales (electrolíticos o película metálica) y las baterías. Los condensadores electroquímicos funcionan mediante procesos no farádicos, por lo que idealmente el material del electrodo no presenta mayores cambios durante el proceso de almacenamiento de energía el cual es mucho más rápido que el realizado por las baterías, razón por la cual a pesar de poseer generalmente densidades de energía más bajas que las de las baterías estos presentan mayores densidades de potencia. Los SCs pueden utilizarse en sistemas que requieran energía durante tiempos comprendidos entre 10^{-2} s ≤ t ≤ 10^{2} s. En comparación con las baterías recargables, los SCs tienen una densidad de 1 a 500 veces menor y una potencia de 1 a 3 órdenes de magnitud superior, alta reversibilidad de carga/descarga. Adicionalmente, los SCs no tienen partes móviles, son dispositivos seguros, no requieren enfriamiento ni otras instalaciones o servicios auxiliares, no necesitan mantenimiento, son ampliamente modulares respecto al voltaje y capacidad, se pueden producir a bajo costo y muy poco contaminantes. Las baterías almacenan energía mediante reacciones químicas capaces de generar carga mientras que los SCs almacenan energía electroquímica directamente como carga.

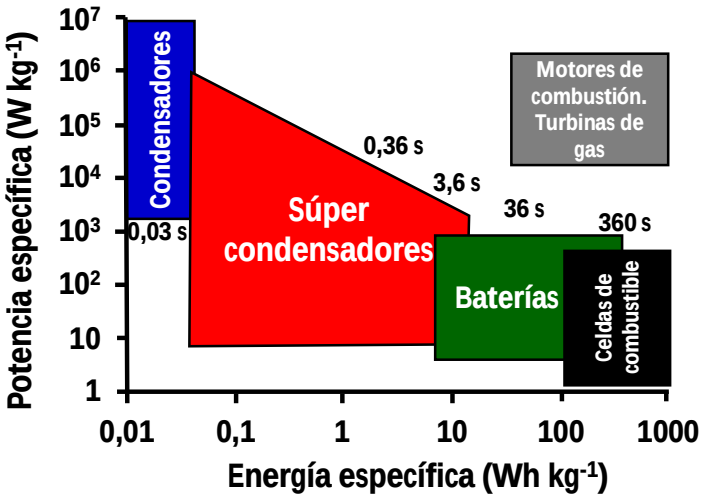

Figura 3. Diagrama de Ragone para los principales dispositivos empleados para el almacenamiento de energía.

El la Tabla 1 se comparan las características más importantes entre condensadores electrolíticos, supercondensadores y baterías [5]. En comparación con las baterías recargables, los SCs tienen una densidad de 1 a 500 veces menor y una potencia de 1 a 3 órdenes de magnitud superior, alta reversibilidad de carga/descarga. Adicionalmente, los SCs no tienen partes movibles, son dispositivos seguros, no requieren enfriamiento ni otras instalaciones o servicios auxiliares, no necesitan mantenimiento, son ampliamente modulares respecto al voltaje y capacidad, se pueden producir a bajo costo y muy poco contaminantes [6,7]. Las baterías almacenan energía mediante reacciones químicas capaces de generar carga mientras que los SCs almacenan energía electroquímica directamente como carga.

Tabla 1. Características de los dispositivos para almacenamiento de energía eléctrica

Característica	Condensador	Supercondensador	Batería
Energía específica (Wh/kg)	< 0,1	1 – 10 h	10-100
Potencia específica (W/kg)	>> 10000	500 – 10000	<1000
Tiempo de descarga (s)	10^{-6} a 10^{-3}	10^{-2} s ≤ t ≤ 10^{2} s	0,3 – 3 h
Tiempo de carga (s)	10^{-6} a 10^{-3}	10^{-2} s ≤ t ≤ 10^{2} s	1 – 5 h
Eficiencia carga/descarga (%)	~100	85-98	75 – 85
Ciclos de vida	Infinito	>500000	~1000
Determinante máximo potencial	Espesor y resistencia dieléctrico	Potencial de estabilidad entre electrodo y electrolito	Termodinámica de las reacciones de fase
Determinante carga almacenada	Área electrodo y dieléctrico	Microestructura del electrodo y composición del electrolito	Masa activa y termodinámica

Otra línea de investigación muy ligada a la apuesta por la transición del modelo energético es la Reacción de Electro - Reducción de Oxígeno (ORR) [8]. Esta reacción forma parte del proceso catódico de las pilas de combustible, siendo también motivo de estudio de la presente Tesis Doctoral. Las pilas de combustible son dispositivos electroquímicos capaces de convertir energía química en energía eléctrica mediante la electro-oxidación de un combustible, como por ejemplo hidrógeno o metanol. Dicha oxidación se lleva a cabo en el compartimento anódico, mientras que en el catódico se lleva a cabo la reacción de electro-reducción, usualmente una ORR en la que la fuente de oxígeno utilizada es aire en la mayoría de los casos. Sin embargo, Las pilas de combustible todavía se enfrentan a algunos problemas que retrasan su incorporación al mercado energético, tales como factores económicos, problemas de diseño de materiales, así como otras cuestiones técnicas de operación del dispositivo. Ya a principios del siglo XX las pilas de combustible experimentaron una gran atención debido al aumento del uso de la electricidad y su obtención. La primera implementación exitosa de las pilas de combustible giró en torno a las tecnologías espaciales, proporcionando la energía eléctrica requerida en el vehículo, calor y además agua potable para la tripulación. El agua es el único producto de reacción cuando el combustible utilizado es hidrógeno. Desde un punto de vista del mecanismo de funcionamiento del dispositivo, las pilas de combustible tienen similitudes con las baterías y los motores, sin embargo, tiene una gran ventaja y es que no necesitan recargase. Además cuando solamente se obtiene agua como “residuo”, estos dispositivos son muy interesantes en un contexto medio ambiental. En resumen, las pilas de combustible pueden encontrar aplicaciones comerciales muy interesantes en el ámbito del transporte, la generación de energía estacionaria, y en dispositivos portátiles de baja potencia. Sin embargo, todavía presentan dos limitaciones significativas que afectan su disponibilidad en el mercado: coste y fiabilidad [8]. El abaratamiento del coste pasa fundamentalmente por el desarrollo de nuevos electro-catalizadores más económicos para la reacción catódica, es decir la electro-reducción de oxígeno.

1.1. SUPERCONDENSADORES

El primer condensador electroquímico fue patentado en 1957 por General Electric Company, quienes diseñaron un dispositivo basado en el modelo de almacenamiento de energía eléctrica en la doble capa, propuesto inicialmente por Helmholtz, este condensador compuesto por electrodos de carbón poroso usaba el mecanismo de almacenamiento de energía en la doble capa para cargarse; a partir de entonces se han diseñado una serie de dispositivos para el almacenamiento de energía entre los que merece la pena destacar los recogidos en la Tabla 2 [5].

Los supercondensadores son una nueva generación de condensadores similares a los dispositivos de almacenamiento químico de energía, baterías, que pueden almacenar una carga eléctrica moderada, entre 10 a 1000 veces superior a los condensadores convencionales, pero manteniendo prácticamente la misma densidades de potencia. Los SCs también poseen alta capacidad de almacenamiento de energía y altas densidades de potencia (10 - 10^6 W kg^{-1}), tiempo de respuesta más bajos (0,3 - 3 s) y estabilidad en cada ciclo carga y descarga sin afectar su rendimiento [6,9].

Los SCs se fundamentan en procesos electroquímicos, estos dispositivos están constituidos por un electrolito, dos electrodos (ánodo y cátodo) y un separador poroso que impide el contacto electrónico entre los materiales conductores [10]. El electrolito debe tener una elevada conductividad iónica y una baja conductividad eléctrica de manera que los electrones son obligados a circular por el exterior del dispositivo, proporcionando así la energía deseada. En el caso de los electrodos las conductividades iónica y electrónica deben ser elevadas.

Las principales limitaciones de los SCs son la baja densidad de energía, mayor velocidad de auto-descarga y costes de fabricación más elevados que las baterías. Hoy día se están llevando a cabo grandes esfuerzos para aumentar la densidad de energía mediante la preparación de electrodos con materiales de mayor capacidad específica, materiales con una porosidad que se adapte al

tamaño de los iones del electrolito y electrolitos líquidos con un mayor rango de voltaje de trabajo [10].

Tabla 2. Condensadores comercialmente disponibles, voltaje de operación y capacidad de almacenamiento de energía.

Fabricante	Nombre comercial	Capacidad (F)	Voltage (V)	Electrodo/electrolito
Asahi Glass	EDLC	500–2000	3.14/42	Carbon/non-aqueous
AVX	Bestcap	0.022–0.56	3.5–12	Carbon/polymer/ aqueous
Cap-XX	Supercapacitor	0.09–2.8	2.25–4.5	Carbon/non-aqueous
Cooper	PowerStor	0.47–50	2.3–5	Aerogel/non-aqueous
ELNA	Dynacap	0.333–100	2.5–6.3	Carbon/non-aqueous
Epcos	Ultracapacitor	5–5000	2.3, 2.5	Carbon/non-aqueous
Evans	Capattery	0.01–1.5	5.5, 11	Carbon/aqueous
Maxwell	Boostcap/Power Cache	1.8–2600	2.5	Carbon/non-aqueous
NEC	Supercapacitor	0.01–6.5	3.5–12	Carbon/aqueous Carbon/organic
Nippon Chemi-Con	DLCAP	300–3000	2.3, 2.5	Carbon/non-aqueous
Ness	NessCap	3–5000	2.3, 2.7	Carbon/organic
Matsushita/ Panasonic	Gold capacitor	0.1–2500	2.3–5.5	Carbon/organic
Tavrima/ECOND	Supercapacitor	0.13–160	14–300	Carbon/aqueous

La introducción de nuevos materiales con propiedades electro-activas y área superficial elevada tales como carbón, polímeros conductores y óxidos

metálicos han facilitado el desarrollo de electrodos con una mayor capacidad por unidad de área y mayor eficiencia [4,6,11]. Los SCs un gran interés tecnológico en aplicaciones como acoplamiento con baterías (sistemas híbridos), fuentes de energía portátil, actuadores electroquímicos y en sistemas de generación de potencia con energía solar y eólica [9,12].

En los SCs la carga eléctrica se almacena debido a la acumulación de iones en la superficie interna de ambos electrodos (ánodo-cátodo), los iones sin solvatar del electrolito se ajustan al poro formando una doble capa eléctrica en combinación con los electrones en el material conductor (Figura 4) [13,14]. La energía almacenada en el condensador se da por un exceso y una deficiencia de electrones durante la carga que es reversible durante la descarga. Idealmente no hay transferencia de electrones en la interfase del electrodo, y el almacenamiento de carga eléctrica es electrostático. La capacidad de almacenamiento de energía en la doble capa se conoce como capacidad de la doble capa eléctrica y la capacidad debido a la presencia de reacciones de oxidación-reducción se conoce como pseudocapacidad [6].

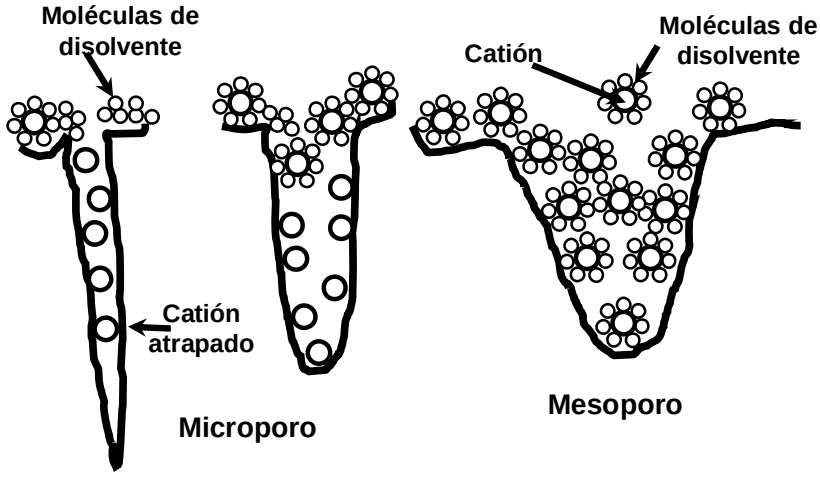

Figura 4. Esquema de adsorción de los iones del electrolito en la superficie de poros con diferentes tamaños.

La clasificación mayoritariamente aceptada para los SCs de acuerdo con diversos autores [9,12,15] es:

i) *Por la forma de almacenamiento de energía:* doble capa electroquímica, pseudocondensadores o híbridos

ii) *Por el material de los electrodos:* carbón, óxidos de metales de transición o polímeros conductores

iii) *Por la naturaleza del electrolito:* acuoso, orgánico o líquido iónico

iv) *Por la simetría de los electrodos:* simétricos (SSCs) si los dos electrodos están construidos del mismo material y asimétricos (ASCs) si los materiales de los dos electrodos son diferentes.

En los condensadores de doble capa electroquímica (EDLCs) el almacenamiento de carga se da por efectos electrostáticos. La corriente generada durante este proceso se debe esencialmente a acumulación de cargas cuando se aplica una diferencia de voltaje. La carga se acumula en la superficie del electrodo siguiendo la atracción natural de las cargas opuestas. Este proceso es altamente reversible y no hay transferencia de cargas por reacciones químicas o asociadas con procesos farádicos. La ausencia de transformaciones de fase y limitaciones cinéticas ayudan a prolongar el tiempo de vida del condensador [16].

El concepto de doble capa fue desarrollado a partir de los estudios realizados por Helmholtz (1879), Gouy (1910), Chapman (1913) y posteriormente ajustado por Stern y Geary (1924) [17,18,19]. La doble capa se establece cuando un conductor eléctrico está en contacto con un conductor iónico (

Figura 5). En una solución electrolítica, los iones se comportan dependiendo del lugar donde se encuentren en la solución y de acuerdo a su propia naturaleza. Los iones que se encuentran en el seno de la solución están rodeados por moléculas polares del disolvente (iones solvatados) y se encuentran rodeados por otros iones también solvatados es decir se hallan en un equilibrio dinámico de cargas. A medida en que los iones se encuentran más cerca de la interfaz (electrodo), los iones solvatados son atraídos por la superficie del sólido,

por una carga igual pero de signo opuesto y difunden hacia el interior. En la interfase electrodo/electrolito se forma una doble capa electroquímica en la cual se almacena la energía [20].

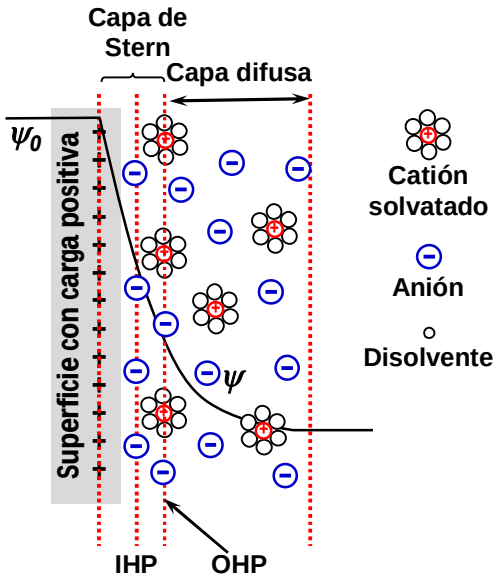

Figura 5. Modelo de Stern para la doble capa eléctrica

La capacidad de la doble capa eléctrica se correlaciona con las propiedades superficiales y porosas de los electrodos (superficie, volumen y distribución del tamaño de poros), y con la concentración de iones en disolución y el tamaño de los mismos. La atracción electrostática de los iones se da principalmente en los microporos, sin embargo la presencia de mesoporos es necesaria para un transporte eficiente de los iones. La principal ventaja de los EDCLs es la habilidad de propagar la carga dinámica, lo que permite una liberación rápida de la energía. La doble capa en la interfase se puede formar rápidamente lo que se traduce en altas tasas de potencia, propiedad inherente de un EDLC en comparación con una batería convencional donde se requiere el transporte de masa a través de distancias más largas [7].

El comportamiento de un condensador de doble capa eléctrica durante la carga y la descarga se representa mediante el esquema de la Figura 6. En el diseño de EDCLs los principales objetivos son optimizar la estructura porosa para adaptarla a los iones del electrolito, aumentar el área superficial, disminuir la distancia entre los electrodos y aumentar la ventana de potencial [2,9,21].

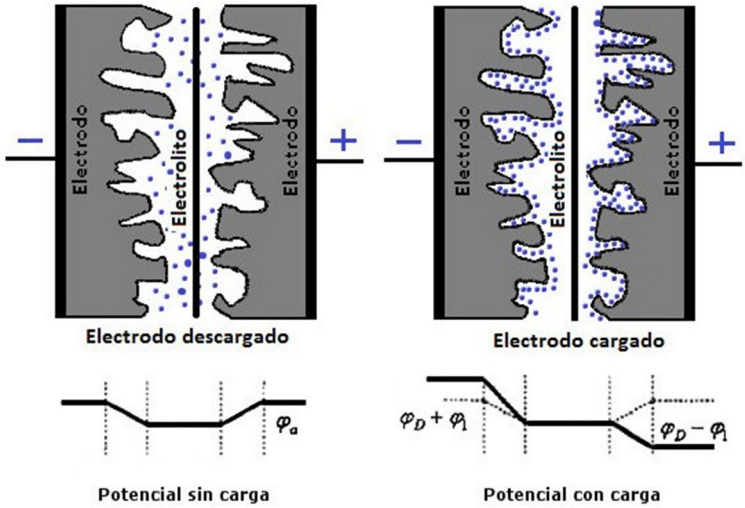

Figura 6. Esquema de carga y descarga de un supèrcondensador de doble capa

A pesar de la necesidad de electrodos con un área superficial alta, para obtener una elevada energía almacenada en un dispositivo razonablemente pequeño, existen otros aspectos químico-físicos de la superficie que son críticos para el rendimiento del electrodo. La capacidad interfacial de la doble capa ($\mu F/cm^2$) depende en primer lugar de la distribución de tamaños de poros y de la mojabilidad de la superficie, parámetros que determinan la accesibilidad del sistema poroso a un electrolito dado, y en segundo lugar de las características estructurales de la fase sólida [22]. La conductividad de los electrodos de carbón depende del tratamiento térmico, microestructura, hibridación y contenido en heteroátomos que modifican las propiedades electrónicas y el comportamiento electroquímico [17,23,24].

Los materiales de carbón más utilizados para EDLC son los carbones activados debido a que están disponibles comercialmente, son económicos y pueden producirse con un área superficial y una microporosidad alta. Sin embargo, estas dos últimas no son suficientes para un buen desempeño electroquímico, debido a que es necesario que los microporos estén bien interconectados mediante una proporción adecuada de mesoporos [25,26].

La carga en los pseudocondensadores o supercondensadores redox se almacena por medio de la formación de la doble capa eléctrica a partir de rápidas reacciones farádicas en las que se da una transferencia de carga en la interfase entre el electrodo y el electrolito. Este almacenamiento de carga se da por medio de diferentes procesos tales como electro-adsorción, reacciones de óxido-reducción y procesos de intercalación en un rango amplio de potencial. La capacidad se asocia con un proceso de transferencia de carga originada por el material activo [25].

En los materiales de carbón la capacidad puede verse incrementada por efectos pseudocapacitivos [27] debido a la presencia de grupos superficiales oxígeno y/o nitrógeno que permiten obtener una capacidad adicional a la capacidad de la doble capa mediante de reacciones farádicas. El incremento de la capacidad se debe principalmente a mecanismos de óxido-reducción y son más significativos que los aportes de la doble capa. La pseudocapacidad originada por grupos funcionales nitrógeno se da por la presencia de funcionalidades tipo piridina, pirrol, piridona y nitrógeno cuaternario que interactúan con los iones del electrolito y son especies activas [28]. La introducción de grupos quinona, debido a la presencia de grupos funcionales oxígeno, promueve fenómenos pseudofarádicos que pueden influir positivamente en la capacidad del supercondensador.

La deposición de partículas de un óxido de metal de transición es uno de los métodos más prometedores debido a que la capacidad específica se puede mejorar entre 10 a 100 veces dependiendo de la naturaleza del óxido y de carácter netamente pseudocapacitivo. Los óxidos de metales de transición, tienen un área

superficial moderada (~100 m^2/g), alta conductividad electrónica (>10 S/cm), fácil procesamiento mediante mecanismos electro-adsorción y/o reacciones redox dominantes. El óxido de rutenio hidratado, RuOx(OH), se ha estudiado extensamente como material de electrodo para supercondensadores debido a su alta capacidad (720 F/g) en electrolito acuoso [29,30]. Las capacidades específicas obtenidas mediante RuO_2 son muy altas, pero el precio de este material ha limitado sus aplicaciones y le han dado preferencia a otros materiales como óxido de manganeso hidratado (α-$MnO_2.nH_2O$) [30]. Algunos de los materiales que se han estudiado como electrodos de supercondensadores son: NiO, $Ni(OH)_2$, MnO_2, Co_2O_3, IrO_2, FeO, TiO_2, SnO_2, V_2O_5, MoO y In_2O_3, de los cuales ninguno se ha usado comercialmente y todavía siguen los trabajos a escala de laboratorio [29].

Otros materiales con propiedades pseudocapacitivas son los polímeros conductores eléctricos (ECPs), conocidos como metales sintéticos debido a su alto grado de dopado y rápido cambio electroquímico. Estos materiales se caracterizan por tener alta conductividad eléctrica, fácil procesado y ser más económicos que los óxidos metálicos. Los procesos de carga y descarga son generalmente rápidos, el almacenamiento de carga está dominado por mecanismos pseudocapacitivos y se caracterizan por altas capacidades específicas (400 F/g). A diferencia de los carbones activados la carga almacenada se acumula en todo el volumen del electrodo. Durante la oxidación (dopado) los iones son transferidos a la cadena principal del polímero y cuando ocurre la reducción (desdopado) los iones son devueltos a la solución. La oxidación de la cadena provoca la apertura de la red polimérica para la penetración de los contra-iones solvatados o su cierre al ser expulsados durante la reducción. Estos cambios de volumen hacen que la estructura se contraiga o se hinche, conduciendo a la degradación mecánica del electrodo, baja estabilidad y disminución de la eficiencia electroquímica durante los ciclos de carga y descarga. Los ECPs más comunes son polianilina (PANI), polipirrol (PPy), poli-tiofenos (PEDOT) [31,32].

En los supercondensadores híbridos los mecanismos de almacenamiento de carga que se llevan a cabo en el ánodo y en el cátodo son diferentes. Los efectos electrostáticos y farádicos se combinan para obtener capacidades de almacenamiento y densidades de energía mayores respecto a los EDCLs, manteniendo la misma densidad de potencia, y sin sacrificar la estabilidad cíclica y accesibilidad que ha limitado a los pseudocondensadores. El mecanismo de operación de los condensadores híbridos se fundamenta en las propiedades intrínsecas de los materiales de los dos electrodos. Algunos supercondensadores híbridos están conformados por un electrodo de doble capa de carbono y otro tipo batería, de tal forma que se aprovecha la alta densidad de energía de las baterías y la alta densidad de potencia de los ECs.

Los electrolitos líquidos empleados en la fabricación de supercondensadores idealmente deben tener una alta conductividad iónica y baja conductividad electrónica (~10 mS/cm). Adicionalmente, los electrolitos deben tener una baja viscosidad, permanecer líquidos en el intervalo de temperatura de trabajo y ser muy estables durante los ciclos de carga y descarga. El potencial de descomposición del electrolito condiciona el voltaje de trabajo. Así, cuanto mayor sea el intervalo de potencial de trabajo mayor será la capacidad de carga y la densidad energética.

En las soluciones electrolíticas el tamaño del catión y el anión del electrolito y el tipo de disolvente son importantes para lograr una adsorción efectiva de los iones sobre la superficie del electrodo y la formación de la doble capa. La selección del tipo de electrolito depende de la distribución de la porosidad del material de carbón para facilitar la entrada y salida del ion. Los electrolitos se clasifican como acuosos, orgánicos y líquidos iónicos. Los electrolitos acuosos requieren que los electrodos posean un tamaño de poro mínimo de 0,5 nm, tienen bajas tensiones de ruptura y baja conductividad electrónica (~1 S/cm para H_2SO_4 1 M). Aunque la ventana termodinámica del agua es 1,23 V, en la práctica el voltaje de operación máximo varía entre 0,7 y 1 V, debido a factores experimentales que son difíciles de controlar y reducen significativamente la energía disponible [27]. La densidad

de energía que se puede conseguir con los electrolitos acuosos está alrededor de 3,5 Wh/kg.

Los electrolitos acuosos son los más interesantes desde el punto de vista industrial debido a su bajo costo, manipulación a presión atmosférica, largo tiempo de vida y baja resistencia interna. Los más empleados son ácido sulfúrico, sulfatos e hidróxidos de sodio y potasio.

Los electrolitos orgánicos más usados son sales de amonio cuaternario tales como tetraetilamonio tetraflouroborato ($TEABF_4$), tetraetilamonio trifluorometilsulfonato (TEATFS) o tetraetilamonio metilsulfonato ($TEAMeSO_3$) con propilencarbonato o acetonitrilo como disolventes [27,33,34]. En un medio aprótico el tamaño de los iones solvatados es mayor que en un medio acuoso por lo que los poros más estrechos no son accesibles para los iones y no contribuyen a la capacidad de la doble capa [25].

Este tipo de electrolitos se caracterizan por tener una conductividad electrónica muy baja (~0,05 S/cm) y una resistencia específica más alta que el medio acuoso, lo cual disminuye la potencia máxima. Este efecto se puede compensar con un incremento de la ventana de potencial. Así, Los electrolitos orgánicos permiten un potencial de operación hasta 2,3–2,7 V, superior a los electrolitos acuosos. Un aumento de potencial significa un aumento en la densidad de energía y una disminución del número de celdas requeridas para un banco de potencia. En el caso de los electrolitos orgánicos se han reportado densidades de energía de hasta 18 Wh/kg.

Sin embargo, los electrolitos apróticos tienen un alto coste debido a que necesitan unas condiciones específicas de producción (hay que evitar el contacto con el aire y la humedad), son muy viscosos lo que dificulta su manipulación, inestables en presencia de los electrodos de carbón y contaminantes [4,27].

Los líquidos iónicos (ILs) son sales orgánicas en estado líquido a temperatura ambiente, sintetizados mediante la combinación de un catión orgánico con una amplia variedad de aniones poliatómicos, muy asimétricos y

voluminosos, unidos por fuerzas atractivas más débiles que las sales iónicas convencionales. Las propiedades de los ILs dependen principalmente del tipo de catión y el anión, así como de la longitud del grupo alquilo [35]. Se trata de una nueva clase de electrolitos propuestos como una opción muy prometedora para obtener un alto potencial en un ambiente favorable para su aplicación en dispositivos EES [36]. Estos se caracterizan porque son no volátiles, no inflamables, fáciles de manipular, de baja conductividad iónica y conductividad electrónica relativamente alta, de bajo coste de producción y muy alta viscosidad [37,38]. Aunque la característica más atractiva es su estabilidad a elevados valores de potencial (3–3,5 V).

1.1.1. Parámetros característicos de los supercondensadores

La carga almacenada, Q, en un condensador es directamente proporcional a la capacidad equivalente y a la diferencia de potencial, ΔV, como indica la ecuación (1).

$$Q = C \times \Delta V \tag{1}$$

donde Q es la carga en Coulombios, V el voltaje en Voltios y la capacidad C en Faradios. Un condensador electroquímico opera bajo el mismo principio de los condensadores electrostáticos convencionales. La capacidad de un condensador viene determinada por la ecuación (2).

$$C = \frac{Q}{V} = \frac{S\varepsilon}{d} \tag{2}$$

Donde ε es la permitividad o constante dieléctrica del electrolito, S el área superficial de la interfase electrodo/electrolito y d es el grosor del dieléctrico. Sin embargo, cuando se aplica un voltaje entre los dos electrodos de un SC, Figura 6, se forma una doble capa sobre cada electrodo. Por tanto, el mecanismo completo se comporta como dos condensadores conectados en serie y su capacidad, C_t, viene dada por la ecuación (3) [26].

$$\frac{1}{C_t} = \frac{1}{C_1} + \frac{1}{C_2} \quad (3)$$

dónde C_1 y C_2 son los valores de la capacidad de la doble capa eléctrica en cada electrodo. Si el condensador está compuesto por dos electrodos de diferente capacidad, el componente con menor capacidad es el que contribuye más al valor de la capacidad total debido a la proporcionalidad inversa. La capacidad depende esencialmente del material del electrodo.

La capacidad de cada electrodo de un condensador de doble capa se puede calcular mediante la ecuación (2) pero ahora d es el grosor de la doble capa eléctrica. Este grosor depende de la concentración del electrolito y del tamaño de sus iones, y está entre 0,5 y 1 nm para los electrolitos concentrados. Si este valor de d se introduce en la ecuación (2) se puede tener una idea de la gran ventaja de los SCs sobre los condensadores convencionales. Debido a la distancia extremadamente corta entre cargas en la interfase la capacidad alcanza los 10–20 $\mu F/cm^2$. Adicionalmente, al aumentar la superficie de los electrodos mediante el uso de materiales porosos se pueden obtener altas capacidades específicas.

A veces puede surgir además otro tipo de capacidad debida a transferencia de carga farádica y no debida a cargas electrostática y que se denomina pseudocapacidad para distinguirla de la capacidad debida a la doble capa eléctrica. Esta pseudocapacidad tiene su origen en las rápidas reacciones redox que pueden ocurrir entre el electrodo y el electrolito, como ya se ha explicado anteriormente.

La energía específica almacenada en un SC, E ($kWh\ kg^{-1}$), es proporcional a la capacidad y al cuadrado del voltaje según la ecuación (4) [39]. El voltaje de carga depende principalmente del potencial de estabilidad del electrolito, por lo que este es uno de los factores que limita la densidad de energía.

$$E = \frac{1}{2} C V^2 \quad (4)$$

La potencia específica de un SC, P (W/kg), indica la rapidez con que la energía específica almacenada puede extraerse del sistema para ser utilizada, y se define mediante la ecuación (5).

$$P = \frac{V^2}{4 \times ESR} \tag{5}$$

donde *ESR* representa la resistencia equivalente en serie o resistencia interna y es igual a la suma de las resistencias de todos los materiales que componen el dispositivo entre los contactos externos (material del electrodo, negro de carbón conductor, aglomerante, separador y electrolito). Con objeto de aumentar la potencia, es necesario minimizar dicha resistencia.

Conocida la resistencia y la capacidad se puede obtener la constante de tiempo, τ (s), según la ecuación (6). Esta constante de tiempo indica la rapidez con la que puede cargarse o descargarse un condensador.

$$\tau = ESR \times C \tag{6}$$

Si el comportamiento del electrodo es capacitivo, es decir, el sistema almacena energía electrostáticamente y no existen reacciones redox, el circuito equivalente consiste en un condensador y una resistencia en serie (Figura 7) [27].

Figura 7. Circuito equivalente RC en serie

La movilidad de los iones depende del tamaño y volumen de los poros y de la tortuosidad de la matriz carbonosa, por lo que un circuito equivalente está compuesto por las resistencias distribuidas a través de todo el material [25]. Los poros con tamaños diferentes tienen diferentes constantes de tiempo. Adicionalmente, se debe tener en cuenta la resistencia entre las partículas y el electrolito y la resistencia de contacto interparticular. Estas consideraciones pueden ser representadas por un circuito equivalente RCC, en el cual están involucrados una serie de resistencias y capacidades debidas a los poros de

diferente tamaño (Figura 8). Este modelo se ajusta más para aplicaciones reales de almacenamiento de energía [40,41].

La capacidad de un condensador varía durante cada carga y descarga, aunque idealmente un condensador debe almacenar siempre la misma carga. Sin embargo, en la práctica estos dispositivos experimentan una auto-descarga en el estado de carga que es causada por fugas de corriente, por el deterioro de los electrodos o por mecanismos de transferencia de carga a través del medio dieléctrico. Este comportamiento no ideal debe ser mínimo para mejorar la eficiencia de carga-descarga y la fiabilidad de los dispositivos comerciales [42].

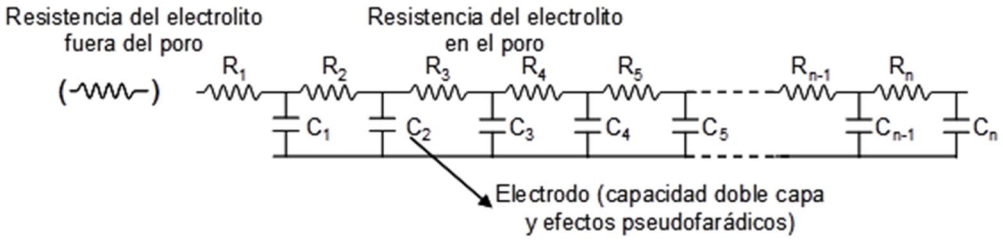

Figura 8. Modelo de circuito equivalente de un material poroso

La auto-descarga a través de una resistencia R, está dada por el cambio de potencial en función del tiempo según la ecuación (7) [43].

$$V(t) = V_0 \exp\left(-\frac{t}{RC}\right) \qquad (7)$$

En la actualidad se emplean diversas técnicas experimentales para determinar el rendimiento electroquímico de un material, siendo los más usuales la voltametría cíclica, espectroscopía galvanostática de carga/descarga y la espectroscopía de impedancia electroquímica, técnicas que se describirán más adelante.

1.2. ELECTRO-REDUCCIÓN DE OXÍGENO

La ORR puede transcurrir bien a través de un proceso de cuatro electrones reaccionando directamente el oxígeno con agua o protones, o a través de un proceso de dos electrones, que transcurre en dos etapas, menos eficiente, y que

implica la formación de peróxidos como intermedio; en ambos casos la eficiencia también depende del pH del medio. A continuación se detallan las correspondientes reacciones que se producen con ambos tipos de electrolitos y medio acuoso:

1) Proceso directo vía cuatro electrones:
   a) Medio básico:

$$O_2 + 2H_2O + 4e^- \rightarrow 4OH^- \qquad E^o = 0.401\,V$$

   b) Medio ácido:

$$O_2 + 4H^+ + 4e^- \rightarrow 2H_2O \qquad E^o = 1.229\,V$$

2) Proceso de dos electrones:
   a) Medio básico:

   formación de peróxido

$$O_2 + H_2O + 2e^- \rightarrow HOO^- + OH^- \qquad E^o = -0.065\,V$$

   reducción de peróxido

$$HOO^- + H_2O + 2e^- \rightarrow 3OH^- \qquad E^o = 0.867\,V$$

   o descomposición de peróxido

$$2HOO^- \rightarrow 2OH^- + O_2$$

   b) Medio ácido:

   formación de peróxido

$$O_2 + 2H^+ + 2e^- \rightarrow HOOH \qquad E^o = 0.670\,V$$

   reducción de peróxido

$$HOOH + 2H^+ + 2e^- \rightarrow 2H_2O \qquad E^o = 1.77\,V$$

   o descomposición de peróxido

$$2HOOH \rightarrow 2H_2O + O_2$$

Naturalmente el proceso preferido es el que transcurre directamente vía cuatro electrones ya que la eficiencia faradaica es mayor, y además se evita la formación de peróxidos. Existen varios factores que pueden influir en la cinética de esta reacción sobre la superficie del electrodo, siendo aquellos aspectos relacionados directamente con el tipo de electro-catalizador, el número de sitios activos disponibles por unidad de superficie y la accesibilidad de los mismos, los que tienen un mayor efecto.

En cuanto al tipo de electro-catalizador, los basados en platino son los que se han estudiado más ampliamente, debido a que es el metal más activo en ORR [44], sin embargo, el elevado precio de este metal, y de igual manera el de otros metales preciosos que también catalizan eficientemente esta reacción, como paladio o iridio, complica mucho la implementación y comercialización de los dispositivos. Por esta razón, se están llevando a cabo numerosísimos trabajos donde se estudia el comportamiento electro-catalítico en ORR de electrodos basados en metales no preciosos [45]. En esta línea, también se ha planteado el empleo como electro-catalizadores para ORR de materiales de carbón funcionalizados, o dopados, con diferentes heteroátomos que puedan modificar la densidad electrónica grafénica [46]. Estos dopantes pueden ser boro, nitrógeno, fósforo o azufre, entre ellos nitrógeno [47] y azufre [48] son hasta la fecha los más estudiados, habiendo mostrado muy buenas actividad electro-catalítica. Este tipo de materiales además pueden ser una alternativa real a los catalizadores basados en platino, ya que son sustancialmente más baratos, tienen una mayor durabilidad potencial, y también presentan un impacto medioambiental menor.

1.3. MATERIALES DE CARBÓN COMO ELECTRODOS

Los materiales de carbón generalmente usados como electrodos de son geles de carbón, carbones activados, carbones mesoporosos ordenados, nanotubos y materiales de carbón compuestos. Todos estos materiales son muy versátiles en cuanto a sus propiedades tales como área superficial, porosidad y química superficial. Además suelen presentar alta conductividad eléctrica y algunos de ellos pueden prepararse con distintas formas como monolitos,

microesferas y láminas. Los materiales de carbón usados en la presente Tesis Doctoral han sido carbones activados, y geles de carbón dopados con metales, óxidos metálicos o heteroátomos modificadores de la densidad electrónica.

1.3.1. Geles de carbón

Los geles de carbón son un grupo de materiales avanzados de carbón introducidos por Pekala en 1989 [49,50] que se obtienen por carbonización de geles orgánicos. Estos geles orgánicos se preparan mediante una polimerización sol-gel de ciertos monómeros orgánicos como veremos más adelante. La síntesis sol-gel se aplicó originalmente a la preparación de sólidos inorgánicos y la química-física del proceso se ha detallado en varios trabajos y libros [51,52,53,54,55]. La ventaja de la síntesis sol-gel es que se obtienen materiales de alta pureza, homogeneidad y porosidad controlada.

Los geles de carbón se pueden obtener en forma de monolitos, esferas, cuentas, polvos, y láminas y poseen una micro y mesoporosidad bien desarrollada y una superficie específica elevada, propiedades que pueden diseñarse al controlar los ingredientes usados y los diferentes pasos del proceso de obtención. Por estas características los geles de carbón se utilizan en distintas aplicaciones como adsorbentes [56,57,58], soportes catalizadores [59,60,61,62,63], aislantes térmicos y/o acústicos [64,65,66,67], para el refuerzo de fibras [68,69,70], y como electrodos en celdas de combustibles [71,72] y supercondensadores [73,74,75,76].

Los geles de carbón están formados por un retículo tridimensional de nanopartículas primarias interconectadas entre sí. Los microporos se desarrollan en las partículas primarias y los meso y macroporos se forman en los espacios entre las partículas primarias inicialmente ocupados por el disolvente. Por tanto, se puede controlar independientemente la concentración de micro y mesoporos, lo que es una ventaja de los geles de carbón como materiales porosos.

En la preparación de los geles de carbón se pueden distinguir tres etapas importantes. La primera es la preparación de la mezcla del sol, su gelificación y

subsiguiente curado. La segunda etapa es el secado del gel orgánico húmedo y la tercera es la carbonización del gel seco y a veces la activación del producto carbonizado. Un esquema del proceso se representa en la Figura 9.

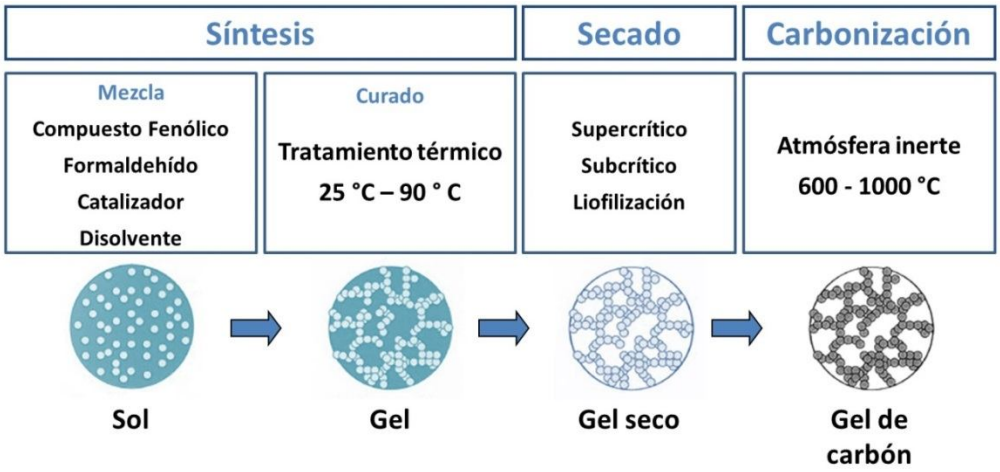

Figura 9. Esquema de preparación de geles de carbón

Varios precursores se han utilizado en la preparación de los geles orgánicos como resorcinol-formaldehído [49,77], melamina-formaldehído [78,79], furfural-fenol [80,81,82], fenol-formaldehído [83], etc., usando diferentes disolventes (agua, metanol, etanol y otros disolventes orgánicos) y utilizando catalizadores básicos (carbonatos e hidróxidos) o ácidos (orgánicos e inorgánicos). La reacción de resorcinol (R) con formaldehído (F) es la que más se ha estudiado. La Figura 10 muestra un esquema del mecanismo de reacción propuesto para la polimerización de mezclas RF [84,85,86]. El mecanismo comienza con la formación de los aniones R^- debido a la presencia del catalizador. Los aniones R^- son más activos que las moléculas R y continúa con la reacción de adición de las moléculas F a las posiciones libres del anillo aromático (posiciones 2, 4 y 6) formando derivados hidroximetil-R. En seguida comienzan las reacciones de policondensación de los grupos hidroxílicos, por lo que el subproducto es agua. En esta segunda etapa de reacción se forman estructuras poliaromáticas en las que los anillos aromáticos están enlazados entre sí mediante puentes metilen $(-CH_2-)$ y metileneter $(-CH_2-O-CH_2-)$. Los productos de

condensación forman “clusters” de macromoléculas debido a la agrupación de partículas primarias coloidales que se comienzan a formar dando lugar a una estructura entrelazada [85]. La disolución final pierde fluidez y se forma el gel.

El pH inicial de la disolución es una variable muy importante en la preparación de los geles orgánicos porque controla la cinética de polimerización, el entrecruzamiento y, por tanto, la morfología, el tamaño de partícula y la porosidad de los geles finales [87]. La concentración del catalizador es la variable que permite controlar el número y el tamaño de los “clusters” generados durante la polimerización R-F. La variación de la relación molar resorcinol/catalizador (R/C) influirá sobre la densidad el área superficial y las propiedades mecánicas de los geles resultantes (Figura 11). La gelificación es la transición gradual de un líquido viscoso a un sólido viscoelástico y antes de que se produzca la formación del gel es cuando se le da la forma que tendrá finalmente el gel de carbón. Así, si se quiere obtener en forma de monolito la disolución coloidal se vierte en moldes de la forma deseada donde se procede a la formación del gel y al curado del mismo. Para la preparación de los geles de carbón en forma de microesferas es necesario la técnica de emulsión inversa, para ello la disolución coloidal antes de que se forme el gel se vierte en un disolvente orgánico (por ejemplo ciclohexano) que contiene un surfactante. Las suspensiones obtenidas se agitan a una velocidad constante y a una temperatura determinada hasta la separación de las microesferas, las cuales se filtran y lavan. Las características finales de las microesferas dependen de los ingredientes usados, la velocidad de agitación, temperatura y del balance hidrófilo-lipófilo del surfactante entre otros factores.

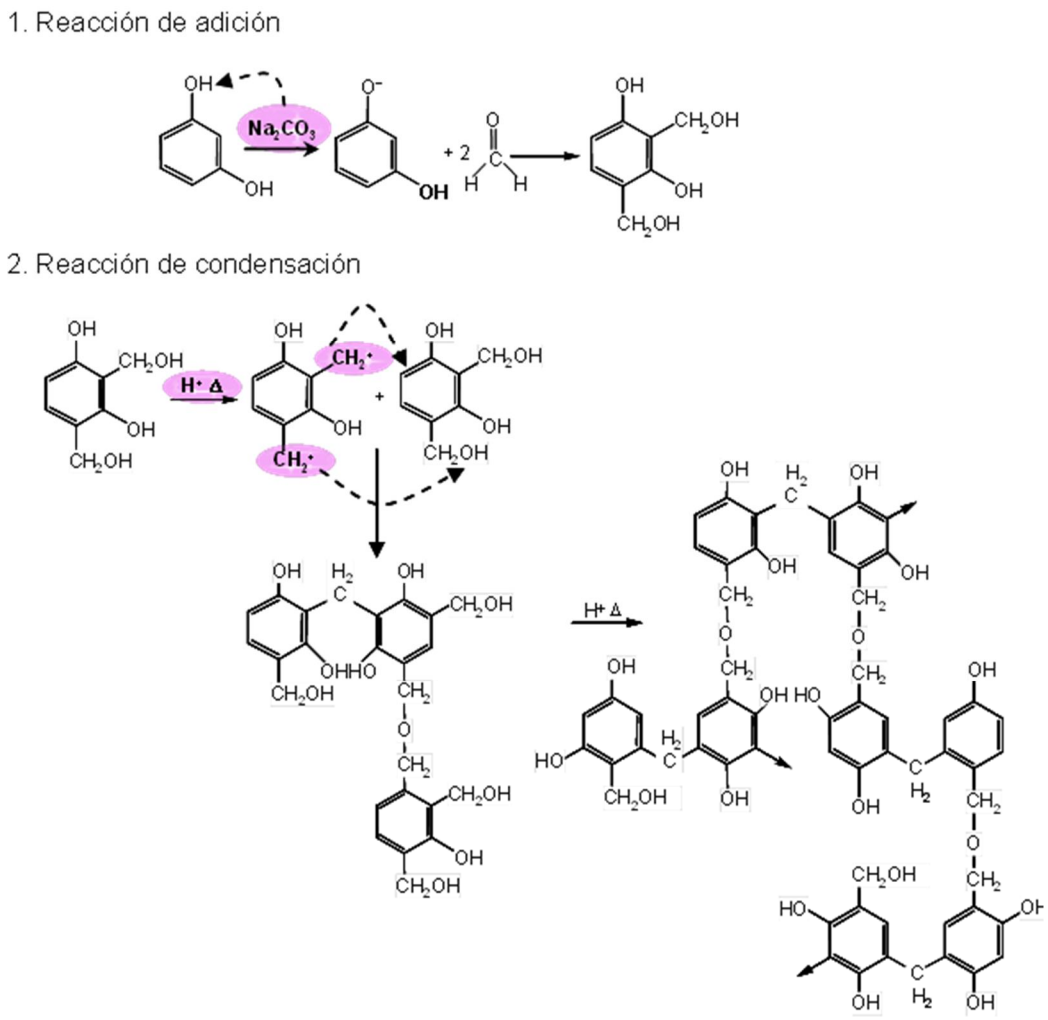

Figura 10. Esquema del mecanismo de la reacción de polimerización de mezclas RF.

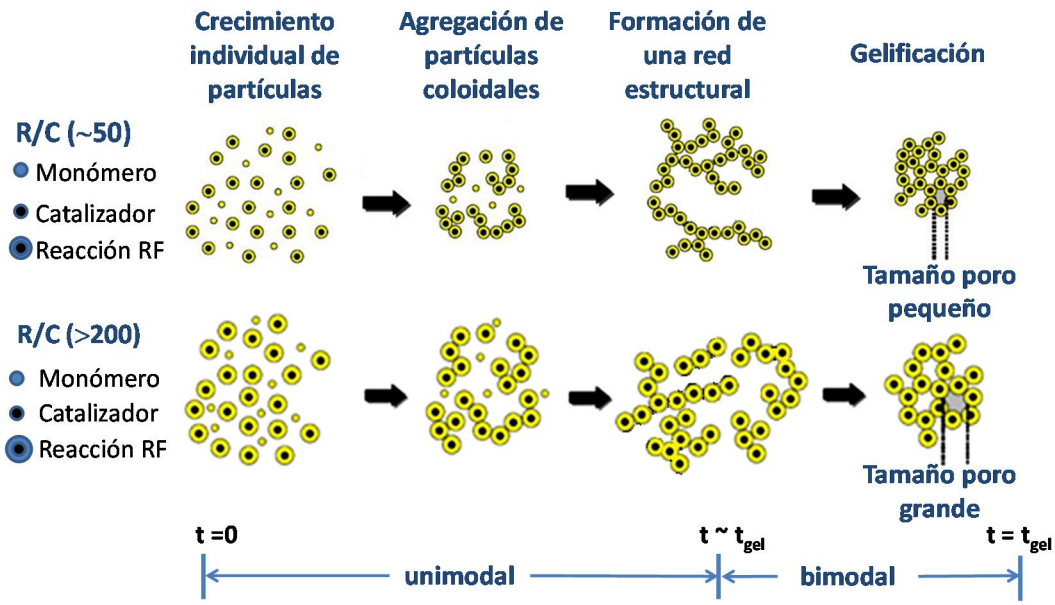

Figura 11. Influencia de la concentración del catalizador en la polimerización RF.

La segunda etapa en la preparación de los geles de carbón consiste en el secado del gel orgánico una vez obtenido. Mediante el secado se elimina el disolvente utilizado como medio de reacción, lo que deja un espacio vacío entre las partículas primarias dando lugar al desarrollo del retículo meso- y macroporoso. Los cambios en la textura porosa del gel orgánico están asociados a procesos de encogimiento y depende esencialmente del método de secado utilizado, encogimiento que en algunos casos puede llevar al colapso de la porosidad. Por tal motivo, este es un paso muy importante en la síntesis de los geles de carbón, ya que controla la meso y macroporosidad del producto final y, por tanto, su densidad [88]. El secado del gel orgánico húmedo está controlado por la permeabilidad y la presión capilar y se puede realizar bajo condiciones subcríticas, supercríticas o mediante liofilización (congelación - sublimación), lo que da lugar a xerogeles, aerogeles y criogeles, respectivamente [77,84,85,89,90]. En el secado subcrítico los geles se secan por simple evaporación del disolvente a presión por debajo de la crítica, a veces a presión atmosférica o a vacío, y

temperaturas entre 100 y 150 ºC. Este tipo de secado puede conducir a un colapso de la textura porosa, debido a los cambios en tensión superficial del disolvente durante la formación de la interfase líquido-vapor. El colapso conduce a una contracción del gel seco dando lugar a un polímero denso [59]. En algunos casos se realiza un cambio de disolvente antes del secado con objeto de reducir las fuerzas capilares responsables del colapso de la textura porosa [91]. El secado utilizando CO_2 supercrítico es el mejor método para eliminar el disolvente y preservar la textura porosa de los geles húmedos. Sin embargo, este método de secado es más complicado y caro que el secado subcrítico.

La tercera etapa en la preparación de los geles de carbón es la carbonización o pirólisis de los geles orgánicos secos. Este proceso se lleva a cabo calentando a una temperatura entre 600 y 1500 ºC en presencia de un flujo de gas inerte (N_2, Ar, He). A bajas temperaturas de carbonización el volumen de macroporos disminuye y el de mesoporos aumenta debido al encogimiento del material, mientras que el volumen de microporos y el área superficial incrementan como consecuencia de la evolución de gases durante la carbonización [51,87]. A altas temperaturas de carbonización todos estos parámetros tienden a disminuir y a muy altas temperaturas de carbonización (≥ 2000 ºC) ocurre una grafitización parcial de diferentes zonas del gel de carbón [92].

1.3.2. Geles de carbón dopados

Los geles de carbón pueden doparse con metales, óxidos metálicos o heteroátomos modificadores de la densidad electrónica, en este último, caso estaríamos hablando de una modificación directa de la química superficial del material de carbón, aspecto que será descrito en detalle en la Sección 1.3.4.

El dopado con metales se realiza generalmente mediante la adición del compuesto precursor metálico a la mezcla polimérica [59], actuando este compuesto precursor como catalizador de polimerización. Así, para el dopado con metales alcalinos o alcalinotérreos de geles R-F y que polimericen en medio acuoso, se suelen utilizar carbonatos [93], mientras que para el dopado con

metales de transición [94,95,96,97,98] es necesario emplear otros compuestos solubles en agua como por ejemplo acetatos, nitratos o cloruros. Los geles dopados obtenidos muestran muy diferentes propiedades texturales, ya que los compuestos precursores metálicos modifican el pH inicial y el número y tamaño de clústeres. En general, la mayor parte del metal dopante queda incrustado en la matriz orgánica del gel, y posteriormente en la correspondiente matriz carbonosa del gel. Algunos de estos metales como Fe, Co o Ni catalizan la formación de clústeres grafíticos durante la etapa de carbonización [92], mejorando la conductividad eléctrica del material final.

Por otro lado, para el dopado con óxidos metálicos tales como Al_2O_3, TiO_2, ZrO_2, V_2O_5 el método de síntesis difiere sustancialmente si se pretende obtener una verdadera interacción sinérgica entre fases. Éste consiste en la polimerización de resorcinol - formaldehído en medio orgánico simultáneamente con la hidrólisis de un alcóxido metálico, precursor del óxido inorgánico. Uno de los métodos más efectivos, recientemente patentado [99], consiste en una secuencia metódica y eficiente de pasos específicos que determinan las excelentes propiedades catalíticas finales de estos materiales, por ejemplo: el uso de compuestos tensoactivos, un estricto control de la temperatura de polimerización, velocidad de agitación, velocidad de adición de soluciones o el uso de microondas durante la etapa de secado. En estas condiciones se consigue una dispersión muy alta del óxido metálico en la matriz de xerogel de carbono, maximizando las interacciones metal-carbono en los materiales dopados, y obteniéndose así en muchos casos un efecto sinérgico entre ambas fases. En estos materiales, normalmente la proporción de óxido dopante respecto a la de gel de carbón es elevada, y por tanto la nomenclatura más correcta sería la de materiales compuestos, o *composites*.

1.3.3. Carbones activados

Los carbones activados [100] están formados mayoritariamente por Csp^2, existiendo en ellos unidades estructurales básicas a nivel nanométrico o micrométrico con un cierto ordenamiento grafítico y que se encuentran unidas entre sí, de una forma desordenada, por carbono amorfo con hibridación sp^2 y sp^3.

Los carbones activados son sólidos esencialmente microporosos, aunque en la mayoría de los casos también contienen meso y macroporos, presentando una distribución polimodal de poros. Los microporos son los más abundantes y es donde se desarrolla la mayor parte del área superficial de estos materiales. La estructura porosa de un carbón activado se representa esquemáticamente en la Figura 12, ésta se dice que es arborescente porque para llegar a los microporos hay que pasar por los macro (tronco del árbol) y mesoporos (ramas), que constituyen así arterias de transporte para las moléculas o iones del adsorbato hacia los microporos que es donde se producen los fenómenos de adsorción. Una característica de los microporos de los materiales carbonosos en general es que estos tienen forma de rendija, ya que las paredes de los mismos están formadas por láminas grafénicas.

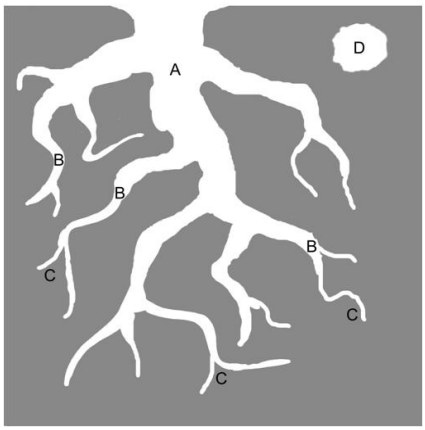

Figura 12. Representación esquemática de la porosidad de un carbón activado. A: macroporos, B: mesoporos, C: microporos y D: poros cerrados

La materia prima usada en la preparación de los carbones activados debe tener un alto contenido en C, bajo contenido en materia inorgánica, debe ser abundante y barata y fácil de activar. En la práctica estas materias primas son de origen vegetal y fósil, como son los residuos agrícolas (madera, huesos y cáscaras de frutas, etc.) y carbones minerales (lignitos, antracitas, etc.). Las propiedades

finales del carbón activado dependen del precursor usado y del proceso de activación seguido [101].

La activación puede ser física o química. La activación física generalmente se lleva a cabo en dos pasos. Primero se realiza una carbonización de la materia prima en atmósfera inerte a alta temperatura (~800 ºC), durante la cual se desprende la materia volátil (gases y vapor de agua) y alquitranes dejando un residuo de mayor contenido en C que la materia prima original, y con un retículo poroso rudimentario que se desarrollará posteriormente durante la activación. El segundo paso es la activación, que tiene como objetivo incrementar el volumen de poros mediante la creación de nuevos poros y el ensanchamiento de los ya existentes. Este paso se lleva a cabo a temperaturas entre 800 y 1000 ºC en flujo de vapor de agua o CO_2, a veces se introduce aire en el horno de activación junto a algunos de los gases anteriores. Las reacciones de gasificación son las siguientes:

$$C + H_2O \rightarrow CO + H_2 \qquad \Delta H = +117 \text{ kJ/mol}$$

$$C + CO_2 \rightarrow 2\ CO \qquad \Delta H = +159 \text{ kJ/mol}$$

La reacción con vapor de agua también conduce a la de desplazamiento del gas de agua catalizada por la superficie del carbón

$$CO + H_2O \rightarrow CO_2 + H_2$$

Al ser las reacciones endotérmicas se pueden controlar bastante bien. A veces se introduce aire en el horno que oxida al CO y al H_2 de acuerdo con las reacciones exotérmicas:

$$CO + 1/2\ O_2 \rightarrow CO_2 \quad \Delta H = -285 \text{ kJ/mol}$$

$$H_2 + 1/2\ O_2 \rightarrow H_2O \qquad \Delta H = -238 \text{ kJ/mol}$$

Estas reacciones suministran un calor extra a las reacciones de activación (haciendo que se use menos energía en calentar el horno) y al mismo tiempo eliminan del reactor el CO y el H_2 que son fuertes inhibidores de las reacciones de gasificación.

El volumen y distribución del tamaño de los poros en el carbón activado final se pueden controlar mediante el agente activante usado y la temperatura y tiempo de activación.

La activación química generalmente se usa con la materia prima de origen vegetal y se suele llevar a cabo en una sola etapa. Para ello, la materia prima se impregna con un agente activante en la forma de disolución de carbonatos o hidróxidos alcalinos (K o Na) o H_3PO_4. El material impregnado se seca y se piroliza en atmosfera inerte entre 400 y 700 ºC. El sólido obtenido se lava para eliminar el agente activante. Durante la pirólisis el agente activante reacciona con la materia prima lo que da lugar a su carbonización y aromatización y a la creación de la textura porosa. En el caso de la activación química las propiedades superficiales del carbón activado obtenido dependen de la materia prima usada, la proporción materia prima/agente activante y la temperatura y tiempo de activación [100].

Los carbones activados se preparan en forma de polvo ($10 < Ø < 50$ μm) o granular ($0,5 < Ø < 4$ mm). El polvo se puede compactar a presión y con la ayuda de aglutinantes que dan lugar a monolitos de diferentes formas. El monolito tiene un área superficial y porosidad menor que el material en polvo del que procede. El área superficial y textura porosa de los carbones activados varía mucho en función de la materia prima y método de preparación seguido. El área superficial suele estar entre 800 y 2000 m^2/g y el volumen de microporos puede ser de hasta 0,7 cm^3/g. Se ha llegado a preparar un carbón activado con un área superficial de ~ 3000 m^2/g y un volumen de total de poros excepcionalmente elevado, entre 2,0 y 2,6 cm^3/g. Este carbón activado es conocido como súper carbón activado, lo comercializa Kansai Coke (Japón), y se prepara a partir de coque y carbón mineral mediante activación química con KOH. Este carbón activado debido a su pequeñísima densidad de partícula es muy difícil de manejar por lo que su utilización no es muy exitosa.

Evidentemente cuanto mayor es el volumen de poros de un material (cualquiera) menor es su densidad de partícula, lo que hace que sea difícil de

manejar y que no sea útil para ser usado en sistemas de volumen fijo, ya que se necesitaría un reactor de enorme volumen.

1.3.4. Química superficial de los materiales de carbón

La química superficial de los materiales de carbón determina su carácter ácido-básico, carga superficial y carácter hidrófobo, la cual depende de la presencia de heteroátomos y de regiones ricas en electrones π.

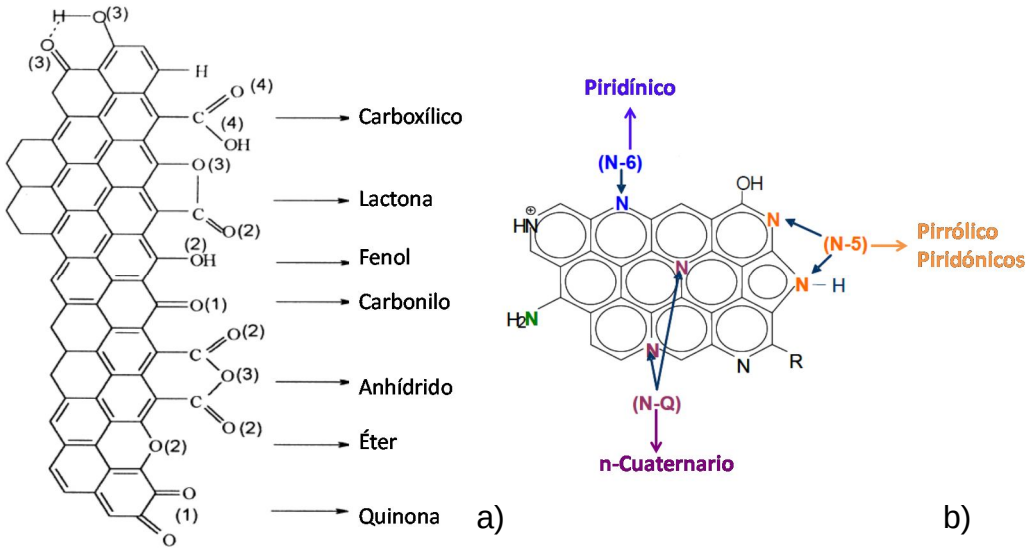

Figura 13. Representación esquemática de los grupos a) oxígeno y b) nitrógeno en superficies carbonosas. N-6: nitrógeno piridínico, N-5: nitrógeno pirrólico o piridónico, N-Q: nitrógeno cuaternario o sustitucional, N-X: formas oxidadas de nitrógeno piridínico.

Los heteroátomos más comunes son oxígeno, nitrógeno e hidrógeno y en menor medida azufre, fósforo y cloro. Estos heteroátomos pueden provenir de la materia prima y del método de preparación usado para la obtención de los materiales de carbón o bien ser introducidos en ellos mediante tratamientos químicos adecuados [102]. Los heteroátomos se encuentran enlazados en los bordes de las capas grafénicas y a veces en defectos localizados en el interior de

ellas formando diferentes grupos funcionales orgánicos como puede verse en la Figura 13 para el caso de los grupos funcionales de oxígeno y nitrógeno.La química superficial de los materiales de carbón es muy importante cuando estos se usan como electrodos de supercondensadores, ya que pueden dar lugar a fenómenos de pseudocapacidad, por ejemplo mediante reacciones redox, o incrementando la atracción hacia los iones del electrolito. También pueden afectar a la capacidad de mojado de los electrodos, cuando estos se usan en disoluciones acuosas, y a su conductividad eléctrica [103,104].

Los grupos superficiales oxígeno pueden ser de carácter ácido (ácidos carboxílicos, lactonas y fenoles), básicos (quinonas y pironas) y neutros (éteres y aldehídos). En muchos materiales de carbón usados como electrodos de supercondensadores con medio a alto contenido de oxígeno la reacción redox hidroquinona/quinona es la considerada como la mayor responsable de la pseudocapacidad. Los grupos superficiales de oxígeno se pueden introducir en los materiales de carbón mediante tratamientos en fase líquida o gaseosa usando oxidantes como ácido nítrico, peróxido de hidrógeno, peroxidisulfato amónico, aire o vapor de agua [105,106]. La naturaleza de los grupos funcionales de oxígeno incorporados no sólo depende del tipo de agente oxidante utilizado, sino también de las condiciones en las que se lleva a cabo el proceso oxidativo [107,108].

La incorporación de grupos superficiales nitrogenados en los materiales de carbón se puede realizar de dos formas i) directamente durante la síntesis mediante la selección de precursores ricos en grupos nitrogenados como melamina y urea [109,110,111,112], y ii) modificación post-síntesis mediante tratamientos que introduzcan estos grupos, como por ejemplo el tratamiento con amoniaco a alta temperatura [109].

Las diferentes funcionalidades nitrogenadas pueden ser nitrógeno piridínico (N-6), nitrógeno pirrólico o piridónico (N-5), nitrógeno cuaternario o sustitucional (N-Q), formas oxidadas de nitrógeno piridínico (N-X), así como grupos aminas (Figurab) [111]. La presencia de las funcionalidades N-5 y N-6 incrementan la carga negativa en las láminas de grafeno, mientras que las

funcionalidades N-Q incrementan la carga positiva e influyen sobre la adsorción de los iones del electrolito y la pseudocapacidad [113].

Cómo ya se ha indicado en esta Introducción, también es muy interesante el desarrollo de electro-catalizadores para ORR de materiales de carbón dopados con diferentes heteroátomos que puedan modificar la densidad electrónica grafénica [46], siendo hasta la fecha los dopados con nitrógeno [47] y azufre [48] los más estudiados. Otros dopantes como boro, o fósforo también son de interés en el desarrollo de nuevos electrodos para ambas aplicaciones.

El dopado con azufre puede modificar la estructura electrónica grafénica mejorando la conductividad eléctrica, y la adsorción de especies de los electrolitos. Así, para el dopado con azufre la mayoría de los trabajos emplean tratamientos con H_2S como agente dopante [48,107,114] cuando el dopado es una etapa posterior a la de obtención del material de carbono. Para otros materiales de carbono como nanotubos, aerogeles, el empleo durante la síntesis, de compuestos precursores de carbono que también contengan azufre es una estrategia igualmente interesante. El tipo de funcionalidades de azufre varía sensiblemente con el método de dopado, y con el contenido en oxigeno de los materiales. Algunas de las funcionalidades de azufre analizadas en los materiales de carbono son: tioles, tioésteres, sulfóxidos, sulfonas, o grupos sulfónicos. Es decir, los átomos de azufre se pueden enlazar a los bordes de las capas grafénicas mediante simple o doble enlace, y a su vez enlazarse también o no a átomos de oxígeno. A pesar de esta variada combinatoria, muchos trabajos proponen al azufre tiofénico como centro activo principal basado en azufre en ORR [115,116], aunque también podemos encontrar en la bibliografía propuestas resaltando un papel adicional de los grupos superficiales de azufre en configuraciones con oxígeno (sulfóxido, sulfonas y ácidos sulfónicos) en dicho proceso electro-catalítico [117]. Estos mismos grupos superficiales, de azufre con oxígeno sobre los materiales de carbono, también se ha demostrado que pueden aumentar la capacidad electro-química de almacenamiento [107,118].

Finalmente, funcionalidades de fósforo también pueden introducirse o fijarse en las capas grafénicas de los materiales de carbono, siendo el método más utilizado el tratamiento directo con H_3PO_4. Se ha demostrado que los grupos de fósforo introducidos en los materiales de carbón tienen un importante efecto sobre la capacidad electroquímica [119,120,121,122,123]. Esto es así porque el fósforo, cuando puede proporcionar un par de electrones a la capa grafénica puede modificar significativamente las características donador-aceptora de la misma, dando lugar a una reacción pseudocapacitiva. Además, también se ha demostrado que la presencia de grupos fosfato pueden mejorar la estabilidad del electrodo en un electrolito acuoso permitiendo trabajar en una ventana de potencial más amplia [119,121,122].

1.4. BIBLIOGRAFÍA

[1] Key World Energy Statistics. Paris FRA: International Energy Agency; 2016.https://www.iea.org/publications/freepublications/publication/KeyWorld2016.pdf

[2] Nishino A. Capacitors: Operating principles, current market and technical trends. J. Power Sources. 1996; 60(2):137–47.

[3] Brooks R, Harris J. Factors affecting the use of ceramic capacitors in pulse-discharge applications. Albuquerque USA: Department of Energy; 1998.

[4] Kötz R, Carlen M. Principles and applications of electrochemical capacitors. Electrochim. Acta. 2000;45:2483–98.

[5] Pandolfo A, Hollenkamp A. Carbon properties and their role in supercapacitors. J. Power Sources. 2006;157(1):11–27.

[6] Inagaki M, Konno H, Tanaike O. Carbon materials for electrochemical capacitors. J. Power Sources. 2010;195(24):7880–903.

[7] Shi H. Activated carbons and double layer capacitance. Electrochim. Acta. 1996;41(10):1633–9.

[8] Shao M, Chang Q, Dodelet JP, Chenitz R. Recent Advances in Electrocatalysts for Oxygen Reduction Reaction, Chemical Reviews 2016; 116: 3594-3657.

[9] Shukla A, Banerjee A, Ravikumar M, Jalajakshi A. Electrochemical capacitors: Technical challenges and prognosis for future markets. Electrochim. Acta. 2012;84:165–73.

[10] Sanz Lázaro J, Álvarez Amarilla JM, Alonso Alonso JA, Rojo Martín JM. Energía eléctrica y materiales: baterías recargables, supercondensadores y pilas de combustible. Madrid, ESP: CSIC - Ministerio de Economía y Competitividad; 2012.

[11] Butler P, Miller J, Taylor P. Energy Storage Opportunities Analysis Phase II Final Report A Study for the DOE Energy Storage Systems Program. Albuquerque USA: Sandia National Laboratories; 2002.

[12] Sharma P, Bhatti TS. A review on electrochemical double-layer capacitors. Energ. Convers. Manage. 2010;51(12):2901–12.

[13] Adhyapak P V, Maddanimath T, Pethkar S, Chandwadkar AJ. Application of electrochemically prepared carbon nanofibers in supercapacitors. J. Power Sources. 2002;109(1):105–10.

[14] Miller JR, Simon P. Fundamentals of electrochemical capacitor design and operation. Electrochem. Soc. Interface. 2008;17(1):31–2.

[15] Halper MS, Ellenbogen JC. Supercapacitors: A Brief Overview. McLean VA: The MITRE; 2006. p. 41.

[16] Lota G, Centeno T, Frackowiak E, Stoeckli F. Improvement of the structural and chemical properties of a commercial activated carbon for its application in electrochemical capacitors. Electrochim. Acta. 2008;53(5):2210–6.

[17] Zhang Y, Feng H, Wu X, Wang L, Zhang A, Xia T, et al. Progress of electrochemical capacitor electrode materials: A review. Int. J. Hydrogen Energy. 2009;34(11):4889–99.

[18] Simon P, Burke A. Nanostructured Carbons: Double-Layer Capacitance and More. Electrochem. Soc. Interface. 2008;17(1):38–43.

[19] Qu D, Shi H. Studies of activated carbons used in double-layer capacitors. J. Power Sources. 1998;74(1):99–107.

[20] Chang B-Y, Park S-M. Electrochemical impedance spectroscopy. Annu. Rev. Anal. Chem. 2010;3:207–29.

[21] Béguin F., Presser V., Balducci A., Frackowiak E. Carbons and Electrolytes for Advanced Supercapacitors. Adv. Mater. 2014; 2219-2251.

[22] Béguin F., Presser V., Balducci A., Frackowiak E. Carbons and Electrolytes for Advanced Supercapacitors. Adv. Mater. 2014; 2219-2251.

[23] Menéndez R, Cazorla-Amorós D, Cordero T. Carbon for energy storage and environment protection 2009 special issue. Energy Fuels. 2010;24(6):3301.

[24] Dandekar M, Arabale G, Vijayamohanan K. Preparation and characterization of composite electrodes of coconut-shell-based activated carbon and hydrous ruthenium oxide for supercapacitors. J. Power Sources. 2005;141(1):198–203.

[25] Frackowiak E, Béguin F. Carbon materials for the electrochemical storage of energy in capacitors. Carbon. 2001;39(6):937–50.

[26] Li W, Chen D, Li Z, Shi Y, Wan Y, Wang G, et al. Nitrogen-containing carbon spheres with very large uniform mesopores: The superior electrode materials for EDLC in organic electrolyte. Carbon. 2007;45(9):1757–63.

[27] Raymundo-Piñero E, Béguin F. Application of nanotextured carbons for supercapacitors and hydrogen storage. In: Bandosz T, editor. Activated Carbon Surfaces in Environmental Remediation. Oxford: Elsevier; 2006. p. 293–343.

[28] Hulicova D, Kodama M, Hatori H. Electrochemical Performance of Nitrogen-Enriched Carbons in Aqueous and Non-Aqueous Supercapacitors. Chem. Mater. 2006;18(9):2318–26.

[29] Jayalakshmi M, Balasubramanian K. Simple Capacitors to Supercapacitors - An Overview. Int. J. Electrochem. Sci. 2008;3:1196–217.

[30] Prasad KR, Koga K, Miura N. Electrochemical Deposition of Nanostructured Indium Oxide: High-Performance Electrode Material for Redox Supercapacitors. Chem. Mater. 2004;16(22):1845–7.

[31] Khomenko V, Raymundo-Piñero E, Frackowiak E, Béguin F. High-voltage asymmetric supercapacitors operating in aqueous electrolyte. Applied Physics A. 2006;82(4):567–73.

[32] Frackowiak E, Khomenko V, Jurewicz K, Lota K, Béguin F. Supercapacitors based on conducting polymers/nanotubes composites. J. Power Sources. 2006;153(2):413–8.

[33] Bleda-Martínez MJ, Lozano-Castelló D, Cazorla-Amorós D, Morallón E. Kinetics of Double-Layer Formation: Influence of Porous Structure and Pore Size Distribution. Energy Fuels. 2010;24(6):3378–84.

[34] Simon P, Gogotsi Y. Materials for electrochemical capacitors. Nature Materials. 2008;7(11):845–54.

[35] Sato T, Masuda G, Takagi K. Electrochemical properties of novel ionic liquids for electric double layer capacitor applications. Electrochim. Acta. 2004;49(21):3603–11.

[36] Sato T, Marukane S, Morinaga T. Ionic Liquids for the Electric Double Layer Capacitor Applications. In: Handy S, editor. Applications of Ionic Liquids in Science and Technology. Tennessee: Middle Tennessee State University; 2011. p. 109–34.

[37] Ohno H. Electrochemical Aspects of Ionic Liquids. Ohno H, editor. Hoboken NJ: John Wiley & Sons, Inc.; 2005.

[38] Pandey G.P., Kumar Y., Hashmi S.A. Ionic liquid incorporated polymer electrolytes for supercapacitor application. Indian Journal of Chemistry 2010; 49A:743-751

[39] Taberna P, Simon P, Fauvarque J. Electrochemical characteristics and impedance spectroscipy studies of carbon-carbon supercapacitors. J. Electrochem. Soc. 2003;150(3):A292–300.

[40] Sakka M Al, Gualous H, Omar N. Batteries and Supercapacitors for Electric Vehicles. In: Stevic Z, editor. New Generation of Electric Vehicles. InTech; 2012. p. 135–65.

[41] De Levie R. On porous electrodes in electrolyte solutions - IV*. Electrochim. Acta. 1964;9:1231–45.

[42] Jang JH, Yoon S, Ka BH, Jung Y-H, Oh SM. Complex Capacitance Analysis on Leakage Current Appearing in Electric Double-layer Capacitor Carbon Electrode. J. Electrochem. Soc. 2005;152(7):A1418–22.

[43] Conway B. Electrochemical Supercapacitors Scientific Fundamentals and Technological Applications. New York: Kluwer Academic; 1996.

[44] Sui S, Wang X, Zhou X, Su Y, Riffat S, Liu CJ. A comprehensive review of Pt electrocatalysts for the oxygen reduction reaction: Nanostructure, activity, mechanism and carbon support in PEM fuel cells. J. Mater. Chem. A 2017; 5:1808-1825.

[45] Banham D, Ye S, Pei K, Ozaki JI, Kishimoto T, and Imashiro Y. A review of the stability and durability of non-precious metal catalysts for the oxygen reduction reaction in proton exchange membrane fuel cells. Journal of Power Sources 2015:285; 334-348.

[46] Yang Z, Nie H, Chen X, and Huang S. Recent progress in doped carbon nanomaterials as effective cathode catalysts for fuel cell oxygen reduction reaction. Journal of Power Sources 2013:236; 238-249.

[47] Dou S, Shen A, Ma Z, Wu J, Tao L, and Wang S. N-, P- and S-tridoped graphene as metal-free electrocatalyst for oxygen reduction reaction. Journal of Electroanalytical Chemistry 2015:753;21-27.

[48] Seredych M, László K, Rodríguez-Castellón E, and Bandosz T.J. S-doped carbon aerogels/GO composites as oxygen reduction catalysts. Journal of Energy Chemistry 2016:25;236-245.

[49] Pekala R. Low density, resorcinol-formaldehyde aerogels. US patent 4873218; 1989. p. 8.

[50] Pekala R. Organic aerogels from the polycondensation of resorcinol with formaldehyde. J. Mater. Sci. 1989;24:3221–7.

[51] Pajonk G. Catalytic aerogels. Catalysis Today. 1997;35(3):319–37.

[52] Pierre A, Pajonk GM. Chemistry of aerogels and their applications. Chem. Rev. 2002;102(11):4243–65.

[53] Livage J, Sanchez C. Sol-gel chemistry. J Non-Cryst Solids. 1992;145:11–9.

[54] Gonzalez R, Lopez T, Gomez R. Sol—Gel preparation of supported metal catalysts. Catalysis Today. 1997;35(3):293–317.

[55] Pierre A. Introduction to Sol-Gel Processing. 2nd ed. Norwell: Kluwer Academic; 1998.

[56] Kabbour H, Baumann T, Satcher J, Saulnier A, Ahn C. Toward New Candidates for Hydrogen Storage: High Surface Area Carbon Aerogels. Chem. Mater. 2006;18:6085–7.

[57] Maldonado-Hódar FJ, Moreno-Castilla C, Carrasco-Marín F, Pérez-Cadenas AF. Reversible toluene adsorption on monolithic carbon aerogels. J. Hazard. Mater. 2007;148(3):548–52.

[58] Kadirvelu K, Goel J, Rajagopal C. Sorption of lead, mercury and cadmium ions in multi-component system using carbon aerogel as adsorbent. J. Hazard. Mater. 2008;153(1-2):502–7.

[59] Moreno-Castilla C, Maldonado-Hódar FJ. Carbon aerogels for catalysis applications: An overview. Carbon. 2005;43(3):455–65.

[60] Du H, Li B, Kang F, Fu R, Zeng Y. Carbon aerogel supported Pt–Ru catalysts for using as the anode of direct methanol fuel cells. Carbon. 2007;45(2):429–35.

[61] Maldonado-Hódar F, Moreno-Castilla C, Pérez-Cadenas A. Surface morphology, metal dispersion, and pore texture of transition metal-doped monolithic carbon aerogels and steam-activated derivatives. Micropor. Mesopor. Mater. 2004;69(1-2):119–25.

[62] Moreno-Castilla C, Maldonado-Hódar FJ, Rivera-Utrilla J, Rodríguz-Castellón E. Group 6 metal oxide-carbon aerogels . Their synthesis, characterization and catalytic activity in the skeletal isomerization of 1-butene. Applied Catalysis A. 1999;183:345–56.

[63] Padilla-Serrano M, Maldonado-Hódar F, Moreno-Castilla C. Influence of Pt particle size on catalytic combustion of xylenes on carbon aerogel-supported Pt catalysts. Applied Catalysis B. 2005;61(3-4):253–8.

[64] Forest L, Gibiat V, Woignier T. Biot's theory of acoustic propagation in porous media applied to aerogels and alcogels. J Non-Cryst Solids. 1998;225:287–92.

[65] Baetens R, Jelle BP, Gustavsen A. Aerogel insulation for building applications: A state-of-the-art review. Energy and Buildings. 2011;43(4):761–9.

[66] Wei G, Liu Y, Zhang X, Yu F, Du X. Thermal conductivities study on silica aerogel and its composite insulation materials. Int. J. Heat Mass Tran. 2011;54(11-12):2355–66.

[67] Hostler S, Abramson A, Gawryla M, Bandi S, Schiraldi D. Thermal conductivity of a clay-based aerogel. Int. J. Heat Mass Tran. 2009;52(3-4):665–9.

[68] Finlay K, Gawryla MD, Schiraldi DA. Biologically Based Fiber-Reinforced/Clay Aerogel Composites. Ind. Eng. Chem. Res. 2008;47(3):615–9.

[69] Sander MT. Ultra-thin prestressed fiber reinforced aerogel honeycomb catalyst monoliths. US patent 5972254; 1999.

[70] Nguyen BCN, Meador MAB, Medoro A, Arendt V, Randall J, McCorkle L, et al. Elastic behavior of methyltrimethoxysilane based aerogels reinforced with tri-isocyanate. ACS Applied Materials & Interfaces. 2010;2(5):1430–43.

[71] Smirnova A, Dong X, Hara H, Vasiliev A, Sammes N. Novel carbon aerogel-supported catalysts for PEM fuel cell application. Int. J. Hydrogen Energy. 2005;30(2):149–58.

[72] Petričević R, Glora M, Fricke J. Planar fibre reinforced carbon aerogels for application in PEM fuel cells. Carbon. 2001;39(6):857–67.

[73] Hwang S-W, Hyun S-H. Synthesis and characterization of tin oxide/carbon aerogel composite electrodes for electrochemical supercapacitors. J. Power Sources. 2007;172(1):451–9.

[74] Fang B, Binder L. A modified activated carbon aerogel for high-energy storage in electric double layer capacitors. J. Power Sources. 2006;163(1):616–22.

[75] Li J, Wang X, Huang Q, Gamboa S, Sebastian P. Studies on preparation and performances of carbon aerogel electrodes for the application of supercapacitor. J. Power Sources. 2006;158(1):784–8.

[76] Schmitt C, Pröbstle H, Fricke J. Carbon cloth-reinforced and activated aerogel films for supercapacitors. J Non-Cryst Solids. 2001;285:277–82.

[77] Czakkel O, Marthi K, Geissler E, László K. Influence of drying on the morphology of resorcinol–formaldehyde-based carbon gels. Micropor. Mesopor. Mater. 2005;86(1-3):124–33.

[78] Pekala R. Melamine-formaldehyde aerogels. US patent 5086085; 1992.

[79] Long D, Zhang J, Yang J, Hu Z, Cheng G, Liu X, et al. Chemical state of nitrogen in carbon aerogels issued from phenol–melamine–formaldehyde gels. Carbon. 2008;46(9):1259–62.

[80] Pekala R, Alviso C, Lu X, Gross J, Fricke J. New organic aerogels based upon a phenolic-furfural reaction. J Non-Cryst Solids. 1995;188:34–40.

[81] Wu D, Fu R. Synthesis of organic and carbon aerogels from phenol–furfural by two-step polymerization. Micropor. Mesopor. Mater. 2006;96(1-3):115–20.

[82] Long D, Zhang J, Yang J, Hu Z, Li T, Cheng G, et al. Preparation and microstructure control of carbon aerogels produced using m-cresol mediated sol-gel polymerization of phenol and furfural. New Carbon Materials. 2008;23(2):165–70.

[83] Scherdel C, Reichenauer G. Carbon xerogels synthesized via phenol–formaldehyde gels. Micropor. Mesopor. Mater. 2009;126(1-2):133–42.

[84] Al-Muhtaseb S, Ritter J. Preparation and Properties of Resorcinol-Formaldehyde Organic and Carbon Gels. Adv. Mater. 2003;15(2):101–14.

[85] Pekala R, Alviso C, LeMay J. Organic aerogels: microstructural dependence of mechanical properties in compression. J Non-Cryst Solids. 1990;125(1-2):67–75.

[86] Yamamoto T, Yoshida T, Suzuki T, Mukai SR, Tamon H. Dynamic and static light scattering study on the sol-gel transition of resorcinol-formaldehyde aqueous solution. J. Colloid Interface Sci. 2002;245(2):391–6.

[87] Fairén-Jiménez D, Carrasco-Marín F, Moreno-Castilla C. Inter- and intra-Primary-Particle Structure of Monolithic Carbon Aerogels Obtained with Varying Solvents. Langmuir. 2008;24:2820–5.

[88] Calvo EG, Menéndez JÁ, Arenillas A. Designing Nanostructured Carbon Xerogels. In: Rahman MM, editor. Nanomaterials. InTech; 2011. p. 189–238.

[89] Job N, Pirard R, Marien J, Pirard J-P. Porous carbon xerogels with texture tailored by pH control during sol–gel process. Carbon. 2004;42(3):619–28.

[90] Zubizarreta L, Arenillas A, Pirard J-P, Pis JJ, Job N. Tailoring the textural properties of activated carbon xerogels by chemical activation with KOH. Micropor. Mesopor. Mater. 2008;115(3):480–90.

[91] E. Gallegos-Suarez, A.F. Perez-Cadenas, F.J. Maldonado-Hodar, F. Carrasco-Marin, On the micro- and mesoporosity of carbon aerogels and xerogels. The role of the drying conditions during the synthesis processes, Chem. Eng. J. 181-182 (2012) 851-855.

[92] Maldonado-Hódar F, Moreno-Castilla C, Rivera-Utrilla J. Catalytic Graphitization of Carbon Aerogels by Transition Metals. Langmuir. 2000;16(9):4367–73.

[93] Morales-Torres S, Maldonado-Hodar FJ, Perez-Cadenas AF, Carrasco-Marin F. Textural and mechanical characteristics of carbon aerogels synthesized by polymerization of resorcinol and formaldehyde using alkali carbonates as basification agents. Phys. Chem. Chem. Phys. 2010:12; 10365-10372.

[94] Moreno-Castilla C, Maldonado-Hodar FJ, Perez-Cadenas AF. Physicochemical Surface Properties of Fe, Co, Ni, and Cu-Doped Monolithic Organic Aerogels. Langmuir 2003:19; 5650-5655.

[95] Maldonado-Hódar FJ, Pérez-Cadenas AF, Moreno-Castilla C. Morphology of heat-treated tunsgten doped monolithic carbon aerogels, Carbon 2003:41;1291-1299.

[96] Maldonado-Hódar FJ, Moreno-Castilla C, Pérez-Cadenas AF. Catalytic combustion of toluene on platinium-containing monolithic carbon aerogels, Appl. Catal. B. 2004:54; 217-224.

[97] Maldonado-Hodar FJ, Jirglová H, Perez-Cadenas AF, Morales-Torres S. Chemical control of the characteristics of Mo-doped carbon xerogels by surfactant-mediated synthesis, Carbon 2013:51;213-223.

[98] Abdelwahab A, Castelo-Quibén J, Pérez-Cadenas M, Elmouwahidi A, Maldonado-Hódar FJ, Carrasco-Marín F, Pérez-Cadenas AF. Cobalt-doped carbon gels as electro-catalysts for the reduction of CO2 to hydrocarbons, Catalysts 2017:7;25

[99] Carbon-gel-based catalysts. Francisco J. Maldonado-Hódar, Francisco Carrasco-Marín, Agustín F. Pérez-Cadenas, Esther Bailón-García. Patente: WO2016174295. 03/11/2016

[100] Rodríguez-Reinoso F. Carbón activado: Estructura, preparación y aplicaciones. Alicante, España; 1981.

[101] Rodríguez-Reinoso F. Activated carbon: Structure, preparation and applications. In: Marsh H, Heinz E, Rodríguez-Reinoso F, editors. Introduction to carbon technologies. Alicante: Universidad de Alicante; 1977. p. 35–101.

[102] Bandosz, Teresa J., in: Surface Chemistry of Carbon Materials. Serp, Philippe and Figueiredo, J. L. (Eds.), Carbon Materials for Catalysis, John Wiley & Sons, Inc., 2008.

[103] Frackowiak E. Carbon materials for supercapacitor application. Phys. Chem. Chem. Phys. 2007;9(15):1774–85.

[104] Shukla A, Sampath S, Vijayamohanan K. Electrochemical supercapacitors: Energy storage beyond batteries. Current Science. 2000;79(12):1656–61.

[105] Mahata N, Pereira M, Suárez-García F, Martínez-Alonso A, Tascón J, Figueiredo J. Tuning of texture and surface chemistry of carbon xerogels. J. Colloid Interface Sci. 2008;324(1-2):150–5.

[106] Moreno-Castilla C, Ferro-García M, Joly J, Bautista-Toledo I, Carrasco-Marín F, Rivera-Utrilla J. Activated Carbon Surface Modifications by Nitric Acid, Hydrogen Peroxide, and Ammonium Peroxydisulfate Treatments. Langmuir. 1996;11(19):4386–92.

[107] Seredych M, Hulicova-Jurcakova D, Lu GQ, Bandosz TJ. Surface functional groups of carbons and the effects of their chemical character, density and accessibility to ions on electrochemical performance. Carbon. 2008;46(11):1475–88.

[108] Shen W, Li Z, Liu Y. Surface Chemical Functional Groups Modification of Porous Carbon. Recent Patents Chem. Eng. 2008;1(1):27–40.

[109] Gorgulho HF, Gonçalves F, Pereira MFR, Figueiredo JL. Synthesis and characterization of nitrogen-doped carbon xerogels. Carbon. 2009;47(8):2032–9.

[110] Chen XY, Chen C, Zhang ZJ, Xie DH, Deng X, Liu JW. Nitrogen-doped porous carbon for supercapacitor with long-term electrochemical stability. J. Power Sources. 2013;230:50–8.

[111] Pérez-Cadenas M, Moreno-Castilla C, Carrasco-Marín F, Pérez-Cadenas AF. Surface chemistry, porous texture, and morphology of N-doped carbon xerogels. Langmuir. 2009;25(1):466–70.

[112] Barbosa MB, Nascimento JP, Martelli PB, Furtado CA, Mohallem NDS, Gorgulho H. Electrochemical properties of carbon xerogel containing nitrogen in a carbon matrix. Micropor. Mesopor. Mater. 2012;162:24–30.

[113] Moreno-Castilla C, Dawidziuk MB, Carrasco-Marín F, Morallón E. Electrochemical performance of carbon gels with variable surface chemistry and physics. Carbon. 2012;50(9):3324–32.

[114] Yang S, Zhi L, Tang K, Feng X, Maier J, and Müllen K. Efficient Synthesis of Heteroatom (N or S)-Doped Graphene Based on Ultrathin Graphene Oxide - Porous Silica Sheets for Oxygen Reduction Reactions. Advanced Functional Materials 2012:22; 3634-3640.

[115] Nie R, Bo X, Luhana C, Nsabimana A, and Guo L. Simultaneous formation of nitrogen and sulfur-doped carbon nanotubes-mesoporous carbon and its electrocatalytic activity for oxygen reduction reaction. International Journal of Hydrogen Energy 2014:39;12597-12603.

[116] Liang J, Jiao Y, Jaroniec M, Qiao SZ. Sulfur and nitrogen dual-doped mesoporous graphene electrocatalyst for oxygen reduction with synergistically enhanced performance. Angew Chem Int Ed, 2012:51;1-6.

[117] Seredych M, László K, Bandosz TJ. Sulfur-Doped Carbon Aerogel as a Metal-Free Oxygen Reduction Catalyst. ChemCatChem, 2015:7; 2924-2931.

[118] Zhao X, Zhang Q, Chen CM, Zhang B, Reiche S, Wang A, *et al.* Aromatic sulfide, sulfoxide, and sulfone mediated mesoporous carbon monolith for use in supercapacitor. Nano Energy, 2012:1; 624-630.

[119] Carriazo D, Gutierrez M.C, Picó F, Rojo JM, Fierro JLG, Ferrer ML, del Monte F. Phosphate-Functionalized Carbon Monoliths from Deep Eutectic Solvents and their Use as Monolithic Electrodes in Supercapacitors. ChemSusChem 2012; 5(8):1405-1409.

[120] Chen M, Kang X, Wumaier T, Dou J, Gao B, Han Y, Xu G, Liu Z, Zhang L. Preparation of activated carbon from cotton stalk and its application in supercapacitor. Journal of Solid State Electrochemistry 2013; 17(4):1005-1012.

[121] Fan X, Yu C, Ling Z, Yang J, Qiu J. Hydrothermal Synthesis of Phosphate-Functionalized Carbon Nanotube-Containing Carbon Composites for Supercapacitors with Highly Stable Performance. ACS Appl. Mater. Interfaces 2013; 5(6):2104-2110.

[122] Wang C, Zhou Y, Sun L, Wan P, Zhang X, Qiu J. Sustainable synthesis of phosphorus- and nitrogen-co-doped porous carbons with tunable surface properties for supercapacitors. Journal of Power Sources 2013; 239:81-88.

[123] Hulicova-Jurcakova D, Puziy AM, Poddubnaya OI, Suarez Garcia F, Tascón JMD, Lu GQ. Highly Stable Performance of Supercapacitors from Phosphorus-Enriched Carbons. J. Am. Chem. Soc. 2009; 131(14):5026-5027.

2. OBJETIVOS DE LA TESIS DOCTORAL

En la presente tesis doctoral se recoge la síntesis y caracterización de varias series de materiales basados en carbono, como son carbones activados y materiales compuestos de carbón y óxidos metálicos para su utilización como electrodos de supercondensadores. Con ellos se ha estudiado el efecto de los precursores de carbono, de los heteroátomos superficiales, O, N, P y S, y de los óxidos de Ti, Zr y V sobre la morfología de los materiales obtenidos, así como la química superficial, textura porosa, área superficial y capacidad de almacenamiento de energía electroquímica de todos los materiales obtenidos. Por otra parte, muestras seleccionadas han sido utilizadas como electro-catalizadores en la reacción de reducción de oxígeno.

Los carbones activados se prepararon mediante activación química con KOH o H_3PO_4 empleando como materiales precursores diferentes subproductos agrícolas abundantes en el sur de España tales como, alpechín, alperujo y maderas de olivo, chirimoya e higuera. Con los carbones activados preparados se realizó un exhaustivo estudio de la influencia de los complejos superficiales de N, O, P y S sobre la capacidad de almacenamiento de energía al ser usados como electrodos de supercondensadores. Los objetivos de estos trabajos fueron:

1. Estudio del efecto del agente activante en la química superficial y la textura porosa de carbones activados obtenidos a partir de alpechín y alperujo.
2. Estudio del efecto de los complejos superficiales de S sobre las propiedades texturales y químicas de carbones activados obtenidos a partir de alpechín y alperujo, y la influencia del comportamiento de los carbones dopados cuando se emplean como electrodos de supercondensadores, y como catalizadores en la reacción de electro-reducción de oxígeno.
3. Estudio de la viabilidad del empleo de diferentes tipos de maderas para la preparación de carbones activados. Estudio del efecto del agente

activante en la química superficial y la textura porosa de carbones activados obtenidos.

4. Evaluación del comportamiento de los carbones activados preparados partir de diferentes tipos de madera como electrodos de supercondensadores.
5. Funcionalización de los carbones activados con diferentes heteroátomos mediante procesos solvotermales.
6. Estudio del comportamiento de los carbones activados funcionalizados como electrodos de supercondensadores.

Puesta a punto del método para la síntesis de materiales compuestos carbón - óxido metálico. Para ello se ha empleado un proceso de emulsión inversa.

7. Preparación materiales compuestos carbón - TiO_2 y carbón - ZrO_2 mediante la técnica de polimerización de resorcinol con formaldehído en presencia de un alcóxido metálico mediante emulsión inversa.
8. Preparación de esferas de carbón recubiertas con óxido de vanadio
9. Estudio de los materiales compuestos carbón-óxido metálico como electrodos de supercondensadores. Evaluación de la influencia de dichos óxidos en la capacidad de almacenamiento de energía, la ciclabilidad de los supercondensadores, la energía almacenada y la velocidad a la que el condensador puede ceder esa energía.
10. Estudio de la actividad catalítica de los materiales compuestos carbón – óxido de vanadio en la reacción de electro-reducción de oxígeno.

Todos estos objetivos se llevaron a cabo usando una amplia batería de técnicas experimentales que se expondrán adecuadamente en el siguiente Capítulo.

CAPÍTULO II: *MÉTODOS Y TÉCNICAS DE CARACTERIZACIÓN*

1. MÉTODOS Y TÉCNICAS DE CARACTERIZACIÓN

En este capítulo se detallan las distintas técnicas utilizadas para caracterizar los materiales de carbón preparados tanto a nivel textural como químico donde se detallan las ecuaciones y modelos que permiten analizar los resultados obtenidos, incluyendo los fundamentos teóricos en los que se basan cada una de las técnicas usadas. Igualmente se describen tanto los sistemas experimentales empleados para la caracterización electroquímica de los electrodos de carbón como los modelos empleados para ello.

1.1. CARACTERIZACIÓN TEXTURAL

1.1.1. Porosimetría de intrusión de mercurio

La porosimetría de intrusión de mercurio permite obtener la curva de distribución de tamaño de poros para los macroporos y mesoporos más anchos, complementando así los resultados obtenidos por adsorción de gases. Esta técnica permite también calcular la densidad aparente del sólido. El mercurio es un líquido que no moja la superficie del sólido. Para que acceda a la porosidad hay que aplicar una presión externa mayor a la atmosférica. A medida que el poro sea más estrecho, mayor será la presión que tenemos que aplicar al mercurio para que se introduzca.

La presión externa aplicada (P) se relaciona con el radio de poro (r) mediante la ecuación de Ecuación de Washburn [1] (ecuación 2.1). Ésta nos indica que el radio de poro, suponiendo poros con geometría cilíndrica, está inversamente relacionado con la presión aplicada.

$$r = \frac{-2\cos\theta}{P} \qquad \text{Ecuación 2.1}$$

En esta ecuación P es la presión total aplicada, σ la tensión superficial del mercurio, θ el ángulo de contacto del mercurio con las paredes del poro y r el radio del propio poro. El mercurio tiene un ángulo de contacto con la superficie

comprendido entre 135º y 150º. Los valores empleados en los experimentos fueron: σ = 480 mN m^{-1}, θ = 140º y un valor máximo de P = 275,6 MPa.

Con esta técnica se ha determinado el área superficial externa porosa (S_{ext}) de poros con diámetro superior a 4,4 nm; V_2, volumen de poros con un diámetro comprendidos entre 4,4 y 50 nm; V_3, volumen de poros con diámetro mayor a 50 nm (macroporos).

El equipo utilizado ha sido un porosímetro de mercurio de la casa Quantachrome, modelo Autoscan 60. Los resultados obtenidos se trataron con el software "Poro2Pc" ver.2.01 de la misma casa de acuerdo con la ecuación de Washburn.

1.1.2. Adsorción física de gases

La adsorción física de gases N_2 a -196 °C y de CO_2 a 0 °C se obtuvieron QUADRASORB-SI y en un AUTOSORB-1C ambos de la casa comercial Quantachrome Instruments. Para ello aproximadamente 0.050 g fueron desgasificadas a un vacío dinámico de 10^{-6} bar a 110 °C durante 12 h. Los adsorbatos fueron nitrógeno (99.999 %) y dióxido de carbono (99.999 %) suministrados por Air Liquide.

A partir de las isotermas de N_2 se calcularon los siguientes parámetros: la superficie específica (S_{BET}) mediante el modelo propuesto por Brünauer, Emmett y Teller [2] (B.E.T.), el volumen de microporos (W_0) por el método de Dubinin-Radushkevich [3], la anchura media de microporos (L_0) a partir de la ecuación de Stoeckli [4] y el volumen de mesoporos (V_{meso}) aplicando el método de Barrett, Joyner y Halenda [5] (B.J.H.). En el caso de la isoterma de adsorción de CO_2 se obtuvieron también el volumen y la anchura media de los microporos más estrechos de la misma forma. Las ecuaciones y los distintos modelos empleados se describen a continuación.

Ecuación de B.E.T.

El modelo de Brünauer-Emmett-Teller [2] se basa en la formación de una monocapa a bajas presiones, de manera que sabiendo la cantidad de moléculas

adsorbida y la superficie que ocupa cada una de estas moléculas, podemos calcular la superficie total del adsorbente. El cálculo de la S_{BET} se lleva a cabo aplicando las Ecuaciones 2.1 y 2.2.

$$\frac{P}{V_{ads}(P_0 - P)} = \frac{1}{V_m C} + \frac{C-1}{V_m C} \times \frac{P}{P_0} \qquad \text{Ecuación 2.2}$$

$$S_{BET} = V_m \times \frac{1}{22400} \times N_A \times 0.162 \times 10^{-18} \qquad \text{Ecuación 2.3}$$

Ecuación de Dubinin-Radushkevich y ecuación de Stoeckli.

El modelo de Dubinin-Radushkevich [3], DR, es utilizado para describir sólidos microporosos y en vez del concepto de superficie específica se utiliza el de volumen de microporos. La teoría de Dubinin asume que la adsorción en los microporos se produce mediante un mecanismo de llenado de su volumen con un adsorbato en estado similar al líquido y supone que el tamaño de los poros es heterogéneo y sigue una distribución Gaussiana. Cuando se habla de sólidos microporosos, es más coherente el concepto de volumen de microporos que el de área superficial. La ecuación de DR está expresada por la ecuación

$$W = W_0 \times \exp\left[-\left({A}/{\beta E_0} \right)^2 \right] \qquad \text{Ecuación 2.4}$$

donde A es el trabajo molar diferencial, $A = RT \ln\left({P_0}/{P} \right)$, W ($cm^3g^{-1}$) es el volumen adsorbido como líquido a una presión relativa de equilibrio P_0/P, y W_0 (cm^3g^{-1}) es el volumen de microporos

Los parámetros E_0 y β son específicos del sistema adsorbato-adsorbente; E_0 es la energía característica de adsorción, la cual es inversamente proporcional a la anchura media de los microporos (L_0) y β es el coeficiente de afinidad del adsorbato. En el caso del N_2 a -196 °C β = 0,33 [6] y para CO_2 a 0 °C β =0,35 [7]; los volúmenes molares para N_2 y CO_2 a esas temperaturas son 34,65 cm^3 mol^{-1} y 43,01 cm^3 mol^{-1}, respectivamente.

La anchura media de los microporos se determina mediante la Ecuación de Stoeckli [4] (Ecuación 2.5) para valores de E_0 comprendidos entre 40 y 20 kJ mol^{-1} o de Dubinin [8] (Ecuación 2.6) cuando E_0 es menor de 20 kJ mol^{-1}.

$$L_0(nm) = \frac{10.8}{(E_0 - 11.4\,kJ/mol)} \qquad \text{Ecuación 2.5}$$

$$L_0(nm) = \frac{24}{E_0\,(kJ/mol)} \qquad \text{Ecuación 2.6}$$

Una vez obtenidos los parámetros relativos al volumen de microporos, energía de adsorción característica y anchura media de poro, al aplicar las ecuaciones anteriores, podemos encontrarnos distintas situaciones:

1. $W_0(N_2) < W_0(CO_2)$. Este caso se produce en carbonizados y carbones con un bajo grado de activación, por la presencia de constricciones a la entrada de los microporos que restringen el acceso del N_2 a su interior, debido a la baja temperatura a la que se lleva a cabo la adsorción. Sin embargo, al realizarse la adsorción de CO_2 a mayor temperatura esta puede acceder a estos microporos. En este caso se dice que la adsorción es activada.

2. $W_0(N_2) = W_0(CO_2)$. Ocurre cuando la accesibilidad a la microporosidad de ambos adsorbatos es la misma en carbones con un grado de activación medio. En este caso no existen constricciones debido al mayor grado de activación de los carbones y se puede considerar que hay una distribución homogénea del tamaño de los microporos.

3. $W_0(N_2) > W_0(CO_2)$. Se produce en carbones con un alto grado de activación, en los que existe una distribución muy ancha en el tamaño de los microporos. Esta diferencia en volumen de microporos se debe a la gran diferencia en la presión de saturación que existe entre ambos adsorbatos. Así, el N_2 llena todo el volumen de microporos (ultramicroporos y supermicroporos), mientras que con CO_2 solo medimos a 0 ºC, los microporos más estrechos (menores de 0,7 nm en anchura) o ultramicroporos.

Método de B.J.H.

El método BJH propuesto por Barrett, Joyner y Halenda (BJH) [5] se emplea para determinar la distribución del tamaño de los mesoporos. Este método supone que los poros son de geometría cilíndrica y cuando la presión relativa es cercana a la unidad, todos los poros se llenan de adsorbato en forma líquida y a medida que ésta se reduce sólo los poros más pequeños permanecen llenos con el líquido. Los adsorbentes que presentan isotermas de N_2 a -196 ºC tipo IV, se caracterizan por la presencia de un ciclo de histéresis durante la desorción. En este caso se puede estimar una distribución de tamaños de poros (PSD) por medio de la aplicación de la ecuación de Kelvin [6]. Sin embargo, desde el un punto de vista termodinámico, esta ecuación es únicamente aplicable a procesos reversibles.

La existencia de un ciclo de histéresis genera una incertidumbre hacia qué proceso elegir (adsorción o desorción) que cumpla con esta condición. Por tal motivo, en general es más apropiado utilizar la isoterma de desorción, debido a que para un mismo volumen de gas, se presenta una presión relativa más baja, obteniendo un estado de energía libre más bajo y estará sujeta a situación verdadera de estabilidad termodinámica. Sin embargo, para las muestras que presentan histéresis de tipo H2 se recomienda utilizar la rama de adsorción para el análisis de la PSD.

El cálculo del tamaño de los mesoporos, se realiza asumiendo poros con geometría cilíndrica, aplicando la ecuación de Kelvin a los datos de desorción de la isoterma de nitrógeno a –196 ºC. El radio de Kelvin es el radio del poro en el cual la condensación ocurre a una presión relativa determinada.

$$r_K = \frac{-2\gamma V_m}{RT\ln(P/P_0)} \qquad \text{Ecuación 2.7}$$

Donde γ es la tensión superficial del nitrógeno ($8{,}85\times10^{-7}$ J cm^{-2}), V_m es el volumen molar de N_2 líquido (34,7 cm^3 mol^{-1}), *R* la contante universal de los gases ideales 8,314 J mol^{-1}K^{-1}, *T* la temperatura de evaporación del nitrógeno (77 K),

P/P_0 es la presión relativa y r_K el radio de Kelvin del poro. Esta ecuación es válida para poros vacíos, pero el problema que presenta es que en la pared de los poros se queda adsorbida una capa de nitrógeno cuyo grosor depende de la presión relativa (P/P_0).

Dado que antes de la condensación se produce alguna adsorción sobre las paredes del poro, r_K no representa el radio del poro. El radio real del poro r_P se define por la ecuación 2.8:

$$r_P = r_K + t \qquad \text{Ecuación 2.8}$$

donde t es el espesor de la capa adsorbida y se puede calcular empleando la ecuación 2.9 propuesta por Lippens [9]:

$$t = \left[\frac{13{,}99}{\log\left(\frac{P}{P_0}\right) + 0{,}334} \right]^{1/2} \qquad \text{Ecuación 2.9}$$

El poro de mayor radio, r_{P1}, tiene una capa fisisorbida de moléculas de nitrógeno de espesor t_1. Dentro de este espesor hay un capilar interno con radio r_K, en el cual se produce la evaporación cuando la presión relativa disminuye. La relación entre el volumen y el poro, V_{P1} y el volumen del capilar interno (Kelvin) V_{K1} viene dada por:

$$V_{P1} = V_{K1} \times \frac{r_{P_1}^2}{r_{K_1}^2} \qquad \text{Ecuación 2.10}$$

Cuando la presión relativa disminuye de $(P/P_0)_1$ a $(P/P_0)_2$ un volumen V_1 se desorbe en la superficie. El volumen de líquido V_1 no solo representa el vaciado del condensado en el poro de mayor tamaño, sino también una reducción en el espesor de su capa fisisorbida. Después de esta disminución de presión relativa,

el promedio de espesor es $\Delta t_{1/2}$ y el volumen de poro de mayor tamaño viene dado por:

$$V_{P1} = V_1 \times \left(\frac{r_{P1}}{r_{K1} + \Delta t_1 / 2} \right)^2 \qquad \text{Ecuación 2.11}$$

Cuando la presión relativa disminuye de nuevo $(P/P_0)_3$ el volumen de líquido desorbido incluye no sólo la parte condensada en el próximo poro más grande sino también el volumen de una delgada segunda capa fisisorbida situada detrás del poro más grande. El volumen desorbido V_{P2} del poro de menor tamaño vienen dado por:

$$V_{P2} = (V_2 - V_{\Delta t_2}) \times \left(\frac{r_{P2}}{r_{K2} + \Delta t_2 / 2} \right)^2 \qquad \text{Ecuación 2.12}$$

$$V_{\Delta t_2} = \Delta t_2 \times Ac_1 \qquad \text{Ecuación 2.13}$$

$$V_{\Delta t_n} = \Delta t_n \sum_{j=1}^{n-1} Ac_j \qquad \text{Ecuación 2.14}$$

donde Ac_1 es el área expuesta por los poros anteriormente vaciados de gas fisisorbido, el volumen de la segunda etapa de desorción $V_{\Delta t_2}$ y $V_{\Delta t_n}$ para cualquier etapa de desorción gradual, el cual es considerado como la suma del promedio de las áreas de poros no llenos, sin incluir los poros que fueron vaciados por desorción.

El área de cada poro A_p es constante y puede ser calculada a partir del volumen de poro asumiendo poros de geometría cilíndrica

$$V_{Pn} = (\Delta V_n - \Delta t_n \sum_{j=1}^{n-1} Ac_j) \times \left(\frac{r_{Pn}}{r_{Kn} + \Delta t_n / 2} \right)^2 \qquad \text{Ecuación 2.15}$$

Todos los poros vaciados de su condensado durante la disminución de la presión relativa, tienen un radio promedio r_p calculado a partir de la ecuación de Kelvin, a presiones relativas más altas y más bajas durante la etapa de desorción. El término *c* está definido como:

$$c = \frac{\bar{r}_c}{\bar{r}_p} = \frac{\bar{r}_p - t_{\bar{r}}}{\bar{r}_p} \qquad \text{Ecuación 2.16}$$

El promedio del radio capilar, r_c, se expresa como:

$$\bar{r}_c = \bar{r}_p - t_{\bar{r}} \qquad \text{Ecuación 2.17}$$

donde t_C es el espesor de la capa adsorbida para un radio promedio dado en el intervalo de disminución de la presión correspondiente calculado por la ecuación de Boer.

Teoría de la Densidad Funcional

Esta teoría fue propuesta por Evans y Tarazona [10] en 1984, posteriormente Seaton et al. [11] la desarrollaron para obtener la distribución de tamaño de poros.

La idea se basa en la construcción en un potencial funcional, Ω[ρ(r)], de la densidad del fluido, ρ(r):

$$\Omega[\rho_L(\bar{r})] = F[\rho_L(\bar{r})] + \int dr \rho_L(\bar{r})[V_{ext} - \mu] \qquad \text{Ecuación 2.18}$$

donde F[ρ(r)] es la energía libre de Helmholtz "intrínseca" del fluido, V_{ext} es el potencial externo provisto por el sólido, μ es el potencial químico y la integral es sobre todo el volumen. F[ρ(r)] se la suma de $F_{repulsiva}$ + $F_{atractiva}$, y a la parte repulsiva se aproxima a la energía libre de un fluido de esferas rígidas:

$$F[\rho_L(\bar{r})] = F_{ed}[\rho_L(\bar{r})] + 1/2\int dr \rho_L(\bar{r})U(r) \text{ donde } U(r) = \int dr' \rho_L(r')u_{gg}(r,r')$$

Ecuación 2.19

y para obtener el perfil de densidad en equilibrio se minimiza el potencial funcional respecto de la densidad, es decir:

$$\delta\Omega\left[\frac{\rho_L(r)}{\delta\rho_L(r)}\right]_{\rho_L,Eq} = 0 \qquad \text{Ecuación 2.20}$$

Los potenciales que correspondientes a los términos que describen las partes repulsivas y atractivas de las interacciones fluido-fluido y fluido-sólido varían de acuerdo al sistema a tratar. Esto ha dado lugar a diferentes aproximaciones DFT como lo son la teoría de la densidad funcional local (LDFT) y la no local (NLDFT). La aproximación LDFT se utiliza a menudo, pero no es capaz de describir correctamente la fuerte oscilación en el perfil de densidad de un fluido en la interfase fluido-sólido lo que lleva a una inadecuada descripción de las isotermas de adsorción, en especial para microporos estrechos. En contraste la NLDFT [12] proveen una visión más realista de lo que le ocurre a un fluido confinado en un poro.

1.1.3. Microscopia Electrónica de Barrido (SEM)

Con objeto de visualizar la morfología de la superficie de los adsorbentes se tomaron microfotografías de la superficie por Microscopía Electrónica de Barrido (SEM). Estas fueron realizadas en el Centro de Instrumentación Científica de la Universidad de Granada, con un microscopio electrónico de alta resolución modelo AURIGA (FIB-FESEM) de Carl Zeiss SMT.

1.1.4. Microscopia Electrónica de Transmisión (TEM)

La HRTEM se basa en la interacción que se produce cuando un haz de electrones de energía elevada (100 – 200 keV) incide sobre una muestra. Los electrones llevan asociada una longitud de onda y es posible determinar sus propiedades oscilatorias para obtener imágenes, así como diagramas de difracción.

La técnica HRTEM se realizó con un equipo Philips, modelo CM-20 equipado con sistema EDAX de microanálisis mediante dispersión de energía de rayos X y con una magnificación de 660.000X. La máxima resolución fue de 0,27

nm entre puntos y 0,14 nm entre líneas, y la tensión de aceleración es de pasos seleccionables de 20, 40, 80, 120, 160 y 200 KV.

1.2. CARACTERIZACIÓN QUÍMICA

1.2.1. Análisis elemental

El análisis elemental de las muestras se realizó en un analizador elemental THERMO SCIENTIFIC Modelo Flash 2000 del Centro de Instrumentación Científica de la Universidad de Granada, el cual determina el contenido de C, H, N y S; el contenido de O se calculó por diferencia.

1.2.2. Análisis termogravimétrico (TGA)

El contenido en cenizas de los precursores lignocelulósicos y de los carbones activados se ha determinado mediante análisis termogravimétrico. En este estudio el análisis termogravimétricos se obtuvieron en el Centro de Instrumentación de la Universidad de Granada con un instrumento TGA-50H de la casa Shimadzu. Los análisis se realizaron en flujo de aire hasta 950 °C y con una velocidad de calentamiento de 10 °C min^{-1}.

1.2.3. Espectroscopía de fotoemisión de Rayos-X

La espectroscopía de fotoemisión de Rayos-X (XPS) se utiliza para caracterizar la química superficial de la muestra en su superficie más externa.

Los espectros fueron obtenidos en el Centro de Instrumentación Científica de la Universidad de Granada, con un espectrómetro Kratos Axis Ultra-DLD usando como fuente la radiación de MgKα (hu = 1253.6 eV) y un analizador hemiesférico de electrones operando a 12 kV y 10 mA. Las muestras analizadas se colocaron en un portamuestras de acero y fueron introducidas en la cámara de análisis siendo desgasificadas a una presión inferior a 10^{-8} Torr. Las regiones analizadas fueron las correspondientes a los elementos C, O, N, S, P, V, Ti y Zr (C_{1s}, O_{1s}, N_{1s}, S_{2p}, P_{2p}, V_{2p}, Ti_{2p}, y Zr_{3d},). Estas señales fueron deconvolucionadas usando funciones de tipo suma Gaussianas-Lorentzianas para determinar el

número de componentes, la energía de ligadura de los picos (B.E.) y las áreas de los mismos (análisis cuantitativo). La energía de ligadura del pico de la región C_{1s}, correspondiente a C=C (aromático-alifático) se tomó como pico de referencia para conocer la posición de los demás, asignándole el valor de 284,6 eV y la asignación de los distintos picos se llevó a cabo en función de la bibliografía disponible [15-17] (Tabla 1)

1.2.4. Espectroscopía Raman

Cuando la luz incide sobre una molécula, el campo eléctrico oscilante de la radiación incidente provoca una oscilación de la densidad electrónica de la molécula. Este efecto viene representado por la aparición de un momento dipolar eléctrico oscilante inducido que actúa, a su vez, como fuente de radiación, originando las dispersiones Rayleigh y Raman. La dispersión está dirigida en todas las direcciones, excepto en la de la propia dirección del dipolo, con un valor máximo de intensidad a 90° con respecto al eje del dipolo y tomando para el resto de ángulos un valor $I(q)=I_{max}\times sen^2 q$. La mayor parte de la luz es elásticamente dispersada, dando lugar a la dispersión Rayleigh, sin cambio en la energía de los fotones, pero algunos fotones intercambian energía con la muestra y son dispersados inelásticamente, con un cambio en su longitud de onda, indicando la pérdida o ganancia de energía. Este es el llamado efecto Raman, descubierto por el físico indio Chandrasekhara Venkata Raman en 1928. Dicho efecto proporciona una gran cantidad de información cualitativa de la muestra a partir de los cambios característicos en la energía de los fotones dispersados.

Los espectros Raman se obtuvieron usando un espectrómetro dispersivo Micro-Raman JASCO NRS-5100 con una radiación láser de 532 nm.

1.2.5. Difracción de rayos X (DRX)

Los difractogramas de rayos X (XRD) en polvo se registraron con un difractómetro BRUKER D8 ADVANCE (BRUKER, Rivas-Vaciamadrid, España) usando la radiación CuKα con λ=0.1545 nm. Los difractogramas se registraron

entre 5º y 70º (2θ) con un paso de 0,02º y un tiempo por paso de 96 s. El tamaño medio de los cristales se determinó usando la ecuación de Scherrer.

1.2.6. Microcalorimetría de inmersión

Para la determinación de la hidrofobicidad (HF) de los materiales se han obtenido las entalpías de inmersión tanto en benceno como en agua, $\Delta_i H(C_6H_6)$ and $\Delta_i H(H_2O)$, para lo cual, se ha empleado un calorímetro isotérmico tipo Tian-Calvet modelo SETARAM C80. La hidrofobicidad de las muestras se calculó de acuerdo con la ecuación 2.21. La entalpía de inmersión en el agua depende de interacciones específicas y no específicas; en contraste, en el caso del benceno la entalpía de inmersión depende sólo de la superficie del carbono accesible a las moléculas de benceno.

$$HF = \frac{\Delta_i H(C_6H_6) - \Delta_i H(H_2O)}{\Delta_i H(C_6H_6)} \qquad \text{Ecuación 2.21}$$

1.3. CARACTERIZACIÓN ELECTROQUÍMICA

Los electrodos de trabajo se prepararon mezclando los materiles compuestos de xerogeles de carbón-óxido metálico o carbones activados preparados los cuales constituyen el material electroactivo. Esto materiales (excepto las microesferas) se molturaron para obtener un tamaño de partícula <350 µm y se mezclaron con politetrafluroetileno (PTFE) como aglomerante, en una proporción de 90:10. La mezcla se extendió sobre una superficie de vidrio y se adicionaron unas gotas de agua para formar una pasta y asegurar la homogeneidad de la mezcla. La pasta obtenida se secó en una estufa a 110 ºC durante 24 h.

Los estudios de almacenamiento de enrgía se llevaron a cabo en una celda de dos electrodos (Figura 1). Para ello se prepararon dos electrodos de trabajo soportados cada uno sobre dos discos de papel de grafito separados por un aislante de microfibra de vidrio con poros de 1,6 µm. El material se prensó sobre los discos a una presión de 3 bar durante 5 min

Electrodo de trabajo

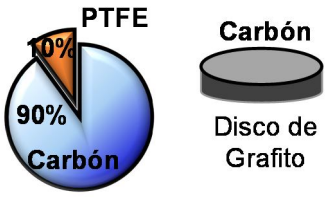

Celda de dos electrodos

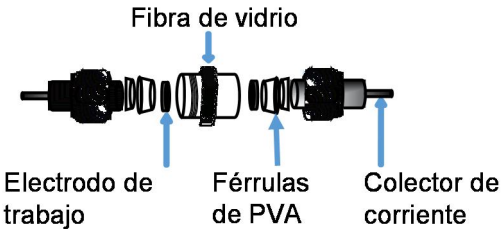

Figura 1. Electrodos de trabajo y esquema del montaje experimental para celdas de dos electrodos

Los materiales carbonosos preparados como electrodos se caracterizaron electroquímicamente utilizando las técnicas de voltametría cíclica (VC), cronopotenciometría (CP) y espectroscopía de impedancia electroquímica (EIS). Los experimentos se realizaron en un potenciostato VMP3 de Biologic Science Instrument utilizando una configuración dos electrodos.

1.3.1. Voltametría Cíclica (VC)

La VC es una de las técnicas más utilizadas en electroquímica. Esta técnica consiste en aplicar a un electrodo de trabajo una variación lineal del potencial en el tiempo con una velocidad de barrido determinada, *s*, entre un límite superior y uno inferior una o varias veces mientras se registra el cambio de corriente, I, que circula por el sistema [18].

La voltametría cíclica también es útil para obtener información acerca de los procesos farádicos que puedan tener lugar. Si durante el barrido se llega a un

potencial en el que tiene lugar una reacción química, se produce un aumento de corriente que permanecerá mientras quede especie que pueda reaccionar.

En la **Figura 2** se presentan los diferentes tipos de voltagramas que se pueden obtener en condensadores. La curva 1 indica el comportamiento ideal de un condensador, forma rectangular e imagen espejo. La curva 2 representa un condensador con resistencia interna que se aleja relativamente de la idealidad. La curva 3 presenta una contribución farádica a altos y bajos voltajes debido a una descomposición del electrolito, incluyendo unos picos 4 debido a reacciones redox [19].

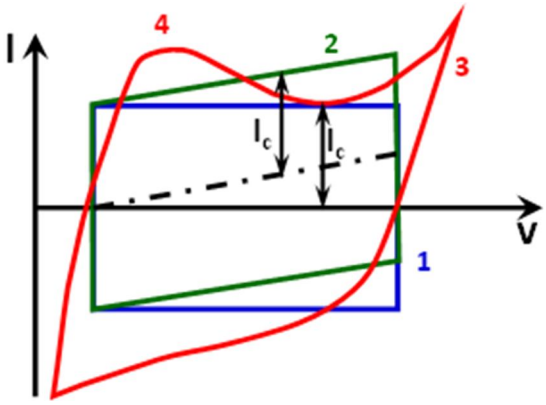

Figura 2. Voltagramas típicos en condensadores

1.3.2. Cronopotenciometría (GD)

En la técnica GD el condensador se carga a una corriente constante, I_c, hasta llegar a un voltaje elegido, V, momento en el que se invierte la corriente, I_d, y se da inicio a la descarga. La corriente generalmente varía en un intervalo de 1 mA g^{-1} a varios A g^{-1}. El cambio de potencial, $\triangle V$ (V), en un proceso de carga interfacial a una densidad de corriente constante, I_d (A) varía linealmente con el tiempo t (s) de acuerdo con la Ecuación 2.22.

$$C = I_d \times \frac{\Delta t}{\Delta V} \qquad \text{Ecuación 2.22}$$

Al fijar la corriente, la representación del potencial frente al tiempo será una línea recta, de cuya ordenada en el origen puede obtenerse la resistencia y a partir de la pendiente la capacidad. En el caso de un condensador ideal, la curva de V=f(t) de la carga debe ser igual a la descarga, presentando una forma triangular perfecta [20]. En la Figura 3 se presenta una curva de cronopotenciometría típica ideal.

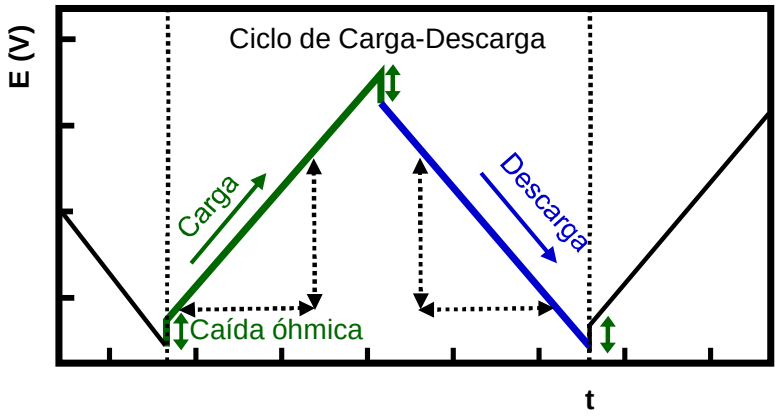

Figura 3. Cronopotenciograma típico de un proceso de carga y descarga sin contribución farádica

La resistencia equivalente en serie del supercondensador, ESR, puede calcularse utilizando esta técnica midiendo la caída óhmica (IR) al principio de la carga y al principio de la descarga [21] en una curva cronopotenciometría típica.

$$ESR = \frac{\Delta V_{IR}}{\Delta I}$$ Ecuación 2.23

1.3.3. Espectroscopía de Impedancia Electroquímica (EIS)

La EIE es una de las técnicas más frecuentemente utilizadas para la caracterización de sistemas y procesos electroquímicos (propiedades eléctricas de los materiales y las interfases). Esta se basa en la aplicación de un potencial de corriente alterna (AC) a una celda electroquímica, midiendo la corriente a través

de la celda en equilibrio [26,163,164]; la señal de la corriente se puede analizar como la suma de funciones sinusoidales.

Las mediciones para los materiales preparados se realizaron mediante la perturbación del sistema por una variación de potencial de forma sinusoidal:

$$V_t = V_o \times \text{sen}(2\pi ft) \qquad \text{Ecuación 2.24}$$

donde V_t es el voltaje aplicado en un tiempo t, V_0 es la amplitud máxima del voltaje y f la frecuencia.

Por lo tanto, la respuesta de la corriente también será sinusoidal a la misma frecuencia pero desplazada en fase:

$$I_t = I_o \times \text{sen}(2\pi ft\phi) \qquad \text{Ecuación 2.25}$$

donde I_t es la corriente en un tiempo t, I_0 la amplitud de la corriente y Φ el desplazamiento de fase de la corriente frente al voltaje aplicado.

La EIS se mide normalmente utilizando una pequeña señal de excitación y la respuesta de la celda es pseudo-lineal. La impedancia se define de manera análoga a la resistencia en el caso de un circuito de corriente continua como:

$$Z_t = \frac{V_t}{I_t} \qquad \text{Ecuación 2.26}$$

La impedancia tiene una magnitud Z_0 y una fase Φ:

$$Z_0 = \frac{V_0}{I_0} \qquad \text{Ecuación 2.27}$$

La impedancia en notación compleja se considera como:

$$Z_t = Z_0 \times (\cos\phi + j\text{sen}\,\phi) = Z' + jZ'' \qquad \text{Ecuación 2.28}$$

Donde $j = \sqrt{-1}$, Z' es la parte real de la impedancia y Z" es la parte compleja.

Los valores de impedancia obtenidos experimentalmente se suelen representar principalmente de dos formas, mediante el diagrama Nyquist o mediante el diagrama de Bode. El diagrama de Nyquist (Figura 4) representa la parte compleja de la impedancia (Z") frente a la parte real (Z') y son muy útiles para obtener parámetros de los espectros de impedancia con arcos simples o múltiples en el plano complejo. Los materiales de carbón se caracterizan por tener una parte resistiva a altas frecuencias (semicírculo) y un comportamiento capacitivo a bajas frecuencias (<1 Hz). A bajas frecuencias el espectro se aproxima a una línea recta perpendicular a la abscisa (Figura 4). El punto de inflexión entre el semicírculo y la línea vertical, es conocido como "knee frequency", punto que indica que la mayoría de la energía es almacenada accesible a esta frecuencia y la frecuencia a la cual el comportamiento capacitivo es dominante (línea vertical a bajas frecuencias) respecto al resistivo, arriba de este límite la parte real de la impedancia es dependiente de la frecuencia [18,22].

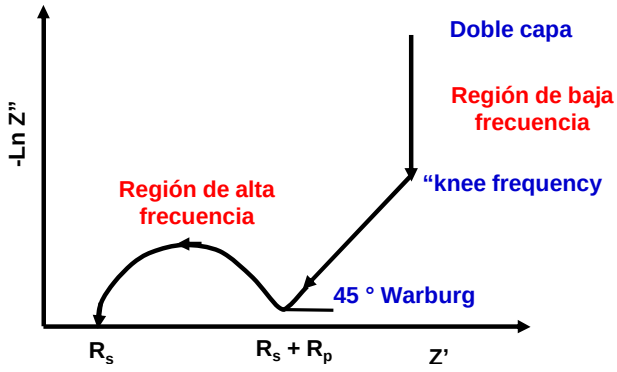

Figura 4. Diagrama de Nyquist típico para una celda con cinética mixta y transferencia de carga

En las frecuencias de rango medio (100 – 1 Hz) se observa la influencia de la porosidad del electrodo y la velocidad de migración de los iones desde el electrolito al centro del electrodo. La impedancia de Warburg está asociada con los efectos difusivos de las especies químicas a los largo del electrodo [23].

La expresión de la impedancia depende del elemento de circuito equivalente que se esté estudiando. Los diagramas Nyquist son muy útiles para obtener parámetros de los espectros de impedancia con arcos simples o múltiples en el plano complejo.

La relación de la magnitud de la impedancia (|Z|) y el ángulo de fase (ϕ) con el ángulo de frecuencia (ω), se conoce como el diagrama de Bode, a partir del cual también puede obtener información importante del sistema electroquímico [23]. El diagrama de Bode también se puede representar como el logaritmo de la magnitud de la impedancia frente a la frecuencia (Figura 5).

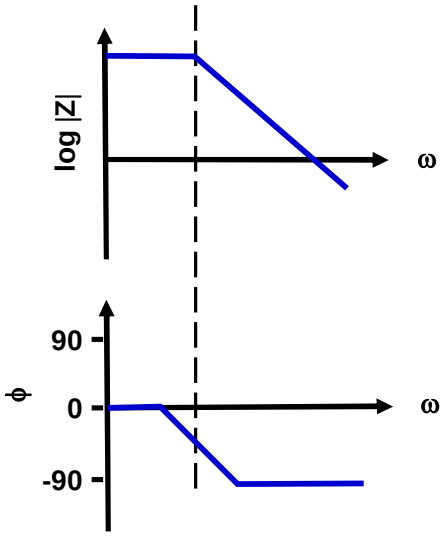

Figura 5. Diagrama de Bode con una constante de tiempo

El tratamiento de los datos obtenidos se suele realizar mediante la obtención de un circuito equivalente que reproduzca el espectro de impedancia obtenido durante el experimento. Estos circuitos están formados por elementos eléctricos como resistencias, condensadores, etc., (expuestos en la Figura 8, Capítulo I) que reproducen el comportamiento de los procesos reales como la resistencia del electrolito entre los electrodos referencia y trabajo, la doble capa (capacidad) que se forma en la interfase electrodo-disolución o la transferencia de

carga que ocurre durante un proceso farádico.Es necesario destacar que para aplicar correctamente la técnica es necesario suponer el menor número de elementos de circuito posible. A fin de cuentas, con este proceso lo que hacemos es modelar un sistema experimental (real) mediante un circuito equivalente. Si este circuito contiene muchos elementos, lo que hacemos es simular una curva experimental con un modelo que incluye muchos parámetros. Sin duda, el ajuste al modelo será tanto mejor cuantos más parámetros incorporemos, pero se nos presentará una gran dificultad a la hora de interpretar los resultados: no podremos dotar de significado físico todos los parámetros del proceso. Si esto sucede, poco o nada aprenderemos sobre el sistema experimental.

1.4. BIBLIOGRAFÍA

[1] W. Washburn, Note on a method of determining the distribution of pore sizes in a porous material; Proc. of the Nat. Acad. Sci. of the USA **7**, 115-116, (1921).

[2] S. Brunauer, P.H. Emmett, E. Teller, Adsorption of gases in multimolecular layers, *Journal of the American Chemical Society*, **60** (1938) 309-319.

[3] M.M. Dubinin, Inhomogeneous microporous structures of carbonaceous adsorbents, *Carbon*, **19** (1981) 321-324.

[4] Stoeckli F., *Porosity in carbon. Characterization and applications*, Eds. Patrick, J. Arnold, London, 1995.

[5] Barrett, E.P. Joyner, L.G. Halenda, P.P. The Determination of Pore Volume and Area Distributions in Porous Substances. I. Computations from Nitrogen Isotherms, *Journal of the American Chemical Society*, **73** (1951) 373-380.

[6] Gregg S, Sing K. Adsorption, surface area, and porosity. 2nd ed. London: Academic Press; 1982.

[7] Reichenauer G, Emmerling A, Fricke J, Pekala R. Microporosity in carbon aerogels. J Non-Cryst Solids. **225** (1998) 210-214.

[8] Dubinin, M.M. Generalization of the theory of volume filling of micropores to nonhomogeneous microporous structures, *Carbon*, **23** (1985) 373-380.

[9] Lippens B, De Boer J. Studies on Pore Systems in Catalysts: V. The t method. Journal of Catalysis. **4(3)**; (1965), 319–23.

[10] Evans R., Tarazona P. Theory of condensation in narrow capillaries. Phys. Rev. Lett., **52** (1984), 557-560

[11] Seaton N.A., Walton J., Quirke N. A new analysis method for the determination of the pore-size distribution of porous carbons from nitrogen adsorption measurements. Carbon, **27** (1989), 853-861

[12] C. Lastoskie, K.E. Gubbins, N. Quirke. Pore-size distribution analysis of microporous carbons - a density-functional theory approach. J. Phys. Chem., **97** (1993), 4786-4796

[13] Foord, R., Jakeman, E., Oliver, C. J., Pike, E. R., Blagrove, R. J., Wood, E., Peacocke, A. R., Determination of diffusion coefficients of haemocyanin at low concentration by intensity fluctuation spectroscopy of scattered laser light, Nature **227**, (1970), 242-245.

[14] Cummins, H. Z. Knable, N. Yeh, Y. Observation of diffusion broadening of rayleigh scattered light, Physical Review Letters, 12(6), (1964), 150-153.

[15] Pérez-Cadenas, A.F. Maldonado-Hódar, F.J. Moreno-Castilla C., On the nature of surface acid sites of chlorinated activated carbons, Carbon, **41** (2003) 473-478.

[16] Desimoni, E. Casella, G.I. Salvi, A.M. XPS/XAES study of carbon fibres during thermal annealing under UHV conditions, Carbon, **30** (1992) 521-526.

[17] Pérez-Cadenas, M. Moreno-Castilla, C. Carrasco-Marín, F. Pérez-Cadenas, A.F. Surface Chemistry, Porous Texture, and Morphology of N-Doped Carbon Xerogels. Langmuir, **25** (2009) 466-470.

[18] Frackowiak E, Béguin F. Carbon materials for the electrochemical storage of energy in capacitors. Carbon. 2001;39(6):937–50.

[19] Bard, A.J. Electrochemical Methods. Fundamentals and Applications. John Wiley & Sons, Nueva York, 2001.

[20] Raymundo-Piñero E, Béguin F. Application of nanotextured carbons for supercapacitors and hydrogen storage. In: Bandosz T, editor. Activated Carbon Surfaces in Environmental Remediation. Oxford: Elsevier; 2006. p. 293–343.

[21] Li W, Chen D, Li Z, Shi Y, Wan Y, Wang G, et al. Nitrogen-containing carbon spheres with very large uniform mesopores: The superior electrode materials for EDLC in organic electrolyte. Carbon. 2007;45(9):1757–63.

[22] Du C, Pan N. High power density supercapacitor electrodes of carbon nanotube films by electrophoretic deposition. Nanotechnology. 2006;17(21):5314–8.

[23] Liu X, Zhang R, Zhan L, Long D, Qiao W, Yang J, et al. Impedance of carbon aerogel/activated carbon composites as electrodes of electrochemical capacitors in aprotic electrolyte. New Carbon Materials. 2007;22(2):153–8.

[24] Bleda-Martínez MJ, Lozano-Castelló D, Cazorla-Amorós D, Morallón E. Kinetics of Double-Layer Formation: Influence of Porous Structure and Pore Size Distribution. Energy Fuels. 2010;24(6):3378–84.

[25] Taberna P, Simon P, Fauvarque J. Electrochemical characteristics and impedance spectroscipy studies of carbon-carbon supercapacitors. J. Electrochem. Soc. 2003;150(3):A292–300.

CHAPTER III: *ACTIVATED CARBONS FROM KOH AND H_3PO_4- ACTIVATION OF OLIVE RESIDUES AND ITS APPLICATION AS SUPERCAPACITOR ELECTRODES*

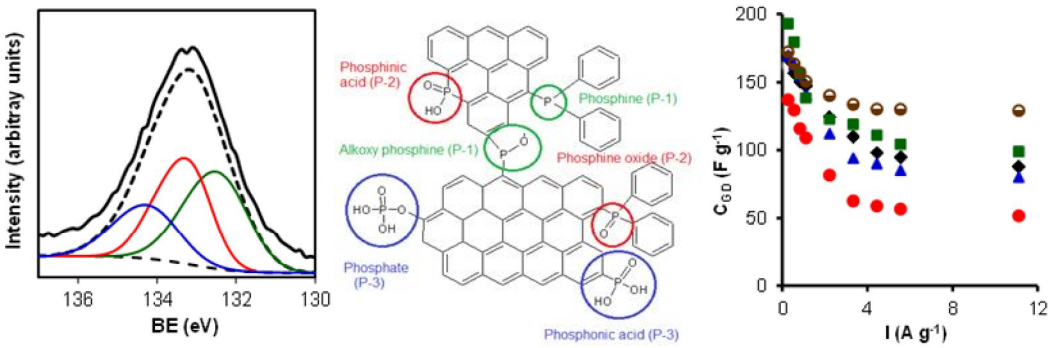

1. ABSTRACT

Activated carbons from a mixture of olive-residue, oil and vegetable water, known as alperujo, OR, were prepared by KOH and H_3PO_4 activation. KOH activations were made following two different methods (carbonization-activation and impregnation-activation) with two different KOH/carbon ratios. Textural characterization with N_2 and CO_2 reveals that a prior carbonization of samples followed by the activation with KOH, produces samples with similar textural and chemical properties to the impregnated ones at low KOH ratio, while at high KOH ratio; more porous samples are obtained by carbonization. However, no differences are observed increasing the KOH ratio for the impregnated samples. As a consequence, similar or even more porous samples are obtained by using an easier preparation method such as carbonization-activation. On the other side, H_3PO_4 activation leads to samples with less surface area but with a more developed mesoporosity. In addition, the chemical surfaces of KOH and H_3PO_4 activated samples are very different as shown by XPS and TPD results. XPS data denote a similar chemical texture in KOH activated samples in spite of the different preparation methods and KOH ratio, whereas the H_3PO_4 method fixed different phosphorus surface groups. Analysing TPD data while on KOH activated samples, oxygenated surface groups (OSG) decompose mainly as CO_2 (carboxylic acid, anhydrides, lactones, etc.) during the TPD experiments, on H_3PO_4 activated one those OSG ones evolve as CO (semiquinone, carbonyl, etc.) which has been attributed to the presence of –C–O–P– species that decompose in the form of CO at around 860 °C. As a consequence, similar electrochemical capacitances are obtained using KOH activated samples, which depend linearly on the surface area while the H_3PO_4 activated one presents higher capacitance value and capacitance stability in spite of its smaller surface area. This fact was related with the presence and nature of phosphorus surface groups.

Keywords: Mixture of olive-residue, oil and vegetable water, Activated carbons, KOH and H_3PO_4 activation, Supercapacitors, Energy storage.

2. INTRODUCTION

Activated carbons are attractive materials for industrial applications due to their good chemical and physical properties as well as their high surface area and well developed porosity, which can be doped and adapted with different active surface functionalities. These properties make them very good candidates for several applications such as adsorption of liquid [1,2] and gas pollutants [3,4], catalysis [5], biomedical applications [6], as well as energy storage like supercapcitor devices [7-9]. For this purpose, many types of activated carbons have been prepared from several lignocellulosic precursors such as argan shell [8], wood [10,11], coconut [12], sugar cane bagasse [13], olive-mill waste water [14] and olive stone [15]; cheap biomass residues and wastes which make them cheaper than others materials for different applications.

Several preparation methods were reported in the literature for the preparation of activated carbons from different lignocellulosic precursors [8,14,15]. Different activating agents are used to produce materials with optimum textural properties and a designed surface chemistry depending on the activating agent and the preparation method used.

The use of activated carbons as supercapacitor electrodes gives good and promising results providing a high specific capacitance ranging from 100 to 400 F g^{-1} [8,16]. This capacitance is influenced by the porous structure and especially by the homogeneity of this porous structure. Furthermore, the surface chemistry plays a crucial role in the electrochemical properties of activated carbons. In this sense, the introduction of different functional groups on the activated carbon surface and the influence of these groups on their electrochemical properties are a very interesting and worldwide studied field [17-19]. The presence of heteroatom groups such as nitrogen [8], oxygen and phosphorus groups [20] on the activated carbon surface has a very important effect on the electrochemical properties. However, not only is important the presence of different heteroatoms on the carbon surface, the nature of these groups is also quite significant. Several authors reported that the presence of phosphorus groups can decrease or ameliorate the capacitance

of the activated carbon depending on the nature of the phosphorus groups [20]. This fact indicates that it is very important to study the introduction of a doping agent to the surface chemistry of activated carbons for its use as supercapacitor electrodes but also the nature of these functional groups to improve their supercapacitor behaviour.

The objectives of this study are firstly to analyse the effect of the preparation method of activated carbons from a mixture of olive-residue, oil and vegetable water, OR, by KOH and H_3PO_4 activation on their textural and chemical properties. Secondly, to study the effect of these properties on their electrochemical behaviour, mainly to check the effect of the presence of phosphorus surface groups on the activated carbon in its electrochemical performance.

3. MATERIALS AND METHODS

3.1. Preparation of activated carbons

Activated carbons were prepared by three different activation methods as reported in other works [8,15] with a few modifications. Activation with KOH was performed by two different methods. The first one is an impregnation of OR with KOH using two different KOH/OR weight ratios (1 and 2). For that, the precursor was previously mixed with the proper amount of a concentrated KOH solution until complete dry. After that, the dry solid was submitted to a thermal carbonization-activation program under inert atmosphere consisting in a step at 300 ºC for 2 h and then at 840 ºC for 2 h at a heating rate of 10 ºC min. The resulting samples were designated as AK1 and AK2 for KOH/OR ratios of 1 and 2, respectively.

The second one consists in the carbonization of the OR in a first step at 300 ºC for 2 h under a nitrogen flow of 300 cm^3 min^{-1} before treatment with KOH. Then, chemical activation was carried out using a physical mixture of the previously carbonized material with solid KOH in a 1/1 or 1/2 mass ratio. This mixture was treated under nitrogen flow for 2 hours at 840 °C. The final products were designated as CK1 and CK2, for 1/1 and 1/2 mass ratios, respectively.

Finally, the activation with H_3PO_4 was prepared by impregnation of OR with H_3PO_4 in a mass ratio of 1/4 and then the dry slurry was treated under nitrogen flow for 2 hours at 300 °C followed by 2 hours at 700 °C. This sample was referred to as AP.

All thermal treatments were performed in a horizontal tubular furnace (from Heraeus) under a nitrogen flow of 300 cm^3 min^{-1} at a heating rate of 10 ºC min^{-1}. Finally, all the prepared activated carbons were washed with 1 M HCl solution and then with distilled water until neutral pH and until chloride ions were no longer detected in the washing water by using a silver nitrate solution.

3.2. Characterization of activated carbons

The textural characterization of the synthesized samples was carried out by N_2 and CO_2 adsorption at -196 and 0 °C, respectively using a Quantachrome Autosorb-1 equipment after outgassing the samples overnight at 110 ºC under dynamic vacuum (10^{-6} mbar). The total micropore volume (W_0 (N_2)) and the narrow micropore volume (W_0 (CO_2)) were obtained by the application of Dubinin–Radushkevich (DR) to the N_2 and CO_2 adsorption isotherms, respectively, and the mean micropore width (L_0) for both adsorbates were obtained by applying the Stoeckli equation. The BET equation was applied to N_2 adsorption isotherms to obtain the apparent BET surface area (S_{BET}). The pore size distribution (PSD) was determined by applying Quenched Solid Density Functional Theory (QSDFT) to the N_2 adsorption isotherms, assuming slit-shaped pores.

The content of carbon, hydrogen and nitrogen was determined using an elemental analyzer THERMO SCIENTIFIC Model Flash 2000. The content of phosphorous was obtained using ICPOES from Perkin Elmer model Optima 8300.

The surface chemistry of activated carbons was studied by temperature programmed desorption coupled with mass spectrometry (TPD) and X-ray photoelectron spectroscopy (XPS). TPD was performed by heating samples up to 1000 ºC at 20 ºC min^{-1} and analysing the CO and CO_2 evolved by means of a mass spectrometer model Prisma from Pfeiffer. Each sample was analysed at least three

times in order to get an error lower than 3%. The total oxygen content, O_{TPD}, was calculated from the amount of CO and CO_2 evolved. XPS was obtained using an Escalab 200R system (VG Scientific Co.) with MgKα X-ray source (hυ = 1253.6 eV) and hemispherical electron analyzer. Survey and multi-region spectra were recorded at C_{1s}, O_{1s}, and P_{2p} photoelectron peaks. Each spectral region of photoelectron interest was scanned several times to obtain good signal-to-noise ratios. The C_{1s} peak at 284.6 eV was used as internal standard. Given that the depth recorded with this technique is around 2-3 nm below the external surface, it gives the surface content of oxygen, O_{XPS}, or phosphorus, P_{XPS}.

3.3. Electrochemical measurements

The electrochemical measurements were carried out in a two electrodes system using an EC-lab VMP system (Biologic) at 25 ºC with H_2SO_4 1M and Na_2SO_4 1M as acid and neutral electrolytes, respectively and glass fibrous material as a separator. The working electrodes were two 5 mm graphite discs, identical in size and weight (22 mg/cm^2), on which 4.4 mg of a homogeneous mixture of 90 % of carbon sample and 10 % of PTFE binder (60 % suspension in water), previously dried overnight at 100 ºC, was pasted by pressure at 5 bar. The graphitic electrodes prepared like this were impregnated with the respective electrolyte for 48 h before electrochemical measurements were made. Each sample was analysed at least three times in order to get an error lower than 1 %.

Prior to the electrochemical measurements, the voltage window in each electrolyte was calculated by cyclic voltammetry. These voltage windows were 0 V-0.75 V in H_2SO_4 and 0 V-1.0 V in Na_2SO_4. Cyclic voltammetry in the voltage interval of each electrolyte was performed at different scan rates (0.5, 2.5, 5, 10 and 20 mV s^{-1}) and the gravimetric capacitance, C_{CV} (F/g), was calculated using the following equation [22,23]:

$$C_{CV} = 4\frac{\sum |I| \times \Delta t}{m \times \Delta V} \qquad \text{(Eq. 1)}$$

where $\sum |I| \Delta t$ was the area of the current (A) against time (s) curve, m was the total mass of active sample in both two electrode (g), ΔV the voltage window (V) and the 4 factor traduces the relation between single electrode capacitance and cell capacitance. Typically, the specific capacitance for one single electrode C_{one} (F g^{-1}) is calculated according to C_{one}=4 C where C is the specific cell capacitance for the two-electrode supercapacitor calculated from the CV curve or charge–discharge curve.

The galvanostatic charge-discharge analyses were obtained at different current density from 0.125 A g^{-1} to 10 A g^{-1} in a voltage interval of each electrolyte. The gravimetric capacitance from these measurements, C_{GD} (F/g), was calculated by Eq. 2 [9,24]:

$$C_{GD} = 4 \frac{I_d \times \Delta t}{m \times \Delta V} \qquad \text{(Eq. 2)}$$

where I_d was the current density (A/g), Δt the discharge time (h), ΔV the voltage interval without the IR drop and m was the total mass of active sample (g). The impedance spectroscopy measurements were carried out from a frequency of 1 mHz to 100 kHz with a sinusoidal signal amplitude of 10 mV. The capacitance value, C_{max}, was obtained by Eq. (3)

$$C_{max} = \frac{-Z''}{2\pi f |Z|^2} \qquad \text{(Eq. 3)}$$

where f was the frequency and $|Z|^2 = |Z'^2| + |Z''^2|$, where Z' and Z" are the real and imaginary parts of the complex impedance, respectively [25].

The electrical energy and the power density were calculated by using the Eq. 4 and Eq. 5, respectively for two-electrode cell [26,27]:

$$E(Wh\,kg^{-1}) = \frac{C_{GD}\,(F\,g^{-1}) \times (V_{max}^2 - V_{min}^2)(V)}{2 \times 3.6} \qquad \text{(Eq. 4)}$$

$$P(W\ kg^{-1}) = \frac{1}{2} \times \frac{I(A) \times \Delta V(V)}{m\ (kg)} \qquad \text{(Eq. 5)}$$

The stability of supercapacitors was studied by floating tests and constant current charge-discharge cycling over 12500 cycles, the capacitance was calculated after the IR drop has been subtracted. The floating test is described as follows [28]: After every 10 h of aging, five constant current galvanostatic charge-discharge sequences at the maximum voltage were followed and the specific capacitance was calculated from the first and fifth discharge respectively. These sequences were reiterated 20 times, i.e. a total floating time of 200 h. The resistance (ESR) which is a measure of the conductivity of the material was also estimated from the IR drop at the initial step discharge curve.

4. RESULTS AND DISCUSSION

4.1. Textural and chemical characterization

N_2 adsorption–desorption isotherms at -196 ºC on activated carbons are shown in Figure 1a. KOH activated carbons present different textural properties depending on the preparation procedure. Both samples AK1 and AK2 show type I isotherms according to the IUPAC classification, typical of microporous materials. Also, there is some mesoporosity, because the N_2 uptake slightly increases at a higher relative pressure after micropore filling. However, the samples CK1 and CK2 show a mixture of type I and type IV isotherms with a hysteresis loop, indicating the presence of mesopores. These differences on the textural properties could be related with the initial pre-carbonization of the CK carbon samples in which the mesoporosity of the samples could be developed, while the major microporosity is developed by the subsequent KOH activation. On the other hand, the H_3PO_4 activated samples show mainly a type IV isotherm, typical of mesoporous materials with lower N_2 uptake at low relative pressure indicating the presence of some microporosity. Figure 1b depicts the pore size distribution obtained by applying the QSDFT method to N_2 isotherms. Effectively, this Figure points out that samples CK1, CK2 and AP, possess mesopores in the range of 2.5-4.5 nm. However, very low mesoporosity is observed in the AK1 and AK2 samples.

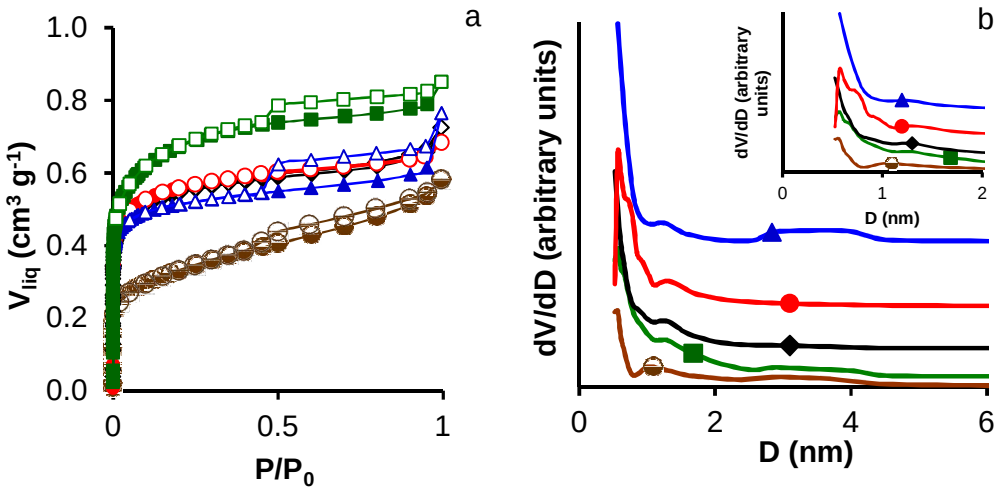

Figure 1. (a) N_2 isotherms at 77 K, closed symbols: N_2 adsorption curve and open symbols: N_2 desorption curve (b) QSDFT pore size distribution applied on the adsorption N_2 isotherms. ● AK1, ◆AK2, ▲ CK1, ■ CK2 and ◒ AP.

Table 1 summarizes the results obtained from isotherm data. The activation of alperujo produces in all cases activated carbons with high surface area ranging from 800 to 1700 m^2g^{-1} and with a large micro and mesoporosity. Both micropores and mesopores are very important for their use as electrodes in energy storage applications because they have different roles with respect to fast charge transfer and the double layer formation of electrolyte ions in the networks of the electrode [9,29]. The micropore volume obtained from CO_2 adsorption yields the volume of narrow micropores or ultramicropores (below about 0.7 nm width), whereas the total micropore volume is obtained from N_2 adsorption if there are no very narrow micropores or pore constrictions at their entrance. In this sense, in all samples $W_0(N_2) > W_0(CO_2)$ and L_0 (CO_2) around 0.7 nm denoting the absence of N_2 diffusional restrictions to the microporosity indicating an adequate activation degree of all samples.

Table 1. Textural properties of the samples obtained by gas (N_2 and CO_2) adsorption.

Sample	S_{BET}	$W_0(N_2)$	W_0 (CO_2)	$L_0(N_2)$	L_0 (CO_2)	$^aV_{0.95}$	V_{meso}
	m^2/g	cm^3/g	cm^3/g	nm	nm	cm^3/g	cm^3/g
AK1	1390	0.51±0.01	0.48±0.03	0.81±0.03	0.79±0.01	0.61	0.10
AK2	1350	0.50±0.01	0.44±0.04	0.92±0.02	0.78±0.02	0.62	0.12
CK1	1295	0.49±0.01	0.44±0.01	0.77±0.02	0.73±0.01	0.67	0.18
CK2	1626	0.59±0.01	0.44±0.04	1.08±0.03	0.78±0.02	0.83	0.24
AP	771	0.29±0.02	0.25±0.07	1.27±0.02	0.68±0.02	0.57	0.28

$^aV_{0.95}$ = volume of nitrogen adsorbed at P/P_0 of 0.95

Besides, the pore diameter as well as the pores volume are affected by the carbon preparation method and also with the ratio of KOH used. No significant differences between samples prepared with 1, and 2 KOH ratios are observed when the impregnation method is used. However, a significant increase of surface area as well as of micro and mesopore volumes are obtained when increasing the KOH ratio from 1 to 2 using the carbonization-activation method. These differences could be related with the activation method. Using liquid KOH in a first step, which acts degrading the cellulosic and lignin constituents of the precursor, being intercalated in the raw structure. Finally during the carbonization process the alkali metal intercalated in the lattices of the carbon can act as an electron donor which promotes the gasification reaction, responsible of the creation of pores within the matrix of carbon [30]. However, using solid KOH, a first carbonization step has been made in which a porous structure is developed and then activation is performed. It is well known that the interaction with the activating agent is more intensive for the non-carbonized material than for the carbonized one, so impregnated samples show higher S_{BET} and wider microporosity than carbonized ones [8,15]. This fact is corroborated comparing AK1 and CK1 samples. Impregnated sample (AK1) presents higher S_{BET} as well as wider microporosity

(1.02 nm vs 0.77 nm) than the carbonized one (CK1). However, using more amount of KOH (KOH/OMW = 2) the opposite trend is obtained; more developed porous texture is obtained in the CK2 sample. This manifests that the amount of KOH plays a more important role in the carbonized samples than in the impregnated ones. Therefore, KOH intercalated on the structure is very sensitive to the primary porous structure, using a high amount of activating agent.

Moreover, the microporosity of the samples with $L_0(N_2)$ between 0.77 and 1.22 nm, would be fully accessible to the hydronium ions, 0.36–0.42 nm [31] and hydrated bisulphate ions, 0.53 nm [32], produced by a dissociation of the electrolyte (1 M H_2SO_4). $L_0(N_2)$ of all samples ranges from 0.77 to 1.22 nm, being completely accessible to the electrolyte.

Nevertheless, the activation mechanism using KOH and H_3PO_4 is very different in spite of the similar impregnation method. KOH activation (AK1 or AK2) leads to activated carbons with a higher surface area and porosity than the H_3PO_4 activation (AP) according to previous works [11,33]. Also note that the AP sample is a micro, mesoporous sample while AK samples are mainly microporous ones according to Salame and Bandosz [34] who obtained a significant contribution of mesopores when phosphoric acid activation was applied, while KOH-activated carbons have a microporous structure.

The chemical composition and the surface chemistry of the activated carbons are summarized in Tables 2 and 3 respectively.

Table 2. Elemental analysis and ICPOES data.

Sample	C	H	N	O+P	P (ICPOES)
AK1	91.38	0.69	0.76	7.81	0.00
AK2	89.45	1.05	0.77	9.50	0.00
CK1	91.37	1.58	0.58	6.68	0.00
CK2	90.52	1.93	0.64	7.89	0.00
AP	79.66	1.97	0.97	17.40	4.34

O+P obtained by difference

Table 3. TPD and XPS analysis of the activated carbons

Sample	TPD analysis			XPS analysis		
	CO	CO_2	O	C	O	P
	mmol g^{-1}	mmol g^{-1}	wt. %	wt.%	wt.%	wt.%
AK1	0.24	0.54	2.10	87.6	8.4	-
AK2	0.15	1.04	3.55	75.0	9.1	-
CK1	0.27	0.45	1.89	92.9	7.1	-
CK2	0.23	0.45	1.82	93.9	6.1	-
AP	1.12	0.18	2.37	81,3	11.7	5.9

It is observed that the amount of oxygen detected for all carbons is around 2 % which is typical for activated carbons carbonized at high temperature. However, O_{DTP} is lower than O_{XPS} in all samples denoting a distribution of oxygen mainly localized on the external surface of the sample, which is typical for activated carbons pointing out that this oxygen is due to a surface oxidation of samples after their exposure at room atmosphere. Also note that the fixed oxygen on KOH activated carbons has a different nature than the phosphoric acid activated one. While for KOH activated samples, oxygenated surface groups (OSG) decompose mainly as CO_2 (carboxylic acid, anhydrides, lactones, etc.) during TPD experiments, for H_3PO_4 those OSG evolved as CO (semiquinone, carbonyl, etc.) are the most abundant. These differences are clearly observed in the TPD profiles (Figure 2). Therefore, for the KOH activated carbon, the CO_2 release takes place mainly below 500 ºC, with a maximum at around 280 ºC (associated to carboxylic acids). A shoulder is also observed around 600 ºC which indicates the presence of carboxyl anhydrides and/or lactone groups. The TPD profile clearly differs from the H_3PO_4 activated one: the evolution of CO_2 at low temperatures decreases and another peak develops between 700 and 950 ºC, which can be related to carboxyl anhydride groups [35]. In the same temperature range (600–900 ºC), CO evolution is maximal, which is indicative of the presence of carboxyl anhydrides (this species

is known to produce both CO and CO_2 peaks). The formation of these groups could be attributed to the decomposition of phosphate like-structures formed during the chemical activation process at temperatures < 750 ºC [36]. The O–P bond in the C–O–P system is the weakest one, so at high temperature this bond is broken leaving only an O atom bonded to a carbon site which produced a high desorption of CO at high temperature [37]. So, the well-defined CO evolutions between 800 and 950 °C have been assigned to the presence of –C–O–P– species that decompose in the form of CO at around 860 °C. Also, noted that no water is desorbed at a temperature higher than 200 ºC for KOH activated samples, while a peak is obtained at 750 ºC characteristic of phosphoric acid activated carbons related with dehydratation reactions. The chemical nature of the activated carbon surface is also analysed by the peak deconvolution of XPS high resolution regions (Table 4).

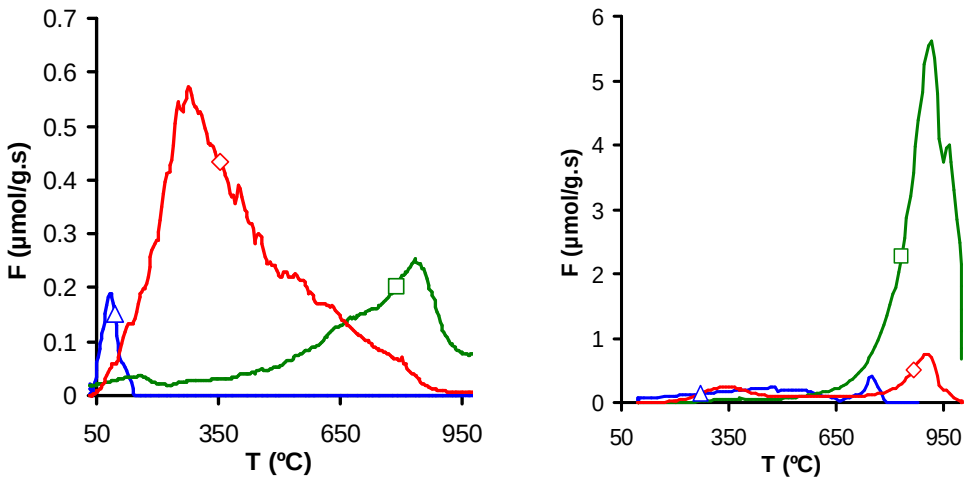

Figure 2. TPD profile of AK1 (left) and AP (right). Water, △; CO_2, ◇; and CO, □.

Table 4. Relative surface concentration (%) of O, C and P functionalities from the deconvolution of C_{1s}, O_{1s} and P_{2p} spectra.

Peak	Binding energy	Assignment	AK1	AK2	CK1	CK2	AP
O_{1s}	531.0-531.5	C=O/P=O*	44	40	39	37	43
	533.0	C-O/C-O-P-O/C-PO*	56	60	61	63	57
C_{1s}	284.6	C=C/ C-O-P*	67	61	66	63	67
	285.8-286.0	C-O	18	19	17	18	17
	287.0-287.4	C=O	8	9	7	8	7
	288.4-288.8	O=C-OR	5	6	5	6	4
	290.1-290.6	CO_3^{2-} / CO_2	4	4	4	4	4
	291.6-291.8	π-π*	1	1	1	1	1
P_{2p}	132.3	Reduced phosphorus compound C-P (P-1)	-	-	-	-	31
	133.1	Pyrophosphate, C-PO_3 (P-2)	-	-	-	-	49
	134.1	Polyphosphates and/or phosphates, C–O–PO_3 groups (P-3)	-	-	-	-	20

* for sample AP.

The deconvolution of C1s spectrum gives six peaks representing carbon atoms bonded to carbon and oxygen atoms. These six peaks are related to C=C bonds at (284.6 eV), C–O bonds at (286.01eV), C=O bonds at (287.6 eV), O=C-OR bonds at (288.7-289.1 eV), CO_3^- and CO_2 at 290.1 eV and plasmon at 291.3 eV [38-40]. Analysing the O1s spectrum, all samples present two different peaks, one at 531-531.5 eV which corresponds to the presence of the oxygen double bonded C=O and/or P=O groups [38,41,42] and the peak at 533 eV indicating the presence of the singly bonded oxygen (C-O) and/or C-O-P [38,41,42] .

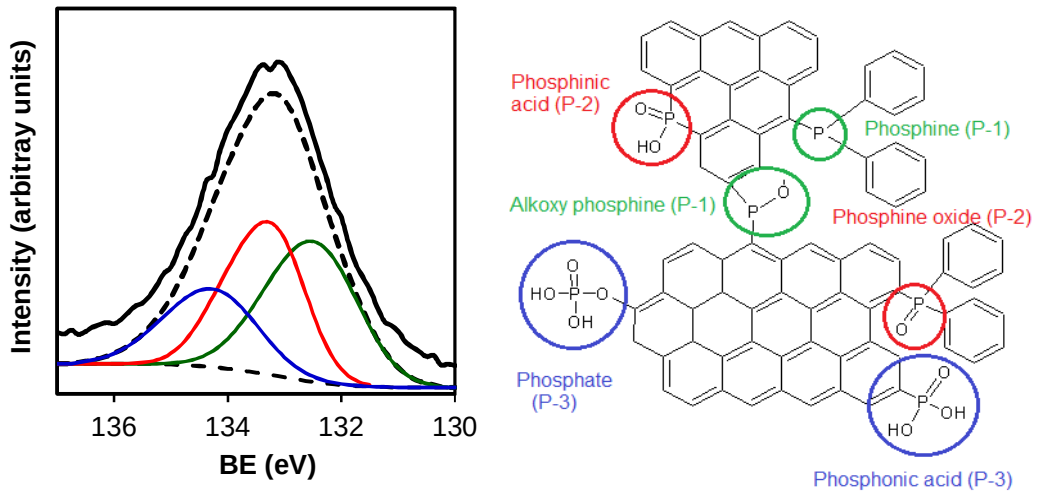

Figure 3. Left: P_{2p} core level XPS spectra of P-doped activated carbon (AP) and right: type of P-containing functional groups in the carbon matrix (adapted from [47]).

Regarding the P_{2p} region for AP sample (Figure 3), three different peaks were found: a peak centred at 132.5eV associated with reduced phosphorus compound as C-P [43-45] (P-1); the peak at 133.1 eV is characteristic of P atom bonded to one C atom and three O atoms, as in $C–PO_3$ [43-45] (P-2), and finally the peak at 134.1 eV is characteristic of pentavalent tetracoordinated phosphorus, PO_4, (P-3), as in polyphosphates and/or phosphates ($C–O–PO_3$ groups) [37,46]. The higher concentration of P surface groups is attributed to the pyrophosphate which can ameliorate the capacitance of the sample and especially the stability of the capacitance with the variation of the current density [43]. At activation temperatures as high as 550 °C, the formation of $C–PO_3$ groups (probably from $C–O–PO_3$ groups) seems to be favoured [46] which could explain the higher amount (around 50%) of pyrophosphate, $C\text{-}PO_3$. Hasegawa *et al* [47] observed that P atoms are introduced into carbon matrix mainly as reduced states and these unstable groups are gradually oxidized and/or hydrolyzed by oxygen and humidity, leading oxidized P-containing functional groups. In the AP sample, 70 % of phosphorus compound correspond to oxidized groups.

As described above, the KOH activated carbons present a very similar chemical surface, so the differences on their electrochemical behaviour must be correlated with their textural properties, while on the H_3PO_4 activated carbons, the electrochemical behaviour depends on both textural and chemical characteristics. The amount and nature of phosphorus groups could affect the formation of the electrochemical double layer and the retention of the capacitance with the increase of the potential scan rate, and with the increase of the current density during the charge discharge experiments.

4.2. Electrochemical characterization

Figure 4 depicts the cyclic voltammograms of the entire sample at a scan rate of 0.5 mV s^{-1} using H_2SO_4 1M as electrolyte for the five cells prepared. All activated carbons showed a quasi-rectangular voltammograms typical for electrochemical double-layer (EDL) capacitors with a low diffusional restriction to the electrolyte. However, a clear difference in the voltammograms shape between the KOH and H_3PO_4 activated samples is observed, so different contributions must be taken into account, thus sample AP shows the wider microporosity and more developed mesoporosity, Table 1.

Chronopotentiograms (CPs) obtained are depicted in Figure 5a at a current load of 250 mA g^{-1} in H_2SO_4 as electrolyte. CPs show quasi-triangular shapes, which indicate again that the samples behave as an ideal electrochemical double-layer (EDL) with low resistance and a good diffusion of the electrolyte inside the pores. C_{GD} values (Table 5) at the lowest current load (250 mA/g) were close to C_{CV} values at 0.5 mV s^{-1}. The variation in C_{GD} with the increase of the current load is depicted in Figure 5b. The same conclusions are obtained with both technics; CK2 presents the highest capacitance value due to the more developed porosity and surface area, the AP sample has a C_{GD} value close to the CK2 one in spite of the lower surface area together with the highest capacitance retention, which is due to the presence of phosphorous surface groups and a very well developed pore network.

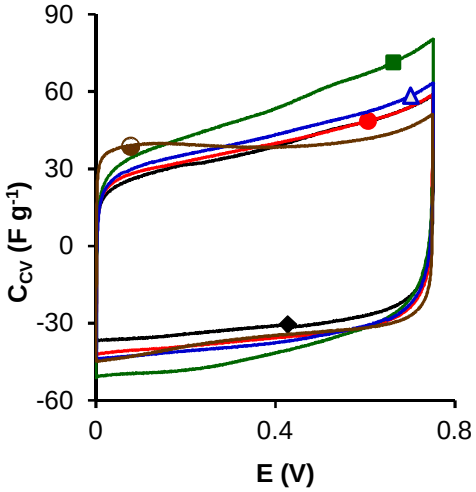

Figure 4. Cyclic voltammetry at 0.5 mV/s for cells in 1 M H_2SO_4 as electrolyte. Samples: AP (◒), AK1 (●), AK2 (◆), CK1 (▲) and CK2 (■).

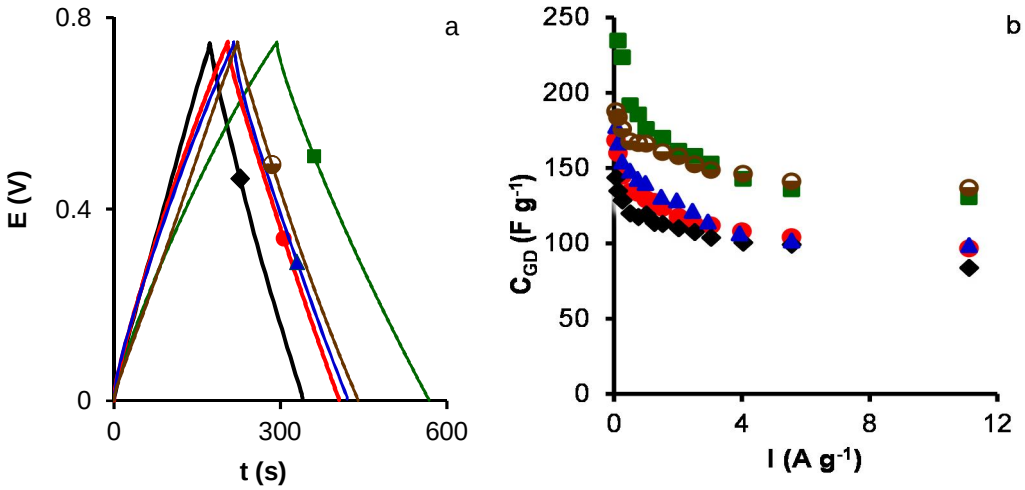

Figure 5. (a) Chronopentiometric charge discharge at a current density of 250 mA g^{-1} and (b) the effect of the current density on the capacitance of samples: AP (◒), AK1 (●), AK2 (◆), CK1 (▲) and CK2 (■). Electrolyte: 1 M H_2SO_4.

Table 5. C_{GD} at 0.25 A g^{-1} and 10 A g^{-1}, C_{max}, ESR and τ from EIS.

Sample	1 M H_2SO_4						1 M Na_2SO_4		
	C_{GD} 0.25 Ag^{-1} F g^{-1}	C_{GD} 10 Ag^{-1} F g^{-1}	RC_{GD} %	C_{max} F g^{-1}	ESR Ω	τ s	C_{GD} 0.25 Ag^{-1} F g^{-1}	C_{GD} 10 Ag^{-1} F g^{-1}	RC_{GD} %
AK1	145±2	97±4	62	150	1.42	1.61	137±3	52±2	38
AK2	140±1	119±3	69	140	1.55	2.16	167±2	88±3	53
CK1	154±2	114±2	56	133	1.37	1.65	170±3	80±3	47
CK2	224±3	175±3	52	263	1.38	2.89	193±3	99±2	51
AP	176±2	166±2	73	166	1.33	1.61	172±2	130±4	75

RC_{GD} percentage of retention capacity at 10 A g^{-1} compare to 0.25 A g^{-1}

Figure (5b) shows the variation of the capacitance against the current density because the formation of the electrochemical double-layer within the micropores is slower and less complete in comparison to current density applied to the supercapacitor. For all samples, the capacitance decreases with the increasing of the current density due to the difficulty of the formation of the electrochemical double layer in the micropores at high current intensities. Different capacitance retentions, CGD, comparing data obtained at 250 mA g^{-1} and 10 A g^{-1}, depend on the pore size and also the amount of oxygen in the surface which can retard/delay the diffusion of the electrolyte in the micropores [8]. Therefore, the KOH activated samples present a similar capacitance retention due to their similar pore width and chemical surface. However, a higher capacitance retention is obtained using the AP sample which indicates that larger micropores, higher mesopore volume and surface phosphorous groups not only improve the capacitance value but also increase the capacitance stability. This is due to the presence of phosphate and specially polyphosphate in the surface which contributes to the increase of the capacitance [43] by decreasing the surface hydrophobicity, and the metaphosphate which contributes to the stability of the capacitance [43]. Furthermore, its higher mesoporosity, facilitates the diffusion at higher current densities. Therefore, we can conclude that both the specific

capacitance and capacitance retention can be improved by controlling the pore structure and phosphorus environment.

Chronopotentiograms in Na_2SO_4 as electrolyte are depicted in Figure 6a and the variation of the capacitance against the current density is presented in Fogure 6b, the gravimetric capacitance values are collected in Table 5. Similar conclusions are obtained comparing with the H_2SO_4 electrolyte. CK2 presents the highest capacitance value (193 F g^{-1} at 250 mA g^{-1}) due to their more developed meso micropore network. This value is close to the AP one (172 F g^{-1} at 250 mA g^{-1}), in spite of its lower surface area in micropore volume which denotes again the importance of the presence of phosphorous surface groups. Lower values of capacitance are obtained using Na_2SO_4 vs H_2SO_4 in all samples at higher current density, 10 Ag^{-1}, (Table 5) which must be related to the nature and size of the cation (H^+ vs Na^+). Due to the higher size of Na^+ cations, their mobility is more limited than the H^+ ones and consequently, the resistance to the electrolyte increases as the capacitance value decreases.

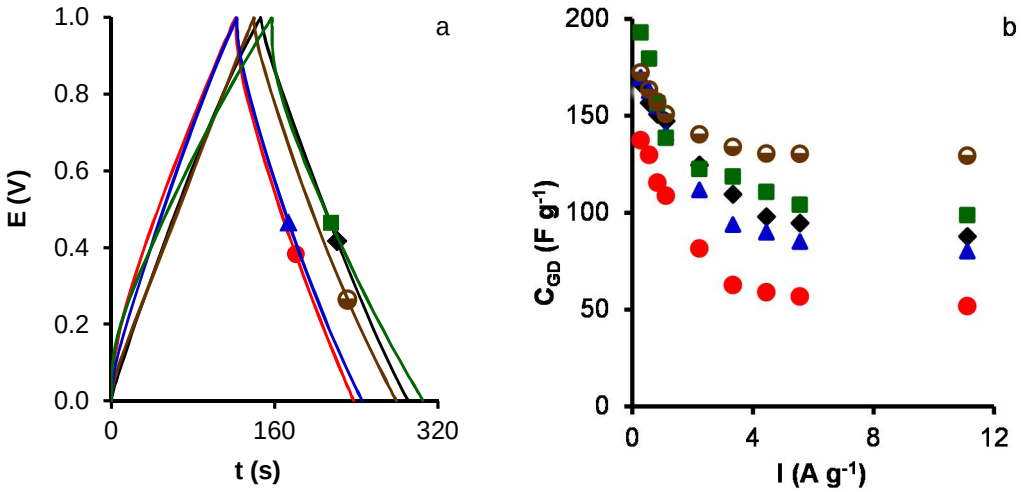

Figure 6. (a) Chronopentiometric charge discharge at a current density of 250 mA g^{-1} and (b) the effect of the current density on the capacitance of samples: AP (◒), AK1 (●), AK2 (◆), CK1 (▲) and CK2 (■). Electrolyte: Na_2SO_4.

A linear relationship between BET surface area and capacitance, CGD, is observed for the four KOH activated carbons, which present similar chemical characteristics (Figure 7). Bibliographic data using similar activation method and experimental conditions were added [48]. Similar trend can be found if CGD is plotted against micropore volume or cumulative DFT surface area, Figures 8 and 9 respectively. Moreno-Castilla et al. [49] described previously the same behaviour. They observed an increase in gravimetric capacitance for samples with a higher micropore volume and a larger surface area, indicating that these are both key parameters for EDL formation on carbon gels. The sample CK2 shows the highest capacitance attributed to its largest surface area and microporosity (Table 5). In addition, not only textural properties must be considered; chemical surface properties are also important. In this sense, taking into account the textural properties and pore width for the AP sample, it must present lower capacitance (Figure 7). However, the AP sample possesses a capacitance similar than AK1, in spite of its lower (half of the) surface area and 60 % of pore volume. This fact demonstrates that the surface phosphorus groups, as well as the more developed mesoporosity, greatly influence the performance of this capacitor. In conclusion, AP sample is always out of all the trends, which suggests that textural properties only determine capacitance in carbons with the same chemistry and structure, Figures 7 and 9. Carbon processing/activation and the associated solid-side capacitance component are clearly as important as textural properties.

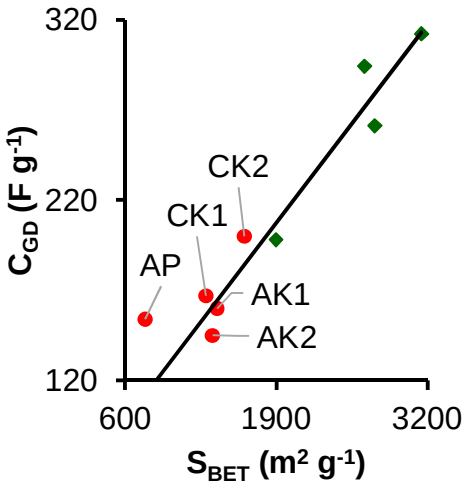

Figure 7. Relationship between gravimetric capacitance C_{GD}, (1 M, H_2SO_4) and S_{BET}. (●) Present work (at 125 mAg^{-1}), (◆) bibliographic data (at 125 mA g^{-1}) from [48].

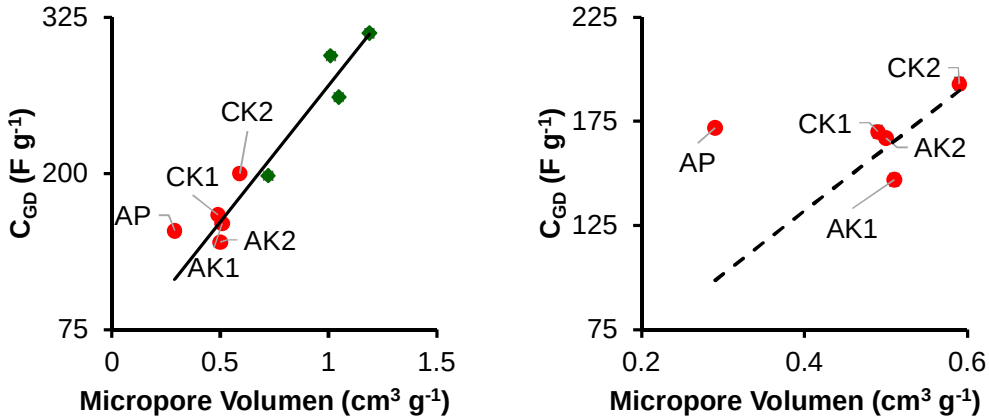

Figure 8. Relationship between gravimetric capacitance obtained by chronopentiometric charge discharge at a current density of 0.125 A g^{-1}. Left: H_2SO_4 and right: Na_2SO_4 electrolyte. ●, present work data. ●, bibliographic data from reference 48.

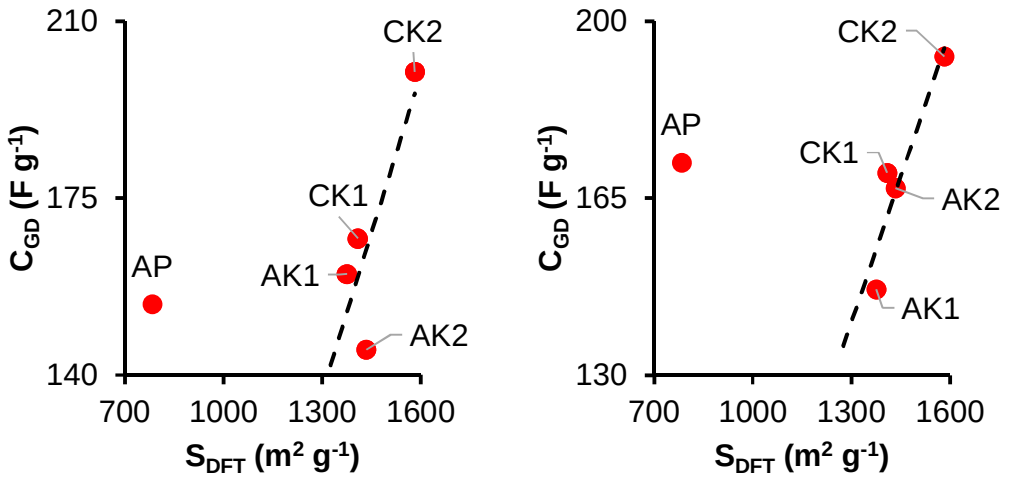

Figure 9. Relationship between gravimetric capacitance CGD and cumulative DFT surface area. Left:1 M, H_2SO_4 and right: Na_2SO_4 electrolyte.

The resistance to the diffusion of the electrolyte inside the carbon pores can be measured by the electrochemical impedance spectroscopy EIS.Figure 10a presents the EIS spectra in the shape of Nyquist plots. The measurements of these spectra were taken at frequencies ranging from 100 kHz to 10 mHz at an open circuit potential with an AC perturbation of 10 mV. In an ideal capacitor, the imaginary part of the impedance in the low-frequency region increases and the plot approaches a vertical line. Deviation from the vertical line in pseudocapacitance-free samples is attributed to their pore size distribution [49].

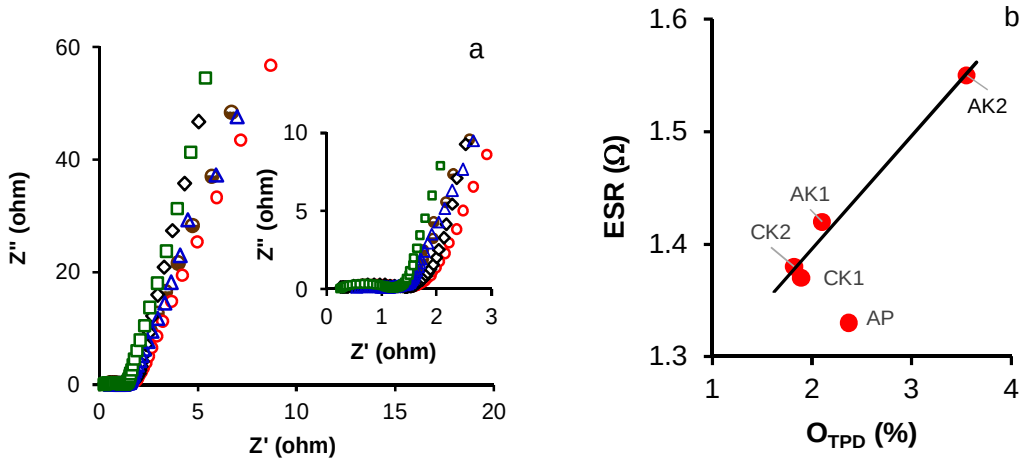

Figure 10. a) Nyquist plot for samples: AP (◒), AK1 (●), AK2 (◆), CK1 (▲) and CK2 (■). b) Variation of the equivalent series resistance with the total oxygen content.

The values of ESR (equivalent series resistance, obtained from the intersection point of the impedance with the real axis in the low frequency region) of all the cells are listed in Table 5. According to the literature [1,50], ESR should be higher for samples with lower micropore size due to a inhibition of the penetration of the electrolyte into the micropores. In our work, low values of ESR were obtained for all tested samples, which indicate that a well-developed porous structure is obtained for all activated carbons. Also note that the smaller resistance values are obtained for CK series and AP, which can be explained on the base of the more developed mesoporosity in these samples. However, the highest ESR value is obtained for the AK2 sample which could be related to the higher amount of oxygen groups on its surface. It is known that the interaction of the H^+ ions with negative charged surface of carbons, induced by oxygen surface groups, increases the ESR [51]. Therefore, a linear relation between ESR and O_{TPD} is obtained for KOH activated carbons (Figure 10b). For the AP sample, a lower ESR value than expected is obtained which could be related to the more developed mesoporosity of that sample and to the presence of phosphorous surface groups.

The relaxation time constant (τ) can be obtained from the frequency f_0 at the maximum of the curves of the imaginary part of the capacitance versus frequency, by the equation $\tau = 1/2 \times \pi f_0$. The relaxation time constant is a quantitative measure of the time necessary for the total discharge of the supercapacitors [52]. Results obtained are compiled in Table 5 and show that samples with lower porosity have the lowest τ, indicating that the sites for EDL formation are more readily available in AK1, CK1 and AP samples than AK2 and CK2 samples. This can be attributed to a more developed meso and micropore network in the case of the AP sample and to the greater regularity in the micropore sizes in AK1 and CK1 samples, facilitating the diffusion of the electrolyte in the pore network, than in carbons with a broader porosity and lower mesopore volume proportions.

The long-term stability of electrodes is another important factor that limits the application of carbon materials as supercapacitors. Figure 11 presents the variation in the gravimetric capacitance with the number of charge-discharge cycles at a constant current density of 1 A g^{-1} in H_2SO_4 as electrolyte, as well as the results of floating test in both electrolytes.

Figure 12 shows the Ragone diagram obtained from a galvanostatic discharge at different current loads. Results show that the energy density at a power range of 20-30 W kg^{-1} vary from 3 to 5 Wh kg^{-1} for all samples. A gradual decrease in energy density was observed when increasing the power density and at shorter current drain times. Thus, for a current drain time of 36 s, the energy and power densities are practically the same for CK2 and AP samples and lower for AK1, AK1 and CK1. The superior performance of sample CK2 is due to its more developed porosity, with one of the highest values of mesopore volume, Table 1.

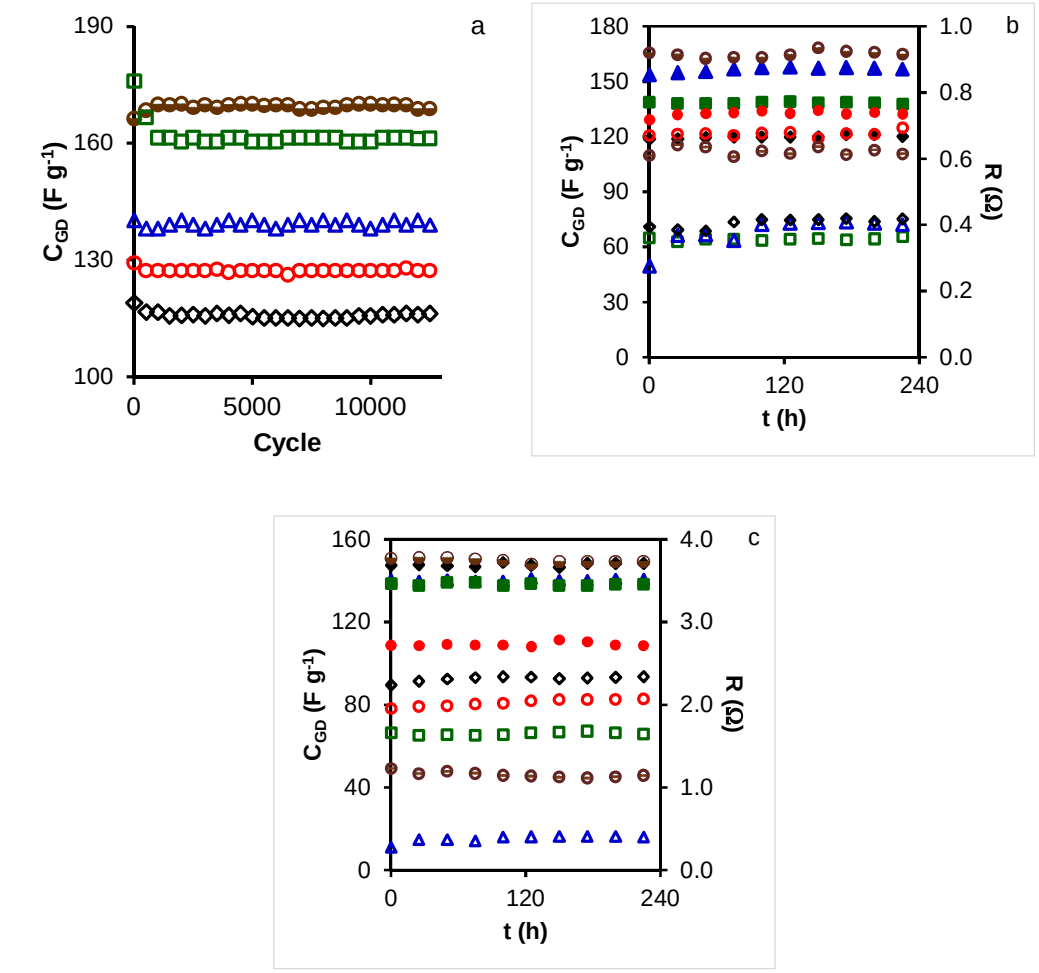

Figure 11. a) Variation of the gravimetric capacitance (C_{GD}) with a) the number of charge-discharge cycles at a current density of 1 A g^{-1} in the voltage window between 0 and 0.75 V in H_2SO_4. b and c) Floating tests results in H_2SO_4 and Na_2SO_4, respectively. Samples AP (◒), AK1 (●), AK2 (◆), CK1 (▲) and CK2 (■).

For the performance of sample AP, this is also due to the presence of P groups as discussed before, proving that the presence of the phosphorus surface groups generated during the H_3PO_4 activation produce carbon with very interesting electrochemical performances, similar or higher than other carbon materials reported in the literature [53-56].

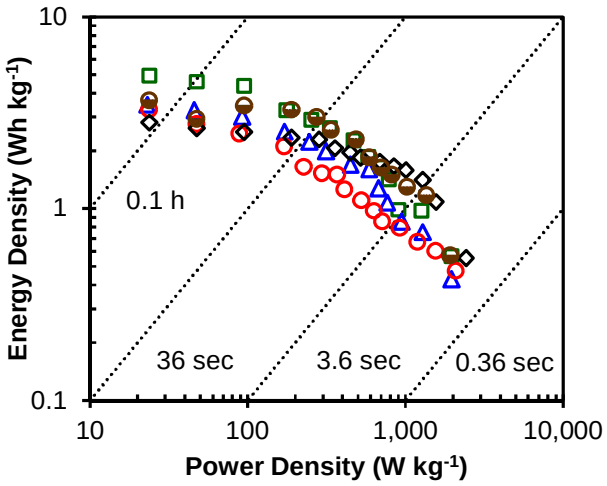

Figure 12. Ragone plots for samples AP (◒), AK1 (●), AK2 (◆), CK1 (▲) and CK2 (■).

5. CONCLUSIONS

A series of activated carbons were prepared from olive mill wastewater using two chemical agents H_3PO_4 and KOH. A surface area as high as 1626 $m^2\ g^{-1}$ is obtained after KOH activation. H_3PO_4 activation produces P-containing functional groups with lower surface area than KOH activated carbons. OR is an excellent biomass residue for the preparation of porous activated carbons with a very well developed pore network.

The electrochemical performance of activated carbons shows that the performance of activated carbons obtained is similar to that obtained from other biomass residues. The highest capacitance obtained was 224 F g^{-1} at 250 mA g^{-1} with a 91 % retention capacity after 12500 cycles and 2.9 s of relaxation time constant. AP presents the highest retention capacity, practically 100 %, with 176 F g^{-1} and τ = 1.6 s due to the presence of phosphorous surface groups and adequate micro-mesopore network.

6. REFERENCES

[1] C. Moreno-Castilla, Adsorption of organic molecules from aqueous solutions on carbon materials, Carbon 42 (2004) 83-94.

[2] C. Moreno-Castilla, M.A. Ferro-Garcia, J.P. Joly, I. Bautista-Toledo, F. Carrasco-Marin, J. Rivera-Utrilla, Activated Carbon Surface Modifications by Nitric Acid, Hydrogen Peroxide, and Ammonium Peroxydisulfate Treatments, Langmuir 11 (1995) 4386-4392.

[3] P. Navarri, D. Marchal, A. Ginestet, Activated carbon fibre materials for VOC removal, Filtr. Separat. 38 (2001) 33-40.

[4] P. Dwivedi, V. Gaur, A. Sharma, N. Verma, Comparative study of removal of volatile organic compounds by cryogenic condensation and adsorption by activated carbon fiber, Sep. Purif. Technol. 39 (2004) 23-37.

[5] A.F. Pérez-Cadenas, C.H. Ros, S. Morales-Torres, M. Pérez-Cadenas, P.J. Kooyman, C. Moreno-Castilla, F. Kapteijn, Metal-doped carbon xerogels for the electro-catalytic conversion of CO_2 to hydrocarbons, Carbon 56 (2013) 324-331.

[6] A. Fraczek-Szczypta, S. Rabiej, G. Szparaga, E. Pabjanczyk-Wlazlo, P. Krol, M. Brzezinska, S. Blazewicz, M. Bogun, The structure and properties of the carbon non-wovens modified with bioactive nanoceramics for medical applications, Mater. Sci. Eng. C 51 (2015) 336-345.

[7] T.E. Rufford, D. Hulicova-Jurcakova, K. Khosla, Z. Zhu, G.Q. Lu, Microstructure and electrochemical double-layer capacitance of carbon electrodes prepared by zinc chloride activation of sugar cane bagasse, J. Power Sources 195 (2010) 912-918.

[8] A. Elmouwahidi, Z. Zapata-Benabithe, F. Carrasco-Marín, C. Moreno-Castilla, Activated carbons from KOH-activation of argan (Argania spinosa) seed shells as supercapacitor electrodes, Bioresource Technol. 111 (2012) 185-190.

[9] L.L. Zhang, X.S. Zhao, Carbon-based materials as supercapacitor electrodes, Chem. Soc. Rev. 38 (2009) 2520-2531.

[10] Y. Huang, E. Ma, G. Zhao, Thermal and structure analysis on reaction mechanisms during the preparation of activated carbon fibers by KOH activation from liquefied wood-based fibers, Ind. Crops Prod. 69 (2015) 447-455.

[11] S. Yorgun, D. Yildiz, Preparation and characterization of activated carbons from Paulownia wood by chemical activation with H_3PO_4, J. Taiwan Inst. Chem. Eng. 53 (2015) 122-131.

[12] V.O. Njoku, M.A. Islam, M. Asif, B.H. Hameed, Preparation of mesoporous activated carbon from coconut frond for the adsorption of carbofuran insecticide, J. Anal. Appl. Pyrol. 110 (2014) 172-180.

[13] B.S. Girgis, L.B. Khalil, T.A.M. Tawfik, Activated carbon from sugar cane bagasse by carbonization in the presence of inorganic acids, J. Chem. Technol. Biotechnol. 61 (1994) 87-92.

[14] C. Moreno-Castilla, F. Carrasco-Marín, M.V. López-Ramón, M.A. Álvarez-Merino, Chemical and physical activation of olive-mill waste water to produce activated carbons, Carbon 39 (2001) 1415-1420.

[15] R. Ubago-Pérez, F. Carrasco-Marín, D. Fairén-Jiménez, C. Moreno-Castilla, Granular and monolithic activated carbons from KOH-activation of olive stones, Micropor. Mesopor. Mat. 92 (2006) 64-70.

[16] W.H. Qu, Y.Y. Xu, A.H. Lu, X.Q. Zhang, W.C. Li, Converting biowaste corncob residue into high value added porous carbon for supercapacitor electrodes, Bioresource Technol. 189 (2015) 285-291.

[17] D. Lozano-Castelló, D. Cazorla-Amorós, A. Linares-Solano, S. Shiraishi, H. Kurihara, A. Oya, Influence of pore structure and surface chemistry on electric double layer capacitance in non-aqueous electrolyte, Carbon 41 (2003) 1765-1775.

[18] G. Gryglewicz, J. Machnikowski, E. Lorenc-Grabowska, G. Lota, E. Frackowiak, Effect of pore size distribution of coal-based activated carbons on double layer capacitance, Electrochim. Acta, 50 (2005) 1197-1206.

[19] O. Barbieri, M. Hahn, A. Herzog, R. Kötz, Capacitance limits of high surface area activated carbons for double layer capacitors, Carbon 43 (2005) 1303-1310.

[20] X. Yan, Y. Yu, X. Yang, Effects of electrolytes on the capacitive behavior of nitrogen/phosphorus co-doped nonporous carbon nanofibers: an insight into the role of phosphorus groups, RSC Adv. 4 (2014) 24986-24990.

[21] F. Carrasco-Marín, M.V. López-Ramón, C. Moreno-Castilla, Applicability of the Dubinin-Radushkevich equation to CO_2 adsorption on activated carbons, Langmuir 9 (1993) 2758-2760.

[22] J. Gamby, P.L. Taberna, P. Simon, J.F. Fauvarque, M. Chesneau, Studies and characterisations of various activated carbons used for carbon/carbon supercapacitors, J. Power Sources 101 (2001) 109-116.

[23] L. Bonnefoi, P. Simon, J.F. Fauvarque, C. Sarrazin, J.F. Sarrau, A. Dugast, Electrode compositions for carbon power supercapacitors, J. Power Sources, 80 (1999) 149-155.

[24] D. Hulicova-Jurcakova, M. Seredych, G.Q. Lu, T.J. Bandosz, Combined Effect of Nitrogen- and Oxygen-Containing Functional Groups of Microporous Activated Carbon on its Electrochemical Performance in Supercapacitors, Adv. Funct. Mater. 19 (2009) 438-447.

[25] P.L. Taberna, P. Simon, J.F. Fauvarque , Electrochemical Characteristics and Impedance Spectroscopy Studies of Carbon-Carbon Supercapacitors, J. Electrochem. Soc. 150 (2003) A292-A300.

[26] A. Bello, F. Barzegar, D. Momodu, J. Dangbegnon, F. Taghizadeh, N. Manyala, Symmetric supercapacitors based on porous 3D interconnected carbon framework, Electrochim. Acta 151 (2015) 386-392.

[27] Y. Korenblit, M. Rose, E. Kockrick, L. Borchardt, A. Kvit, S. Kaskel, G. Yushin, High-Rate Electrochemical Capacitors Based on Ordered Mesoporous Silicon Carbide-Derived Carbon, ACS Nano 4 (2010) 1337-1344.

[28] A. Bello, F. Barzegar, M.J. Madito, D.Y. Momodu, A.A. Khaleed, T.M. Masikhwa, J.K. Dangbegnon, N. Manyala, Stability studies of polypyrole-

derived carbon based symmetric supercapacitor via potentiostatic floating test, Electrochim. Acta 213 (2016) 107-114.

[29] P. Simon, Y. Gogotsi, Materials for electrochemical capacitors, Nat. Mater. 7 (2008) 845-854.

[30] F.H. Franke, M. Meraikib, Catalytic influence of alkalis on carbon gasification reaction, Carbon 8 (1970) 423-433.

[31] L. Eliad, G. Salitra, A. Soffer, D. Aurbach, Ion Sieving Effects in the Electrical Double Layer of Porous Carbon Electrodes: Estimating Effective Ion Size in Electrolytic Solutions, J. Phys. Chem. B

[32] M. Endo, T. Maeda, T. Takeda, Y.J. Kim, K. Koshiba, H. Hara, M.S. Dresselhaus, Capacitance and Pore-Size Distribution in Aqueous and Nonaqueous Electrolytes Using Various Activated Carbon Electrodes, J. Electrochem. Soc. 148 (2001) A910-A914.

[33] N.M. Haimour, S. Emeish, Utilization of date stones for production of activated carbon using phosphoric acid, Waste Manage. 26 (2006) 651-660.

[34] I.I. Salame, T.J. Bandosz, Comparison of the Surface Features of Two Wood-Based Activated Carbons, Ind. Eng. Chem. Res. 39 (2000) 301-306.

[35] T. Durkic, A. Peric, M. Lausevic, A. Dekanski, O. Neskovic, M. Veljkovic, Z. Lausevic, Boron and phosphorus doped glassy carbon: I. Surface properties, Carbon 35 (1997) 1567-1572.

[36] A. Castro-Muñiz, F. Suárez-García, A. Martínez-Alonso, J.M.D. Tascón, Activated carbon fibers with a high content of surface functional groups by phosphoric acid activation of PPTA, J. Colloid Interface Sci. 361 (2011) 307-315.

[37] X. Wu, L.R. Radovic, Inhibition of catalytic oxidation of carbon/carbon composites by phosphorus, Carbon 44 (2006) 141-151.

[38] S. Biniak, G. Szymanski, J. Siedlewski, A. Switkowski, The characterization of activated carbons with oxygen and nitrogen surface groups, Carbon 35 (1997) 1799-1810.

[39] C. Moreno-Castilla, M.V. López-Ramón, F. Carrasco-Marín, Changes in surface chemistry of activated carbons by wet oxidation, Carbon 38 (2000) 1995-2001.

[40] E. Desimoni, G.I. Casella, A.M. Salvi, XPS/XAES study of carbon fibres during thermal annealing under UHV conditions, Carbon 30 (1992) 521-526.

[41] J.L. Figueiredo, M.F.R. Pereira, M.M.A. Freitas, J.J.M. Órfão, Modification of the surface chemistry of activated carbons, Carbon 37 (1999) 1379-1389.

[42] U. Zielke, K.J. Hüttinger, W.P. Hoffman, Surface-oxidized carbon fibers: I. Surface structure and chemistry, Carbon 34 (1996) 983-998.

[43] D. Hulicova-Jurcakova, M. Seredych, G.Q. Lu, N.K.A.C. Kodiweera, P.E. Stallworth, S. Greenbaum, T.J. Bandosz, Effect of surface phosphorus functionalities of activated carbons containing oxygen and nitrogen on electrochemical capacitance, Carbon 47 (2009) 1576-1584.

[44] J.M. Rosas, R. Ruiz-Rosas, J. Rodríguez-Mirasol, T. Cordero, Kinetic study of the oxidation resistance of phosphorus-containing activated carbons, Carbon 50 (2012) 1523-1537.

[45] A.M. Puziy, O.I. Poddubnaya, R.P. Socha, J. Gurgul, M. Wisniewski, XPS and NMR studies of phosphoric acid activated carbons, Carbon 46 (2008) 2113-2123.

[46] J.M. Rosas, J. Bedia, J. Rodríguez-Mirasol, T. Cordero, HEMP-derived activated carbon fibers by chemical activation with phosphoric acid, Fuel 88 (2009) 19-26.

[47] G. Hasegawa, T. Deguchi, K. Kanamori, Y. Kobayashi, H. Kageyama, T. Abe, K. Nakanishi, High-Level Doping of Nitrogen, Phosphorus, and Sulfur into Activated Carbon Monoliths and Their Electrochemical Capacitances, Chem. Mater. 27 (2015) 4703-4712.

[48] K. Kierzek, E. Frackowiak, G. Lota, G. Gryglewicz, J. Machnikowski, Electrochemical capacitors based on highly porous carbons prepared by KOH activation, Electrochim. Acta 49 (2004) 515-523.

[49] Z. Zapata-Benabithe, C. Moreno-Castilla, F. Carrasco-Marín, Effect of dilution ratio and drying method of resorcinol-formaldehyde carbon gels on

their electrocapacitive properties in aqueous and non-aqueous electrolytes, J Sol-Gel Sci. Techn. 75 (2015) 407-412.

[50] L. Li, P.A. Quinlivan, D.R.U. Knappe, Effects of activated carbon surface chemistry and pore structure on the adsorption of organic contaminants from aqueous solution, Carbon 40 (2002) 2085-2100.

[51] X. Liu, Y. Wang, L. Zhan, W. Qiao, X. Liang, L. Ling, Effect of oxygen-containing functional groups on the impedance behavior of activated carbon-based electric double-layer capacitors, J. Solid State Electrochem. 15 (2011) 413-419.

[52] B. Batalla García, A.M. Feaver, Q. Zhang, R.D. Champion, G. Cao, T.T. Fister, K.P. Nagle, G.T. Seidler, Effect of pore morphology on the electrochemical properties of electric double layer carbon cryogel supercapacitors, J. Appl. Phys. 104 (2008) 014305.

[53] W. Xing, S.Z. Qiao, R.G. Ding, F. Li, G.Q. Lu, Z.F. Yan, H.M. Cheng, Superior electric double layer capacitors using ordered mesoporous carbons, Carbon 44 (2006) 216-224.

[54] J.A. Fernández, M. Arulepp, J. Leis, F. Stoeckli, T.A. Centeno, EDLC performance of carbide-derived carbons in aprotic and acidic electrolytes, Electrochim. Acta 53 (2008) 7111-7116.

[55] J.A. Fernández, T. Morishita, M. Toyoda, M. Inagaki, F. Stoeckli, T.A. Centeno, Performance of mesoporous carbons derived from poly(vinyl alcohol) in electrochemical capacitors, J. Power Sources 175 (2008) 675-679.

[56] M. Olivares-Marín, J.A. Fernández, M.J. Lázaro, C. Fernández-González, A. Macías-García, V. Gómez-Serrano, F. Stoeckli, T.A. Centeno, Cherry stones as precursor of activated carbons for supercapacitors, Mater. Chem. Phys. 114 (2009) 323-327.

CHAPTER IV: *FREE METAL OXYGEN-REDUCTION ELECTRO-CATALYSTS OBTAINED FROM BIOMASS RESIDUE OF THE OLIVE OIL INDUSTRY*

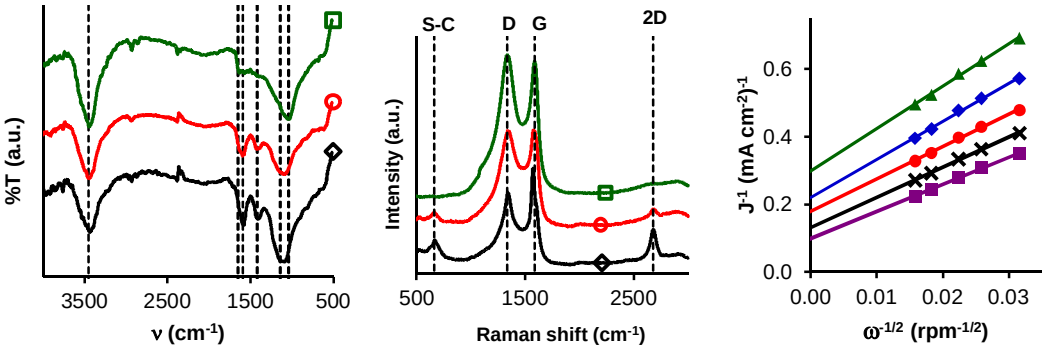

1. ABSTRACT

Advanced carbon materials are obtained from a solid residue of waste water used in the olive oil industry. Solvothermal treatments with different amounts of thioglycolic acid are carried out in order to develop specific sulphur functionalities on the carbon surface. Samples are exhaustively characterized to determine the textural, chemical and electrochemical properties. These materials are tested as electro-catalysts for oxygen reduction reaction in a three electrode electrochemical set-up. Correlations between the characteristics of the carbons and their electrochemical performance are established. Electrodes containing sulphur functionalities show a very good electro-catalytic behaviour with larger kinetic current densities and lower activation potentials. Linear sweep voltammetry is performed at different rotation speeds in order to calculate the number of electrons transferred and kinetic current densities by applying Koutecky-Levich equation. Thus, it is pointed out that oxygen reduction takes place through the desired four electrons pathway on the sulphur doped electro-catalysts. These carbon materials show a similar catalytic performance to that of other free-metal electro-catalysts based in graphene recently reported in the bibliography.

Keywords: Activated carbon; Sulphur; Solvothermal; Oxygen reduction; Electro-catalyst.

2. INTRODUCTION

There is a growing interest in finding new environmentally friendly sources of energy for automotive applications. The development of electric vehicles is nowadays one of the most promising alternatives to replace combustion engines. Therefore, the production of electrical energy from chemical reactions by using fuel cells is a really interesting matter from both the industrial and fundamental research point of view [1-4]. Oxygen Reduction Reaction (ORR) is the one that takes place on the cathode in a fuel cell and several works can be found on published literature about the synthesis and optimization of electro-catalytic materials for this reaction [2-12].

Of these, platinum-based electro-catalysts happen to be the most widely studied, since Pt is the most active metal for ORR [4,6-10]. Nevertheless, the rising prize of platinum and other precious metals as Pd or Ir makes it more difficult to commercialize devices containing them. This is the reason why non precious metal electro-catalysts are more numerous and more studied in order to lower the costs of fuel cells [2,3,11-14].

Along this line, carbon materials functionalized with different heteroatoms happen to be a sound alternative. Although heteroatoms such as boron and phosphorous have been tested, nitrogen and sulphur are the most widely studied ones, sometimes even combined within the same carbon material. These materials overcome some of the Pt-based catalyst problems, such as cost, durability and environmental impact. Moreover, they have excellent electro-catalytic activities [3,5,14-20]. Functionalization of carbon surface can take place by means of a wide variety of methods. However, the use of hydrothermal methods is relatively new [21,22].

Hydrothermal methods for carbon precursor synthesis, carbonization or activation have been widely used. For instance, materials obtained from carbohydrates or proteins through hydrothermal routes at high pressure are being published with increasing frequency [17,22-26]. The main advantage of hydrothermal or solvothermal synthesis is the possibility of synthesizing materials

in a much shorter time than at atmospheric pressure. Typical procedures to obtain sulphur doped carbon materials imply the reaction of the material with H_2S or SO_2 for several hours at high temperature, which is energy and time consuming, and produces a higher volume of residues. Chemical functionalities generated on carbon surface are also limited due to the simplicity of the attached molecules and to the low thermal stability of the generated sulphur groups [14,15,17,18]. Despite these advantages, it is not so common to find works where hydrothermal or solvothermal technology is applied in chemical surface modification treatments. Nevertheless, some works can be found, mainly related to controlled oxidation of carbon materials [21,22].

The objective of this work was the preparation of carbon-based electro-catalysts doped with sulphur obtained from the olive oil industrial waste. These electro-catalysts present a good performance in the oxygen reduction reaction. After the preparation of these materials, which involves three synthesis steps: pyrolysis, chemical activation and solvothermal functionalization, their catalytic performance is discussed in terms of their differences in porous texture and surface chemistry.

3. MATERIALS AND METHODS

3.1. Synthesis of activated carbon and S functionalization.

Activated carbon was obtained by chemical activation of solid residues contained in olive mill wastewater (OMW). This residue is a paste, which contains diverse waste from olive oil industry, produced when olives are crushed to extract the oil. The chemical composition of the OMW is complex, but it is approximately formed by an 83 % of water, nearly 15 % of organic matter and 2 % of minerals (Table 1).

Table 1. Chemical composition of Olive Mill Wastewater.

Compound	Percentage (%)
Water	83
Organic matter	14.8
Lipids	0.02 – 1
Proteins	1.2 - 2.4
Sugars	2.8
Organic acids	0.5 - 1.5
Polyalcohols	1.0 - 1.5
Pectines, gums, tannins	0.5 - 1.5
Glucosides and polyphenols	0.5 - 1.0
Minerals	1.8
Carbon	21
Phosphates	14
Potassium salts	47
Sodium salts	7
Others	7

Firstly, the solid extract of the OMW was carbonized under nitrogen atmosphere (300 cm^3 min^{-1}) at 350 °C for two hours in order to create a solid with a stable 3D structure before the activation step [27,28]. After that, the product of the carbonization was impregnated with potassium hydroxide (KOH) in a mass ratio 1:2 and heated up to 60 °C for 12 hours. KOH to carbon mass ratio was chosen so as to obtain a highly microporous material, based on previous studies with other olive residues (olive stones) [27,28]. This mixture was dried at 110 °C overnight and activated at 840 °C for 2 hours (10 °C min^{-1} heating rate) under nitrogen atmosphere (300 cm^3 min^{-1}). The final product was neutralized and demineralised by treating it with HCl 1 M. Finally, it was washed several times with distilled water until chloride absence was determined and the sample was subsequently dried at 110 °C. This sample was named CK2.

Two portions of CK2 were taken to perform chemical surface modifications. Each of these fractions weighed 2 grams and they were mixed with different volumes (4 mL and 7 mL) of thioglycolic acid (supplied by Sigma-Aldrich). The final volume of both treatments was 7 mL; when 4 mL of thioglycolic acid were used, the volume was completed with ethanol. The solvothermal reaction was carried out in a 25 mL stainless steel teflon-lined autoclave at 120 °C for 24 hours. After the treatment, samples were washed with carbon disulphide (CS_2) in order to remove reaction by-products and elementary sulphur which could have been formed. Carbon disulphide was washed with acetone and samples were dried at 110 °C overnight, named CK2S4 and CK2S7 (where the number indicates the volume of thioglycolic acid used). To our knowledge, this solvothermal method using thioglycolic acid for doping carbon materials with different sulphur functionalities had not been described until now.

3.2. Textural characterization.

Textural characterization of the activated carbon samples was carried out by gas adsorption (N_2 at -196 °C and CO_2 at 0 °C) with an AUTOSORB 1 (Quantachrome Ins.). N_2 adsorption isotherms were analysed by BET equation in order to obtain the surface area, S_{BET}. Dubinin–Radushkevich's and Stoeckli's equations were applied to N_2 and CO_2 isotherms so as to determine micropore volume (W_0) and micropore mean width (L_0) [27]. The volume of nitrogen adsorbed at a relative pressure of 0.95, $V_{0.95}$, was obtained from the N_2 adsorption isotherms, equivalent to the sum of the micro- and mesopore volumes according to Gurvitch's rule. The mesopore volume, V_{meso}, was obtained from the difference between $V_{0.95}$ and $W_0(N_2)$. In the absence of restrictions, $W_0(N_2)$ yields the total micropore volume, while $W_0(CO_2)$ estimates the narrowest microporosity (diameter < 0.7 nm).

3.3. Surface chemistry characterization.

Several techniques were applied to qualitatively and quantitatively analyse the chemical surface: Fourier Transform Infrared (FTIR) and Raman Spectroscopies were used to observe the presence of different chemical

functionalities. X-Ray photoelectron spectroscopy (XPS) was employed to analyse carbon, oxygen and sulphur bonds and to quantify sulphur and oxygen proportion on the sample external surface. Elemental analysis (CHNS analysis) was performed in order to get the total S content on bulk samples.

FTIR spectra were obtained with a NICOLET IR200 by mixing samples with solid potassium bromide (KBr), 0.1 % weight of carbon. A JASCO NRS-5100 equipped with a green-light laser (523 nm) was used for Raman Spectroscopy. For CHNS analysis, a THERMO SCIENTIFIC Flash 2000 coupled to a METTLER XP-6 microbalance was employed. XPS analysis was performed with an ESCA 5701 Physical Electronics instrument. Deconvolution of spectra and peak assignment were made according to the results from other authors [16,24,26,29-31]. Surface acidity was studied by determining zero-point charge pH_{ZPC}, employing the method proposed by Leon et al. [32]. Around 250 mg of each sample were immersed in 4 mL of previously degasified distilled water, and then, the pH of suspensions was measured periodically until constant value.

3.4. Electrochemical measurements on three electrode set-up.

Cyclic Voltammetry (CV) and Linear Sweep Voltammetry (LSV) experiments were conducted on a three electrode cell controlled by a Biologic VMP multichannel potentiostat. A Rotating Disk Electrode (RDE) Metrohm AUTOLAB RDE-2, 3 mm Glassy Carbon tip, was used as working electrode. 5 mg of electro-catalyst were suspended on 1 mL of a solution which contained Nafion (5 %) and water in a 1:9 (v:v) ratio. Subsequently, 10 µL of this suspension were loaded on RDE tip and dried under an infrared lamp. The glassy carbon electrode had been previously polished with 1, 0.3 and 0.05 µm alumina powder and sonicated in deionized water and ethanol. Ag/AgCl was chosen as reference electrode and Pt-wire as counter electrode. The three electrodes were immersed in a 0.1 M KOH (electrolyte) solution in water.

CV experiments were carried out while N_2 or O_2 bubbled through the electrolyte solution during measurements. The chosen potential window ranged

from -0.8 to 0.4 V (50 mV s^{-1}). LSV curves were obtained in O_2-saturated 0.1 M KOH solutions at different rotation speed and sweeping voltage, from 0.4 to -0.8 V (5 mV s^{-1}). Data were fitted to the Koutecky-Levich model (Equations 1 and 2) in order to evaluate the electro-catalytic performance of samples and the transferred electron number for each of them [4,5,16,19,33].

$$\frac{1}{j} = \frac{1}{jk} + \frac{1}{B\omega^{0.5}} \qquad \text{(Equation 1)}$$

$$B = 0.2nF \times (D_{O_2})^{2/3} \upsilon^{-1/6} C_{O_2} \qquad \text{(Equation 2)}$$

where *j*, current density; j_k, kinetic current density; ω, rotation speed; *F*, Faraday constant; D_{O_2}, oxygen diffusion coefficient (1.9 10^{-5} cm^2 s^{-1}); ν, viscosity (0.01 cm^2 s^{-1}); C_{O_2}, oxygen concentration (1.2 10^{-6} mol cm^{-3}).

4. RESULTS AND DISCUSSION

4.1. Gas physical adsorption

N_2 adsorption isotherm for CK2 (Figure 1) is type I - type IV (mainly type I). This activated carbon is a micro-mesoporous material with high micropore volume ($W_0(N_2)$ = 0.589 cm^3 g^{-1}, DR) and high surface area (S_{BET} = 1626 m^2 g^{-1}). After functionalization with sulphur, a considerable fraction of pores were blocked, which induced a reduction on S_{BET}, $W_0(N_2)$ and V_{meso} and an increase in the $L_0(N_2)$ (Table 2). The same trend was observed for CO_2 adsorption isotherms, micropore volume $W_0(CO_2)$ was reduced and the narrow micropore mean width, $L_0(CO_2)$, was increased when surface functionalities were introduced in activated carbon. Although some authors [34,35] recently reported possible chemical interactions between sulphur groups and CO_2 molecules, it does not seem to be the case in our samples, probably because, at low pressures, physical interactions are still the main responsible for CO_2 adsorption. In any case, these results indicate that sulphur functionalities are introduced in the entire pore structure of the carbon.

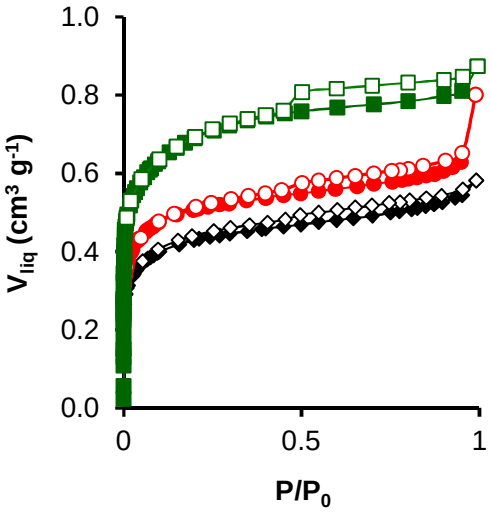

Figure 1. N_2 adsorption, closed symbols,-desorption, open symbols, isotherms for activated carbons CK2 (■), CK2S4 (●), CK2S7 (◆)

Table 2. Textural characteristics of activated carbons

Sample	S_{BET}	W_0 (N_2)	L_0 (N_2)	$V_{0.95}$	V_{meso}	W_0 (CO_2)	L_0 (CO_2)
	m^2g^{-1}	cm^3g^{-1}	nm	cm^3g^{-1}	cm^3g^{-1}	cm^3g^{-1}	nm
CK2	1626	0.59	1.08	0.811	0.222	0.44	0.78
CK2S4	1221	0.51	1.52	0.628	0.122	0.35	0.88
CK2S7	969	0.43	1.58	0.544	0.116	0.29	0.90

4.2. Surface chemistry analysis

FTIR spectra (Figure 2.a) were analysed in order to obtain information about different chemical functionalities [16,24,26]. The spectrum of the CK2 sample is relatively simple, with two main bands: the one centred at 1050 cm^{-1}, corresponding to single bonds (C-C and C-O), and the other at 3460 cm^{-1}, corresponding to O-H. There is also a small shoulder at around 1600 cm^{-1} after the

signal, related to single bonds. This band is related to the C=C present in carbon. From these bands, it can be understood that the oxygen of this carbon is mainly in the form of phenol groups. After the functionalization with thioglycolic acid, the band at 1050 cm^{-1} is shifted at higher wavenumbers, which is due to the appearance of C-S band (1140 cm^{-1}). Two more bands showed up after solvothermal treatment: the first one at 1420 cm^{-1}, due to S=O bond, and the second one at 1590 cm^{-1}, from C=O on the carboxylic acids and thioesters. These bands became more intense in CK2S7 compared to CK2S4 [16,24,26].

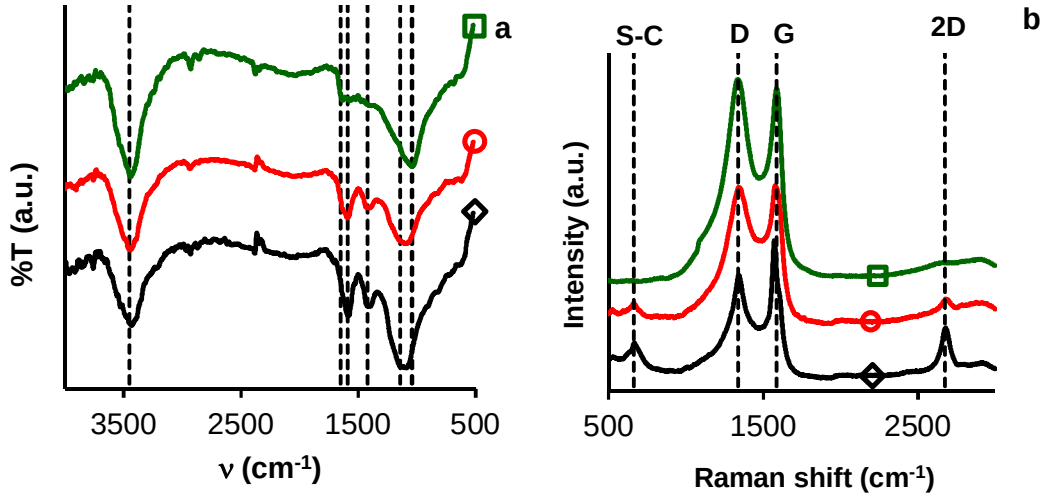

Figure 2. a) FTIR and b) Raman spectra of samples: CK2 (□), CK2S4 (○), CK2S7 (◇).

Raman shift spectra (Figure 2.b) showed two main bands: the disordered-induced (D) band at 1336 cm^{-1} and the graphitic (G) band at 1587 cm^{-1}. The intensity of the two bands was similar ($I_D/I_G \approx 1$) for all the samples, which is usually found for activated carbons, but more intense in the case of original CK2 than in sulphur-doped samples. Nevertheless, after sulphur functionalization, two low intensity peaks appeared: one at around 660 cm^{-1}, which is related to S-C stretching, according to bibliography, and the second one at high Raman shift values (near 2680 cm^{-1}), which is commonly assigned to an overtone of the D-band (2D) [24,36,37].

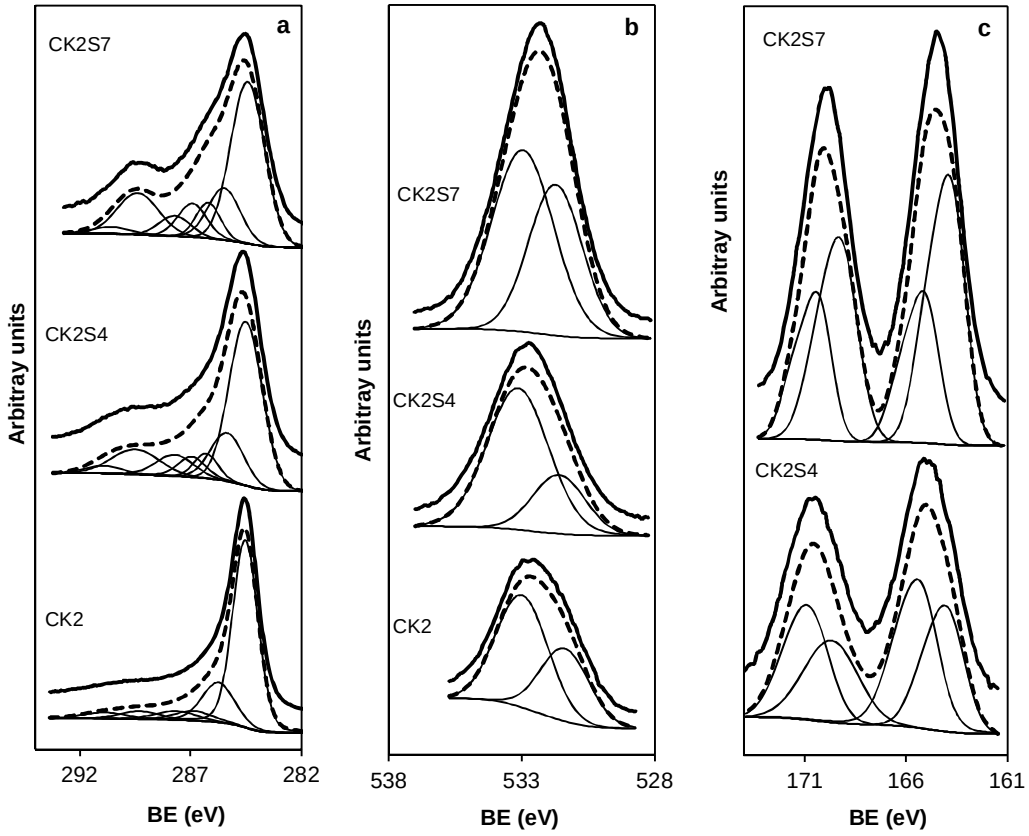

Figure 3. Deconvolution of C_{1s} (a), O_{1s} (b) and S_{2p} (c) of high resolution XP spectra.

XP spectra (Figure 3) are in good agreement with FTIR ones. The band assignment was performed according to the published bibliography [16,24,26,29-31] and the values can be found on Table 3, together with the relative intensities of each peak analysed by deconvolution. Although each S_{2p} peak is the resultant of two components ($2p_{1/2}$ and $2p_{3/2}$), for clarity, only the sum of both was plotted in Figure 3.c, while $2p_{3/2}$ binding energy was the one used to assign different peaks to chemical functionalities. In the case of CK2, the deconvolution of C_{1s} signal leads to very weak peaks in the high binding energy interval (related to oxygenated functionalities) and only C=C and C-C peaks present a high intensity.

Table 3. Peak assignments for the XP spectra of the samples after deconvolution.

Sample	C_{1s}	Group	FW_{HM}	Peak	O_{1s}	Group	Peak	$S_{2p3/2}$	Group	Peak
			eV	%			%			%
CK2	284.5	C=C	1.34	64	531.4	O=C	38	-	-	-
	285.8	C-C		18	533.0	O—C	62			
	286.9	C-O		5						
	287.7	C=O		5						
	289.3	COO^{-}		4						
	290.9	π-π*		3						
CK2S4	284.5	C=C	1.77	52	531.6	O=C O=S	26	163.8	C-SH	24
	285.4	C-C		15	533.1	O—C O—S	74	165.2	R_2-SO	31
	286.3	C-S		6				169.4	C-OSO_3H	21
	286.9	C-O		6				170.6	C-O-SO_2-O-C	24
	287.7	C=O		8						
	289.5	COO^{-}		11						
	290.9	π--π*		3						
CK2S7	284.4	C=C	1.81	47	531.7	O=C O=S	41	163.7	C-SH	35
	285.5	C-C		14	533.0	O—C O—S	59	165.0	R_2-SO	19
	286.2	C-S		7				169.1	C-OSO_3H	28
	286.9	C-O		9				170.3	C-O-SO_2-O-C	18
	287.7	C=O		6						
	289.4	COO^{-}		15						
	290.6	π-π*		2						

In the O_{1s} region, there are only two peaks: the one at the higher binding energy was more intense for CK2 than the one at the lower binding energy. The first one is related to the presence of C-O simple bonds, which is consistent with FTIR spectrum for this sample (oxygen functionalities are mainly in the form of phenolic groups in this sample). Once the solvothermal treatment was carried out, the complexity of C_{1s} grew up and new peaks appeared on the spectrum (Figure 3). These groups are mainly related to the presence of carboxylic functionalities and other species containing both sulphur and oxygen atoms (Table 3). Only C_{1s} and O_{1s} regions were analysed for the CK2 sample, while these regions, together with the S_{2p} region, were studied for CK2S4 and CK2S7, since no other signals were found on the wide XP spectra (Figure 4).As it can be observed, not only the expected peaks relative to thiol (SH) groups and carboxylic acids (COOH) appeared, but also peaks at higher binding energies on the S_{2p} region. These peaks are associated with oxidized forms of sulphur, coming part of them from the oxidation of thiols (sulphonic groups at 169.1 eV). Nevertheless, this signal at higher binding energy values is broad and it may not only come from these sulphonic groups, but from others with even higher binding energy. These groups were identified by Chiang et al. and, lately, by Yang et al. as cyclic species where 4, 5 or 6 member rings are formed from carbon surface with sulphur and oxygen [30,31].

Taking into account the surface chemistry of the CK2 sample (mainly phenols) and the chemical functionalities on thioglycolic acid (thiol and carboxylic acid), the reactions which can take place between them are mainly two: the one leading to the formation of esters (leaving the thiol group free) and the other leading to the formation of thioethers (carboxylic acid will be exposed in this case). Both reactions occurred in our case according to XPS and FTIR. Therefore, different surface groups could be formed in our sample by two different mechanisms: the first one is the reaction between thiol groups and carboxylic acids and the second one is the reaction between oxidized thiol groups (converted to sulphonic ones)

and phenol groups present on the carbon surface. Both pathways may be happening at the same time and there is no evidence to discard any of them.

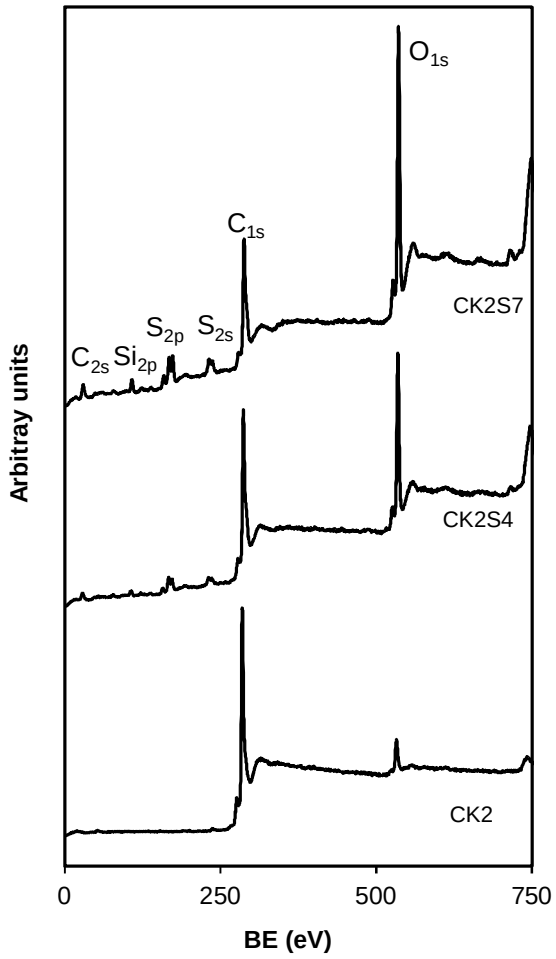

Figure 4. Wide XP Spectra of the samples. CK2, CK2S4, CK2S7.

After determining the different chemical groups present on the samples, XP spectra were further analysed to quantify oxygen and sulphur proportions on the external carbon surface. In order to know the sulphur content in bulk samples, a CHNS analysis was performed. Results obtained from both techniques are compared in Table 4. The pH_{ZPC} values were also obtained, which showed a high increase on the surface acidity by introducing sulphur and oxygen surface groups. This increase in heteroatoms surface concentration increments the wettability of

the treated carbons. Sulphur content obtained from XPS is larger than the one obtained by CHNS elemental analysis. Therefore, sulphur groups are mainly located on the external surface of the samples.

Table 4. Chemical characteristics of samples from XPS, CHNS and pH_{ZPC} analysis.

Sample	% C_{XPS}	% O_{XPS}	% S_{XPS}	% C_{EA}	% H_{EA}	% N_{EA}	% S_{EA}	% O_{EA}*	pH_{ZPC}
CK2	94.0	6.0	0.0	75.9	0.4	0.7	0.0	23.0	7.8
CK2S4	66.6	23.6	9.8	67.5	0.8	0.5	4.8	26.4	4.1
CK2S7	46.1	36.9	17.0	64.6	0.8	0.4	7.2	27.0	3.3

*, by difference

As it can be observed, there are significant differences between the values of % S_{XPS} (9.8 and 17.0 %) and those of %S_{EA} (4.8 and 7.2 %) in the two sulphur functionalized samples, CK2S4 and CK2S7. Therefore, sulphur groups were mainly formed on the external surface of the carbon. This increase on the sulphur percentage produced a decrease in pH_{ZPC}, whose value decreased as the sulphur and oxygen content increased, due to the acidic nature of the groups generated after the solvothermal treatment (thiols, carboxylic groups and derivatives). The presence of N functionalities is very low (the percentage of N varies between 0.7 and 0.4, as determined by elemental analysis), and they are not detected by XPS, Figure 4.

4.3. Oxygen Reduction Reaction: CV and LSV

Cyclic Voltammetry (CV) curves were obtained while N_2 or O_2 bubbled in a 0.1 M KOH solution. They were measured at a RDE rotation speed of 1000 rpm and at a scan rate of 50 mV s^{-1}.

Differences are observed in the negative potential region (Figure 5). Since these experiments were only performed to see the difference between CV under N_2 and O_2 (no parameter was obtained), only results for CK2 and CK2S4 are shown. It can be seen that oxygen reduction takes place at around -0.2 V versus Ag/AgCl. At a glance, it is clear that the CK2S4 sample is more active for ORR than CK2. This will be better observed after analysing LSV experiments, Figure 6.

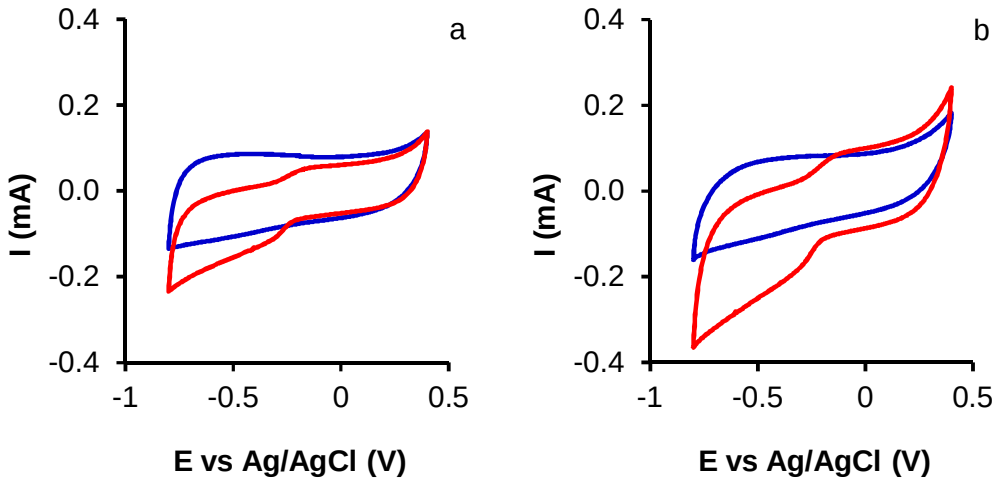

Figure 5.CV of CK2 (a) and CK2S4 (b) on N_2 (blue) and O_2 (red).

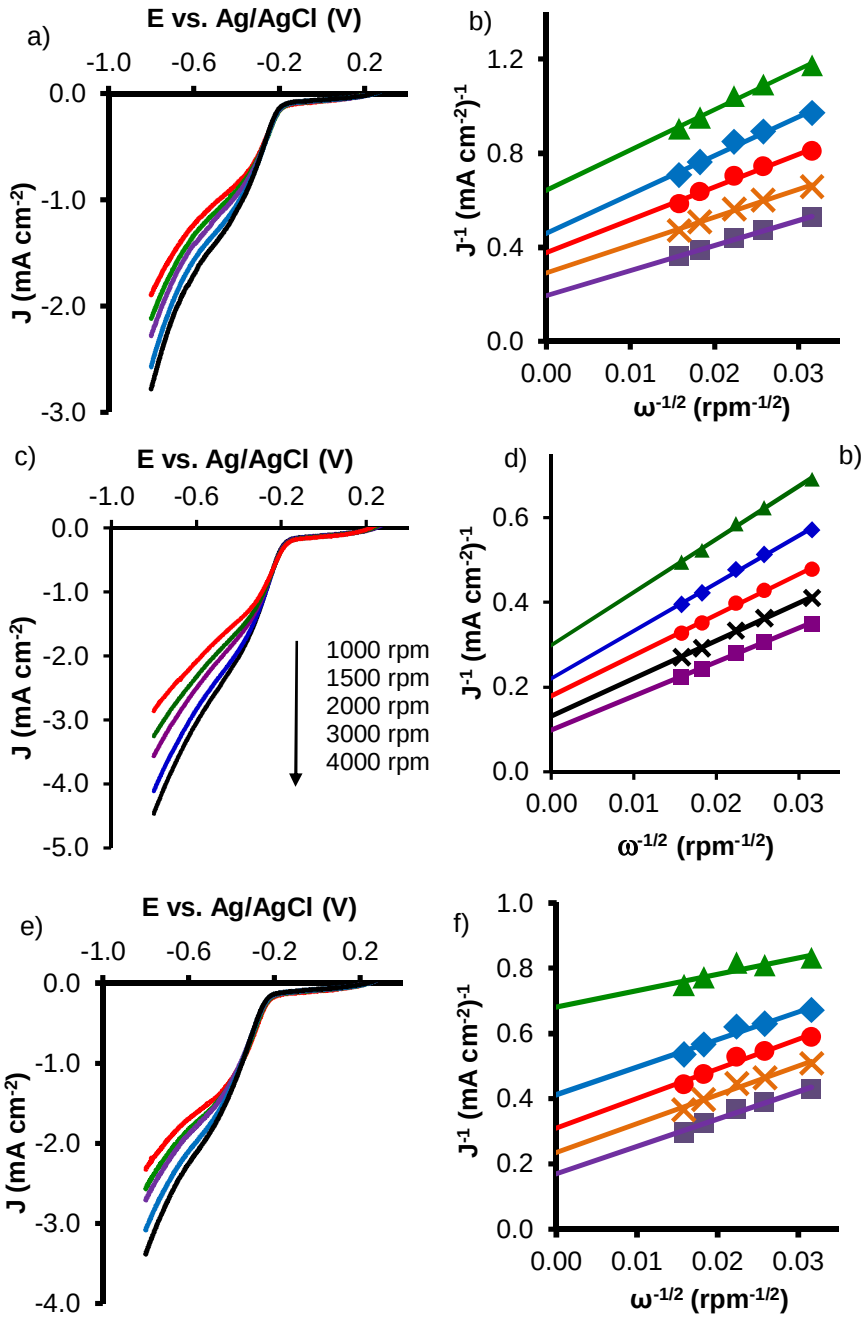

Figure 6. LSV at different rotation speed for a) CK2, c) CK2S4 and e) CK2S7. K-L plots for b) CK2, d) CK2S4 and f) CK2S7 at different electrochemical potentials: from -0.4 V (▲) to -0.8 V (■).

LSV curves were obtained at different rotation speeds for all the samples in order to apply the Koutecky-Levich equation. It needs to be considered that ORR can take place by two different mechanisms in basic media (equations 3 and 4) [1-3,16].

$$O_2 + 2\,H_2O + 4\,e_s^- \longrightarrow 4\,OH^- \qquad \text{(Equation 3)}$$

$$O_2 + H_2O + 2\,e_s^- \longrightarrow HO_2^- + OH^- \qquad \text{(Equation 4)}$$

It would be desirable that ORR takes place by the 4 electron pathway, rather than by the 2 electron pathway, since the former implies higher current densities on the electrochemical cell and the latter leads to the formation of peroxide species, which may deactivate and damage the electro-catalytic layer. Therefore, it is crucial to determine whether our sample is catalysing ORR by the first or the second mechanism. In order to discern that, LSV curves were obtained at different RDE rotation speed for all the samples. The obtained data were fitted to K-L equation so as to get the number of electrons transferred on each sample at each potential [2,3,5,14,16,19]. This analysis was performed for all the samples and the graphic results obtained are shown in Figure 6. Nevertheless, in order to compare the performance of all the samples with different sulphur contents, LSV curves at a RDE rotation speed of 1500 rpm, as well as the variation in the number of electrons transferred with the electrochemical potential for each sample, are shown in Figure 7 (a) and (b), respectively.

It became evident that sulphur functionalization was successful to improve the activated carbon performance on ORR in both cases, but especially if we compare CK2 with CK2S4. Two electrons were transferred in the case of CK2, while a four electron pathway was obtained when CK2S4 was used, which implies higher values of kinetic current densities at all electrochemical potentials. Also, a lower activation potential (E^0_{onset} versus Ag/AgCl) was required for the ORR to start (Table 5). However, when CK2S7 was tested, its performance proved to be better than the original activated carbon (CK2), but not better than CK2S4 with lower

sulphur content. The lower surface area of CK2S7 could be responsible for this behaviour.

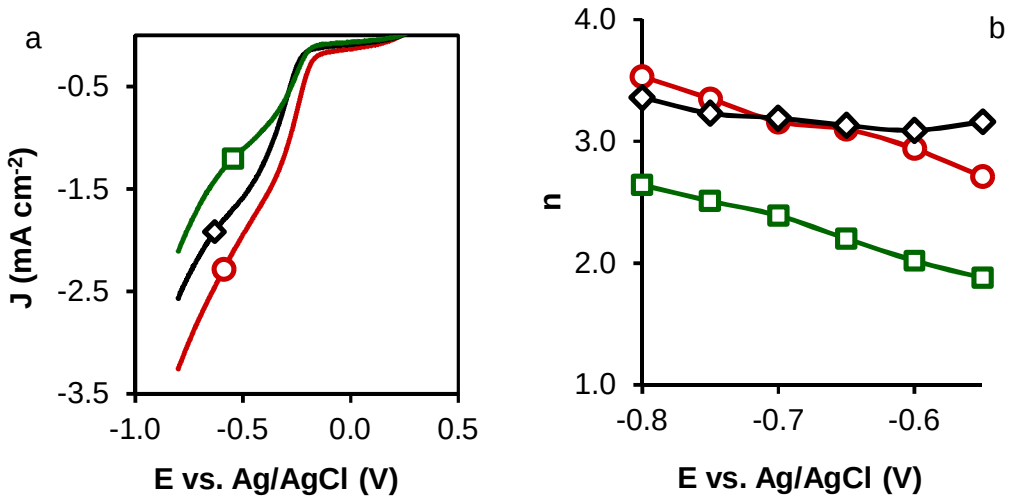

Figure 7. a) LSV curves at 1500 rpm and b) variation of n with E^0 vs Ag/AgCl for samples CK2 (□), CK2S4 (○), CK2S7 (◇).

Table 5. Parameters obtained from the analysis of LSV curves (values of j_k and n refer to K-L fitting for data at -0.8 V).

Sample	E^0_{onset}	j_k	N
	V	mA cm^{-2}	
CK2	-0.21	5.1	2.6
CK2S4	-0.17	10.1	3.5
CK2S7	-0.20	5.9	3.4

As it was previously commented on, the introduction of sulphur functionalities comes together with the destruction of a part of the micro and mesoporosity. Finally, the estimation of the optimum sulphur percentage to achieve the best electro-catalytic performance through this surface modification treatment should be studied, but only if it is possible to maintain similar textural characteristics

among the electrodes. Nevertheless, the presented results clearly show that carbon based electro-catalysts obtained from olive oil industrial waste and doped with sulphur had a superior behaviour in the ORR. Our materials showed a similar catalytic performance to other free-metal electro-catalysts based on graphene reported in the bibliography (Table 6) [14-16,18,31]. Therefore, the carbon-based materials prepared in this work are very promising candidates to be applied in the oxygen reduction reaction.

Table 6. Comparison with other S-doped carbon materials reported in the bibliography.

Sample	Functionalization	E^0_{onset} (V)	$*j_k$ (mA cm^{-2})	*n	Reference
CK2S4	Thioglycolic acid	-0.17	10.1	3.5	Our work
CA2-GO	H_2S, 800 °C	0.829**	13.5	3.9	[14]
RGOS	H_2S, 800 °C	-0.165	14.5	3.5	[15]
S-GNs-1000-CB	Na_2S	-0.17	10.0	3.8	[16]
SG900	H_2S, 900 °C	-0.20	5.3	3.2	[18]
S-Graphene-1050	Benzyl disulfide	-0.15	9.3	3.8	[31]

* j_k and n values refer to K-L fitting at the most negative potential tested.
** vs. RHE (the rest of the results are vs. Ag/AgCl)

5. CONCLUSIONS

High electro-catalytic activity in the oxygen reduction reaction can be achieved with activated carbons, obtained from olive oil industrial waste doped with sulphur. Sulphur functionalities were fixed on the porous surface of the carbon

materials by means of a solvothermal method using thioglycolic acid. Sulphur content and porous characteristics influence the electro-catalytic behaviour, but the presence of sulphur functionalities is crucial to develop a four electron mechanism. Carbon-based electro-catalysts doped with sulphur always worked at a lower electrochemical potential and with higher current densities than the raw activated carbon.

6. REFERENCES

[1] F. Si, Y. Zhang, L. Yan, J. Zhu, M. Xiao, C. Liu, W. Xing, and J. Zhang, Electrochemical Oxygen Reduction Reaction, in: Rotating Electrode Methods and Oxygen Reduction Electrocatalysts, Elsevier, Amsterdam, 2014. pp. 133-170.

[2] D. Banham, S. Ye, K. Pei, J.i. Ozaki, T. Kishimoto, and Y. Imashiro, A review of the stability and durability of non-precious metal catalysts for the oxygen reduction reaction in proton exchange membrane fuel cells, Journal of Power Sources 285 (2015) 334-348.

[3] Z. Yang, H. Nie, X. Chen, X. Chen, and S. Huang, Recent progress in doped carbon nanomaterials as effective cathode catalysts for fuel cell oxygen reduction reaction, Journal of Power Sources 236 (2013) 238-249.

[4] D.H. Jung, S.J. Bae, S.J. Kim, K.S. Nahm, and P. Kim, Effect of the Pt precursor on the morphology and catalytic performance of Pt-impregnated on Pd/C for the oxygen reduction reaction in polymer electrolyte fuel cells, International Journal of Hydrogen Energy 36 (2011) 9115-9122.

[5] S. Dou, A. Shen, Z. Ma, J. Wu, L. Tao, and S. Wang, N-, P- and S-tridoped graphene as metal-free electrocatalyst for oxygen reduction reaction, Journal of Electroanalytical Chemistry 753 (2015) 21-27.

[6] J.M. Oh, J. Park, A. Kumbhar, J. Smith, and S. Creager, Electrochemical Oxygen Reduction at Platinum/Mesoporous Carbon/Zirconia/Ionomer Thin-Film Composite Electrodes, Electrochimica Acta 138 (2014) 278-287.

[7] M.S. Ahmed, D. Kim, and S. Jeon, Covalently grafted platinum nanoparticles to multi walled carbon nanotubes for enhanced electrocatalytic oxygen reduction, Electrochimica Acta 92 (2013) 168-175.

[8] J.H. Kim, S. Chang, and Y.T. Kim, Compressive strain as the main origin of enhanced oxygen reduction reaction activity for Pt electrocatalysts on chromium-doped titania support, Applied Catalysis B: Environmental 158□159 (2014) 112-118.

[9] A. Zhao, J. Masa, and W. Xia, Oxygen-deficient titania as alternative support for Pt catalysts for the oxygen reduction reaction, Journal of Energy Chemistry 23 (2014) 701-707.

[10] M. Stojmenovic, M. Momcilovic, N. Gavrilov, I.A. Pasti, S. Mentus, B. Jokic, and B. Babic, Incorporation of Pt, Ru and Pt-Ru nanoparticles into ordered mesoporous carbons for efficient oxygen reduction reaction in alkaline media, Electrochimica Acta 153 (2015) 130-139.

[11] X. Bo, Y. Zhang, M. Li, A. Nsabimana, and L. Guo, NiCo2O4 spinel/ordered mesoporous carbons as noble-metal free electrocatalysts for oxygen reduction reaction and the influence of structure of catalyst support on the electrochemical activity of NiCo2O4, Journal of Power Sources 288 (2015) 1-8.

[12] C.L. Lee, H.P. Chiou, C.M. Syu, and C.C. Wu, Silver triangular nanoplates as electrocatalyst for oxygen reduction reaction, Electrochemistry Communications 12 (2010) 1609-1613.

[13] G. Gotti, K. Fajerwerg, D. Evrard, and P. Gros, Electrodeposited gold nanoparticles on glassy carbon: Correlation between nanoparticles characteristics and oxygen reduction kinetics in neutral media, Electrochimica Acta 128 (2014) 412-419.

[14] M. Seredych, K. László, E. Rodríguez-Castellón, and T.J. Bandosz, S-doped carbon aerogels/GO composites as oxygen reduction catalysts, Journal of Energy Chemistry 25 (2016) 236-245.

[15] M. Seredych and T.J. Bandosz, Confined space reduced graphite oxide doped with sulfur as metal-free oxygen reduction catalyst, Carbon 66 (2014) 227-233.

[16] R.K. Shervedani and A. Amini, Carbon black/sulfur-doped graphene composite prepared by pyrolysis of graphene oxide with sodium polysulfide for oxygen reduction reaction, Electrochimica Acta 142 (2014) 51-60.

[17] H.L. Poh, P. Simek, Z. Sofer, and M. Pumera, Sulfur-Doped Graphene via Thermal Exfoliation of Graphite Oxide in H2S, SO2, or CS2 Gas, ACSNano 7 (2013) 5262-5272.

[18] S. Yang, L. Zhi, K. Tang, X. Feng, J. Maier, and K. Müllen, Efficient Synthesis of Heteroatom (N or S)-Doped Graphene Based on Ultrathin Graphene Oxide - Porous Silica Sheets for Oxygen Reduction Reactions, Advanced Functional Materials 22 (2012) 3634-3640.

[19] R. Nie, X. Bo, C. Luhana, A. Nsabimana, and L. Guo, Simultaneous formation of nitrogen and sulfur-doped carbon nanotubes-mesoporous carbon and its electrocatalytic activity for oxygen reduction reaction, International Journal of Hydrogen Energy 39 (2014) 12597-12603.

[20] C. González-Gaitán, R. Ruiz-Rosas, E. Morallón, and D. Cazorla-Amorós, Functionalization of carbon nanotubes using aminobenzene acids and electrochemical methods. Electroactivity for the oxygen reduction reaction, International Journal of Hydrogen Energy 40 (2015) 11242-11253.

[21] S. Morales-Torres, T.L.S. Silva, L.M. Pastrana-Martinez, A.T.S.C. Brandao, J.L. Figueiredo, and A.M.T. Silva, Modification of the surface chemistry of single- and multi-walled carbon nanotubes by HNO3 and H2SO4 hydrothermal oxidation for application in direct contact membrane distillation, Phys. Chem. Chem. Phys. 16 (2014) 12237-12250.

[22] R.R.N. Marques, B.F. Machado, J.L. Faria, and A.M.T. Silva, Controlled generation of oxygen functionalities on the surface of Single-Walled Carbon Nanotubes by HNO3 hydrothermal oxidation, Carbon 48 (2010) 1515-1523.

[23] S. Román, J.M. Valente Nabais, B. Ledesma, J.F. González, C. Laginhas, and M.M. Titirici, Production of low-cost adsorbents with tunable surface chemistry by conjunction of hydrothermal carbonization and activation processes, Microporous and Mesoporous Materials 165 (2013) 127-133.

[24] M. Xue, L. Zhang, M. Zou, C. Lan, Z. Zhan, and S. Zhao, Nitrogen and sulfur co-doped carbon dots: A facile and green fluorescence probe for free chlorine, Sensors and Actuators B: Chemical 219 (2015) 50-56.

[25] Y. Jiang, M. Lu, X. Ling, Z. Jiao, L. Chen, L. Chen, P. Hu, and B. Zhao, One-step hydrothermal synthesis of three-dimensional porous graphene aerogels/sulfur nanocrystals for lithium□sulfur batteries, Journal of Alloys and Compounds 645 (2015) 509-516.

[26] Z. Peng, W. Fang, H. Zhao, J. Fang, H. Cheng, T.N.L. Doan, J. Xu, and P. Chen, Graphene-based ultrathin microporous carbon with smaller sulfur molecules for excellent rate performance of lithium-sulfur cathode, Journal of Power Sources 282 (2015) 70-78.

[27] J.F. Vivo-Vilches, E. Bailón-García, A.F. Pérez-Cadenas, F. Carrasco-Marín, and F.J. Maldonado-Hódar, Tailoring the surface chemistry and porosity of activated carbons: Evidence of reorganization and mobility of oxygenated surface groups, Carbon 68 (2014) 520-530.

[28] R. Ubago-Pérez, F. Carrasco-Marín, D. Fairén-Jiménez, and C. Moreno-Castilla, Granular and monolithic activated carbons from KOH-activation of olive stones, Microporous and Mesoporous Materials 92 (2006) 64-70.

[29] Y.J. Kim, H.J. Lee, S.W. Lee, B.W. Cho, and C.R. Park, Effects of sulfuric acid treatment on the microstructure and electrochemical performance of a polyacrylonitrile (PAN)-based carbon anode, Carbon 43 (2005) 163-169.

[30] L.Y. Chiang, L.Y. Wang, J.W. Swirczewski, S. Soled, and S. Cameron, Efficient Synthesis of Polyhydroxylated Fullerene Derivatives via Hydrolysis of Polycyclosulfated Precursors, J. Org. Chem. 59 (1994) 3960-3968.

[31] Z. Yang, Z. Yao, G. Li, G. Fang, H. Nie, Z. Liu, X. Zhou, X. Chen, and S. Huang, Sulfur-Doped Graphene as an Efficient Metal-free Cathode Catalyst for Oxygen Reduction, ACS Nano 6 (2012) 205-211.

[32] C.A. Leon, J.M. Solar, V. Calemma, and L.R. Radovic, Evidence for the protonation of basal plane sites on carbon, Carbon 30 (1992) 797-811.

[33] C. Du, Y. Sun, T. Shen, G. Yin, and J. Zhang,Applications of RDE and RRDE Methods in Oxygen Reduction Reaction, in: Rotating Electrode Methods and Oxygen Reduction Electrocatalysts, Elsevier, Amsterdam, 2014, pp. 231-277.

[34] T.J. Bandosz, M. Seredych, E. Rodríguez-Castellón, Y. Cheng, L.L. Daemen, and A.J. Ramírez-Cuesta, Evidence for CO2 reactive adsorption on nanoporous S- and N-doped carbon at ambient conditions, Carbon 96 (2016) 856-863.

[35] M. Seredych, J. Jagiello, and T.J. Bandosz, Complexity of CO2 adsorption on nanoporous sulfur-doped carbons Is surface chemistry an important factor?, Carbon 74 (2014) 207-217.

[36] J. Dong, Z. Zhuang, F. Song, D. Dunaway-Mariano, and P.R. Carey, A thioester substrate binds to the enzyme Arthrobacter thioesterase in two ionization states: evidence from Raman difference spectroscopy, J. Raman Spectrosc. 43 (2012) 65-71.

[37] Y. Huang, S.L. Candelaria, Y. Li, Z. Li, J. Tian, L. Zhang, and G. Cao, Sulfurized activated carbon for high energy density supercapacitors, Journal of Power Sources 252 (2014) 90-97.

CHAPTER V: ACTIVATED CARBONS FROM AGRICULTURAL WASTE SOLVOTHERMALLY DOPED WITH SULPHUR AS ELECTRODES FOR SUPERCAPACITORS

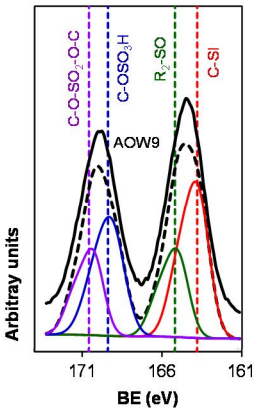

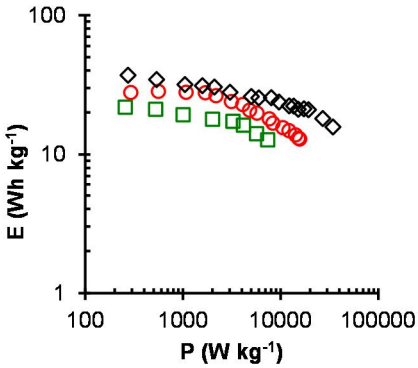

1. ABSTRACT

Revalorization of an agricultural waste from olive oil industry was performed by transforming it into activated carbon. In such a way, a material with excellent textural properties (high surface area and large micro and mesopore volumes) was obtained by carbonization and chemical activation of solid residues from olive oil industry. Moreover, this activated carbon was solvothermally treated in order to improve its electrochemical properties by adding sulphur functionalities on its surface. The treatment was able to introduce a great proportion of sulphur, mainly located on the external surface of sample. This modification lead to functionalized materials with not only larger capacitance (325 versus 158 F g^{-1} at 0.125 A g^{-1} in H_2SO_4 1 M), but also with a greater stability at higher current densities (large capacitance even at current densities as high as 30 A g^{-1}), due to their lower electrical resistance. Furthermore, the amount of electric energy stored by these materials was largely increased (from 21.8 to 37.0 Wh kg^{-1} in H_2SO_4 1 M) as well as their power density (from 7393 to 34360 W kg^{-1} in H_2SO_4 1 M). Several charge/discharge cycles were performed in order to test the cyclability of these materials, showing not significant reduction on their electrochemical properties after 12500 cycles.

Keywords: Sulphur dopped activated carbon. Supercapacitor performance; Galvanostatic charge-discharge; Electrochemical impedance spectroscopy.

2. INTRODUCTION

Agricultural wastes are abundant raw materials and most of them may be transformed into valuable product. Even though lignocellulosic materials commonly present poor yields on carbon (when carbonizing they usually lose more than 75% of their weight), their low price and their intrinsic structure make them very promising candidates to obtain high-performance materials which can be used in many different applications [1-5].

One field where carbon materials are commonly applied is related to their ability to store electrical energy. Therefore, numerous works can be found about the use of activated carbons as electrodes for batteries or supercapacitors [2,6-16]. In the last years, there is an increasing interest in modifying carbon surface by introducing different heteroatoms looking for a better performance of the material in terms of capacitance, corrosion resistance, cyclability, etc. [7,10-13,15]. Among them, sulphur is commonly used when activated carbons are incorporated as battery electrodes, especially for Li-ion batteries which have been widely developed on recent years [9,14-16].

There are several processes which might be applied to modify surface chemistry of carbon by introducing sulphur. The most frequent method consists on treating carbon with sulphuric acid (H_2SO_4). Nevertheless, this treatment is very aggressive and most times it produces a huge decrease on both specific area and pore volume [15-18]. Therefore, other less harmful procedures could be suitable to introduce sulphur functionalities under less drastic conditions (lower temperatures and less corrosive reactants) without destroying the porous texture of the material. Solvothermal methods, which were successfully applied for oxidation and nitrogenation, could serve at this purpose [19,20].

In this work, a series of activated carbon were obtained from solid waste of olive oil industry. The raw material was chemically activated with KOH to develop a high porosity and solvothermally treated with different portions of thioglycolic acid

to introduce sulphur functionalities. This way, we ended up with three activated carbons which mainly differed on their sulphur content. After characterizing their textural and chemical properties, these samples were employed to prepare electrodes which were tested by different techniques.

3. EXPERIMENTAL

3.1. Synthesis

Solid residue contained on Olive Mill Wastewater (OMW) which is mainly constituted by the exocarp, mesocarp, seed and small parts of olive stones was used as raw material. It was carbonized at 450 °C for two hours under nitrogen atmosphere (300 cm^3 min^{-1}) in order to stabilize cellulose and sugars components; after that, it was mixed with the activating agent (KOH) in a 1:2 (carbon:KOH) ratio at 60 °C for 12 h. Once dried, the mixture was heated up to 840 °C for 2 hours (10 °C min^{-1}). The sample was treated with several portions of HCl 1M in order to neutralize the excess of activating agent and to eliminate mineral matter, and then washed with deionized water till chloride absence. Finally, the sample was dried and named as AOW.

Activated carbon AOW was split into three portions. Two of them weighed 2 grams and were mixed with 5 mL and 9 mL of thioglycolic acid (>98%, supplied by Sigma-Aldrich) inside a 25 mL stainless steel Teflon-lined autoclaves which were heated up to 120 °C for 24 hours. To keep the volume constant, when 5 mL of thioglycolic acid were employed, 4 mL of absolute ethanol were added and mixed with the thioglycolic acid before putting it in contact with the activated carbon. The portion of sample AOW was treated in the same conditions but in this case only 8 mL of ethanol were used. Once the solvothermal process was finished, the two sulphur doped samples were washed with CS_2 and acetone to eliminate reaction by-products, and finally dried at 110 °C overnight. These two samples were labelled as AOW5 and AOW9.

3.2. Textural and chemical characterization.

Nitrogen adsorption-desorption isotherms at -196 °C and carbon dioxide adsorption isotherms at 0 °C were obtained in a AUTOSORB 1 (Quantachrome instruments). From the analysis of these isotherms different textural properties such as BET surface area (S_{BET}) and micropore volumes from Dubinin-Radushkevich (W_0) were obtained.

Surface chemistry was characterized by calculating the sulphur content on bulk samples by CHNS Analysis (THERMO SCIENTIFIC Flash 2000 coupled to a METTLER XP-6 microbalance) and the oxygen and sulphur content on the external surface by X-Ray Photoemission Spectroscopy (XPS). XP spectra were obtained with an ESCA 5701 (Physical Electronics). Survey and multi-region spectra were recorded at C_{1s}, O_{1s} and S_{2p} photoelectron peaks. Each spectral region of interest was scanned several times to get a good signal-to-noise ratio. Samples acidity was also evaluated by obtaining the zero-point charge pH (pH_{ZPC}); 250 mg of each sample were suspended on 4 mL of degasified distilled water and the pH of the suspension was periodically measured till constant value, according to the method proposed by Leon et al. [21].

3.3. Electrochemical measurements.

Each of the samples was mixed with polytetrafluorethylene (PTFE) in a 90:10 weight ratio and dried for 12 hours at 100 °C as described elsewhere [2]. The dried electrode material was pressed onto a 9 mm diameter graphite disk used as the working electrode. Final weight of the active material on each electrode was 3 mg. The electrode was impregnated with the electrolyte (an aqueous solution of H_2SO_4 1 M or KOH 6 M) for three days before being tested in order to achieve a good penetration of it inside the active material.

Electrochemical properties of these electrodes were studied in two different electrolytes H_2SO_4 1 M and KOH 6 M, using a two electrodes set-up connected to a EC-lab system (Biologic VMP multichannel potentiostat). Cyclic voltammetry curves were obtained at different scan rates varying from 0.5 mV s^{-1} to 20 mV s^{-1}

and with a voltage range from 0 to 1 V for 1 M H_2SO_4 and 0 to 0.8 V for 6 M KOH to evaluate the electrochemical stability of electrodes.

Galvanostatic charge/discharge experiments (GCD) were carried out at several current densities ranging from 0.125 A g^{-1} to 30 A g^{-1} within the same voltage range used for cyclic voltammetry measurements. Galvanostatic capacitances were determined by the Equation 1 [6,11]:

$$C_{GD} = 4\frac{I_d \times \Delta t}{m \times \Delta V} \qquad \text{Equation 1}$$

where I_d is the discharge current (A), Δt the discharge time (s), m is the total mass of active material (g) and ΔV is the discharge potential excluding the ohmic drop part. The factor 4 was used to calculate capacitance for a three electrodes equivalent system. The coulombic efficiency (%) was calculated from the discharge and charge time, t_d and t_c, respectively, by the formula $(t_d/t_c) \times 100$. From these data, specific energy (Equation 2) and specific power density (Equation 3) were calculated at different current densities, in order to obtain the Ragone plot for all the samples tested [22,23].

$$E(Wh\ kg^{-1}) = \frac{C_{GD}\,(F\,g^{-1}) \times \Delta V^2(V)}{2 \times 3.6} \qquad \text{Equation 2}$$

$$P(W\,kg^{-1}) = \frac{1}{2} \times \frac{I(A) \times \Delta V(V)}{m\,(kg)} \qquad \text{Equation 3}$$

GCDs were conducted for 12500 cycles in order to test the cyclability of the electrodes.

Impedance spectroscopy measurements were conducted in a frequency range from 1 mHz to 100 kHz with a sinusoidal current amplitude of 10 mV. The capacitance value, C_{max}, was obtained by Equation 4

$$C_{max} = \frac{-Z''}{2\pi f\left|Z^2\right|} \qquad \text{Equation 4}$$

where f is the frequency and $|Z|^2 = Z'^2+Z''^2$ where Z' and Z" are the real and imaginary parts of the complex impedance [24-26].

4. RESULTS AND DISCUSSION

4.1. Textural and chemical characterization

Nitrogen adsorption isotherms of the activated carbons (Figure 1) were of type I, typical of microporous solids [27], although they contained also some mesopores since the N_2 uptake slightly increased at high relative pressure after micropore filling. Original activated carbon AOW presents large micropore and mesopore volumes which is usual for carbon materials activated with KOH under similar conditions [2,28,29]. After the solvothermal treatment, there is a reduction on micropore and mesopore volumes (Table 1) due to a widening of the larger micropores and a blockage of part of the porosity by the presence of sulphur functional groups. It is important to note that the $W_0(N_2)/W_0(CO_2)$ ratio is constant for all samples denoting that the blockage affects practically in the same extent to both large and ultramicropores. Nevertheless, mesopore volume, V_{meso}, determined by the Gurvitch rule [30] suffered a sharp drop that results in around a 60 % of blocked pores. This is indicative of a heterogeneous distribution of sulphur on carbon surface being fixed mainly on the external surface area.

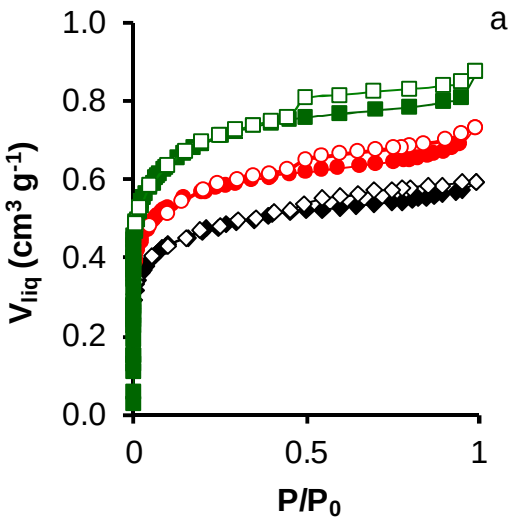

Figure 1. N_2 isotherms at -196 °C (adsorption, closed symbols; desorption, open symbols) for samples: □, AOW; ○, AOW5; ◇, AOW9.

Table 1. Textural characteristics of activated carbons

Sample	S_{BET}	$W_0(N_2)$	$L_0(N_2)$	W_0 (CO_2)	W_0 (N_2)/	$L_0(CO_2)$	V_{meso}
	m^2g^{-1}	cm^3g^{-1}	nm	cm^3g^{-1}	W_0 (CO_2)	nm	cm^3g^{-1}
AOW	1952	0.71	1.08	0.53	1.33	0.78	0.27
AOW5	1353	0.56	1.50	0.42	1.33	0.88	0.13
AOW9	1115	0.47	1.59	0.35	1.33	0.90	0.11

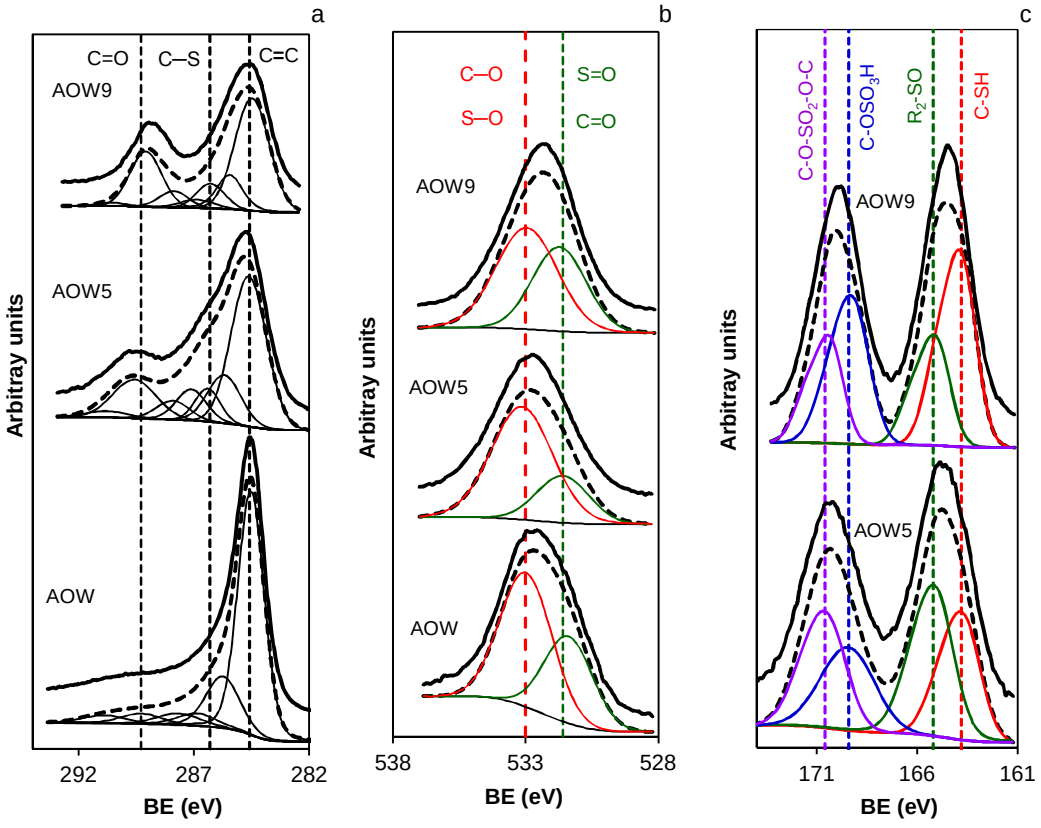

Figure 2. Deconvolution of C_{1s} (a) O_{1s} (b) and S_{2p} (c) high resolution XP spectra.

As expected, a large increase in sulphur content was obtained after the solvothermal treatment. This change had a marked increase on the external surface and a lower one inside the porosity as denoted by the differences between $\%S_{XPS}$ and $\%S_{EA}$ (Table 2). Since thioglycolic acid also contains oxygen in its structure, $\%O_{XPS}$ was incremented as well reaching a value of 38.1 % for sample AOW9. Keeping in mind that sulphur and oxygen groups generated on AOW5 and AOW9 samples present an acidic character, it is not surprising that pH_{ZPC} values of them became such small (Table 2) decreasing the hydrophobicity of the samples.The C_{1s}, O_{1s} and S_{1s} core level spectra of samples are depicted in Figure 2. The deconvolution of these signals and the corresponding peaks fitting showed the presence of diverse contributions to BEs that are displayed in Table 3 together with their corresponding percentages. The C_{1s} spectrum for the pristine activated carbon shows two main peaks centered at 284.6 and 285.6 eV corresponding to C=C and C-C bonds. At higher BE only minor peaks were detected which is usual for an activated carbon with a low oxygen content. After the solvothermal treatment, not only -SH groups are introduced on the carbon surface but the spectrum of C_{1s} is modified (Figure 3) showing a great increase in C-O functionalities together with these related to the formation of C-S functionalities (BE = 286.3 eV). The main increase took place for peak centred at BE ≈ 289.3 eV corresponding to the presence of carboxylic groups and other species containing both sulphur and oxygen (Table 3).

Table 2. Chemical composition (wt.%) of the activated carbons and pH_{PZC}.

Sample	O_{XPS}	S_{XPS}	C_{EA}	H_{EA}	N_{EA}	S_{EA}	O_{EA}*	pH_{ZPC}
AOW	6.0	--	88.1	0.3	0.8	--	10.8	7.8
AOW5	28.1	17.5	66.3	0.8	0.3	5.4	27.2	3.5
AOW9	38.1	25.0	60.6	1.1	0.2	9.5	28.6	2.8

* Value obtained by difference

Table 3. Results obtained from the deconvolution of high resolution XP spectra.

Sample	C_{1s} (eV)	FWHM (eV)	Peak (%)	O_{1s} (eV)	Peak (%)	$S_{2p3/2}$ (eV)	Peak (%)
AOW	284.6	1.43	60	531.3	35	-	-
	285.6		20	533.0	65		
	286.9		7				
	287.7		6				
	289.4		4				
	290.9		3				
AOW5	284.4	1.81	44	531.7	41	163.7	35
	285.5		14	533.0	59	165.0	19
	286.2		10			169.1	28
	286.9		9			170.3	18
	287.7		6				
	289.4		15				
	290.6		2				
AOW9	284.5	1.86	47	531.8	48	163.7	38
	285.5		12	533.0	52	165.0	15
	286.3		9			169.1	30
	286.9		4			170.3	17
	287.9		6				
	289.1		21				
	290.6		1				

Thioglycolic acid solvothermal treatment increased notably the oxygen content and as in the case of the C spectra the main increase occurred in the C=O peak centred at 531.3 eV whereas the contribution from the peak at 533.0 eV corresponding to C-O groups decreased, Table 3. It should be noted that the peaks for the oxygen in S=O and S–O, at BE of 531.77 and 533.17 eV respectively [31], appear at practically the same position as those for C=O and C–O. In this case and due to the slight difference between the BE it was not possible to evaluate both components separately.

As it can be observed, Figure 2c, not only the expected peaks relative to thiol (-SH) appeared, but also peaks at higher binding energies ≈ 165.2 eV corresponding to sulfoxide groups (R-SO-R'). Peaks at higher binding energies had been associated with oxidized forms of sulphur, stemming from the oxidation of thiols (sulfonic groups at 169.1 and dialkyl sulphates 170.6 eV).

4.2. Electrochemical measurements.

Electrochemical behaviour of samples on acidic and basic media (H_2SO_4, 1 M; KOH, 6 M) was evaluated in a two electrodes system by cyclic voltammetry in order to determine the voltage windows for each electrolyte and by chronopotentiometry at different current densities to determine the capacity and stability for the electrodes. Figure 3 shows cyclic voltammograms obtained for all the samples. Electrochemical behaviour of samples became worse when KOH 6 M was employed as electrolyte than in the case of H_2SO_4 1 M. The first matter which needs to be considered is that maximum potential beared in KOH is lower than H_2SO_4 (voltage ranged from 0 V to 0.8 V instead of 1.0 V).

GCDs in H_2SO_4 at 3 A g^{-1} and KOH at 1 A g^{-1} (Figure 4) showed a triangular shape, their gravimetric capacitances are presented in Table 4. The capacitance obtained by chronopotentiometry decreased rapidly as current density was increased when KOH 6 M was used as electrolyte, Figure 5. The capacitance retention in the range 0.125-3.0 A g^{-1} are 66 % for AOW and ≈70 % for AOW5 and AOW9 samples. Under basic conditions, the surface of the sulphur doped samples

is negatively charged, since there are acidic groups (thiols, sulphonics) which lose their proton in basic media. Therefore, electronic repulsions of the negatively charged surface groups and the OH^- may well be responsible for the poorer performance of these samples in KOH 6 M regarding results obtained in H_2SO_4 1 M. In fact, since AOW5 contains a smaller proportion on this kind of surface groups, its capacitance is slightly larger than the one of AOW9 in basic electrolyte. A clear difference between AOW and sulphur-doped samples is observed in H_2SO_4 as electrolyte. Sulphur functionalities were able to increase significantly capacitance under acidic conditions (Table 3). Furthermore, the higher the sulphur content, the larger the capacitance resulted, in contrast with the results found in KOH. Capacitance values, determined by galvanostatic discharge, Figure 5, were also lower in KOH 6 M compared to the ones obtained in H_2SO_4 1 M.

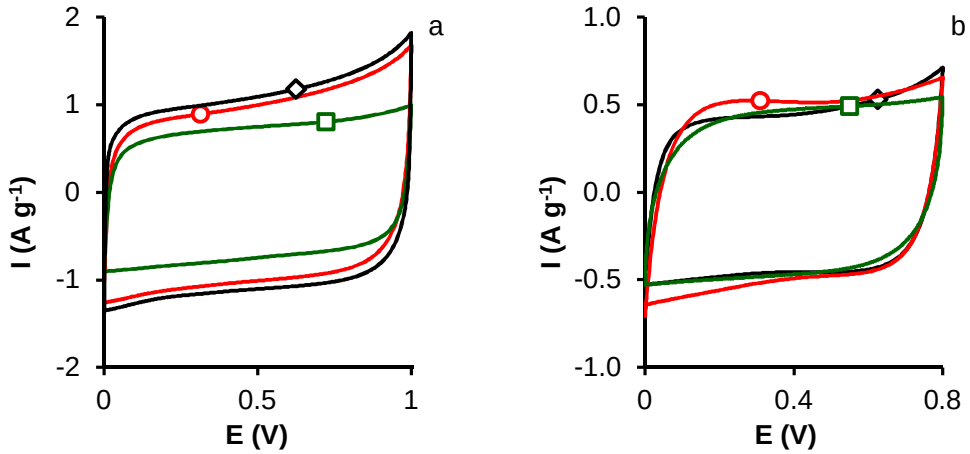

Figure 3. Cyclic voltammograms at 20.0 mV s^{-1} for samples: □, AOW; ○, AOW5; ◇, AOW9. a) H_2SO_4 1 M and b) KOH 6 M.

The main advantage of this sulphur functionalization is the significant increase in the current density that can be used for the charge-discharge experiments.

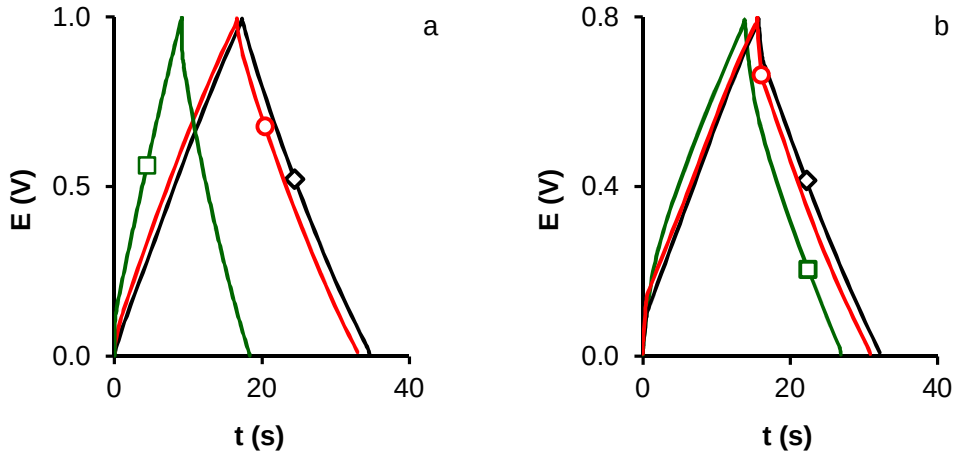

Figure 4. GCDS in a) H_2SO_4 1 M at 3 A g^{-1} and b) KOH 6 M 1 A g^{-1} for samples: □, AOW; ○, AOW5; ◇, AOW9.

Table 4. Electrochemical capacitances of samples in H_2SO_4 1 M and KOH 6 M. Retention capacitance at 30 A g^{-1} in H_2SO_4 and 3 A g^{-1} for KOH

Sample	KOH			H_2SO_4		
	C_{GD} 0.125 A g^{-1} F g^{-1}	C_{GD} 10 A g^{-1} F g^{-1}	Ret %	C_{GD} 0.125 A g^{-1} F g^{-1}	C_{CP} 30 A g^{-1} F g^{-1}	Ret %
AOW	107	71	66	158	105*	66*
AOW5	130	92	71	258	151	59
AOW9	127	85	67	325	225	69

* Value at 10 A g^{-1}, since AOW could not withstand higher current densities.

It is important to highlight that whereas the maximum current density withstood by AOW was just 10 A g^{-1}, sulphur doped samples maintain a

significantly high capacitance up to 30 A g^{-1}. The capacitance retention at 30 Ag^{-1} was 69 % for AOW9 and 59 % for AOW5 similar to that for the sample AOW at 10 A g^{-1}. This is an important result, showing the suitability of sulphur functionalization not only to increase the electronic capacitance of the electrode, but also to achieve a greater stability when high current densities are applied. The coulombic efficiency in all cases was 100 % up to 5 A g^{-1} and it decreased up to ~ 97 % at higher current density due to the cell resistance.

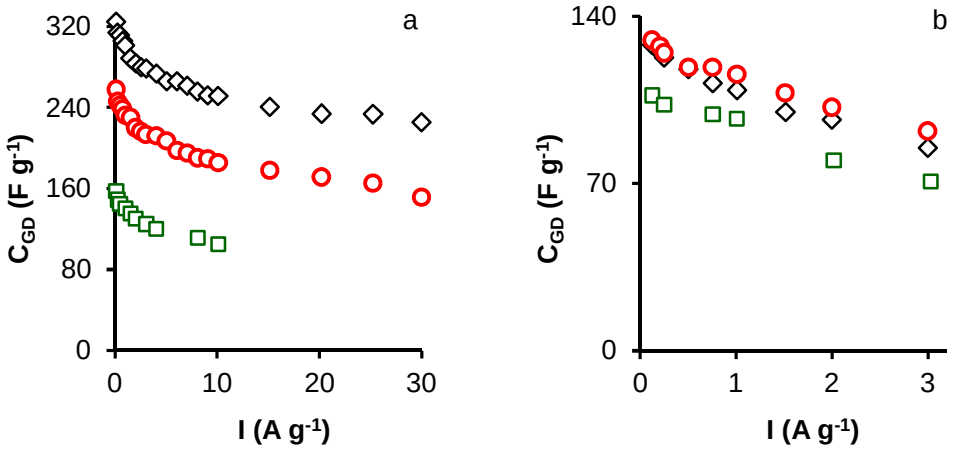

Figure 5. Variation of the specific capacitance with scan rate in a) H_2SO_4 1 M and b) KOH, 6 M. Samples AOW (□), AOW5 (○), AOW9 (◇).

EIS measurements were performed to investigate the variations in charge kinetic properties of the samples towards the capacitive behavior. Figure 6 depicts the Nyquist plots, showing that all samples exhibited typical characteristics of porous carbon electrodes [25,26]. In the high frequency region, the first intersection point on the real axis (Z') was the ESR, which corresponds to the sum of the intrinsic resistance of the active material, the electrolyte resistance, and the contact resistance of interface between material/current collector. By using the same assembly technique, the cells containing the same electrolyte and the same collector high-frequency region reflects the resistive properties of the carbon

electrode material [32]. Results, shown in Table 5, reflect that ESR values were very low, ranging between 0.3 and 0.4 Ω, for the three samples which is related to a very well developed pore structure.

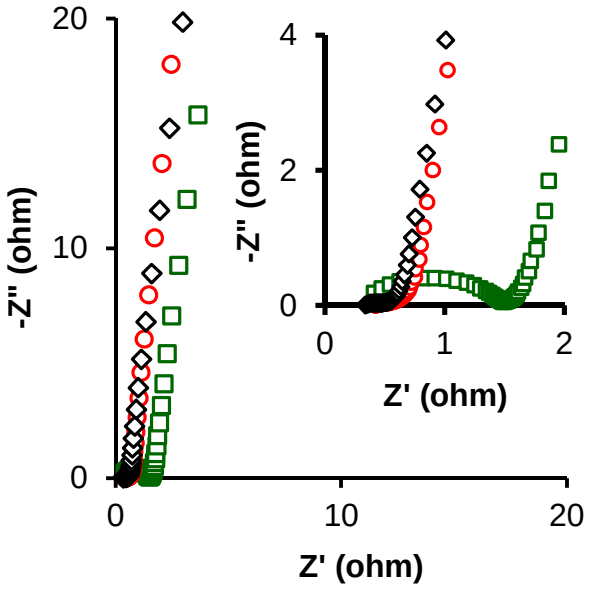

Figure 6. Nyquist plots obtained from EIS experiments on H_2SO_4 1M AOW (□), AOW5 (○), AOW9 (◇)

Table 5. Equivalent series resistance (ESR), charge transfer resistance (R_{CT}), relaxation time constant (τ) and C_{max} at 1 mHz, from EIS

Sample	ESR Ω	R_{CT} Ω	τ s	C_{max} F g^{-1}
AOW	0.41	1.15	0.34	159
AOW5	0.38	0.27	0.19	246
AOW9	0.32	0.27	0.08	293

The interfacial charge transfer resistance, R_{CT}, caused by electric double layer capacitance and faradic reactions was estimated from the two intercepts of the semicircle with the real axis (semicircle diameter) [33], values obtained are displayed in Table 5. R_{CT} values were much lower for sulphur doped activated carbon than for the original one, this is AOW. This fact indicates a faster charge transfer joint to a better electrolyte ions accessibility into pores of electrode materials due to the widening of the ultra and supermicropores during the solvothermal treatment, Table 1. Moreover, the slope for samples AOW5 and AOW9 is steeper than for AOW, implying that sulphur doped samples have better capacitive performance in 1 M H_2SO_4 electrolyte than the pristine sample.

In conclusion, both ESR and R_{CT} decrease with the solvothermal treatment, Figure 6. This was due to several reasons: an increase in the heteroatoms introduced during the treatment, a decrease in contact resistance between particles, which facilitated the mobility of electrons through the carbon electrode (ESR) and a widening of the micropores, which increased the accessibility of the electrolyte to the microporosity (R_{CT}). The main advantage of our functionalization treatment is that the reaction between carbon and thioglycolic acid took place mainly on the external surface. Therefore, our samples present a very high sulphur content measured by XPS which largely increased their conductivity. The gravimetric capacitances obtained from the Nyquist plots at 1 mHz and calculated according to equation 4 expressed per single electrode as the three-electrode cell equivalent, C_{max}, are compiled in Table 5. These values are similar to those obtained by chronopotentiometry at 0.125 A g^{-1}.

The relaxation time constant (τ) can be calculated by the equation $\tau = ½\pi f_0$, where f_0 is the transition frequency between a pure capacitive and a pure resistive behavior that can be obtained from the maximum within the variation of the imaginary part of the capacitance (C'') against the frequency [34]. The relaxation time constant is a quantitative measure of the speed with which the device can be discharged. Results in Table 5 show that the time necessary to discharge the supercapacitor, τ, when AOW9 is used as electrode is just 0.08 s.

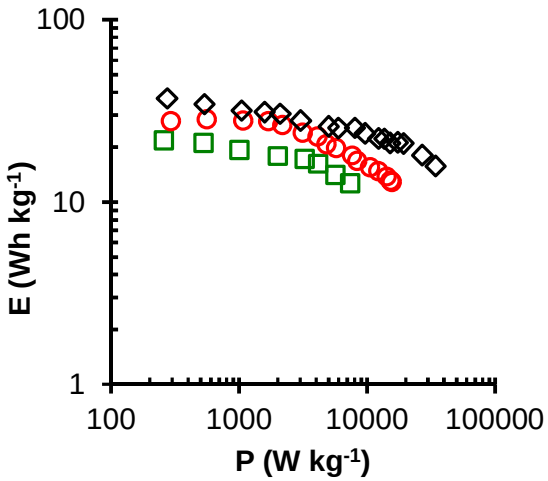

Figure 7. Ragone plots on H_2SO_4 1M for samples AOW (□), AOW5 (○), AOW9 (◇)

Table 6. Maximum and minimum energy densities (Wh Kg^{-1}) from Ragone's plots

Sample	P_{min} W kg^{-1}	E_{max} Wh kg^{-1}	P_{max} W kg^{-1}	E_{min} Wh kg^{-1}
AOW	257	21.8	7393	12.7
AOW5	292	27.9	15661	12.9
AOW9	274	37.0	34360	15.7

The Ragone plots of the ACs are displayed in Figure 7 and the maximum and minimum energies and power densities are shown in Table 6. The maximum energy density increased with the increase in sulphur content attributable to the increase in heteroatoms on the surface area and the widening of the microporosity. The maximum energy density value reached was 37.0 Wh kg^{-1} for sample AOW9

a value of energy density larger than that reported for most of the commercially available supercapacitors (< 10 Wh kg^{-1}) [35]. The energy released decreased at higher power density (Figure 7); thus, the energy densities of AOW, AOW5 and AOW9 decreased to 12.7, 12.9, and 15.7 Wh kg^{-1} at power densities of ~ 7.3, 15.7, and 34.4 kW kg^{-1}, respectively.

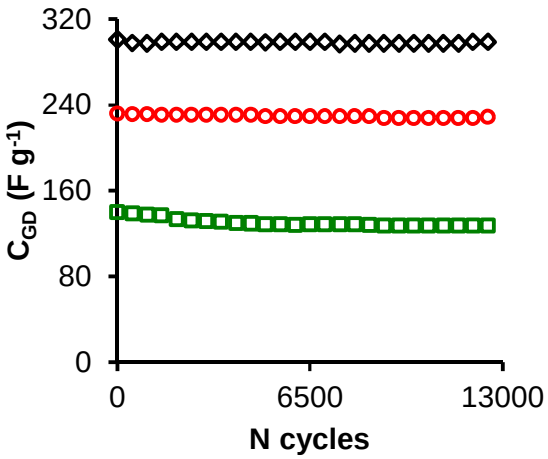

Figure 8. Variation of the gravimetric capacitance (CCP) with the number of charge discharge cycles at 1 A g^{-1} in the potential window between 0 and 1 V in H_2SO_4 1 M for samples AOW (□), AOW5 (○), AOW9 (◇)

The long-term stability of electrodes is a key factor that limits the application of carbon materials as supercapacitors for practical applications. The stability of electrodes was evaluated by 13000 galvanostatic charge-discharge. Figure 8 presents the variation in the gravimetric capacitance with the number of charge-discharge cycles at a constant current density of 1 A g^{-1} employing H_2SO_4 1 M as electrolyte. After 12500 cycles the retention capacity for the three samples are 91.0 %, 98.5 % and 99.3 % for AOW, AOW5 and AOW9. Samples doped by solvothermal treatment with thioglycolic acid exhibit practically no fading in their capacitance showing a very good cycling stability, while the contrary occurs for the

non-doped sample as it loses practically 10 % of its capacitance. It is observed that the best result is obtained for the AOW9 sample in spite of its lowest porosity due to the beneficial effect of sulphur and oxygen surface groups.

5. CONCLUSIONS

The solvothermal treatment developed in this work which is based in the use of thioglycolic acid fixed on the activated carbon surface up to a 38 % of heteroatoms. Oxygen surface groups fixed were mainly as carboxylic acid species. Sulphur groups were not only thiol groups but other coming from the oxidation of –SH as sulfoxide, sulfonic and dialkil sulfates.

Sulphur doped activated carbons showed an excellent performance as electrodes for supercapacitors in H_2SO_4 whereas in KOH showed poorer performance because of the repulsion of the OH^- ions with the negative charge of the carbon surface. Gravimetric capacitances of sulphur doped samples determined in H_2SO_4 1 M increased as the sulphur an oxygen content did, in spite of the reduction in porosity and surface area, reaching very high values of C_{GD} larger than 300 F g^{-1} at 0.125 A g^{-1}. Moreover, C_{GD} retention at higher current densities were also improved with the presence of sulphur. In this line, the porosity widening and the surface groups introduced were responsible for the reduction in resistance and the increase in capacitance. On the other hand, the electrical resistance was higher in the basic electrolyte than in the acid one, and the sample with the highest sulphur content showed the lowest electrical resistance. It should be remarked that virtually no fading is observed for sulphur doped carbons 12500 charge-discharge cycles.

Besides that, the maximum energy density value reached was 37.0 Wh kg^{-1} for a power density of 274 W kg^{-1} and it corresponds again to the sample with the highest sulphur content. Finally, the energy released decreased at highest power density; thus, the energy densities of AOW, AOW5 and AOW9 decreased to 12.7, 12.9, and 15.7 Wh kg^{-1} at power densities of ~ 7.3, 15.7, and 34.4 kW kg^{-1}, respectively. Therefore, the results of this work show clearly the great influence of

the sulphur functionalities on the electro-chemical behavior of the developed carbon based electrodes as well as how the activated carbons can be doped with sulphur using a simple solvothermal method.

6. REFERENCES

[1] T. Maneerung, J. Liew, Y. Dai, S. Kawi, C. Chong, C.H. Wang, Activated carbon derived from carbon residue from biomass gasification and its application for dye adsorption: Kinetics, isotherms and thermodynamic studies, Bioresource Technology, 200 (2016) 350-359.

[2] A. Elmouwahidi, Z. Zapata-Benabithe, F. Carrasco-Marín, C. Moreno-Castilla, Activated carbons from KOH-activation of argan (Argania spinosa) seed shells as supercapacitor electrodes, Bioresource Technology, 111 (2012) 185-190.

[3] J. Fiuza, R. Medeiros de Jesus Neto, L.B. Correia, H.M. Carvalho Andrade, Preparation of granular activated carbons from yellow mombin fruit stones for CO2 adsorption, Journal of Environmental Management, 161 (2015) 198-205.

[4] M.A. Yahya, Z. Al-Qodah, C.W.Z. Ngah, Agricultural bio-waste materials as potential sustainable precursors used for activated carbon production: A review, Renewable and Sustainable Energy Reviews, 46 (2015) 218-235.

[5] B. Tsyntsarski, I. Stoycheva, T. Tsoncheva, I. Genova, M. Dimitrov, B. Petrova, D. Paneva, Z. Cherkezova-Zheleva, T. Budinova, H. Kolev, A. Gomis-Berenguer, C.O. Ania, I. Mitov, N. Petrov, Activated carbons from waste biomass and low rank coals as catalyst supports for hydrogen production by methanol decomposition, Fuel Processing Technology, 137 (2015) 139-147.

[6] Z. Zapata-Benabithe, F. Carrasco-Marín, C. Moreno-Castilla, Electrochemical performance of Cu- and Ag-doped carbon aerogels, Materials Chemistry and Physics, 138 (2013) 870-876.

[7] C. Moreno-Castilla, M.B. Dawidziuk, F. Carrasco-Marín, E. Morallón, Electrochemical performance of carbon gels with variable surface chemistry and physics, Carbon, 50 (2012) 3324-3332.

[8] X. Geng, L. Li, F. Li, Carbon nanotubes/activated carbon hybrid with ultrahigh surface area for electrochemical capacitors, Electrochimica Acta, 168 (2015) 25-31.

[9] R. Sahore, L.P. Estevez, A. Ramanujapuram, F.J. DiSalvo, E.P. Giannelis, High-rate lithium–sulfur batteries enabled by hierarchical porous carbons synthesized via ice templation, Journal of Power Sources, 297 (2015) 188-194.

[10] J.M. Rosas, R. Ruiz-Rosas, J. Rodríguez-Mirasol, T. Cordero, Kinetic study of the oxidation resistance of phosphorus-containing activated carbons, Carbon, 50 (2012) 1523-1537.

[11] Z. Zapata-Benabithe, F. Carrasco-Marín, C. Moreno-Castilla, Preparation, surface characteristics, and electrochemical double-layer capacitance of KOH-activated carbon aerogels and their O- and N-doped derivatives, Journal of Power Sources, 219 (2012) 80-88.

[12] Z. Zapata-Benabihe, C. Moreno-Castilla, F. Carrasco-Marín, Influence of the Boron Precursor and Drying Method on Surface Properties and Electrochemical Behavior of Boron-Doped Carbon Gels, Langmuir, 30 (2014) 1716-1722.

[13] J.Z. Wang, L.Q. Wang, M.M. Chen, C.Y. Wang, C. Zhang, F. He, Nanoporous carbons from oxidized green needle coke for use in high performance supercapacitors, New Carbon Materials, 30 (2015) 141-149.

[14] S. Xiao, S. Liu, J. Zhang, Y. Wang, Polyurethane-derived N-doped porous carbon with interconnected sheet-like structure as polysulfide reservoir for lithium–sulfur batteries, Journal of Power Sources, 293 (2015) 119-126.

[15] Z. Yang, S. Wang, K. Dong, Y. Dai, X. Lei, Electrochemical characterization of sulfur with low depth of charge/discharge in lithium sulfur batteries, Electrochimica Acta, 187 (2016) 629-635.

[16] M.K. Song, E.J. Cairns, Y. Zhang, Lithium/sulfur batteries with high specific energy: old challenges and new opportunities, Nanoscale, 5 (2013) 2186-2204.

[17] R. Niu, H. Li, Y. Ma, L. He, J. Li, An insight into the improved capacitive deionization performance of activated carbon treated by sulfuric acid, Electrochimica Acta, 176 (2015) 755-762.

[18] P. Rechnia, A. Malaika, M. Kozlowski, Synthesis of tert-amyl methyl ether (TAME) over modified activated carbon catalysts, Fuel, 154 (2015) 338-345.

[19] S. Morales-Torres, T.L.S. Silva, L.M. Pastrana-Martinez, A.T.S.C. Brandao, J.L. Figueiredo, A.M.T. Silva, Modification of the surface chemistry of single- and multi-walled carbon nanotubes by HNO3 and H2SO4 hydrothermal oxidation for application in direct contact membrane distillation, Phys. Chem. Chem. Phys., 16 (2014) 12237-12250.

[20] Y. Jiang, M. Lu, X. Ling, Z. Jiao, L. Chen, L. Chen, P. Hu, B. Zhao, One-step hydrothermal synthesis of three-dimensional porous graphene aerogels/sulfur nanocrystals for lithium–sulfur batteries, Journal of Alloys and Compounds, 645 (2015) 509-516.

[21] C.A. Leon, J.M. Solar, V. Calemma, L.R. Radovic, Evidence for the protonation of basal plane sites on carbon, Carbon, 30 (1992) 797-811.

[22] A. Bello, F. Barzegar, D. Momodu, J. Dangbegnon, F. Taghizadeh, N. Manyala, Symmetric supercapacitors based on porous 3D interconnected carbon framework, Electrochimica Acta, 151 (2015) 386-392.

[23] Y. Korenblit, M. Rose, E. Kockrick, L. Borchardt, A. Kvit, S. Kaskel, G. Yushin, High-Rate Electrochemical Capacitors Based on Ordered Mesoporous Silicon Carbide-Derived Carbon, ACS Nano, 4 (2010) 1337-1344.

[24] P.L. Taberna, P. Simon, J.F. Fauvarque , Electrochemical Characteristics and Impedance Spectroscopy Studies of Carbon-Carbon Supercapacitors, Journal of The Electrochemical Society, 150 (2003) A292-A300.

[25] E.Y.L. Teo, L. Muniandy, E.P. Ng, F. Adam, A.R. Mohamed, R. Jose, K.F. Chong, High surface area activated carbon from rice husk as a high performance supercapacitor electrode, Electrochimica Acta, 192 (2016) 110-119.

[26] N. Manyala, A. Bello, F. Barzegar, A.A. Khaleed, D.Y. Momodu, J.K. Dangbegnon, Coniferous pine biomass: A novel insight into sustainable carbon materials for supercapacitors electrode, Materials Chemistry and Physics, 182 (2016) 139-147.

[27] M. Thommes, K. Kaneko, A. Neimark, V, J.P. Olivier, F. Rodriguez-Reinoso, J. Rouquerol, S.W. Sing Kenneth, Physisorption of gases, with special reference to the evaluation of surface area and pore size distribution (IUPAC Technical Report). pac 87 (2015) 1051-1069.

[28] R. Ubago-Pérez, F. Carrasco-Marín, D. Fairén-Jiménez, C. Moreno-Castilla, Granular and monolithic activated carbons from KOH-activation of olive stones, Microporous and Mesoporous Materials, 92 (2006) 64-70.

[29] J.F. Vivo-Vilches, E. Bailón-García, A.F. Pérez-Cadenas, F. Carrasco-Marín, F.J. Maldonado-Hódar, Tailoring the surface chemistry and porosity of activated carbons: Evidence of reorganization and mobility of oxygenated surface groups, Carbon, 68 (2014) 520-530.

[30] F. Duarte, F.J. Maldonado-Hódar, L.M. Madeira, Influence of the characteristics of carbon materials on their behaviour as heterogeneous Fenton catalysts for the elimination of the azo dye Orange II from aqueous solutions, Applied Catalysis B: Environmental, 103 (2011) 109-115.

[31] J.G.C. Shen, T.H. Kalantar, R.G. Herman, J.E. Roberts, K. Klier, Synthesis and Characterization of [NaO3SOCH2CH2OSO3Na] and Its Anchored Form: Surface-Grafted Acid Groups on Zirconium Hydroxide, Chem. Mater., 13 (2001) 4479-4485.

[32] D. Hulicova, M. Kodama, H. Hatori, Electrochemical Performance of Nitrogen-Enriched Carbons in Aqueous and Non-Aqueous Supercapacitors, Chem. Mater., 18 (2006) 2318-2326.

[33] Z. Tian, M. Xiang, J. Zhou, L. Hu, J. Cai, Nitrogen and Oxygen-Doped Hierarchical Porous Carbons from Algae Biomass: Direct Carbonization and Excellent Electrochemical Properties, Electrochimica Acta, 211 (2016) 225-233.

[34] Y. Huang, Y. Liu, G. Zhao, J.Y. Chen, Sustainable activated carbon fiber from sawdust by reactivation for high-performance supercapacitors, Journal of Materials Science, 52 (2017) 478-488.

[35] G. Wang, L. Zhang, J. Zhang, A review of electrode materials for electrochemical supercapacitors, Chem. Soc. Rev., 41 (2012) 797-828.

CHAPTER VI: *H_3PO_4 AND KOH ACTIVATED CARBONS FROM WASTE WOOD AS ELECTRODES FOR ELECTROCHEMICAL CAPACITORS.*

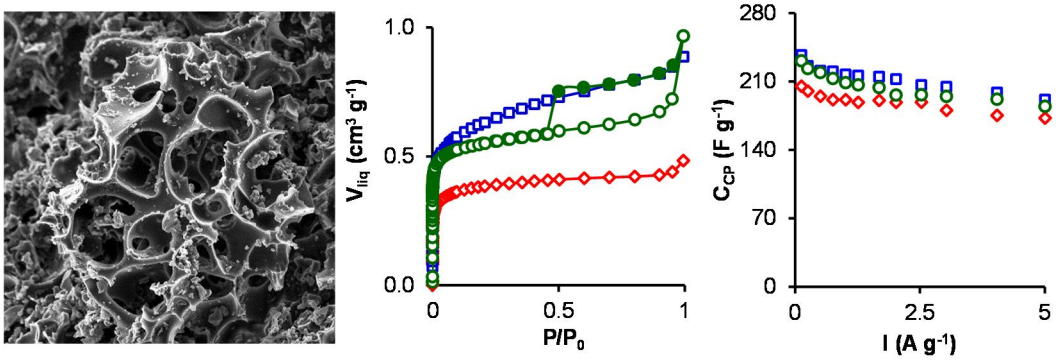

1. ABSTRACT

Two series of activated carbons have been prepared by chemical activation of three different kind of agricultural waste. KOH and H_3PO_4 were used as activating agent of custard apple, fig and olive woods. The main differences between these trees are their growth rate and the hardness of the wood. Due to these differences distinct pore structure, surface areas and chemical composition were found for the different activated carbons prepared. Phosphoric acid activated samples present a high ash content due to the phosphate formation during the activation process.

KOH activated samples are mainly microporous materials with high surface area and pore volumes. On the contrary when H_3PO_4 was used as activating agent activated carbons are meso microporous materials.

Ash content and micropore structure are limiting factors for the application of activated carbons as electrodes for supercapacitors. The best performance correspond to KOH activated samples with high capacitance and energy and power densities.

The stability of the electrodes, evaluated by charge-discharge cycling shows that the KOH activated carbons had a high cyclic stability up to 12000 cycles. For H_3PO_4 samples the capacitance decreases for CP and FP ones due to their high ash content and the poor stability of the acidic surface groups.

Keywords: agricultural waste, chemical activation, activated carbons, electrodes for supercapacitors.

2. INTRODUCTION

Activated carbon are used in different industrial applications due to its good porosity and the developed higher surface area, among them industrial food [1], pharmaceutical application [2], removal of pollutants from gaseous [3,4] and liquid steams [5,6], catalysis [7], gas storage, and electrochemical applications like battery electrode and supercapacitors [8].

Activated carbon are produced from different substances such as waste plastic [9], waste tire [10], waste materials biomass from forest and agricultural crops and residues [11] like rice husk [12], bagasse [6], coconut shell [5], olive stone shell [4,8]. Several method are used for the preparation of activated carbon from the waste biomass materials among them the chemical activation with different chemical agent like, $ZnCl_2$, H_3PO_4, KOH [8,11,13]. The production of activated carbon from wood has become increasingly attractive due to their availability and their economic and commercial promise. in fact, several research have presented on the production of charcoal from wood by chemical activation from different type of wood, olive wood [14], eucalyptus wood [15], fir wood [16], birch wood park [17].

Recent studies have shown that the presence of the heteroatoms on the surface of the activated carbon can enhance the capacity of the supercapacitor. The phosphoric acid activation leads to inclusion of significant amount of phosphorus into carbon structure which had a significant on the electrochemical characteristics of the activated carbon.

The objective of this study was to prepare activated carbon from three different wood produced with higher quantity in Spain; custard apple, fig and olive woods with chemical activation with H_3PO_4 and KOH following the method described previously [4,8] and their application as super capacitors.

The activated carbon were characterized to determine their textural properties, their porosity and surface chemistry and before they were used for the preparation of supercapacitor to their electrochemical characteristics.

3. EXPERIMENTAL

3.1. Preparation of activated carbon

The activated carbon were prepared by chemical activation with H_3PO_4 and KOH of three different woods, custard apple, fig tree and olive tree. The sample prepared with H_3PO_4 activation were designated CP, FP and OP and the other prepared with KOH were named CK, FK and OK.

The sample were prepared were impregnated with KOH/ H_3PO_4 in a weight ratio of 1/1. The mixture were heated at 60 °C to dryness and after that at 110 °C until evaporation total of the water. The solid produced were carbonized under N_2 flow 300 cm^3 min^{-1} and heating rate of 5 °C min^{-1}, at 500 °C for 2 h for the samples impregnated with H_3PO_4, and at 300 °C for 1 h followed by activation at 800 °C for 2 h for the samples impregnated with KOH. The produced activated carbon were washed with 1 M HCl and with distillated water until neutralization of the washing water and total elimination of chloride.

Table 1. Preparation conditions of the activated carbons

Sample	Raw material	Activating agent/ raw material ratio	Pyrolysis temperature(°C)/time (h)
CK	custard apple tree	KOH 1:1	300/1+800/2
FK	Fig tree	KOH 1:1	300/1+800/2
OK	Olive tree	KOH 1:1	300/1+800/2
CP	custard apple tree	H_3PO_4 1:1	500/2
FP	Fig tree	H_3PO_4 1:1	500/2
OP	Olive tree	H_3PO_4 1:1	500/2

3.2. Textural and chemical characterization

The textural characterization of the activated carbons was carried out by N_2 and CO_2 adsorption at -196 and 0 °C, respectively using a Quantachrome Autosorb-1 equipment after outgassing the samples overnight at 110 ºC under dynamic vacuum (10^{-6} mbar). The total micropore volume, $W_0(N_2)$, and the narrow

micropore volume, $W_0(CO_2)$, were obtained by the application of Dubinin–Radushkevich (DR) to the N_2 and CO_2 adsorption isotherms, respectively, and the mean micropore width (L_0) for both adsorbates were obtained by applying the Stoeckli equation. The BET equation was applied to N_2 adsorption isotherms to obtain the apparent BET surface area (S_{BET}). The pore size distribution (PSD) was determined by applying Non Linear Density Functional Theory (NLDFT) to the N_2 adsorption isotherms, assuming slit-shaped pores.

Analysis elemental was performed using an elemental analyzer THERMO SCIENTIFIC Model Flash 2000. The content of phosphorous was obtained using ICPOES from Perkin Elmer model Optima 8300.

XPS was obtained using a Kratos Axis Ultra-DLD, with MgKα X-ray source ($h\upsilon$ = 1253.6 eV) and hemispherical electron analyser connected to a DLD detector. Survey and multi-region spectra were recorded at C_{1s}, O_{1s}, N_{1s} and P_{2p} photoelectron peaks. Each photoelectron spectral region of interest was scanned several times to obtain good signal-to-noise ratios. The C_{1s} peak at 284.6 eV was used as internal standard. Given that the depth recorded with this technique is around 2-3 nm below the external surface, it gives the surface content of oxygen, O_{XPS}, and phosphorus, P_{XPS}.

3.3. Electrochemical Characterization

For the electrochemical characterization, a mixture of active material and tetrafluoethylene (PTFE) binder (60% suspension in water) with a ratio of 90:10 was dried in an oven at 120 ºC overnight. Then, 5mg of the active material was pressed onto a graphite paper disc with 5 mm of diameter. The pasted sample was impregnated with a 1M H_2SO_4 solution for 48 h before to be used for the electrochemical measurements.

The electrochemical performances were determined using a two electrode system with EC-lab equipment at 25 ºC in H_2SO_4 1M medium as electrolyte and glassy fibrous materials as separator. Several electrochemical techniques are used for the electrochemical characterization of the composites. Cycling

voltammetry test (CV) was carried within the range of 0 and 0.75 V; using scan rates from 0.5 to 20 mV s^{-1} and the gravimetric capacitance, C_{CV} (F g^{-1}), was calculated using the Equation (1) [18,19]:

$$C_{CV} = 4\frac{\sum|I|\Delta t}{m\Delta V} \qquad \text{Eq. 1}$$

where $\sum|I|\Delta t$ is the area of the current (A) against time (s) curve, m is the total active mass in both two electrode (g), and ΔV is the potential window (V), the factor 4 traduces the relation between the two electrode and three electrode systems.

The galvanostatic charge-discharge experiments were carried out at different current density from 125 mA g^{-1} to 5 A g^{-1}. The gravimetric capacitance, C_{CP} (F g^{-1}), was calculated using the equation (2)[20,21]:

$$C_{CP} = 4\frac{I_d \Delta t}{m \Delta V} \qquad \text{Eq. 2}$$

where I_d was the current density (A g^{-1}), Δt was the discharge time, ΔV was the voltage interval without the IR drop and m is the total mass active (g).

The stability of the electrodes was evaluated by 12000 charge-discharge cycles at a current density of 1 A g^{-1} between potential value of 0 V and 0.75 V.

The electrical energy and power densities were calculated by using the Eq. 3 and Eq.4, respectively for two-electrode cell [22,23].

$$E(Wh\,kg^{-1}) = \frac{C_{GD}\,(F\,g^{-1}) \times (V_{max}^2 - V_{min}^2)(V)}{2 \times 3.6} \qquad \text{Eq. 3}$$

$$P(W\ kg^{-1}) = \frac{1}{2} \times \frac{I(A) \times (V_{max}^2 - V_{min}^2)(V)}{m\ (kg)} \qquad \text{Eq. 4}$$

4. RESULTS AND DISCUSSION

4.1. Textural and chemical characterizations

Morphology of the samples was studied by scanning electron microscopy, Figure 1 shows the morphology of selected the samples. The different nature of the wood it is clearly revealed, thus fig tree is a fast growth tree with a soft wood, sample FK shows an important degradation of the wood structure leading a very heterogeneous pore structure. Olive and custard trees with slower growth present a harder wood and the wood structure is preserved producing a more developed micropore structure. Also the changes produced by the activation agent used (KOH or H_3PO_4) are different, H_3PO_4produces a heterogeneous porous surface with large pores compared to the KOH activated samples which show relatively homogeneous and highly porous surface.

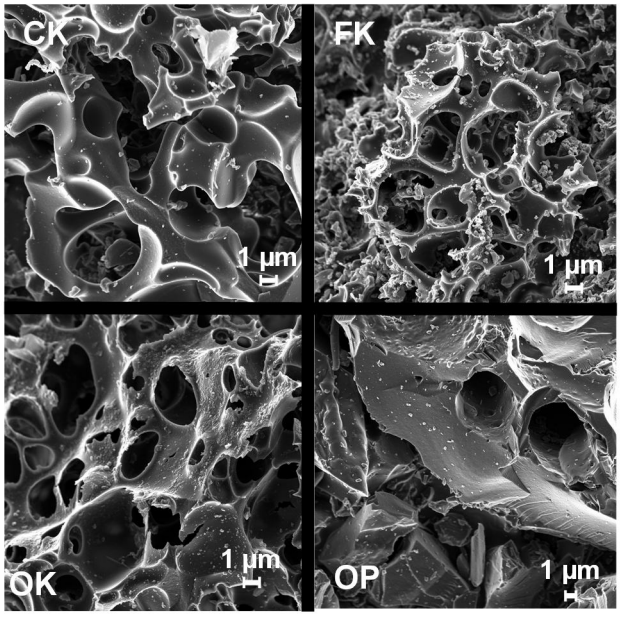

Figure 1. SEM images of the activated carbons prepared

The differences in the morphology of the activated carbon samples are more clearly revealed by the gas adsorption analysis. Figure 2 shows N_2 adsorption-desorption isotherms for the different activated carbons. Sample FK and OK exhibit type I isotherms with a slight slope at medium relative pressure

which is indicative of the presence wider micropores. Sample CK show a Type I-Type IV isotherm with a slope at relatives pressures higher than 0.15indicative of mesopores. The hysteresis cycle, Type H2, for sample OK confirm the heterogeneity of the porosity for this sample. Samples prepared by H_3PO_4 activation present a Type I+IV isotherm indicative of micro-mesopore structure which is confirmed by the pore size distribution showed in the Figure 3.

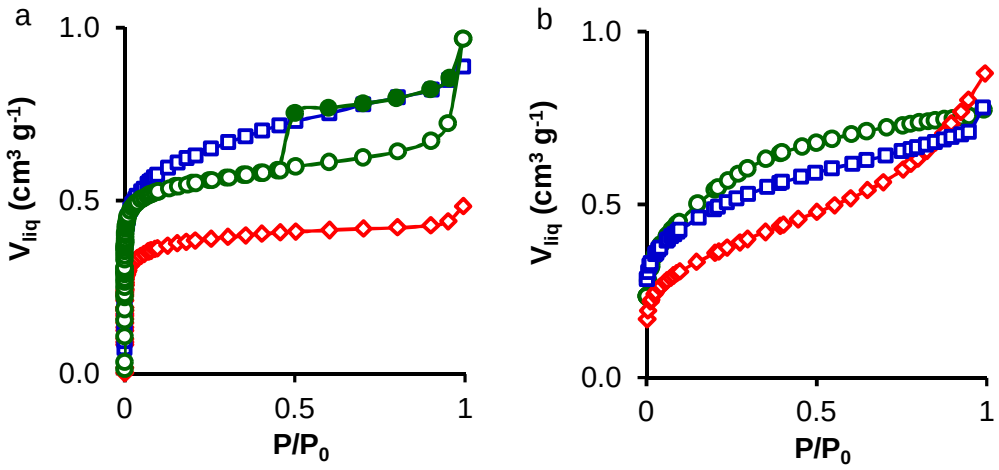

Figure 2. N_2 adsorption isotherms at -196 °C. a) K series; b) P series. Samples: olive tree (○); fig tree (◇); custard apple tree (□). Closed symbols for OK sample correspond to the desorption branch.

Results from the application of BET and DR equations to the N_2 and CO_2 adsorption isotherms are compiled in Table 2 together the mesopore volume obtained according to the Gurvich rule [24]. Apparent surface areas range from 795 m^2 g^{-1} (FP) to 1480 m^2 g^{-1} (CK). As expected KOH activation produces activated carbon with higher surface area and micropore volume [25] varying from 1237 m^2 g^{-1} to 1480 m^2 g^{-1} and large pore volumes varying from 0.44 to 0.52 cm^3 g^{-1}.The lowest surface area were obtained from fig tree, which has a fast growth and softwood.

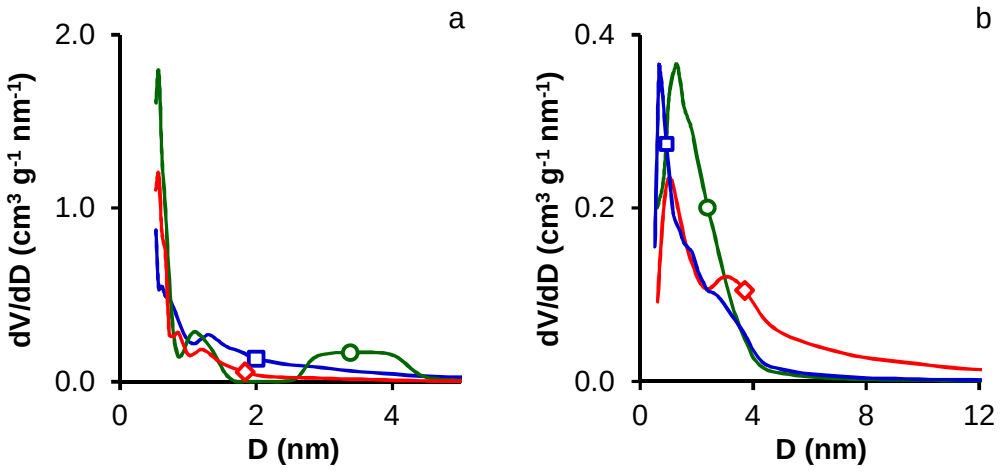

Figure 3. Pore size distribution obtained by NLDFT applied to N_2 adsorption isotherms at -196 °C. a) K series; b) P series. Samples: olive tree (○); fig tree (◇); custard apple tree (□).

Table 2. Porous structure of the activated carbon

Sample	N_2 at -196 °C					CO_2 at 0 °C	
	S_{BET}	$W_0(N_2)$	$L_0(N_2)$	$V_{0.95}(N_2)$	V_{meso}	$W_0(CO_2)$	$L_0(CO_2)$
	m^2/g	cm^3/g	nm	cm^3/g	cm^3/g	cm^3/g	nm
CK	1480	0.52	1.02	0.85	0.33	0.38	0.72
FK	1237	0.44	0.83	0.58	0.14	0.35	0.65
OK	1352	0.52	0.82	0.72	0.20	0.34	0.68
CP	1089	0.40	1.21	0.75	0.35	0.20	0.60
FP	795	0.30	1.55	0.80	0.50	0.13	0.83
OP	1116	0.41	1.46	0.76	0.34	0.19	0.73

For all the samples $W(N_2) > W(CO_2)$ which is indicative of the absence of constriction at micropores entrances and complete accessibility of N_2 molecule at -196 °C [26,27]. $W(CO_2)$ and $W(N_2)$ for samples activated with H_3PO_4 are lower than those prepared by KOH activation indicating that KOH produce activated carbons with high surface areas with large microporosity and on the contrary, H_3PO_4 activation leads to a more developed mesoporosity. The CK activated carbon presents large surface area with a homogeneous pore size distribution which will be very interesting for electrochemical application.

Surface compositions of activated carbon samples were analyzed by XPS. This technique provided information regarding the electronic states and chemical environment of carbon (C), nitrogen (N) oxygen (O) and phosphorous (P) atoms in the activated carbons. Figure 4 shows survey XP spectra in the BE range of 50-750 eV, which provided both a compositional overview and information about main element presents on the surface of both series of activated carbons. All samples showed two different peaks, a strong C_{1s} peak between 284 eV, one O_{1s} peak was also observed at 532 eV, and in addition samples from P series show the presence of P_{2p} and Ca_{2p} peaks even though the intensity of these peaks is lower than the C and O they are very important since they are indicative of the phosphorous fixation on the carbon surface partially appear as phosphates species being this salt the main component of the ashes of the P series.

Deconvolution of the high resolution XP spectra of the P_{2p} region are showed in Figure 4c. Three different peaks were found, Table 3. A peak centered at 132.5 eV associated with reduced phosphorus compound as C-P [28-30]; the peak at 133.1 eV is characteristic of P atom bonded to one C atom and three O atoms, as in C–PO; $C–PO_2H$ [28-30], and a peak at 134.1 eV which is characteristic of pentavalent tetra-coordinated phosphorus, PO_4, as in polyphosphates and/or phosphates ($C–O–PO_3$; $C–PO_3$ groups) [31,32].

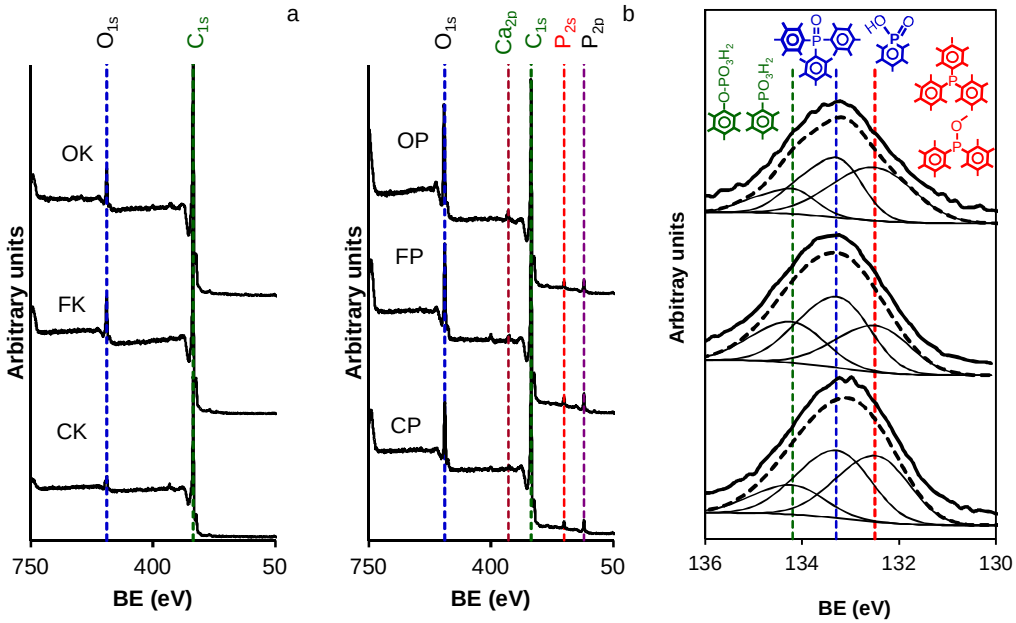

Figure 4. Survey XP spectra for: a) KOH activated carbons. b) H_3PO_4 Activated carbons.

Table 3. Chemical composition of activated carbons (%) from elemental analysis, ICPOES and XPS.

Sample	TG	EA				ICP	XPS		
	Ash	C	H	N	O+P [a]	P	C	O	P
CK	1.4	91.6	1.2	0.7	6.5	0.0	95.5	4.5	0.0
FK	1.1	91.6	1.5	0.6	6.3	0.0	94.6	5.4	0.0
OK	1.5	90.1	1.4	0.7	7.8	0.0	93.6	6.4	0.0
CP	8.5	68.7	2.3	0.5	28.5	5.2	80.1	13.3	6.6
FP	9.3	71.6	2.5	0.7	25.2	6.5	76.5	16.1	7.4
OP	7.6	73.6	2.9	0.4	23.1	5.3	76.6	17.5	5.9

a) By difference

Table 3 shows the results for chemical composition of samples from thermogravimetric and elemental analysis, ICPOES and the results from the deconvolution of high resolution of XP spectra. The ash content for KOH activated samples is very low ranging from 1.1 to 1.5 % due to the solubilization of the mineral matter content in the raw woods. For H_3PO_4 samples the ash content is higher than KOH ones due to the presence of phosphorous surface groups. The P content determined by ICPOES and XPS is very similar for each sample indicating a homogeneous distribution of P on the samples. Furthermore the sum of O_{XPS} + P_{XPS} is approximately equal to the result obtained from EA, confirming the homogeneous distribution of all elements. O_{1s} profile was decomposed in three components. The peak at 530.8 to 531.8 represent the oxygen double bonded C=O groups and the oxygen in the phosphate groups P=O [33]. The presence of the singly bonded oxygen in C-O and in C-O-P is confirmed by the presence of the peak at 532.6-533.0 eV [34,35].

Table 4. Surface functionalities concentrations of O1s, P2s and C1s from the XPS spectra.

B.E. (eV)	Functionality	CK	FK	OK	CP	FP	OP
284.6	C=C/C-O-P	68	64	68	68	69	73
286.0	C-O-C/C-O-P-O/C-PO	19	21	20	21	20	16
287.6	C=O	4	6	5	4	4	4
288.8	-COOH/O=C-O-C	4	5	4	4	3	3
290.1	CO2	3	2	2	2	2	2
291.3	π-π*	1	1	1	1	1	1
530.8-531.5	C=O bonds, P=O bonds	31	31	29	37	33	43
532.7-533.0	C–O–C , C–O–P, P–O–P	69	69	71	63	67	57
132.3	C-P	-	-	-	40	30	45
133.1	C–PO; C–PO2H	-	-	-	42	44	39
134.1	C–O–PO3; C–PO3	-	-	-	18	26	16

From the comparison between of the concentrations of different oxygen groups, it can be remarked that the chemical activation with phosphoric acid produces an increase in the amount of C=O and P=O groups which correspond to the formation P-surface groups during the phosphoric acid activation [32,36]. The oxygen and phosphate-containing groups on the surface of the material can enhance their wettability with the electrolytes, these surface phosphate functional groups can act as active sites for additional pseudocapacitance leading to an enhanced electrochemical performance of activated carbons as a supercapacitor electrode. The data from XPS shows that the three different samples prepared with the same activating agent present similar oxygen content and also the same type of oxygen bonds.

The KOH activated carbons present a very similar chemical surface, so the differences on their electrochemical behaviour must be correlated with their textural properties, while on the H_3PO_4 activated carbons, the electrochemical behaviour will depend on both textural and chemical characteristics. The amount and nature of phosphorus groups could affect the formation of the electrochemical double layer and the retention of the capacitance with the increase of the potential scan rate, and with the increase of the current density during the charge discharge experiments.

Figure 5 shows the FT-IR spectra of activated carbon prepared with KOH and H_3PO_4. All spectra show a band at 3600–3200 cm^{-1} with a maximum at about 3420 cm^{-1} characteristic of the stretching vibration of hydrogen-bonded hydroxyl groups from carboxyls, phenols or alcohols, and water adsorbed in the activated carbons. The band at 2800–3000 cm^{-1} indicates the presence of an aliphatic CH stretching. The spectra shows a pronounced band at 1630 cm^{-1}, which can be assigned to the C-C stretching vibration in the structure of the activated carbon. The band at 1000–1300 cm^{-1} is usually found with oxidized carbons and has been assigned to C-O stretching in acids, alcohols, phenols, ethers, and/or esters groups [36], but in the case of the H_3PO_4 activated carbon this band is also characteristic of phosphorus and phosphorous-carbonaceous compounds. The

peak at 1163 cm^{-1} can be attributed to the stretching mode of hydrogen-bonded. Finally the H_3PO_4 activated carbons show a band at 1080–1065 cm^{-1} which can be assigned as P^+-O^- in acid phosphate esters and to the symmetrical vibration in polyphosphate chain P-O-P [37]. This acidic group had an effect on the capacitance retention of the H_3PO_4 activated carbons based supercapacitors.

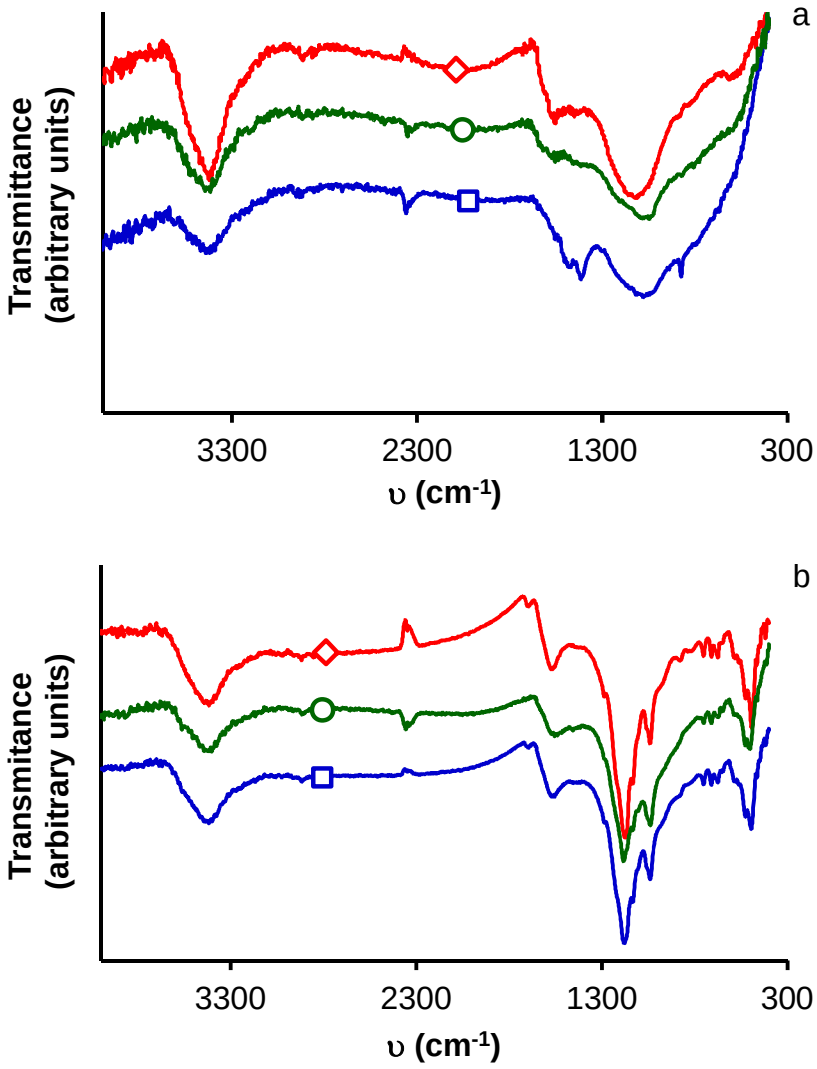

Figure 5. Infrared spectra of the activated carbons a) K series; b) P series. Samples: olive tree (○); fig tree (◇); custard apple tree (□).

4.2. Electrochemical Characterization

Figure 6 shows the cyclic voltammograms, CV, curves of all the samples. It can be see that all the activated carbons have CV with a rectangular shape typical for electrochemical double-layer (EDL) capacitors with a low diffusional restriction to the electrolytedue to a good electrical conductivity and to the porosity of the samples. However, a some differences in the voltammograms shape between the KOH and H_3PO_4 activated samples is observed, so different contributions must be taken into account, thus H_3PO_4 activated carbons show the wider microporosity and more developed mesoporosity, Table 1. Comparing the CV curves, K series show higher capacitance than P series due to the higher surface area and microporosity of the former samples. Furthermore, most rectangular CV's correspond to P series due to their more developed mesoporosity and wider micropores. Sample OK shows a slightly tilted curve which is indicative of some resistance restrictions, this sample has high micropore volume 0.52 cm^3 g^{-1} with narrow micropores, 0.65 and 0.60 nm for N_2 and CO_2, respectively.

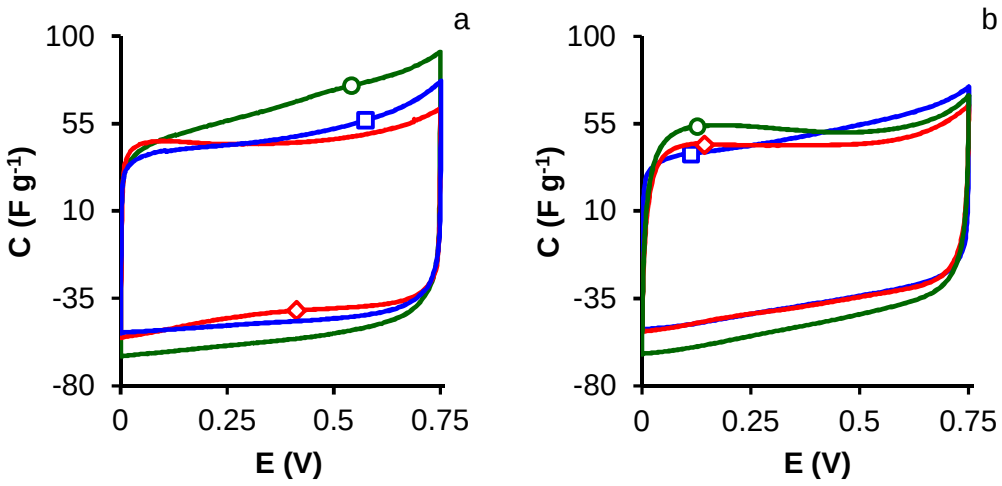

Figure 6. CV for K series (a) and P series (b) in 1 M aqueous H_2SO_4 using two-electrode cell at a scan rate of 0.5 mVs^{-1}. Samples from: olive tree (○); fig tree (◇); custard apple tree (□).

These conclusions can be confirmed with the corresponding gravimetric charge discharge experiments showed in Figure 7. These curves show that the K

series present symmetrical triangular curves which indicates very good penetration of the ions into the pores with low diffusion restrictions. On the contrary the P series presents a slight deviation from the linearity at the discharge branch due the resistance inside the pore structure of the samples.

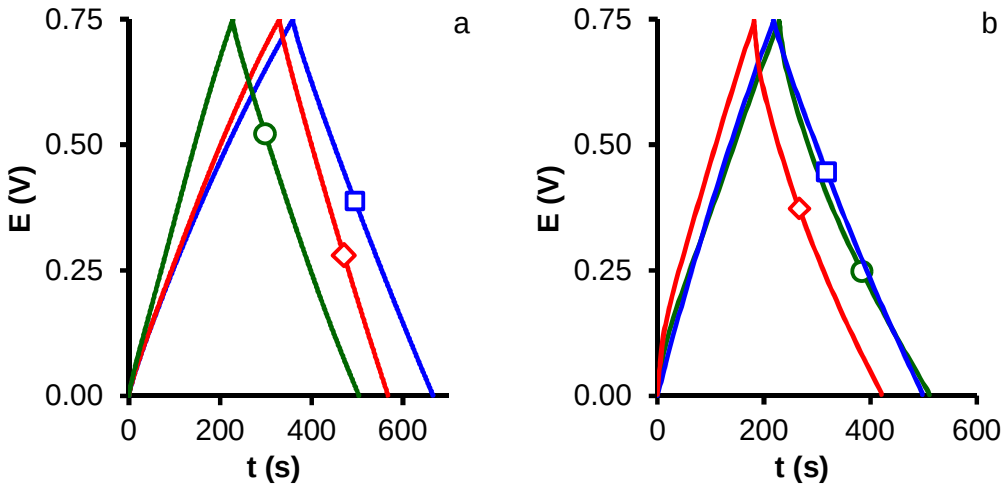

Figure 7. CP for K series (a) and P series (b) in 1 M aqueous H_2SO_4 using two-electrode cell at a current density of 0.125 A g^{-1}. Samples from: olive tree (○); fig tree (◇); custard apple tree (□).

Comparing among the P series, the FP sample shows the higher discharge drop followed with the OP and finally the CP, this result can be explained considering the resistance calculated from the voltage drop in CP experiments according to $R_{CP}=\Delta V/2I$, Table 5. Activated carbons prepared with KOH show lower resistance than sample activated with phosphoric acid probably due to the high ash content in the later ones as previously described by Moreno-Castilla et al. [38]

Table 5. Values of specific capacitance (Fg^{-1}) at 0.5mV s^{-1}, $C_{CV}0.5$, and at current loads, 0.125 and 5 A g^{-1}, ($C_{CP}0.125$ and $C_{CP}5$ respectively),retention capacitance, R_{CP}, and resistance from voltage drop in CP experiments, R.

Sample	$C_{CV}0.5$ Fg^{-1}	$C_{CP}0.125$ F g^{-1}	$C_{CP}5$ F g^{-1}	R_{CP} %	R (Ω)
CK	235	237	191	81	2.3
FK	191	205	172	84	1.9
OK	180	231	184	80	2.7
CP	174	227	152	67	5.0
FP	165	242	156	64	9.0
OP	198	257	180	70	7.3

Figure 8 presents the effect of the variation of the current density on the capacitance of the samples. It can be see that on the one hand that KOH activated carbon shows a good stability of the capacitance with the variation of the current density. Variation indicate good accessibility of the ions into their pore structure. On the contrary, a significant variation in the capacitance value was found for H_3PO_4activated carbons mainly for CP and FP samples, being those, which have the greater ash content. This can be easily understood as follows [39]: firstly, at a low current density, the ions can be transported and diffused into the pores easily. Hence, the capacitance is high. However, when the current density increases, the ion cannot diffuse easily into the pores and especially in the micropores probably due to strong interactions with mineral matter, which results in such a way that the effective ion attachment occurred only at the external surface of the electrode and as consequence the capacitance decreases. This result indicates that the size and the volume of the micropores are very decisive parameters in the application of the activated carbons as supercapacitors and their ash content.

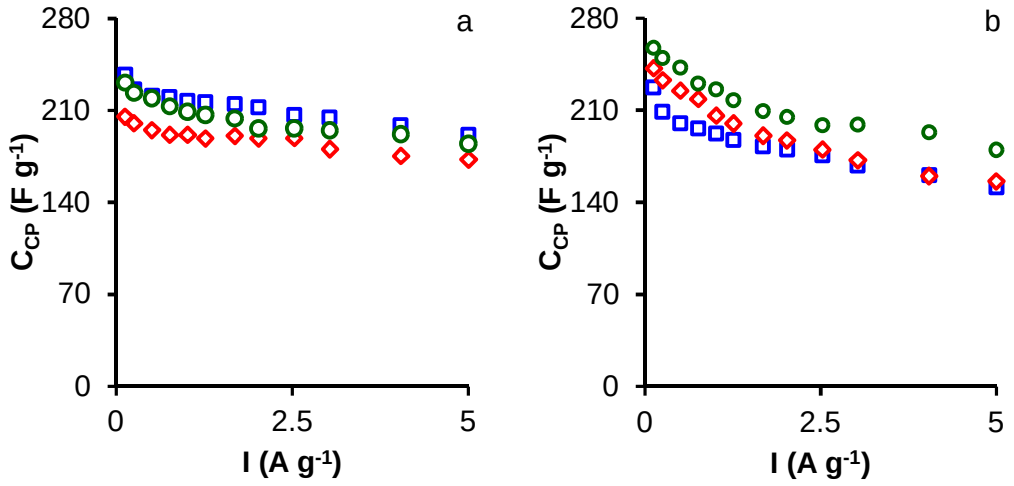

Figure 8. Effect of the current density on the capacitance of the activated carbons in 1M H_2SO_4. a) KOH series, b) H_3PO_4 series. Samples from: olive tree (○); fig tree (◇); custard apple tree (□).

This result is usually due to the increase of ohmic resistance because the presence of micropores and mineral matter that limit the accessibility of the ions to the internal surface of the electrodes [31,40], confirmed with the values of the R_{CP} found for the P series. The dependence of specific capacitance on current density in 1 M H_2SO_4as electrolyte is shown in Table 5. It is noteworthy that the specific capacitances of FP and OP samples dropped down as the current density increased from 0.125 A g^{-1} to 5 A g^{-1}. This is caused by partial inaccessibility of narrow microspores at fast charge/discharge rates (high current densities) [40,41].

The OP sample show a good stability, 70 % of retention capacitance, compared to the FP and OP activated carbons which indicate the stability of the capacitance of the activated not depends only of the micropores structure but also with an adequate mesopore network which favors the exchange of the ions.

In order to identify the origin of the difference between the H_3PO_4 activated carbons behaviors, their surface areas and correspondingly microspore volumes should be taken into account together with the surface chemistries. The main

difference in the surface chemistry of these three samples in comparison to others activated carbons (K series) is the high ash content and the concentration of oxygen groups and specially the acidic group. However, not all surface oxygen functionalities are stable, the deterioration of capacitance are found to be associated with these unstable surface oxygen groups (carboxylic groups COOH and/or chemisorbed O_2/H_2O) [42]. These results indicate that the acidic surface functionalities play a crucial role in deterioration of capacitive properties of carbons at high current density due to ohmic resistance and therefore carbon materials for a practical application in supercapacitors should be rich with the stable oxygen group and low acidic surface groups at the time that the porous structure should be optimized. Finally, we can conclude that these results clearly indicate that activating conditions temperature and activating agent can greatly influence the type of surface chemistry in addition to the various porous structures, and therefore, those two factors are expected to affect the electrochemical performance of activated carbons in different ways.

Another key test of the performance of supercapacitors is the cycling durability. Figure 9 shows the evolution of the capacitance using galvanostatic charge–discharge cycling test at a current density of 1 A g^{-1}. On one hand, the results show that the K series show the best capacitance which is in agreement with the results of the CV and CP in Table 6, on the other, after 12000 cycles, all the samples show highly stable performance and good charge propagation, only samples CP and FP present a slight loss in capacitance due to, as previously commented, their surface chemistry and ash content.

Energy and power densities are two important factors for practical application of activated carbons as electrodes for supercapacitors. Figure 10 shows the variation of the energy density against the power density for all the samples prepared. Generally, for all the sample the energy density decrease with the increase of the power density. From this result, we can say that the K series present a similar behavior independently of the origin of the wood. The variation of the energy is between4 and 2 Wh kg^{-1} at power densities of 47 and 1200 W kg^{-1}

respectively. This results are higher than others showed in previous work. Finally the sample OP showed also very interesting values of energy and power compared to other H_3PO_4 activated samples.

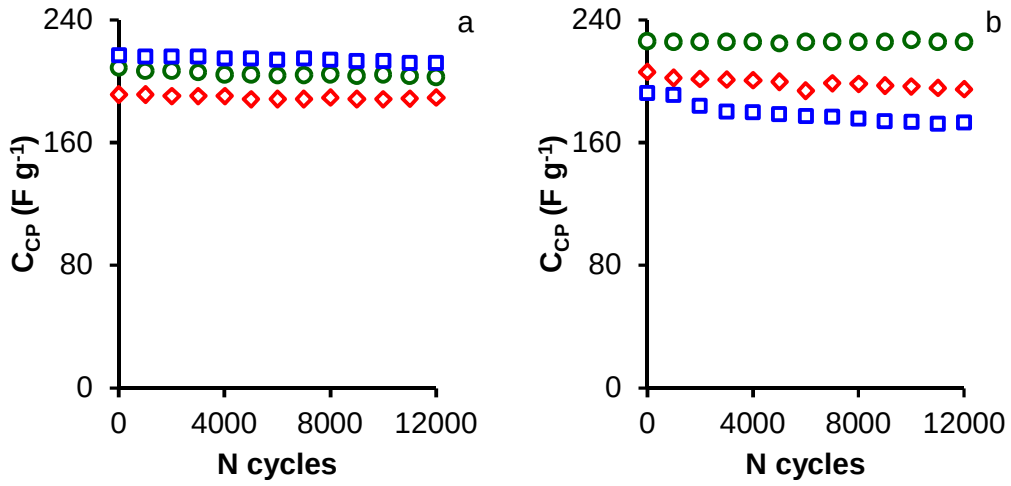

Figure 9: Galvanostatic cycling test at a current load of 1 A g^{-1} within a potential window of 0-0.75 V for 12000 cycles in 1M H_2SO_4. a) KOH series, b) H_3PO_4 series. Samples from: olive tree (○); fig tree (◇); custard apple tree (□).

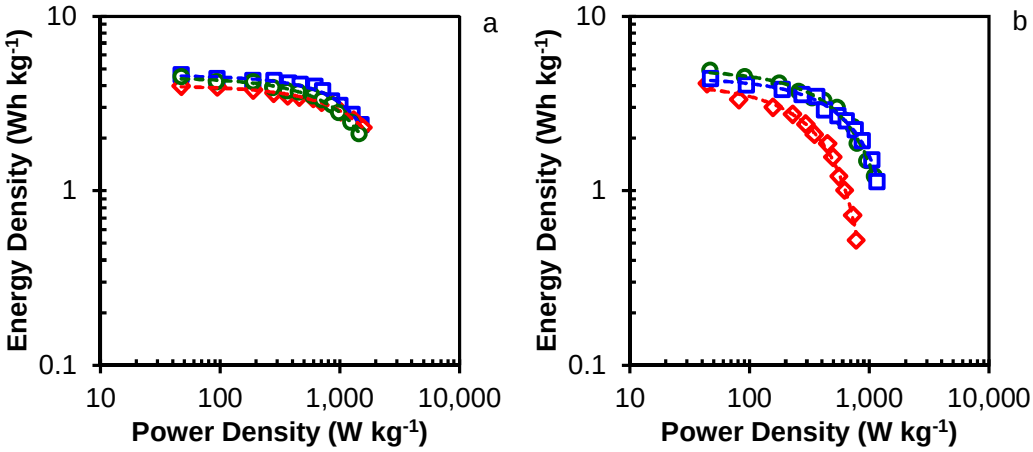

Figure 10. Ragone plot of samples for a) KOH series, b) H_3PO_4 series. Samples from: olive tree (○); fig tree (◇); custard apple tree (□).

5. CONCLUSIONS

Activated carbons based on the KOH and H_3PO_4 activation of wood were prepared. The result shows a very high surface area with a well-developed micro and mesoporosity with different surface function groups.

The electrochemical tests in 1 M H_2SO_4 indicate that the sample prepared from KOH of custard apple had a very good electrochemical characteristics compared to the others carbons with capacitance of 237 F g^{-1} and energy density of 4 Wh kg^{-1} at a power density of 47 W kg^{-1}. In addition the surface chemistry and the pore distribution are very important parameters in the electrochemical application of the carbon. Consequently the H_3PO_4 activated samples show high phosphorous content which improve their electrochemical characteristics but those samples have a lower stability than the KOH activated ones with the current density variation. Exceptionally sample OP showed very interesting stability with high capacity, energy and power densities, which is due to the micro and mesopore volume and to its surface functional groups. The stability of the electrodes against charge-discharge cycles shows that KOH activated carbons have a very good stability whereas H_3PO_4 activation agent leads samples with a poor stability, except in the case of OP sample.

6. REFERENCES

[1] Mahapatra K, Ramteke DS, Paliwal LJ. Production of activated carbon from sludge of food processing industry under controlled pyrolysis and its application for methylene blue removal. Journal of Analytical and Applied Pyrolysis, 95:79-86, (2012).

[2] Grover DP, Zhou JL, Frickers PE, Readman JW. Improved removal of estrogenic and pharmaceutical compounds in sewage effluent by full scale granular activated carbon: Impact on receiving river water. Journal of Hazardous Materials, 185:1005-1011, (2011).

[3] Maldonado-Hodar FJ, Moreno-Castilla C, Carrasco-Marín F, Perez-Cadenas AF. Reversible toluene adsorption on monolithic carbon aerogels. Journal of Hazardous Materials, 148:548-552, (2007).

[4] Ubago-Perez R, Carrasco-Marín F, Fairn-Jiménez D, Moreno-Castilla C. Granular and monolithic activated carbons from KOH-activation of olive stones. Microporous and Mesoporous Materials, 92:64-70, (2006).

[5] Dwivedi CP, Sahu JN, Mohanty CR, Mohan BR, Meikap BC. Column performance of granular activated carbon packed bed for Pb(II) removal. Journal of Hazardous Materials, 156:596-603, (2008).

[6] Mohan D, Singh KP. Single- and multi-component adsorption of cadmium and zinc using activated carbon derived from bagasse an agricultural waste. Water Research, 36:2304-2318, (2002).

[7] Pérez-Cadenas AF, Kapteijn F, Zieverink MMP, Moulijn JA. Selective hydrogenation of fatty acid methyl esters over palladium on carbon-based monoliths: Structural control of activity and selectivity. Catalysis Today, 128:13-17, (2007).

[8] Elmouwahidi A, Zapata-Benabithe Z, Carrasco-Mar+¡n F, Moreno-Castilla C. Activated carbons from KOH-activation of argan (Argania spinosa) seed shells as supercapacitor electrodes. Bioresource Technology, 111:185-190, (2012).

[9] Esfandiari A, Kaghazchi T, Soleimani M. Preparation and evaluation of activated carbons obtained by physical activation of polyethyleneterephthalate (PET) wastes. Journal of the Taiwan Institute of Chemical Engineers, 43:631-637, (2012).

[10] Betancur M, Mart+¡nez JD, Murillo Rn. Production of activated carbon by waste tire thermochemical degradation with CO2. Journal of Hazardous Materials, 168:882-887, (2009).

[11] Castro JB, Bonelli PR, Cerrella EG, Cukierman AL. Phosphoric Acid Activation of Agricultural Residues and Bagasse from Sugar Cane:GÇë

Influence of the Experimental Conditions on Adsorption Characteristics of Activated Carbons. Ind. Eng. Chem. Res., 39:4166-4172, (2000).

[12] Sahu JN, Agarwal S, Meikap BC, Biswas MN. Performance of a modified multi-stage bubble column reactor for lead(II) and biological oxygen demand removal from wastewater using activated rice husk. Journal of Hazardous Materials, 161:317-324, (2009).

[13] Sahu JN, Acharya J, Meikap BC. Optimization of production conditions for activated carbons from Tamarind wood by zinc chloride using response surface methodology. Bioresource Technology, 101:1974-1982, (2010).

[14] Ould-Idriss A, Stitou M, Cuerda-Correa EM, Fernández-González C, Macías-García A, Alexandre-Franco MF, Gómez-Serrano V. Preparation of activated carbons from olive-tree wood revisited. II. Physical activation with air. Fuel Processing Technology, 92:266-270, (2011).

[15] Wu FC, Tseng RL, Juang RS. Preparation of highly microporous carbons from fir wood by KOH activation for adsorption of dyes and phenols from water. Separation and Purification Technology, 47:10-19, (2005).

[16] Wu FC, Tseng RL. Preparation of highly porous carbon from fir wood by KOH etching and CO2 gasification for adsorption of dyes and phenols from water. Journal of Colloid and Interface Science, 294:21-30, (2006).

[17] Dobele G, Dizhbite T, Gil MV, Volperts A, Centeno TA. Production of nanoporous carbons from wood processing wastes and their use in supercapacitors and CO2 capture. Biomass and Bioenergy, 46:145-154, (2012).

[18] J. Gamby, P.L. Taberna, P. Simon, J.F. Fauvarque, M. Chesneau, Studies and characterisations of various activated carbons used for carbon/carbon supercapacitors, J. Power Sources 101 (2001) 109-116.

[19] L. Bonnefoi, P. Simon, J.F. Fauvarque, C. Sarrazin, J.F. Sarrau, A. Dugast, Electrode compositions for carbon power supercapacitors, J. Power Sources, 80 (1999) 149-155.

[20] L. Zhang, X.S. Zhao, Carbon-based materials as supercapacitor electrodes, Chem. Soc. Rev. 38 (2009) 2520-2531.

[21] D. Hulicova-Jurcakova, M. Seredych, G.Q. Lu, T.J. Bandosz, Combined Effect of Nitrogen- and Oxygen-Containing Functional Groups of Microporous Activated Carbon on its Electrochemical Performance in Supercapacitors, Adv. Funct. Mater. 19 (2009) 438-447.

[22] A. Bello, F. Barzegar, D. Momodu, J. Dangbegnon, F. Taghizadeh, N. Manyala, Symmetric supercapacitors based on porous 3D interconnected carbon framework, Electrochim. Acta 151 (2015) 386-392.

[23] Y. Korenblit, M. Rose, E. Kockrick, L. Borchardt, A. Kvit, S. Kaskel, G. Yushin, High-Rate Electrochemical Capacitors Based on Ordered Mesoporous Silicon Carbide-Derived Carbon, ACS Nano 4 (2010) 1337-1344.

[24] Gurvich L.J., Physico-chemical attractive force, Zh. Russ. Fiz-Khim. Obshchestva Chem., 47, 805- 827, (1915)

[25] Romero-Anaya, M. Ouzzine, M.A. Lillo-Ródenas, A. Linares-Solano. Spherical carbons: Synthesis, characterization and activation processes. Carbon, 68, 296-307, (2014)

[26] D.Lozano-Castelló, Linares-Solano A, Shiraishi S, Kurihara H, Oya A. Influence of pore structure and surface chemistry on electric double layer capacitance in non-aqueous electrolyte. Carbon, 41:1765-1775, (2003).

[27] D.Lozano-Castelló, M. A. Lillo-Ródenas A. Linares-Solano. Microporous structure of activated carbons as revealed by adsorption methods. Chemistry and physics of carbon : 1-146, (1988).

[28] D. Hulicova-Jurcakova, M. Seredych, G.Q. Lu, N.K.A.C. Kodiweera, P.E. Stallworth, S. Greenbaum, T.J. Bandosz, Effect of surface phosphorus functionalities of activated carbons containing oxygen and nitrogen on electrochemical capacitance, Carbon 47 (2009) 1576-1584.

[29] J.M. Rosas, R. Ruiz-Rosas, J. Rodríguez-Mirasol, T. Cordero, Kinetic study of the oxidation resistance of phosphorus-containing activated carbons, Carbon 50 (2012) 1523-1537.

[30] A.M. Puziy, O.I. Poddubnaya, R.P. Socha, J. Gurgul, M. Wisniewski, XPS and NMR studies of phosphoric acid activated carbons, Carbon 46 (2008) 2113-2123.

[31] J.M. Rosas, J. Bedia, J. Rodríguez-Mirasol, T. Cordero, HEMP-derived activated carbon fibers by chemical activation with phosphoric acid, Fuel 88 (2009) 19-26.

[32] X. Wu, L.R. Radovic, Inhibition of catalytic oxidation of carbon/carbon composites by phosphorus, Carbon 44 (2006) 141-151.

[33] Kannan AG, Choudhury NR, Dutta NK. Synthesis and characterization of methacrylate phospho-silicate hybrid for thin film applications. Polymer, 48:7078-7086, (2007).

[34] U. Zielke, K.J. Hüttinger, W.P. Hoffman, Surface-oxidized carbon fibers: I. Surface structure and chemistry, Carbon 34 (1996) 983-998.

[35] S. Biniak, G. Szymanski, J. Siedlewski, A. Switkowski, The characterization of activated carbons with oxygen and nitrogen surface groups, Carbon 35 (1997) 1799-1810.

[36] Puziy AM, Poddubnaya OI, Ziatdinov AM. On the chemical structure of phosphorus compounds in phosphoric acid-activated carbon. Applied Surface Science, 252:8036-8038, (2006).

[37] Benadjemia M, Millière L, Reinert L, Benderdouche N, Duclaux L. Preparation, characterization and Methylene Blue adsorption of phosphoric acid activated carbons from globe artichoke leaves. Fuel Processing Technology, 92:1203-1212, (2011).

[38] Moreno-Castilla C. García-Rosero H. Carrasco-Marín F. Symmetric Supercapacitor Electrodes from KOH Activation of pristine, carbonized, and hydrothermally treated Melia Azedarach stones. Materials, 10, 747, (2017).

[39] Huang, Bin, DU, Bing, and ZHAO, Yong. Effect of the Activated Carbon Reactivation on Its Electrochemical Capacitance. Acta Physico-Chimica Sinica 25: 757-761, (2009).

[40] Wang DW, Li F, Liu M, Lu GQL, Cheng HM. 3D Aperiodic Hierarchical Porous Graphitic Carbon Material for High-Rate Electrochemical Capacitive Energy Storage. Angewandte Chemie International Edition, 47:373-376, (2008).

[41] Xing W, Qiao SZ, Ding RG, Li F, Lu GQ, Yan ZF, Cheng HM. Superior electric double layer capacitors using ordered mesoporous carbons. Carbon, 44:216-224, (2006).

[42] Inagaki M, Konno H, Tanaike O. Carbon materials for electrochemical capacitors. Journal of Power Sources, 195:7880-7903, (2010).

CHAPTER VII: *INFLUENCE OF SURFACE CHEMISTRY ON THE ELECTROCHEMICAL PERFORMANCE OF ELECTRODE FROM WASTE WOOD ACTIVATED CARBONS.*

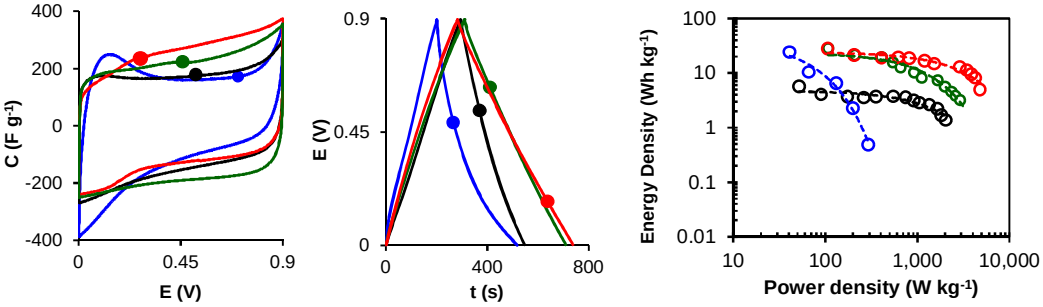

1. ABSTRACT

Three activated carbons prepared by chemical activation from waste wood are treated with four agents, melamine, ammonium carbamate, nitric acid and ammonium persulfate in order to introduce nitrogen and oxygen surface groups on carbon samples. The effect of the surface treatment on the porous structure and the composition of the surface chemistry were studied, the results indicate a large change of the porous structure depending of the type of agent treatment and also the change in the surface chemistry of all samples by introducing a large amount of oxygen 21 wt. % and nitrogen 2.1 wt. % groups. The effect of the presence of nitrogen and oxygen on the electrochemical performance was studied. The results indicate that the presence of the heteroatoms enhances the capacitance, energy density and power density of all samples. For the samples treated with ammonium peroxydisulfate, the sample OKS reached the maximum of capacitance of 312 F g^{-1} while for the melamine, ammonium carbamate and nitric acid treatments, the samples FKM, FKC and FKN reached the maximum capacitances values of 283 F g^{-1}, 280 F g^{-1} and 455 F g^{-1}, respectively. Moreover, the nitrogen doped samples show a good stability at higher current densities and also a higher energy density value at higher power density, on the contrary, the nitric acid oxygenated samples show a fast decrease at higher current density.

Keywords: nitrogen and oxygen doped activated carbon; surface chemistry, Supercapacitor capacitance; energy power density

2. INTRODUCTION

Due to the depleting energy resources and increasing environmental concerns, one of the biggest challenges for researchers is to design high-performance energy storages and conversion devices, such as batteries, fuel cells and supercapacitors, to meet today's power demands [1-3]. Supercapacitors are one of the rechargeable electrochemical energy-storage devices, in that charge carriers migrate reciprocally between electrolytes and electrodes in the processes of charging and discharging. Supercapacitors have high power density, excellent reversibility, and a long life cycle so they are particularly suitable for large-scale applications of portable electronic systems and automotives. However, one of the major barriers of supercapacitors is the relatively low energy density so that efforts are being made in this respect by designing and optimizing the materials for electrodes, which are one of the key components of supercapacitors.

Different types of precursors are used for the preparation of activated carbon from waste agriculture products such as olive stone [4-6], argan shells [7], coconut [8,9], etc, by using different methods of chemical and physical activation [10-13].

For the electrochemical applications, the pore structure, surface chemistry plays a very important key for electrodes with higher electrochemical performance. The capacitive behavior of carbon materials can be further improved by the presence of active species that contribute to the total specific capacitance by the pseudo-capacitive effect [14,15]. In order to further improve the capacitive performance, several studies have found that functional groups containing foreign atoms such as O and N introduced by using methods of dry or wet chemical oxidation, plasma treatment, and electrochemical modifications, are favorable to enhance the capacitance [16-18].

The main aim of the oxidation of a carbon surface is obtaining a more hydrophilic surface structure with groups such as carboxyl groups [19,20]. The presence of oxygenated groups on the surface of the activated carbon most probably affects the capacitance of the materials mainly in improving the wettability

of the material, increasing the capacitance and providing high energy and power densities; and producing pseudo-capacitance effects. Various reagents have been used as oxidizers: concentrated nitric or sulfuric acid, sodium hypochlorite, and permanganate, hydrogen peroxide and ammonium per sulfate.

Furthermore, it has been assumed that nitrogen functionalities change the electron donor/acceptor characteristics of carbon depending on the type of groups formed between the nitrogen and carbon atoms. The nitrogen-containing groups generally provide a basic property, which could enhance the interaction between porous carbon and acid molecules, such as, dipole-dipole, H-bonding, covalent bonding, and so on. The nitrogen groups were introduced by treatment with urea, melamine, nitric acid and some containing nitrogen molecule reaction [14,15,21].

In this work we present the treatment on three types of activated carbon, produced from chemical activation of fig, olive and custard apple waste wood, using four different reagents; nitric acid and ammonium peroxydisulfate for the introduction of oxygen groups, and melamine and ammonium carbamate for the introduction of nitrogen groups on the surface of carbon samples, and finally, the effect of the presence of oxygen and nitrogen on the electrochemical performances of the corresponding electrodes was also studied.

3. EXPERIMENTAL

3.1. Synthesis of modified activated carbons samples

All activated carbon were prepared using the same method from fig, olive and custard apple wood, were chemically activated by using KOH at weight ratio of 1:1 as it was described in the previous Chapter, being the activated carbons (ACs) denoted as FK, OK and CK, respectively. FK original activated carbon was treated with two oxidative agents for the introduction of oxygen groups, nitric acid and sodium peroxidisulfate, and with ammonium carbamate and melamine for the introduction of nitrogen groups. Samples CK and OK were oxidized with sodium

persulfate in order to evaluate the influence of oxygen surface groups in the three samples with different pore structure.

The treatment with nitric acid was carried out with 1 M diluted nitric acid at boiling temperature for 2 hours. The oxidized FKN were washed with distillated water until the absence of nitrates.

The treatment with ammonium peroxydisulfate $(NH_4)_2S_2O_8$ to introduce surface oxygen functionalities was performed as reported by Moreno-Castilla [22]. In details, the treatment was carried out with a saturated solution of this salt in H_2SO_4 1 M (1 g of carbon/10 mL of solution) at 298 K for 48 h. After the treatment, the ACs were washed with distilled water until the absence of sulfates was reached. The prepared samples were denoted FKS, OKS, and CKS.

The treatment with melamine was conducted by mixing 0.5 g of activated carbon with 33 mg of melamine dissolved in 20 mL of ethanol as described in a previous work [7]. After stirring this slurry, the solvent was slowly evaporated and the remaining residue was heat-treated at 750 ºC for 1 h under N_2 flow (60 cm^3 min^{-1}). The corresponding sample was denoted FKM.

Finally, the introduction of the nitrogen functionality by using ammonium carbamate was carried by mixing 2 g of ammonium carbamate and 2 g of activated carbon in 20 ml of distillated water. After stirring the slurry it was dried at 100 °C and the residue was heated at 550 ºC for 1 h, and 600 ºC for 1 h, both under N_2 flow (60 cm^3 min^{-1}). The prepared samples were denoted as FKC.

3.2. Textural and chemical characterization

Textural characterization was carried out by N_2 and CO_2 adsorption at −196 ºC and 0º C, respectively, using Quanta chrome Autosorb-1 equipment. The BET and Dubinin–Radushkevich equations were applied to determine the apparent surface area (S_{BET}) and the micropore volume (W_0), the mean micropore width (L_0) and the microporous surface (S_{mic}), respectively. The total pore volume was considered as the volume of N_2 adsorbed at $P/P_0 = 0.95$.

The surface chemistry of activated carbons was studied by a programmed temperature desorption coupled with mass spectrometry (TPD) and X-ray photoelectron spectroscopy (XPS) was performed using an Escalab 200R system (VG Scientific Co.) equipped with MgKa X-ray source ($h\upsilon$ = 1253.6 eV) and hemispherical electron analyzer. Survey and multi-region spectra were recorded at C1s, O1s, and N1s photoelectron peaks. Each spectral region of photoelectron interest was scanned several times to obtain good signal-to-noise ratios. The C1s peak at 284.6 eV was used as reference.

3.3. Electrochemical Characterization

The electrochemical measurements were carried out in a two electrodes system using an EC-lab VMP system (Biologic) at 25 °C with H_2SO_4, 1 M as electrolyte and glass fibrous material as a separator. The working electrodes were two 5 mm in diameter graphite discs, identical in size and weight (22 mg cm^{-2}), on which 3.3 mg of a homogeneous mixture of 90 % of carbon sample and 10 % of PTFE binder (60 % suspension in water), previously dried overnight at 100 °C, was pasted by pressure at 5 bars. The graphitic electrodes prepared like this were impregnated with the respective electrolyte for 48 h before electrochemical measurements. Prior to the electrochemical measurements, the voltage window in each electrolyte was calculated by cyclic voltametry. These voltage windows were 0 V - 0.9 V in H_2SO_4, 1 M. Cyclic voltametry in the voltage interval of each electrolyte was performed at different scan rates (0.5, 2.5, 5, 10 and 20 mVs^{-1}) and the gravimetric capacitance, C_{CV} (F/g), was calculated using the following Equation [23,24] :

$$C_{CV} = 4\frac{\sum |I|\Delta t}{m\Delta V}$$

where I was the area of the current (A) against time (s) curve, m was the total mass of active sample in both two electrode (g), ΔV the voltage window (V) and the 4 factor traduces the relation between single electrode capacitance and cell capacitance. Typically, the specific capacitance for one single electrode C_{one} ($F\ g^{-1}$) is calculated according to $C_{one} = 4\times C$ where C is the specific cell capacitance for

the two-electrode supercapacitor calculated from the CV curve or charge–discharge curve. The galvanostatic charge-discharge analyses were obtained at different current densities from 0.125 A g^{-1} to 10 A g^{-1} in a voltage interval 0 V - 0.9 V. The gravimetric capacitance from these measurements, C_{GD} (F g^{-1}), was calculated by the following Equation [23,24]:

$$C_{GD} = 4\frac{I_d \Delta t}{m \Delta V}$$

where I_d was the current density (A/g), Δt the discharge time (h), ΔV the voltage interval without the IR drop and m was the total mass of active sample (g). The impedance spectroscopy measurements were carried out from a frequency of 1 mHz to 100 kHz with a sinusoidal signal amplitude of 10 mV. The capacitance value, C_{max}, was obtained by the following Equation [23,24].

$$C_{max} = \frac{-Z''}{2\pi f |Z|^2}$$

where f was the frequency and $|Z|^2 = |Z'^2| + |Z''^2|$, where Z' and Z" are the real and imaginary parts of the complex impedance, respectively [23,24].

The electrical energy and the power density were calculated by using the Equations for two-electrode cell [23,24]:

$$E\,(Wh\,kg^{-1}) = \frac{C_{GD}\,(F\,g^{-1}) \times \Delta V^2(V)}{2 \times 3.6}$$

$$P\,(W\,kg^{-1}) = \frac{1}{2} \times \frac{I(A) \times \Delta V(V)}{m\ (kg)}$$

4. RESULTS AND DISCUSSION

4.1. Structural and textural characterization

Table 1 shows the characterization data obtained from N_2 adsorption - desorption isotherms and CO_2 adsorption; the results indicate a change after the modification with different treatments for the introduction of oxygen and nitrogen functionalities.

Table 1. Textural characteristics of modified activated carbons

Sample	S_{BET} m^2/g	$W_0(N_2)$ cm^3/g	$L_0(N_2)$ nm	V_{total} cm^3/g	V_{MESO} cm^3/g	$W_0(CO_2)$ cm^3/g	$L_0(CO_2)$ nm
CK	1480	0.52	1.02	0.85	0.33	0.38	0.72
CKS	1042	0.41	1.16	0.54	0.13	0.32	0.61
FK	1237	0.44	0.83	0.58	0.14	0.35	0.65
FKM	1575	0.63	1.26	0.80	0.17	0.35	0.67
FKC	1669	0.67	1.28	0.84	0.17	0.36	0.69
FKN	987	0.35	1.40	0.47	0.12	0.24	0.71
FKS	1114	0.44	1.36	0.59	0.15	0.32	0.62
OK	1352	0.52	0.82	0.72	0.20	0.34	0.68
OKS	1075	0.42	1.30	0.58	0.16	0.25	0.61

From data in Table 1 it can be show that oxidation of the activated carbons with ammonium peroxydisulfate induce a decrease in the surface area of the raw material as well as in the pore volumes. The treatment with melamine and ammonium carbamate increase the surface area and also the pore volume increases which can be due to the thermal treatment at high temperature produce the fixation of N surface groups brought about an increase in the pore diameter and an opening of some porosity. Furthermore all samples show an increase of the micropore diameter indicating a destruction or fusion of the microporous

structure. For all samples, $W(N_2)$ is higher than $W(CO_2)$ indicating the absence of constriction at the micropores entrances and total accessibility of N_2 molecule at -196 ºC. The results of the oxidation in the treatment with ammonium peroxydisulfate indicate a decrease in the surface area, the mesoporous and microporous volume, and the mesoporous and microporous diameter by partially destruction of the micro and mesopore walls. The oxidation with nitric acid produces the destruction of the pore structure inducing an increase in the mesopore and microporous width and a decrease in the pore volumes. Furthermore the ammonium peroxydisulfate treated samples presents a very similar surface area and pore structure.

All activated carbon samples were characterized by TPD experiments. Table 2 contains the quantification of the amount of CO and CO_2 desorbed in these experiments, as well as the results for the analysis of the surface chemistry obtained from high resolution XPS. The results of the TPD indicate that samples with a wide range of surface oxygen groups are available being, in all the cases, the CO evolved is lower than the CO_2. The treatment with $(NH_4)_2S_2O_8$ on the three activated carbons produced similar total oxygen contents, O_{TPD}, and CO/CO_2 ratios. The two oxidation treatments provoked the much higher amounts of oxygen, which varying from 14.1 - 25.4 wt. %.

Table 2. Chemical characteristics of the samples from XPS and TPD experiments.

Sample	O_{XPS} wt. %	N_{XPS} wt. %	O_{TPD} wt. %	CO mmol g^{-1}	CO_2 mmol g^{-1}	CO/CO_2
CKS	15.3	0.9	14.1	0.87	3.96	0.22
FKM	1.8	2.1	1.1	0.19	0.23	0.83
FKC	4.3	0.7	2.1	0.48	0.42	1.14
FKN	19.9	0.9	25.4	1.22	7.32	0.17
FKS	15.8	0.5	15.2	0.94	4.26	0.22
OKS	14.6	0.2	14.4	0.89	4.02	0.22

Sample FKN treated with nitric acid has lower oxygen content in the external surface than the internal one, while samples CKS, FKS and OKS show a quite homogeneous distribution of the surface oxygen groups throughout the internal and the external surface of the sample, since the O_{TPD} and O_{XPS} values are reasonable similar. The CO/CO_2 ratio in the oxidized samples was lower than for the rest due to that the oxidation mainly increased the amount of CO_2-evolving groups such as carboxyl acid groups, which are known to increase during peroxydisulfate treatment [22]. This increase in the oxygen surface functionalities is accompanied by a decrease of the hydrophobicity as a consequence of the fixation of oxygen functionalities with large polarity, e.g., carboxyl groups. The surface oxygen groups on carbon materials decompose upon heating, producing CO and CO_2 at different temperatures. It is known that CO_2 evolves at low temperatures as a consequence of the decomposition of the acidic groups such as carboxylic groups or lactones [25]. The evolution of CO occurs at higher temperatures and is originated by decomposition of basic or neutral groups such as phenols, ethers and carbonyls.

The treatment of the activated samples with melamine and ammonium carbamate increased the N content, which was distributed across pyridinic (N-6), pyrrolic, and/or pyridonic (N-5) and quaternary-N (N-Q) groups [21]. The treatment greatly increased the amount of N-6 and N-Q functionalities. The results indicate that the melamine treatment gives more nitrogen contents than the ammonium carbamate and also that samples treated with ammonium carbamate show higher oxygen contents in the surface than that treated with melamine.

The deconvolution of the C_{1s}, O_{1s}, N_{1s} and S_{2p} spectral regions and their corresponding peaks fitting showed the presence of diverse contributions to BEs displayed in Table 3 together with their corresponding percentages. The C_{1s} spectrum for the all the modified activated carbon shows two main peaks centered at 284.6 and close to 286.0 eV corresponding to C=C and C-O bonds [26-28]. After the oxygen treatment, oxygenated samples show the presence of two others peaks around 287.0 and 288.5 eV introduced on the carbon surface indicating the

presence of C=O and O-C=O [26-28]. The main increase took place for the peak centered at BE ≈ 288.5 eV which corresponds to the presence of carboxylic groups and indicating a significant amount of oxygen-containing groups.

The results corresponding to the decomposition of the spectra O_{1s} is presented in the Table 3, it shows the presence of two different regions, with peaks at 530 - 531.8 eV which corresponds to the presence of the oxygen double bonded C=O groups. The peak around 533 eV indicates the presence of the single bonded oxygen (-O-) in C-O [26-28].

Table 3: Results obtained from the deconvolution of high resolution XP spectra

Sample	O_{1s} (eV)	Peak (%)	N_{1S} (eV)	Peak (%)	$S_{2p3/2}$ (eV)
CKS	531.6	39			168.6
	533.0	61			
FKM	531.4	38	398.7	49	
	533.0	62	400.2	35	
			401.3	15	
FKC	531.4	41	398.8	46	
	533.2	59	400.2	37	
			401.2	18	
FKN	531.5	39	398.7	30	
	533.1	61	401.2	32	
			404.4	38	
FKS	531.5	35			168.5
	533.0	65			
OKS	531.5	40			168.4
	533.0	60			

The chemical state of nitrogen present in the treated sample with melamine and ammonium carbamate is further discussed on the basis of the XPS results. The fitting of the peaks shows the existence of three contributions at binding energies of 398.7, 400.2 and 401.3 eV. These peaks can be assigned to pyridine, N6, (398.5 eV), pyridine and pyrrolic nitrogen, N5, (400.0 eV) and quaternary nitrogen, NQ, (401.2 eV) respectively, and in the case of nitric acid sample it appears the oxidized nitrogen, NX, (404.4 eV), [29-31]. The nitric oxidized samples show peaks at higher BE = 404.4 eV corresponding to the presence of nitrate. The

samples treated with ammonium peroxydisulfate have some content of sulphur species as sulphonic groups and sulfates as denoted with the peak centered at 168.5 eV.

4.2. Electrochemical Characterization

The electrochemical characterization was evaluated in sulfuric acid 1 M with a two electrode systems. Figure 1 shows, as an example, the CV curves of all the electrodes of FK treated samples between 0 and 0.9 V at the scan rate of 0.5 mV s^{-1}. It can be see that the sample FKM, FKC and FKS show a quasi-rectangular shape, which is a feature of electrochemical double-layer capacitors. On the contrary, the sample FKN shows a non-rectangular shape due to the effect of the oxygen groups present at higher content, indicating the pseudo capacitive effect of oxygen functional groups in the surface of the sample FKN. So, the nitric acid treatment produces a pseudo capacitive effect due to the high content of oxygen fixed while the other treatments indicate the formation of ideal double layer capacitors.

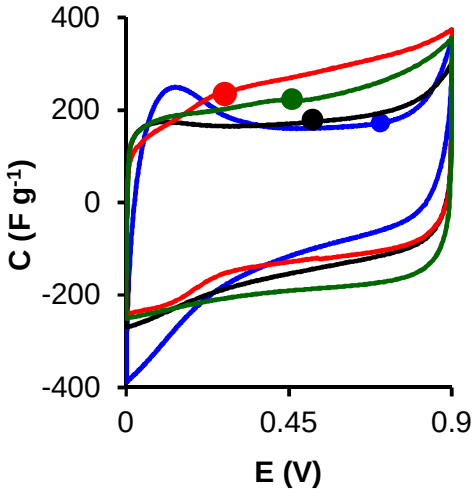

Figure 1. Cyclic voltammograms at 0.5 mV s^{-1} for samples in H_2SO_4 1M: ●, FKM; ●, FKC; ●, FKN; ●, FKS.

Figure 2 shows the the corresponding galvanostatic charge discharge curves for all the samples, it is clear that the curves of all oxidized samples exhibit a slight distorted triangular shape, which is caused by the pseudo-capacitive behavior of the oxygen-containing functional groups. This distortion was more significant for the nitric acid treated sample. On the contrary, the nitrogen doped samples show a symmetric triangular shape indicating a good diffusion inside the pore structure. The plots for the variation of specific capacitance versus current density for all samples have been collected in Figure 3 in order to study the performance of the modified activated carbons.

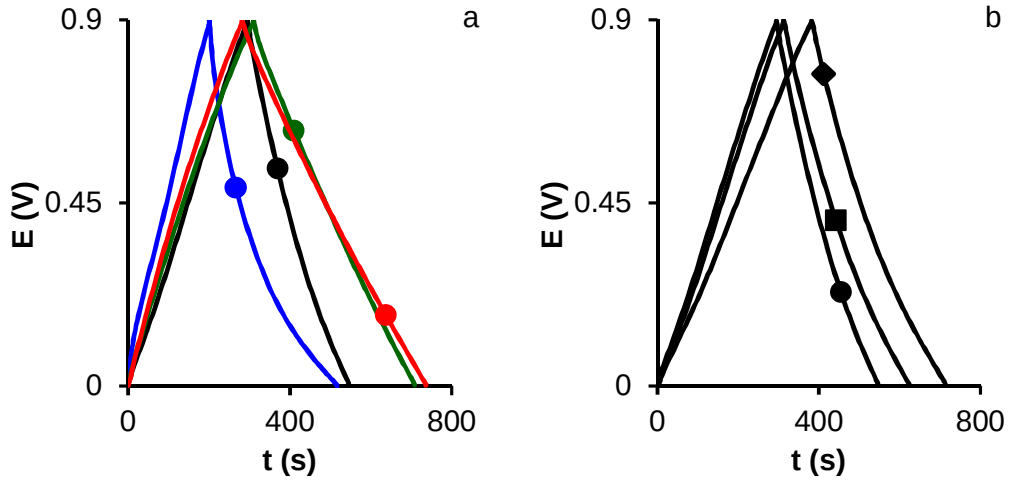

Figure 2. Galvanostatic charge discharge curves at 125 mA g^{-1} for all modified samples a) FK modified samples b) peroxidisulfate oxidized samples, ■, CKS; ●, FKS; ◆, OKS. red, melamine; green, ammonium carbamate; blue, nitric acid; and black, ammonium persulfate.

Results showed that all the treatment processes given to the original samples induce a good stability at high current density, up to 10 A g^{-1}, except for the sample treated with nitric acid which present a lower stability and a fast decrease of the capacitance with the increasing of the current density, furthermore, the nitric acid treated samples present the higher specific capacitance at current density of 125 mA g^{-1} (455 F g^{-1}), Table 4. On the other hand, it is found that the

samples oxidized by ammonium persulfate show the largest specific capacitances at current densities between 125 mA g^{-1} and 10 A g^{-1} for all modified samples except for olive samples at higher current densities. The maximum specific capacitance of 312 F g^{-1} was attained at a current density of 125 mA g^{-1} for OKS, which is much higher than those of FKS (237 F g^{-1}) and CKS (290 F g^{-1}). Remarkably, the specific capacitance of ammonium persulfate treated samples cannot still be maintained at high current densities which is due to the effect of the oxygen functionalities. The retention ratio of those samples from 125 mA g^{-1} to 10 A g^{-1} was between 32 % and 60 %.

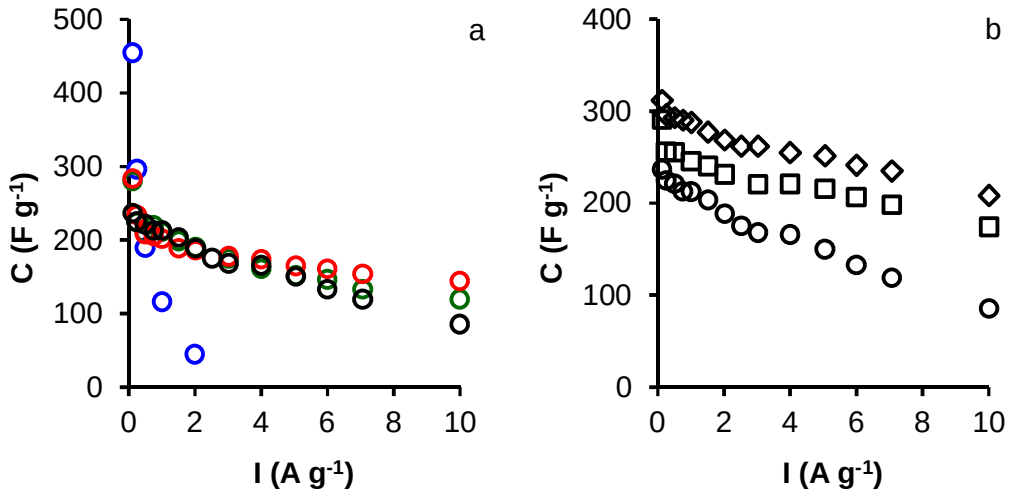

Figure 3. Variation of the specific capacitance with current density in H_2SO_4 1 M a) FK modified samples b) peroxidisulfate oxidized samples, □, CKS; ○, FKS; ◇, OKS. red, melamine; green, ammonium carbamate; blue, nitric acid; and black, ammonium persulfate.

Results confirm that the increased amount of mesopores and the introduction of abundant oxygen-containing groups are effective improving the electrolyte accessibility, leading to a fast ion response and high capacitance. Also the presence of surface quinone groups increases the capacitance of oxidized activated carbons by introducing pseudo-capacitance effects; however, the oxidation also fixes other surface oxygen complexes such as carboxyl groups

which, due to their high polarity, bind water molecules that hinder and retard the electrolyte diffusion into the microporosity, thereby increasing its ohmic resistance [32].

Table 4. Electrochemical capacitances of modified activated carbons in H_2SO_4 1 M. Retention capacitance at 10 A g^{-1}.

Sample	C_{CV} 0.5 mvs^{-1}	C_{CP} 125 mAg^{-1}	C_{CP} 2 Ag^{-1}	C_{CP} 10 Ag^{-1}	Retention (%)
CKS	180	290	231	174	60
FKM	200	283	186	144	51
FKC	210	280	190	119	43
FKN	169	455	20	-	10
FKS	171	237	189	85	36
OKS	218	312	268	188	60

The nitric acid treated sample shows a fast deceasing in the capacitance at higher current densities due to the destruction of the pore structure and also to the higher values of oxygen present in the surface functionalities of the treated sample.

It is known that the increase in the population of the CO-desorbing complexes can have a positive effect on the capacitance, while the CO_2-desorbing complexes show a negative effect in the double-layer formation. Upon heat-treating the oxidized carbon, most of the CO_2-desorbing complexes were removed while the population of CO-desorbing complexes reached a maximum. This treatment has produced electrodes with the highest capacitance. Cyclic voltametry showed that the presence of the CO desorbing complexes significantly enhanced the double-layer formation and thus the capacitance. This indicates that due to the local changes of the electronic charge density, a proton adsorbed by a carbonyl or quinone-type site facilitates an excess specific double-layer capacitance. The

faradic current increased with the total number of oxygen atoms on the surface, indicating than both the CO- and CO_2-desorbing complexes enhanced the redox process.

It has been reported that surface N functionalities (e.g., pyridinic, pyrrolic and pyridonic nitrogen) are electrochemically active because they are electron-rich [33,34]. Protons can therefore be attracted to the electrode surface, giving rise to pseudo-capacitive interactions [35]. For the melamine nitrogen doped samples, the result indicates that the sample FKM presents a high capacitance 283 F g^{-1}. For the ammonium carbamate modified sample, FKC, the nitrogen content 0.8%, is lower than for FKM, 2.1 %. Thus, the difference of the capacitance and the electrochemical performance can be explained by the difference of the porous structure. The results (Table 4) indicate that the sample FKC has a similar capacitance than FKM 280 and 283 F g^{-1}, respectively; those samples present a capacitance retention at current density of 10 A g^{-1} comparing to 0.125 mA g^{-1} varying from 43 % for FKC to 51 % for FKM. These differences are due in part to the pore structure and also to the difference of the nitrogen and oxygen functionalities. It is known that the presence of oxygen in the surface chemistry can affect the capacitance retention especially at high current densities.

Finally, from all the results can be deduced that the specific high capacitance and excellent performance rate could be attributed to the following reasons: (i) the high surface area provides a large adsorption interface for the electrolyte to form the EDL, leading to a great electrochemical double layer capacitance. (ii) The introduction of hetero-atoms containing groups can improve the wettability of carbon samples in aqueous electrolyte. They can not only increase the accessibility of electrolyte ions to make full use of the surface area but also provide a considerable pseudo-capacitance to enhance the overall capacitance.

The resistance of all modified samples was measured by using electrochemical impedance spectroscopy. The Nyquist plots are shown in Figure 4, measured over the frequencies ranging from 0.01 to 100 kHz. For each

electrode, there is a depressed arc in high frequency ranges, and an inclined line in low frequency ranges. The intersection point with the real axis in the high-frequency range is the equivalent series resistance (ESR), which includes the ionic resistance of the electrolyte, the intrinsic resistance of the active material, and the contact resistance at the electrode/current collector interface. It is suggested that the diameter of the semicircles represent the faradic charge transfer resistance (R_{CT}) at the interface between the current collector and the active material. At the low-frequency range, a straight inclined line represents the diffusive resistance (Warburg's impedance) of the electrolyte [36].

The ESR values are similar for samples containing nitrogen surface groups. This indicate that the resistance to the ions mobility is not modified by the treatment with melamine or ammonium carbamate. Similar results are obtained for all the oxidized samples with ESR varying from 0.54 to 0.63 Ω. These values are higher than the corresponding ones for nitrogen enriched samples and point out the increase in the electrical resistance of the oxidized activated carbons.

The charge transfer resistances (R_{CT}) of nitrogen enriched samples are 1.37 Ω for FKM and 2.00 Ω for FKC. The semicircles represent the faradic charge transfer resistance (R_{CT}) of electrodes in H_2SO_4 electrolyte can be hardly seen, indicating a fast ion diffusion and low impedance on the electrode/electrolyte. Those low resistances are due to the low change in the pore structure after the melamine and ammonium carbamate treatments. On the contrary, the oxygenated samples show a higher internal resistance compared to nitrogenated ones. This higher resistance could be due to the intereactions between the strong acidic surface groups introduced by oxidation treaments with the solvated ions and to the modifications in the pore structure resultants from these treatments. In addition, all curves show a Warburg angle higher than 45°, indicating the suitability of the electrode materials for supercapacitors.

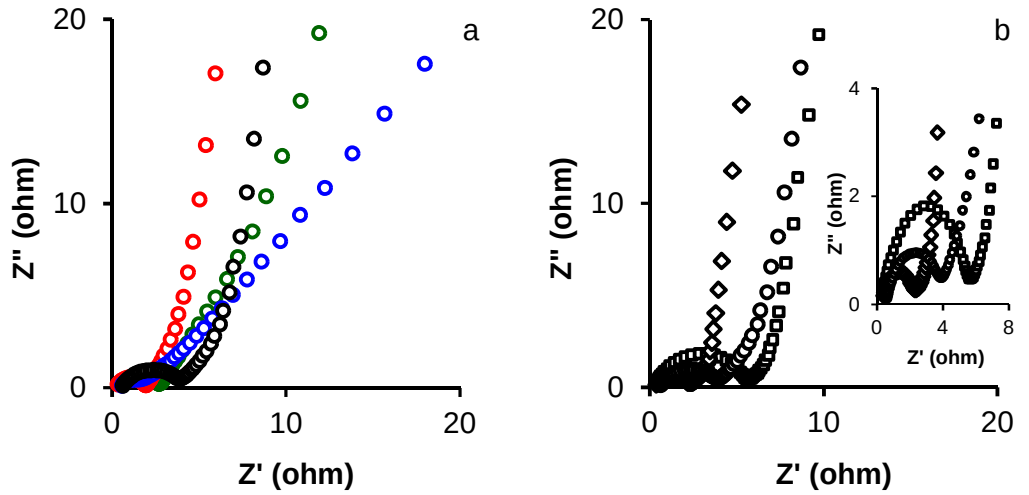

Figure 4. Nyquist plots obtained from EIS experiments on H_2SO_4 1M a) FK modified samples b) peroxidisulfate oxidized samples, □, CKS; ○, FKS; ◇, OKS. red, melamine; green, ammonium carbamate; blue, nitric acid; and black, ammonium persulfate.

Table 5. Equivalent series resistance (ESR), charge transfer resistance (R_{CT}), and C_{max} at 1 mHz, from EIS.

Sample	ESR (Ω)	R_{CT} (Ω)	τ s	C_{max} F g^{-1}
CKS	0.54	5.09	4.6	181
FKM	0.35	1.37	1.1	203
FKC	0.36	2.00	2.6	198
FKN	0.57	3.95	9.4	173
FKS	0.63	3.11	4.4	176
OKS	0.58	2.79	3.8	221

The relaxation time constant (τ) can be calculated by the equation $\tau = 1/(2\pi \times f_0)$, where f_0 is the transition frequency between a pure capacitive and a pure resistive behavior that can be obtained from the maximum within the variation of the imaginary part of the capacitance (C'') against the frequency. The relaxation time constant is a quantitative measure of the speed with which the device can be discharged. Results in Table 5 show that nitrogen doped samples present the faster discharging time compared to the oxygenated ones, and that the acid nitric treated sample present the higher discharge time due to the ions interactions with strong acidic surface groups.

The Ragone plots of the ACs are displayed in Figure 5 and the maximum and minimum energies and power densities are shown in Table 6.

The maximum energy density value reached was 28.34 Wh kg^{-1} for sample FKC, moreover all the treated samples show a maximum energy density value larger than that reported for most of the commercially available supercapacitors (< 10 Wh kg^{-1}) [37]. The energy released decreases at higher power density (Figure 5); but the energy densities of nitrogen doped samples were acceptable at higher power density showing a ver high stability. It is interesting to note that all samples treted with $(NH_4)_2S_2O_8$ present a very similar behavior due to the similarity in pore size distribution and in surface chemistry for this samples.

The long-term stability of electrodes is a key factor that limits the application of carbon materials as supercapacitors for practical applications. The stability of electrodes was evaluated by 2500 galvanostatic charge-discharge. Figure 6 presents the variation in the gravimetric capacitance with the number of charge-discharge cycles at a constant current density of 1 A g^{-1} employing $H_2SO_4$1 M as electrolyte. After 2500 cycles the retention capacity for the all modified samples are between 97.0 %, and 100 %.

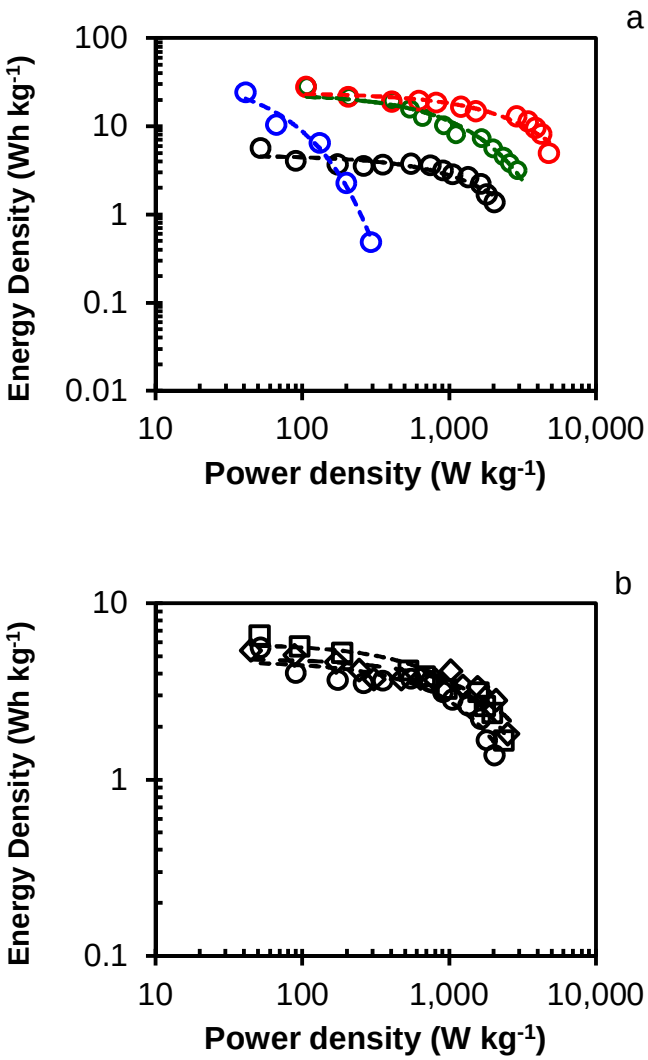

Figure 5. Ragone plots on H_2SO_4 1M for a) FK modified samples b) peroxidisulfate oxidized samples, □, CKS; ○, FKS; ◇, OKS. red, melamine; green, ammonium carbamate; blue, nitric acid; and black, ammonium persulfate.

Table 6. Maximum and minimum energy densities (Wh kg^{-1}) and power densities (W kg^{-1}) of samples from Ragone's plots

Sample	P_{max} W kg^{-1}	E_{min} Wh kg^{-1}	P_{min} W kg^{-1}	E_{max} Wh kg^{-1}
CKS	2360	1.67	51	6.57
FKM	4793	4.90	106	27.76
FKC	2920	3.15	108	28.34
FKN	294	0.48	41	24.07
FKS	2040	1.38	52	5.61
OKS	2506	5.90	45	5.41

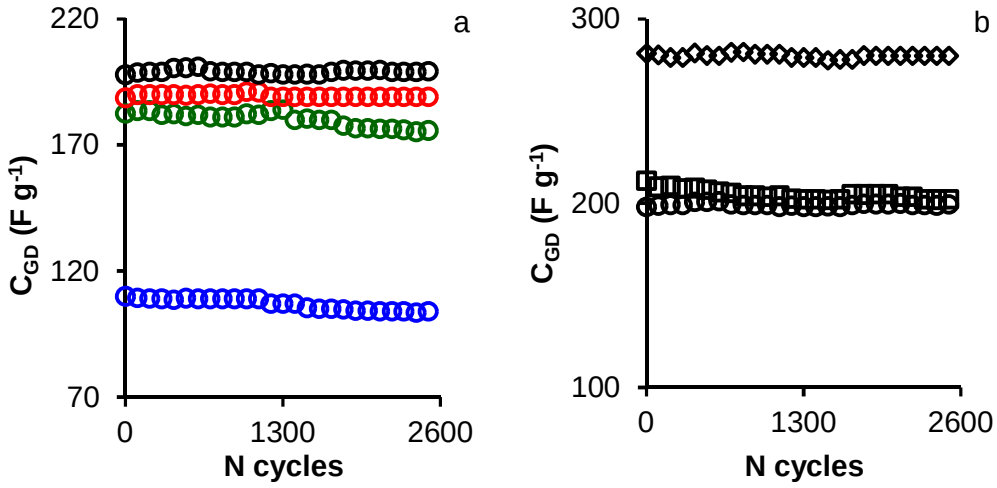

Figure 6. Variation of the gravimetric capacitance (C_{GD}) with the number of charge discharge cycles at 1 A g-1 in the potential window between 0 and 0.9 V in H2SO4 1M for samples a) FK modified samples b) peroxidisulfate oxidized samples, □, CKS; ○, FKS; ◇, OKS. red, melamine; green, ammonium carbamate; blue, nitric acid; and black, ammonium persulfate.

5. CONCLUSIONS

Treatments introduce different nitrogen functionalities as pyridine quaternary-N and oxidized nitrogen which improve the wettability and the ions transfers. The specific high capacitance and excellent performance rate could be attributed to the following reasons: (i) the high surface area provides a large adsorption interface for the electrolyte to form the EDL, leading to a great electrochemical double layer capacitance. (ii) The introduction of hetero-atoms containing groups can improve the wettability of carbon samples in aqueous electrolyte. The maximum energy density value reached was 28.34 Wh kg^{-1} for sample FKC, moreover all the treated samples show a maximum energy density value larger than that reported for most of the commercially available supercapacitors (< 10 Wh kg^{-1}). After 2500 cycles the retention capacity for the all modified samples are between 97.0 %, and 100 %.

6. REFERENCES

[1] Luo X, Wang J, Dooner M, Clarke J. Overview of current development in electrical energy storage technologies and the application potential in power system operation. Applied Energy 2015;137:511-536.

[2] Faraji S, Ani FN. The development supercapacitor from activated carbon by electroless plating-A review. Renewable and Sustainable Energy Reviews 2015;42:823-834.

[3] Weinstein L, Dash R. Supercapacitor carbons. Materials Today 2013;16(10):356-357.

[4] Yakout SM, Sharaf El-Deen G. Characterization of activated carbon prepared by phosphoric acid activation of olive stones. Arabian Journal of Chemistry 2016;9, Supplement 2:S1155-S1162.

[5] Ubago-Perez R, Carrasco-Marin F, Fairen-Jimenez D, Moreno-Castilla C. Granular and monolithic activated carbons from KOH-activation of olive stones. Microporous and Mesoporous Materials 2006;92(1):64-70.

[6] Moreno-Castilla C, Carrasco-Marin F, Lopez-Ramon MV, Alvarez-Merino MA. Chemical and physical activation of olive-mill waste water to produce activated carbons. Carbon 2001;39(9):1415-1420.

[7] Elmouwahidi A, Zapata-Benabithe Z, Carrasco-Marin F, Moreno-Castilla C. Activated carbons from KOH-activation of argan (Argania spinosa) seed shells as supercapacitor electrodes. Bioresource Technology 2012;111:185-190.

[8] Yin L, Chen Y, Zhao X, Hou B, Cao B. 3-Dimensional hierarchical porous activated carbon derived from coconut fibers with high-rate performance for symmetric supercapacitors. Materials & Design 2016;111:44-50.

[9] Arena N, Lee J, Clift R. Life Cycle Assessment of activated carbon production from coconut shells. Journal of Cleaner Production 2016;125:68-77.

[10] Contreras MS, Paez CA, Zubizarreta L, Leonard A, Blacher S, Olivera-Fuentes CG, Arenillas A, Pirard JP, Job N. A comparison of physical activation of carbon xerogels with carbon dioxide with chemical activation using hydroxides. Carbon 2010;48(11):3157-3168.

[11] Demiral H, Demiral I, Karabacakoglu B, Tumsek F. Production of activated carbon from olive bagasse by physical activation. Chemical Engineering Research and Design 2011;89(2):206-213.

[12] Hayashi Ji, Kazehaya A, Muroyama K, Watkinson AP. Preparation of activated carbon from lignin by chemical activation. Carbon 2000;38(13):1873-1878.

[13] Juan Y, Ke-Qiang Q. Preparation of activated carbon by chemical activation under vacuum. Environmental Science & Technology 2009;43(9):3385-3390.

[14] Hou S, Wang M, Xu X, Li Y, Li Y, Lu T, Pan L. Nitrogen-doped carbon spheres: A new high-energy-density and long-life pseudo-capacitive electrode material for electrochemical flow capacitor. Journal of Colloid and Interface Science 2017;491:161-166.

[15] He D, Niu J, Dou M, Ji J, Huang Y, Wang F. Nitrogen and oxygen co-doped carbon networks with a mesopore-dominant hierarchical porosity for high energy and power density supercapacitors. Electrochimica Acta 2017;238:310-318.

[16] Shen HH, Hu CC. Capacitance Enhancement of Activated Carbon Modified in the Propylene Carbonate Electrolyte. Journal of The Electrochemical Society 2014;161(12):A1828-A1835.

[17] Kakhki RMZ, Heydari S. A simple conductometric method for trace level determination of brilliant green in water based on +¦-cyclodextrin and silver nitrate and determination of their thermodynamic parameters. Arabian Journal of Chemistry 2014;7(6):1086-1090.

[18] Zhang Y, Li X, Huang J, Xing W, Yan Z. Functionalization of Petroleum Coke-Derived Carbon for Synergistically Enhanced Capacitive Performance. Nanoscale Research Letters 2016;11(1):163-

[19] Leng C, Sun K, Li J, Jiang J. The reconstruction of char surface by oxidized quantum-size carbon dots under the ultrasonic energy to prepare modified activated carbon materials as electrodes for supercapacitors. Journal of Alloys and Compounds 2017;714:443-452.

[20] Li J, Liu W, Xiao D, Wang X. Oxygen-rich hierarchical porous carbon made from pomelo peel fiber as electrode material for supercapacitor. Applied Surface Science 2017;416:918-924.

[21] Pels JR, Kapteijn F, Moulijn JA, Zhu Q, Thomas KM. Evolution of nitrogen functionalities in carbonaceous materials during pyrolysis. Carbon 1995;33(11):1641-1653.

[22] Moreno-Castilla C, Ferro-Garcia MA, Joly JP, Bautista-Toledo I, Carrasco-Marin F, Rivera-Utrilla J. Activated carbon surface modifications by nitric acid, hydrogen peroxide, and ammonium peroxydisulfate treatments. Langmuir 1995;11(11):4386-4392.

[23] Elmouwahidi A, Bailon-Garcia E, Perez-Cadenas AF, Maldonado-Hodar FJ, Carrasco-Marin F. Activated carbons from KOH and H 3 PO 4-activation of olive residues and its application as supercapacitor electrodes. Electrochimica Acta 2017;229:219-228.

[24] Conway BE. Electrochemical supercapacitors: scientific fundamentals and technological applications. Springer Science & Business Media: 2013:

[25] Figueiredo JL, Pereira MFR, Freitas MMA, Orfao JJM. Modification of the surface chemistry of activated carbons. Carbon 1999;37(9):1379-1389.

[26] Biniak S, Szymanski G, Siedlewski J, Swiatkowski A. The characterization of activated carbons with oxygen and nitrogen surface groups. Carbon 1997;35(12):1799-1810.

[27] Figueiredo JL, Pereira MFR, Freitas MMA, Orfao JJM. Modification of the surface chemistry of activated carbons. Carbon 1999;37(9):1379-1389.

[28] Moreno-Castilla C, Lopez-Ramon MV, Carrasco-Marin F. Changes in surface chemistry of activated carbons by wet oxidation. Carbon 2000;38(14):1995-2001.

[29] Stanczyk K, Dziembaj R, Piwowarska Z, Witkowski S. Transformation of nitrogen structures in carbonization of model compounds determined by XPS. Carbon 1995;33(10):1383-1392.

[30] Raymundo-Piñero E, Cazorla-Amoros D, Linares-Solano A, Find J, Wild U, Schlogl R. Structural characterization of N-containing activated carbon fibers prepared from a low softening point petroleum pitch and a melamine resin. Carbon 2002;40(4):597-608.

[31] Jurewicz K, Babe+é K, Pietrzak R, Delpeux S, Wachowska H. Capacitance properties of multi-walled carbon nanotubes modified by activation and ammoxidation. Carbon 2006;44(12):2368-2375.

[32] Guo Y, Qi J, Jiang Y, Yang S, Wang Z, Xu H. Performance of electrical double layer capacitors with porous carbons derived from rice husk. Materials Chemistry and Physics 2003;80(3):704-709.

[33] Frackowiak E. Carbon materials for supercapacitor application. Phys. Chem. Chem. Phys. 2007;9(15):1774-1785.

[34] Rufford TE, Hulicova-Jurcakova D, Zhu Z, Lu GQ. Nanoporous carbon electrode from waste coffee beans for high performance supercapacitors. Electrochemistry Communications 2008; 10(10): 1594-1597.

[35] Hulicova D, Yamashita J, Soneda Y, Hatori H, Kodama M. Supercapacitors Prepared from Melamine-Based Carbon. Chem. Mater. 2005;17(5):1241-1247.

[36] Xu MW, Zhao DD, Bao SJ, Li HL. Mesoporous amorphous MnO2 as electrode material for supercapacitor. Journal of Solid State Electrochemistry 2007;11(8):1101-1107.

[37] Wang G, Zhang L, Zhang J. A review of electrode materials for electrochemical supercapacitors. Chem. Soc. Rev. 2012;41(2):797-828

CHAPTER VIII: *CARBON TITANIUM OXIDE COMPOSITES AS ELECTROCHEMICAL SUPERCAPACITORS ELECTRODES*

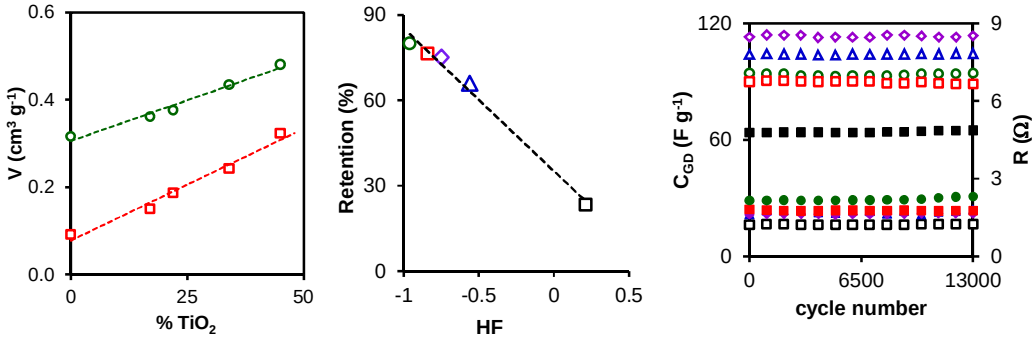

1. ABSTRACT

A series of a carbon xerogel doped with different percentages of TiO_2 has been explored as a tentative via to prepare electrodes for supercapacitors. Carbon composites were obtained by an inverse emulsion method in n-heptane and after carbonization at 900 ° the metal oxide phase is well dispersed on the carbon phase, with a crystal size smaller than 4 and only anatase phase was detected. The increase in % TiO_2 produces a decreases in the hydrophobicity of the composites which improve the wettability of the electrodes. XPS results shown that Ti^{3+} and Ti^{4+} are present on the surface of the samples and the presence of both oxidation states can improve the electron mobility in the inorganic phase. The obtained composite materials possess specific surface areas ranging from 423 to 539 $m^2 g^{-1}$ and a very well developed micro and mesoporosity with a total pore volume ranging from 0.361 to 0.480 $cm^3 g^{-1}$. The supermicropores mean size increase as the TiO_2 increases whereas practically no variation was found for the ultramicroporosity size. A two-electrode symmetric supercapacitor based on the carbon xerogel-TiO_2 composites exhibits a high electrochemical performance with a capacitances (up to 137 F g^{-1} at 0.250 A g^{-1} for 20 % TiO_2 composite), a high retention capacitance (66-80 %) at 20 A g^{-1} and high energy density, 20.15 Wh kg^{-1}, at a power density of 138.11 W kg^{-1} in the voltage range of 0 V to 1.1 V. Sample with a combination of low hydrophobicity and an adequate micro-mesopore network with a medium content in TiO_2 shows the best performance for energy storage. Floating test shows a very good cyclability of the synthetized materials.

Keywords: Carbon TiO_2 composites; Supercapacitor electrodes; Energy storage.

2. INTRODUCTION

The actual demands for clean and sustainable energy with the advantages of high power density, high efficiency, and long life expectancy have made electrochemical supercapacitors one of the major emerging devices for energy storage and power supply [1]. Supercapacitors, commonly called electric double-layer capacitors (EDLCs) have a higher energy density than conventional dielectric capacitors due to the large surface area of porous electrode materials; they also have higher power density, low temperature dependence, as well as nearly unlimited cyclability (>100,000 cycles) [2-4].

In the past decade, various carbon–metal oxide composite electrodes have been developed by integrating metal oxides into deferent carbon nanostructures [5-7]. Currently the electrodes of most commercial supercapacitors are made of carbon because it is inexpensive has good resistance to corrosion and has excellent cyclic stability and long service lifetime since the electrode undergoes no chemical change during the charge/discharge processes [5,8]. However, the active electrode surface area and the pore size distribution restrict the maximum capacitance.

A composite electrode with nano-sized metals oxide incorporated in highly conductive carbon support would be advantageous in designing supercapacitor electrode materials. Over the past few years, various metal oxide , such as manganese, ruthenium, zirconium and MnO_2, NiO, TiO_2, Fe_2O_3 and their hydroxides have been used to prepare metal oxide carbon composites [5-7,9-11]. Titanium dioxide was used for a many applications due to their semiconducting properties, accessible surface, electrochemical behaviour and long-term chemical stability. Among them the preparation of electrochemical composite electrode.

TiO_2 is an interesting electrode materials for electrochemical energy storage systems because of the ideal capacitive response of TiO_2 (rectangular cyclic voltametry curves) observed in some works [12-14] which indicates that the storage mechanism in TiO_2 was due to the conventional electric double layer storage. However, Due to the low conductivity of TiO_2, the preparation of titanium

oxide carbon composite can be one of the effective approaches to improve the capacitance and rate capability of TiO_2.

The specific capacitance of metal oxide-based supercapacitors drops considerably with an increase in the scan rate due to their poor electronic conductivity. Therefore, it is necessary to combine metal oxides with other material, which have a good conductivity to form composites.

This paper describes the preparation of carbon titanium oxide composites by inverse emulsion and after that, the effect of titanium percentage on the porosity, structure and the electrochemical performances of supercapacitors prepared from those materials.

3. EXPERIMENTAL

3.1. Synthesis of TiO_2-carbon xerogel composites

TiO_2-carbon xerogel composites were prepared by mixing the resorcinol-formaldehyde as carbon source and titanium isopropoxide (IV) as titanium oxide precursor. In details, Span 80 (S) was dissolved in 900 ml of n-heptane and heated at 70 °C under reflux and stirring (450 rpm). Then a mixture containing resorcinol (R), formaldehyde (F) and water (W) was added drop by drop into the above solution. After this addition, the amount of titanium isopropoxide was added drop by drop to the mixture. The molar ratio of the mixture was R/F=1/2, R/W=1/14 and R/S=4.5.

The mixture was aged at 70 °C for 24 h under stirring before to be filtered and the solid obtained was placed in acetone (5 days, changing acetone twice daily) to remove the Span used and exchange water within the pores by acetone. This procedure reduces the collapse of porosity during the subsequent drying process. Then, the gel was filtered again and dried by microwave heating under argon atmosphere in periods of 1 minute at 300 W until constant weight using a Saivod MS-287W microwave oven. Pyrolysis of organic xerogel-titanium oxide composite to obtain the corresponding carbon xerogel-titanium oxide composite was carried out at 900 °C in a tubular furnace using a N_2 flow at 300 cm^3 min^{-1}, and

a heating rate of 1 °C min^{-1}, in order to allow a soft removing of pyrolysis gases, and soaking time of 2 h at this temperature. Depend of the amount of titanium oxide (10, 20, 30 and 40 weight % in the carbonized materials), four carbon xerogel-titanium oxide composites were prepared by fitting the alkoxide ratio assuming a weight loss during carbonization of 50 %. The Carbon xerogel-titanium oxide composites prepared was named CTiX (X corresponding to the theorical % of titanium oxide present in the carbonized composite, e.g. CTi40 contains 40 % wt. of TiO_2).

3.2. Textural and chemical characterization

Textural characterization was carried out by N_2 and CO_2 adsorption at −196 °C and 0 °C, respectively, using Quantachrome Autosorb equipment. The BET and Dubinin–Radushkevich equations were applied to determine the apparent surface area (S_{BET}) and the micropore volume (W_0), the mean micropore width (L_0) and the microporous surface (S_{mic}), respectively. Furthermore, the BJH method was used to calculate the mesopore volume of the samples (V_{mes}). Pore size distributions were also obtained by applying the BJH method. The total pore volume was considered as the volume of N_2 adsorbed at P/P_0 = 0.95. The morphology of samples was studied by scanning electron microscopy (SEM) using a LEO (Carl Zeiss) GEMINI-1530 microscope.

The amount of TiO_2 in the samples was determinate by thermogravimetric analysis (TGA). TGA was performed in flowing air with a heating rate of 10 °C/min using a Mettler-Toledo TGA/DSC1 thermogravimetric analyzer.

In order to determine the hydrophobicity of the samples the enthalpies of immersion of the carbons into benzene and water, $\Delta_i H(C_6H_6)$ and $\Delta_i H(H_2O)$, were determined with a calorimeter of the Tian–Calvet type [15,16]. Hydrophobicity of the samples were calculated according to Eq. 1. The immersion enthalpy into water depends upon specific and non-specific interactions; in contrast in the case of benzene the immersion enthalpy depends only to the surface area of the carbon accessible to benzene molecules.

$$HF = \frac{\Delta_i H(C_6H_6) - \Delta_i H(H_2O)}{\Delta_i H(C_6H_6)} \quad \text{(Eq. 1)}$$

The phases of the resulting samples were characterized using a Bruker D8 Advance X-ray diffractometer with Cu Kα radiation at a wavelength (λ) of 1.541 Å. The 2θ angles were scanned from 20 to 70°. The chemical characterization of xerogels was further analyzed by X-ray photoelectron spectroscopy (XPS). The spectra were obtained on a Kratos Axis Ultra-DLD X-ray photoelectron spectrometer equipped with a hemispherical electron analyzer connected to a detector DLD (delay-line detector).

3.3. Electrochemical measurements

Electrodes were prepared by combining 90% CTix and 10% polytetrafluoethylene (PTFE) to from a homogenous mixture. The mixture was dried overnight at 80 after that 5mg of the dried mixture was pasted onto disc graphite paper with 5mm of diameter. Two-electrode cells were assembled with two CTix electrodes sandwiching a porous glassy fibrous materials separator.

Cyclic voltammetry, VC, galvanostatic charge-discharge, CGD, impedance spectroscopy, EIS; and long term stability by charge discharge cycles were performed on electrodes produced from carbon titanium composites in sulfuric acid 1 M as electrolyte using a Biologic VMP-300 potentiostat/galvanostat.

Cycling voltammetry tests (CV) were carried out within the range of 0 and 1.1 V; using scan rates of 0.5, 2.5, 5, 10, 20 and 30 mV s^{-1} and the capacitance was calculated using the relation (1) [17,18]:

$$C = \frac{\sum |I| \Delta t}{m \Delta V} \quad \text{(Eq. 2)}$$

where $\sum |I| \Delta t$ is the area of the current (A) against time (s) curve, m is the total mass of active sample in both two electrode (g), ΔV the potential window (V).

The galvanostatic charge-discharge analysis was carried at different current density from 125 mA g^{-1} to 20 A g-1 and the gravimetric capacitance was calculated using the equation (2) [19,20]:

$$C = \frac{I_d \Delta t}{m \Delta V} \quad \text{(Eq. 3)}$$

where I_d is the discharge current, Δt the discharge time, m, the total mass of the AC in the electrodes, and ΔV the voltage window subtracting the ohmic drop. The coulombic efficiency (%) from chronopotentiometric measurements was calculated from the discharge and charge time, t_d and t_c, respectively, by the formula $(t_d/t_c)\times 100$.

The impedance spectroscopy measurements were carried in the frequency of 100 KHz to 0.01 Hz at an AC amplitude of 10 mV. The capacitance value from EIS, C, was obtained by equation (3):

$$C = \frac{-Z''}{2\pi \times f \times Z^2} \quad \text{(Eq. 4)}$$

where f is the frequency and $Z^2 = Z'^2 + Z''^2$, with Z' and Z'' being the real and imaginary parts of the complex impedance, respectively.

For comparison reasons, the gravimetric capacitances in 2EC obtained from the three techniques were multiplied by 4 to obtain the capacitance per single electrode, which is the 3EC equivalent [21] being named C_{CV}, C_{CP} and C_{EIS} respectively.

However, by convention, the gravimetric capacitances obtained from equation (2) in 2EC were used to calculate the energy density in the Ragone plot using the Eq. 4 and power density was calculated by Eq. 5 [22,23].

$$E = \frac{C_{eq.3}\left(V_{max} - IR_{drop}\right)^2}{2} \quad \text{(Eq. 5)}$$

$$P(W\,kg^{-1}) = \frac{E}{\Delta t} = \frac{I(A) \times \left(V_{max} - IR_{drop}\right)}{2m\,(kg)} \quad \text{(Eq. 6)}$$

4. RESULTS AND DISCUSSION

4.1. Textural and chemical characterization

The actual TiO_2 content in the final carbonized composites were analysed by TGA (Table 1). These % wt. are slightly higher than the theoretical ones due to the weight lost during the carbonization is not exactly 50 %, however the experimental data are closed to the expected ones.

Morphology of sample was studied by scanning electron microscopy (Fig. 1). CTiX samples (Fig. 1a) show a typical structure of carbon xerogels which consists in primary nanospheres connected between them to build a three-dimensional and porous structure. A homogeneous structure is obtained, without differentiation between the TiO_2-carbon phases. The EDX analysis of these samples showed an homogeneous Ti-distribution along all the sample independently of the TiO_2-loading present in each composite (Fig. 1b).

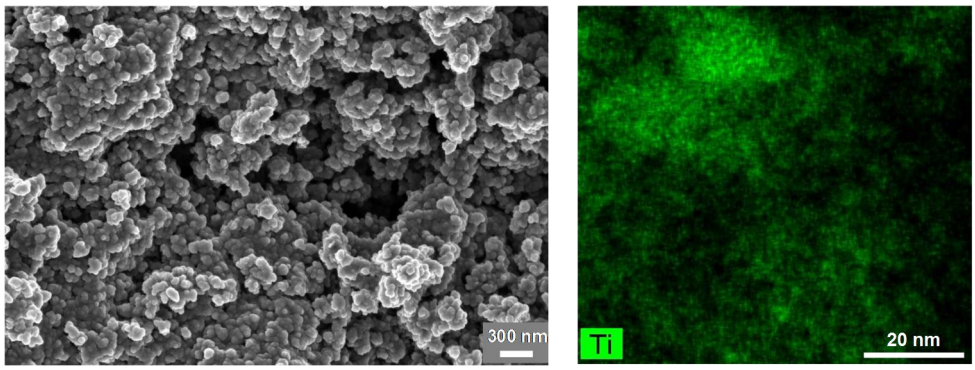

Figure 1. a) SEM and b) EDX images of CTi40

Hydrophobicity of the samples, Table 1, shows that TiO_2-xerogel composites present higher attraction to water molecules, which greatly favored the wettability of the carbon and will increase the mobility of the H^+ and SO_4^{2-} through

the porous network. The hydrophobicity decreases as the TiO_2 content increases due to the presence of the inorganic phase.

Table 1. Textural characteristics of the carbon, CTiX composites and pure phases

Sample	TiO_2	HF	S_{BET}	$W_0(N_2)$	$W_0(CO_2)$	$L_0(N_2)$	$L_0(CO_2)$	V_{mes}	$V_{0.95}$
	%		$m^2\ g^{-1}$	$cm^3\ g^{-1}$		nm		$cm^3\ g^{-1}$	
C100	0	0.21	585	0.228	0.275	0.58	0.56	0.088	0.316
CTi10	17	-0.56	539	0.212	0.223	0.67	0.58	0.149	0.361
CTi20	22	-0.75	479	0.189	0.205	0.75	0.56	0.187	0.376
CTi30	34	-0.84	481	0.192	0.176	0.97	0.58	0.242	0.434
CTi40	45	-0.96	423	0.157	0.174	1.03	0.59	0.323	0.480
TiO_2	100	--	116	0.047	n.d.	1.89	n.d.	0.279	0.326

n.d. non detected

Figure 2 shows the N_2 adsorption isotherms on the carbon and CTiX composites, which were all type I. This is typical of microporous solids [24], although there was an increase in N_2 uptake with the rise in relative pressure after micropore filling, this is indicative of the presence of narrow mesopores $\varnothing \approx 4$ nm. All isotherms also showed a large increase in the amount adsorbed at relative pressures ≈ 0.95, due to N_2 condensation within void spaces. The BET surface area and the porosity properties of the composites are important parameters governing the supercapacitor performance. The details of BET and porosity properties are collected in the Table 1.

The results obtained from CO_2 and N_2 adsorption show a gradual variation of the textural properties between the composites as % TiO_2 increases. Increasing the % of TiO_2, the total porosity ($V_{0.95}$) increases, favored by a development of the volume of mesopores (V_{mes}), Figure 3.

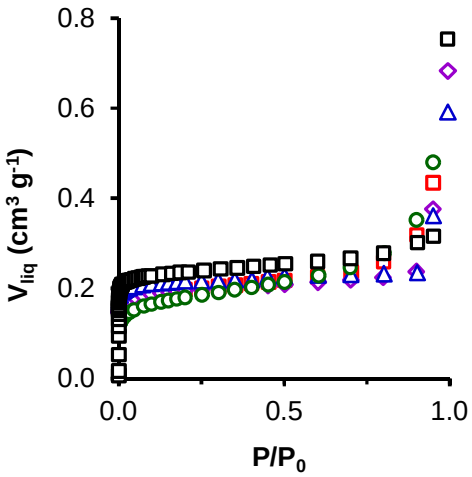

Figure 2. N_2 adsorption isotherms at -196 ºC on samples a) C □, CTi10 △, CTi20 ◇, CTi30 □ and CTi40 ○.

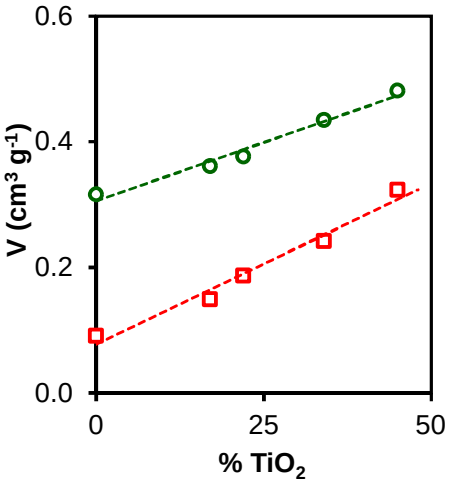

Figure 3. Variation of the V_{meso}, □ and $V_{0.95}$ ○ with the TiO_2 content.

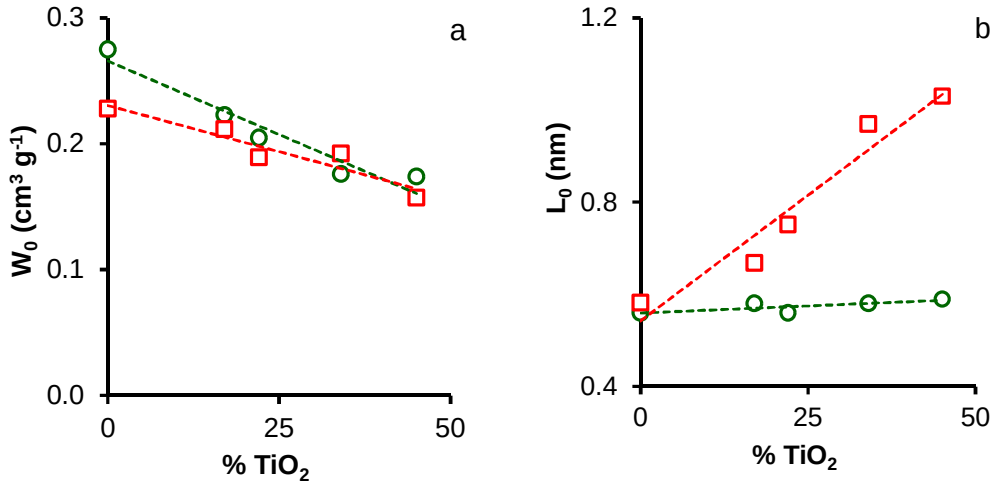

Figure 4. Evolution of pore volumes and mean pore widths with TiO_2 content: a) micropore volume, W_0; b) mean pore width, L_0. □ data from N_2 adsorption, ○ data from CO_2 adsorption.

The micropore distribution can be analyzed by comparing the results from CO_2 and N_2-adsorption experiments. It is well known that the CO_2 adsorption provides the information about the narrow microporosity, ultramicropores, corresponding to micropores with diameter lower than 0.7 nm, while the total microporosity is obtained from N_2 isotherm only in absence of diffusion restrictions, supermicropores. Figure 4a shows the variation of the ultra and supermicropore volume with the variation of the TiO_2 content. The micropore volume (measured by N_2 adsorption) decreases and pores becomes wider ($L_0(N_2)$ increases), Table 1, increasing the titanium oxide content while the ultramicroporosity ($W_0(CO_2)$) progressively decreased and the mean pore size practically is not affected, only a slight increase is detected. (Figure 4b).

Sample C shows $W_0(N_2)<W_0(CO_2)$ denoting diffusion restrictions of N_2 into the microporosity induced by the narrow microporosity of the carbon phase. On the contrary carbon TiO_2 composites show $W_0(N_2) \approx W_0(CO_2)$ as the consequence of the commented pore widening. In this sense, the micropore size (L_0) also increases progressively, and consequently, with the micropore widening the commented

diffusional restriction decreases. The mesopore volume increased more or less linearly with TiO_2 content (Figure 3) while the micropore volume (determined by N_2 or CO_2 adsorption) showed the contrary tendency (Figure 4a).

Powder XRD measurements of CTiX samples were performed in order to identify the crystalline domains of the embedded titanium. As it is known, TiO_2 can be present in two crystalline structures, anatase and rutile. Anatase is a metastable polymorphic form which can be transformed by heating to rutile. For pure oxides, this transformation is fast at temperatures above 730 °C but the phase transition temperature has been shown to depend on impurity content, particle size, and surface area [25]. Figure 5 shows XRD patterns obtained for the CTiX composites series. Below a TiO_2 content of 20 %, XRD patterns do not shown any defined diffraction peak corresponding to the inorganic phase. For a TiO_2 content of 30 % the observed peaks correspond to the anatase polymorphic form. The above results indicate that, in the carbonized composite xerogels the metal oxide phase is well dispersed on the carbon phase, with a crystal size smaller than 4. Since the carbonization temperature of the samples was 900 ºC, only rutile phase was to be expected in the final carbon-titanium oxide composites. Nevertheless, anatase phase was observed in all carbon-titania composite materials. These results point out that the carbon matrix prevents the sintering of titania nanoparticles and stabilizes the anatase form even at high temperature.

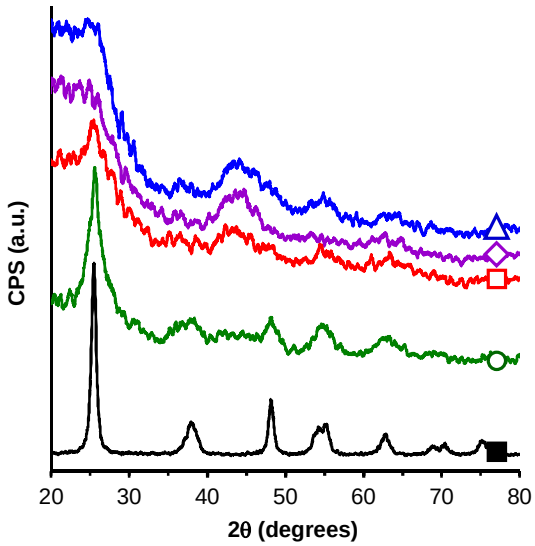

Figure 5. Podwer XRD patterns of samples: CTi10 (△), CTi20 (◇), CTi30 (□), CTi40 (○) and TiO_2 (■).

The surface chemistry of titanium oxide composite were analysed by XPS. Results are collected in Table 2. The deconvolution of Ti_{2p} spectral region of TiO_2 requires only one peak at binding energy BE = 459.2 eV, corresponding to Ti^{+4}, in agreement to the BE values previously published [26], while two component are needed in CTiX samples at binding energy BE = 459 eV, corresponding to Ti^{+4} and at 458.2 eV assigned to Ti^{+3} species. Note that no partially reduced oxides are obtained in both TiO_2 pure phases, while around 55 % of Ti atoms are reduced during carbonization of organic gels.

Table 2. XPS results obtained from the deconvolution of high resolution XP spectra of C_{1s}, O_{1s} and Ti_{2p}.

Sample	BE (eV) C_{1s}	Peak %	BE (eV) $Ti_{3p3/2}$	Peak %	BE (eV) O_{1s}	Peak %	O_{XPS} % wt.	Ti_{XPS} % wt.
TiO_2			459.5	100	530.8	92		
					532.2	8		
C100	284.6	74	-	-	531.6	18	2.65	-
	285.6	13			533.2	82		
	286.6	5						
	287.5	3						
	289.3	3						
	290.9	1						
TiC10	284.6	64	458.3	54	530.4	4	3.17	0.61
	285.5	19	459.2	46	531.3	2		
	286.6	7			532.5	53		
	287.5	3			533.9	41		
	289.2	5						
	290.8	2						
TiC20	284.6	73	458.2	59	530.0	23	3.99	1.41
	285.6	14	458.7	41	531.3	12		
	286.6	5			532.6	36		
	287.6	2			533.9	29		
	289.1	3						
	290.6	2						
TiC30	284.6	71	458.4	54	530.1	62	6.87	10.46
	285.6	14	459.0	46	531.3	14		
	286.7	6			532.7	16		
	287.8	3			533.9	7		
	289.5	4						
	291.1	2						
TiC40	284.6	66	458.7	55	530.2	67	11.75	14.96
	285.5	19	459.2	45	531.1	22		
	287.0	7			532.2	6		
	288.6	3			533.0	5		
	289.9	2						
	291.1	3						

Two components, at 530.8 and 532.2 eV, were used to fit the O_{1s} spectral region of TiO_2. The major component of O_{1s} spectral region corresponds to the 'bulk' oxygen atom in the stoichiometric TiO_2 form, while the high BE component could correspond to various oxygen-containing surface functional groups [27]. Mainly hydroxyl (-OH) or bridge surface oxygen (Ti-O-Ti) groups were described [28]. However, four components were used to fit the O_{1s} spectral region for composites samples which is also influenced by the oxygen content linked to the carbon phase. The components at 530.2 eV and 531.3 eV corresponds to the 'bulk' oxygen atom in the stoichiometric TiO_2 form and oxygen bonded to Ti^{+3}, respectively [27], while the peaks at 532.6 and 533.9 eV are assigned to C=O and C-O of carbon phase. These two last peaks are predominant in the composites with low TiO_2 content, but with the increase of this parameter, the main components are those corresponding with Ti^{4+} and Ti^{3+} species (see the deep change of their O profiles, Table 2). Note also that BE values of Ti and O peaks appear around 0.7 eV higher than those detected for pure titania, which can be due to the ability of the carbon phase to accommodate electrons from the inorganic phase leading to a poorest electronic environment.

It is important to note the very low surface concentration of Ti, especially for samples CTi-10 and CTi-20. This fact is indicative the high dispersion for TiO_2 on carbon matrix and also this can be embedded into the matrix and no detected by XPS.

4.2. Electrochemical Characterization

Figure 6a shows the cyclic voltammograms (CV) for carbon and TiO_2-carbon composites with different titanium oxide ratios at a scan rate of 20 mV s^{-1}. A quasi rectangular shape CV curves are observed for all samples, except for pure carbon, indicating a pure capacitive behavior [29]. Data of C_{cv} obtained from these curves are presented in Figure 6b. All samples show a good capacitance retention with the variation of the scan rate. Higher capacitance values are obtained using composite materials in comparison with the pure carbon phase instead the similar or even lower surface area of the former. This behavior point out that the pore

structure as well as the chemical surface plays an important role. In that sense, TiC10 and C100 present very similar micropore structure, the main difference is the higher mesopore volume for CTi10 and both sample show very different capacitive behavior (C_{cv} = 42 vs 97 F g^{-1} for C100 and CTi10, respectively). That should be related with the presence of TiO_2 on the surface. This TiO_2 could improve the capacitive behavior i) improving the hydrofilicity of the surface which significantly increases the electrolyte contact with the surface favoring the diffusion of the ions and ii) the reduced species Ti^{3+} can act as electron transfer centers decreasing the resistance of the electrode. As usually an increase in the scan rate induce a decreases in capacitance, but in the case of the xerogel-TiO_2 samples this decrease is lower than in carbon electrodes. In fact the retention capacities between 0.5 and 30 mV s^{-1} are 74.2, 78.4, 73.5 and 75.6 % for CTi10, CTi20, CTi30 and CTi40 respectively.

The galvanostatic charge-discharge curves of the samples recorded at 2 A g^{-1} are shown in Figure 7a, the shapes of these curves, for all samples, are almost ideally triangular. As determined by CV the capacitance of the sample CTi20 is higher than for the rest of the samples due to the combination of two factors, its optimal textural characteristics and the low hydrophobicity, Table 1. The low hydrophobicity of the TiO_2-carbon xerogels improve the wettability of the carbon surface and can facilitate EDL formation favoring the ions mobility during the electrochemical measurements. This should be the reason to obtain high capacitance values at high current densities, ranging from 54 to 81 F g^{-1} at 20 A g^{-1}. Figure 7b shows the variation of the capacitance with the current density, it is clear that all sample show a decrease of capacitance when the currents density varies from 62 mA g^{-1} to 20 A g^{-1} which it is due to restrictions to the EDL formation at high current densities.

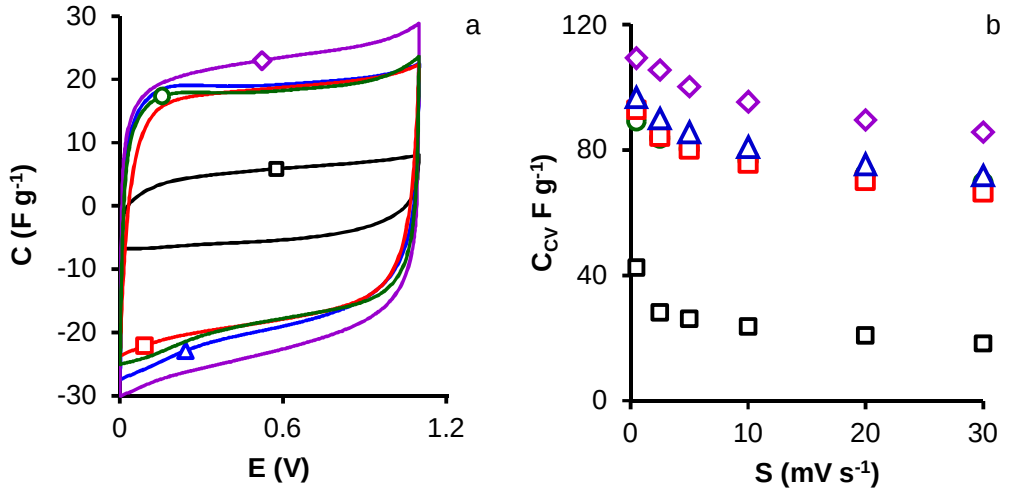

Figure 6. a) Cyclic voltammetries in 1 M H_2SO_4 at scan rate 20 mV s^{-1}. b) Variation of the gravimetric capacitance, C_{CV}, against the scan rate. Samples: C100 (□), CTi10 (△), CTi20 (◇), CTi30 (□), CTi40 (○).

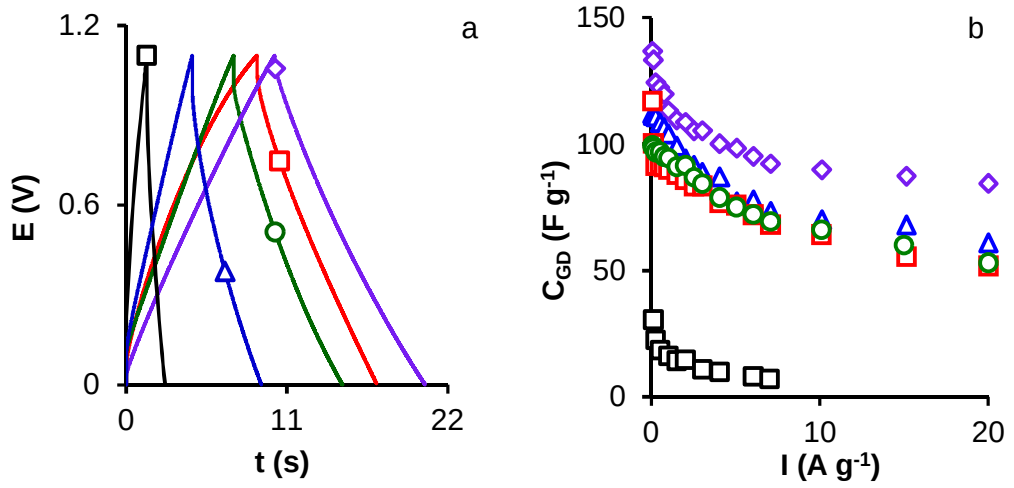

Figure 7. a) Chronoamperomety profiles in 1 M H_2SO_4 at a current density of 2 A g^{-1}. b) Variation of the gravimetric capacitance, C_{GD}, against the scan rate. Samples: C100 (□), CTi10 (△), CTi20 (◇), CTi30 (□), CTi40 (○).

One limiting factor to the use of carbon materials as electrodes for supercapacitors is the poor capacitance retention at high current densities. As can be see, Figure 7b, for TiO_2-carbon xerogels composites this reduction in capacitance is lower than in C100. This fact must be related to the restriction of ion diffusion in the pore network. These restrictions are controlled by two factors the first one is the pore size of the micropore network and the second one the wettability of the carbon surface. Thus, it is necessary an adequate combination of both factors in order to get high capacitance and high capacitance retention. Figure 7a shows the lineal variation in capacitance retention with the hydrophobicity for all samples studied denoting the great influence of this parameter in the efficiency of the electrodes. Figure 8b shows the variation of the capacitance retention against the micropore size determined from the nitrogen adsorption, in this case for a micropore size larger than 0.75 nm the retention, practically, is constant.

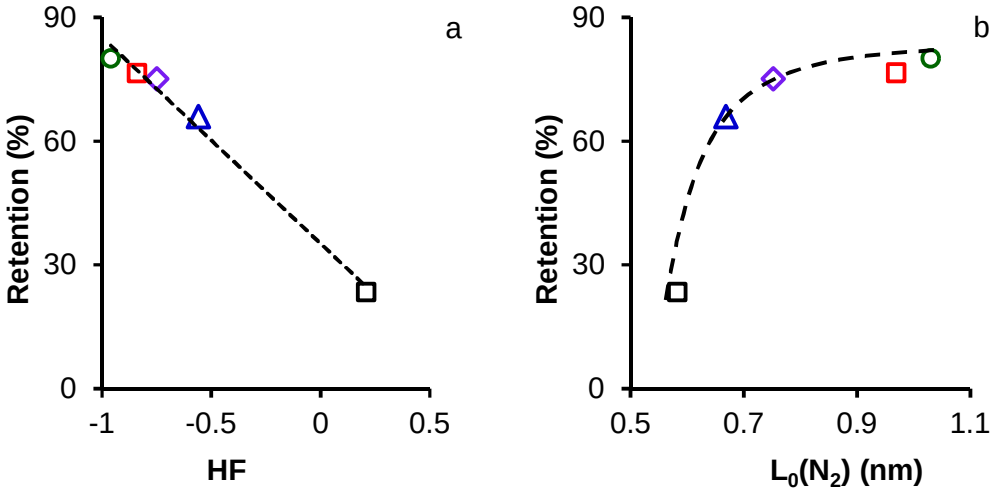

Figure 8. Variation of retention capacitance, C_{GD}, (100×7 A g^{-1}/0.125 A g^{-1}) for carbon and carbon xerogels against a) hydrophobicity; b) mean micropore size from N_2 adsorption. Samples: C100 (□), CTi10 (△), CTi20 (◇), CTi30 (□), CTi40 (○)**.**

The electric conductivities of the samples were evaluated by electrochemical impedance spectroscopy, and the Nyquist plots are shown in

Figure 9a. The equivalent series resistance (ESR) is obtained from the intersection point of the impedance with the real axis at high frequency [30]. The diameter of the semi-circle corresponds to the so called charge-transfer resistance, R_{CT}, [31] at the electrode-electrolyte interface, which is often correlated with the electronic conductivity of the electrode. Results obtained are compiled in Table 3.

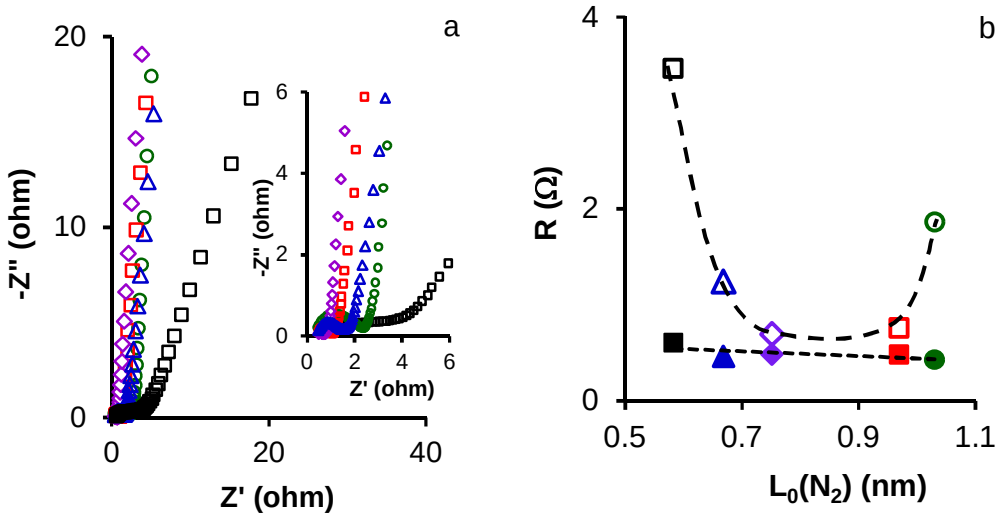

Figure 9. (a) Nyquist plots (b) Relationship between ESR (closed symbols) and R_{CT} (open symbols) with mean micropore size. Samples: C100 (□), CTi10 (△), CTi20 (◇), CTi30 (□), CTi40 (○).

At the high-frequency region the ESR values are obtained. ESR represents the sum of the intrinsic resistance of the active material, the electrolyte resistance, and contact resistance between the carbon material electrode and the current collector. ESR values shown in Table 3, reflect for comparison, approximately, the conductive properties of the activated carbon electrodes, due to that in all cases the same electrolyte, collectors, and type of cell were used to assemble the supercapacitor [30]. ESR values are approximately the same for all carbon xerogel-TiO_2 composites and much lower than in the case of the carbon.

Table 3. C_{EIS} at 1 mHz, equivalent series resistance (ESR), charge transfer resistance (R_{CT}) and relaxation time constant (τ) from EIS.

Sample	C_{EIS}	ESR	R_{CT}	τ
	$F\ g^{-1}$	Ω	Ω	s
C100	59	0.60	3.46	11.44
CTi10	102	0.46	1.25	0.26
CTi20	135	0.48	0.70	0.14
CTi30	101	0.48	0.76	0.19
CTi40	94	0.43	1.86	0.26

Samples CTi20 and CTi30 present the lowest R_{CT} values, 0.70 and 0.76 respectively, samples CTi10 and CTi40 show higher charge transfer resistance (1.25 and 1.86) and sample C100 had the highest value for all samples. These results, clearly show that the presence of TiO_2 on carbon material induce a decrease in the resistance of the electrode improving their performance for energy storage. These trends should be correlated with the pore structure and the conductivity of the sample. Figure 9b shows the correlation between the ESR and R_{CT} resistances and the microporous diameter, a minimum value of charge transfer resistance correspond to a 0.75 nm, which indicate that this is the most adequate pore diameter for energy storage for this kind of materials. In fact sample CTi20 present the higher capacitance and lower R_{CT} resistances with a pore diameter equal to 0.75 nm obtained from N_2 adsorption.

The optimal micropore diameter determined in this work is slightly higher than that obtained by other authors [30,32] and larger than the size of hydronium ions (0.36-0.42 nm) [30] and to the hydrated bisulfate ions (0.53 nm) [32] but in this case the electrodes content a large amount of inorganic material increasing the interaction between ions and electrodes.

Figure 10 shows the variations in the imaginary part of the capacitance (C'') against the frequency which define the transition frequency between a pure capacitive and a pure resistive behavior. The relaxation time constant (τ) is obtained from the frequency, f_0, at the maximum of the curve by the expression $\tau = 1/(2\pi \times f_0)$ [33]. τ is a quantitative measure of the speed of the discharge of the device [34]. Results in Table 3 show that τ for carbon composite materials is lower than for pure carbon and the lowest value correspond to CTi20 showing the excellent performance of this material as electrode for energy storage and release.

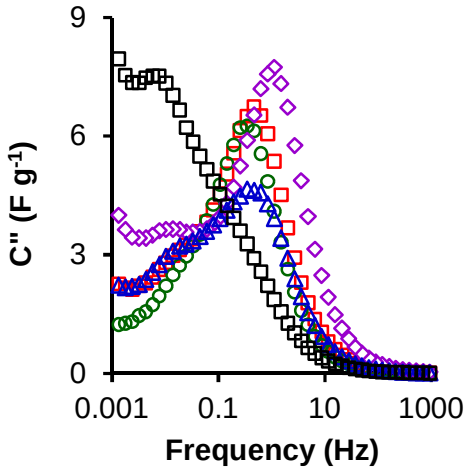

Figure 10. Evolution of imaginary part of capacitance *vs*. frequency. Samples: C100 (□), CTi10 (△), CTi20 (◇), CTi30 (□), CTi40 (○)**.**

The Ragone plots of the carbon xerogels-TiO_2 composites are presented in Figure 11 and show the variation between energy and power densities. Table 4 shows the results for all the samples studied for the maximum energy density and energy density at a power density of 4500 W kg^{-1}, the maximum common value for all samples. The maximum energy density drastically increases with the doping with TiO_2 due to the better wettability of the sample and to the widening of the microporosity. The maximum value reached was 20.7 Wh kg^{-1} for sample CTi20.The energy density of the supercapacitor based on CTi20 was better than

other used for commercially available supercapacitors (usually less than 10 Wh kg^{-1}) [1]. The energy released decreased at higher power density (Table 4) thus, the retention energy density had a maximum for CTi20 with a 65.2 % of energy released at 4.5 kW kg^{-1} compared to that obtained at 69 W kg^{-1}.

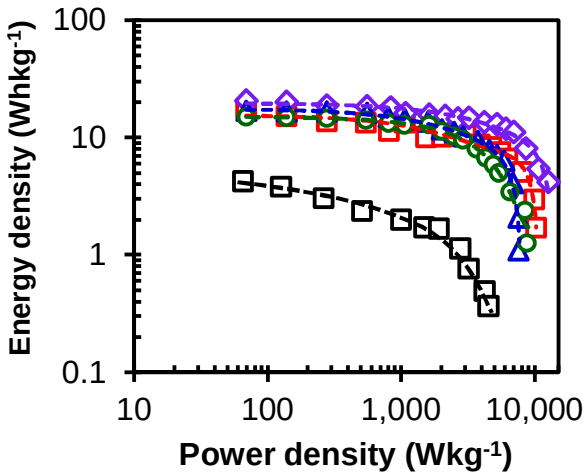

Figure 11. Ragone plots for samples: C100 (□), CTi10 (△), CTi20 (◇), CTi30 (□), CTi40 (○).

Table 4. Maximum (at 69 W kg^{-1}) and minimum (at 4500 W kg^{-1}) energy densities (Wh kg^{-1}) from Ragone's plots

Sample	E_{max} Wh kg^{-1}	E_{min} Wh kg^{-1}	E.Ret. %
C100	4.3	0.5	11.6
CTi10	16.9	7.9	46.7
CTi20	20.7	13.5	65.2
CTi30	17.7	8.3	46.9
CTi40	15.0	6.8	45.3

The stability of the electrodes during charge-discharge cycles is a key factor for their practical application. In this work the stability was evaluated by the galvanostatic charge-discharge cycling. Figure 12 depicts the results of the cycling stability test for samples studied in this work.

The capacitance of samples, practically did not change after 13000 cycles of charge-discharge at 1 A g^{-1}. The resistance was practically constant throughout the cycles except for samples C100 and CTi40 which presented a slight increase in resistance after 6500 cycles indicating a slight degradation of the electrodes. The results for these carbon composites indicated a good stability as potential use as electrodes for supercapacitor, mainly in the case of CTi20.

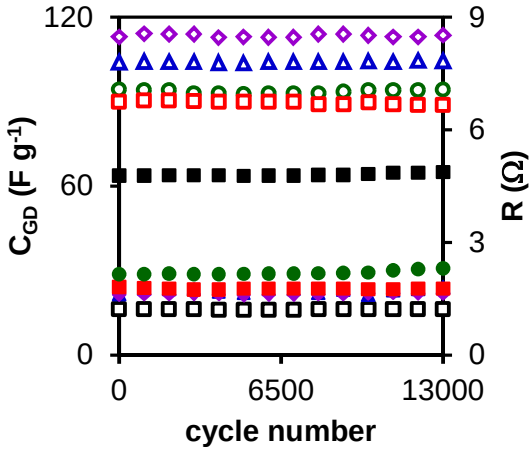

Figure 12. Galvanostatic charge-discharge cycles at a current density of 1 A g^{-1}: C100, □; CTi10, △; CTi20, ◇; CTi30, □; CTi40, ○**.** Capacitance (open symbols), ohmic resistance (closed symbols)

5. CONCLUSIONS

Carbon xerogel-TiO_2 composites (CTiX) were successfully synthesized by sol-gel techniques. Composites present a homogeneous and three-dimensional mesoporous structure, where both phases are also homogenously and intimately distributed. All the textural, chemical, crystallographic and catalytic properties are

determined by the TiO_2 content in the composite and by the synergetic effect between both phases. Carbon xerogels is eminently a microporous supports, but the composites are mesoporous materials, increasing mesoporosity at the expense of microporosity. The presence of carbon in the composite prevents the TiO_2 crystal growth, and difficult the anatase to rutile transition. Due to the interactions between both phases all composites present a high dispersion of anatase TiO_2 nanoparticles on the carbon support in spite that samples are carbonized a 900◦C. These nanoparticles are partially reduced, with an oxygen surface distribution highly dependenton the TiO_2 content.

The supercapacitor performed of samples was analyzed in a two-electrode system. Composites exhibits a high electrochemical performance with a capacitances (up to 137 F g^{-1} at 0.250 A g^{-1} for 20 % TiO_2 composite), a high retention capacitance (66-80 %) at 20 A g^{-1} and high energy density, 20.7 Wh kg^{-1}, at a power density of 69 W kg^{-1} in the voltage range of 0 V to 1.1 V. This better behaviour could be related with different properties of the composites: i) The presence of TiO_2 improve the hydrofilicity of the surface which significantly increases the electrolyte contact with the surface favoring the diffusion of the ions, ii) carbon matrix favors the TiO_2 reduction and these reduced species Ti^{3+} can act as electron transfer centers decreasing the resistance of the electrode and iii) the presence of TiO_2 on carbon material induce a decrease in the resistance of the electrode improving their performance for energy storage due to an optimization of the pore structure. Sample with a combination of low hydrophobicity and an adequate micro-mesopore network with a medium content in TiO_2 shows the best performance for energy storage. Floating test shows a very good cyclability of the synthetized materials.

6. REFERENCES

[1] G. Wang, L. Zhang, and J. Zhang, A review of electrode materials for electrochemical supercapacitors. Chemical Society Reviews, 41 (2012) 797-828.

[2] P. Simon and Y. Gogotsi, Materials for electrochemical capacitors. Nature Materials, 7 (2008) 845-854.

[3] T. Chen and L. Dai, Carbon nanomaterials for high-performance supercapacitors. Materials Today, 16 (2013) 272-280.

[4] B.E. Conway, Similarities and Differences between Supercapacitors and Batteries for Storing Electrical Energy, Springer US, Boston, MA, 1999.

[5] M. Zhi, C. Xiang, J. Li, M. Li, and N. Wu, Nanostructured carbon-metal oxide composite electrodes for supercapacitors: a review. Nanoscale, 5 (2013) 72-88.

[6] T. Lu, Y. Zhang, H. Li, L. Pan, Y. Li, and Z. Sun, Electrochemical behaviors of graphene–ZnO and graphene–SnO_2 composite films for supercapacitors. Electrochimica Acta, 55 (2010) 4170-4173.

[7] X. Sun, M. Xie, G. Wang, H. Sun, A.S. Cavanagh, J.J. Travis, S.M. George, and J. Lian, Atomic Layer Deposition of TiO_2 on Graphene for Supercapacitors. Journal of the Electrochemical Society, 159 (1-1-2012) A364-A369.

[8] R. Górniak and S. Lamperski, Investigation of the Electrical Double Layer with a Graphene Electrode by the Grand Canonical Monte Carlo Simulation. The Journal of Physical Chemistry C, 118 (2014) 3156-3161.

[9] V.D. Patake, C.D. Lokhande, and O.S. Joo, Electrodeposited ruthenium oxide thin films for supercapacitor: Effect of surface treatments. Applied Surface Science, 255 (2009) 4192-4196.

[10] D. Yan, Z. Guo, G. Zhu, Z. Yu, H. Xu, and A. Yu, MnO_2 film with three-dimensional structure prepared by hydrothermal process for supercapacitor. Journal of Power Sources, 199 (2012) 409-412.

[11] U.M. Patil, R.R. Salunkhe, K.V. Gurav, and C.D. Lokhande, Chemically deposited nanocrystalline NiO thin films for supercapacitor application. Applied Surface Science, 255 (2008) 2603-2607.

[12] M.S. Kim, T.W. Lee, and J.H. Park, Controlled TiO2 Nanotube Arrays as an Active Material for High Power Energy-Storage Devices. Journal of the Electrochemical Society, 156 (1-7-2009) A584-A588.

[13] M. Zhou, A.M. Glushenkov, O. Kartachova, Y. Li, and Y. Chen, Titanium Dioxide Nanotube Films for Electrochemical Supercapacitors: Biocompatibility and Operation in an Electrolyte Based on a Physiological Fluid. Journal of the Electrochemical Society, 162 (1-1-2015) A5065-A5069.

[14] M. Salari, S.H. Aboutalebi, A.T. Chidembo, I.P. Nevirkovets, K. Konstantinov, and H.K. Liu, Enhancement of the electrochemical capacitance of TiO_2 nanotube arrays through controlled phase transformation of anatase to rutile. Physical Chemistry Chemical Physics, 14 (2012) 4770-4779.

[15] R.P. Bansal, J.P. Donnet, and F. Stoeckli, Active carbon, Marcel Dekker, New York, 1988.

[16] F. Carrasco-Marin, A. Mueden, A. Centeno, F. Stoeckli, and C. Moreno-Castilla, Water adsorption on activated carbons with different degrees of oxidation. Journal of the Chemical Society, Faraday Transactions, 93 (1997) 2211-2215.

[17] J. Gamby, P.L. Taberna, P. Simon, J.F. Fauvarque, and M. Chesneau, Studies and characterisations of various activated carbons used for carbon/carbon supercapacitors, Journal of Power Sources, 101 (2001) 109-116.

[18] L. Bonnefoi, P. Simon, J.F. Fauvarque, C. Sarrazin, J.F. Sarrau, and A. Dugast, Electrode compositions for carbon power supercapacitors, Journal of Power Sources, 80 (1999) 149-155.

[19] L.L. Zhang and X.S. Zhao, Carbon-based materials as supercapacitor electrodes, Chem. Soc. Rev., 38 (2009) 2520-2531.

[20] D. Hulicova-Jurcakova, M. Seredych, G.Q. Lu, and T.J. Bandosz, Combined Effect of Nitrogen- and Oxygen-Containing Functional Groups of Microporous Activated Carbon on its Electrochemical Performance in Supercapacitors, Adv. Funct. Mater., 19 (2009) 438-447.

[21] T.E. Rufford, D. Hulicova-Jurcakova, E. Fiset, Z. Zhu, and G.Q. Lu, Double-layer capacitance of waste coffee ground activated carbons in an organic electrolyte. Electrochemistry Communications, 11 (2009) 974-977.

[22] G.A. Ferrero, A.B. Fuertes, and M. Sevilla, N-doped microporous carbon microspheres for high volumetric performance supercapacitors. Electrochimica Acta, 168 (2015) 320-329.

[23] T. Liang, C. Chen, X. Li, and J. Zhang, Popcorn-Derived Porous Carbon for Energy Storage and CO_2 Capture. Langmuir, 32 (16-8-2016) 8042-8049.

[24] M. Thommes, K. Kaneko, A. Neimark, V, J.P. Olivier, F. Rodriguez-Reinoso, J. Rouquerol, and S.W. Sing Kenneth, Physisorption of gases, with special reference to the evaluation of surface area and pore size distribution (IUPAC Technical Report). Pure and Applied Chemistry, 87 (2015) 1051-1069.

[25] D.A.H. Hanaor and C.C. Sorrell, Review of the anatase to rutile phase transformation. Journal of Materials Science, 46 (2011) 855-874.

[26] A.R. Gonzalez-Elipe, P. Malet, J.P. Espinos, A. Caballero, and G. Munuera, Effect of Water in the Encapsulation of the Metallic Phase During Smsi Generation in Pt/TiO_2 Catalysts. Studies in Surface Science and Catalysis, 48 (1989) 427-436.

[27] M.E. Nagassa, A.E. Daw, W.G. Rowe, A. Carley, D.W. Thomas, and R. Moseley, Optimization of the hydrogen peroxide pre-treatment of titanium: surface characterisation and protein adsorption. Clinical Oral Implants Research, 19 (1-12-2008) 1317-1326.

[28] A. Samokhvalov, E.C. Duin, S. Nair, and B.J. Tatarchuk, An in situ temperature-programmed XPS study of the surface chemical reactions of thiophene with Ag/titania. Surface and Interface Analysis, 42 (1-9-2010) 1476-1482.

[29] M. Minakshi Sundaram, A. Biswal, D. Mitchell, R. Jones, and C. Fernandez, Correlation among physical and electrochemical behaviour of nanostructured electrolytic manganese dioxide from leach liquor and synthetic for aqueous asymmetric capacitor. Physical Chemistry Chemical Physics, 18 (2016) 4711-4720.

[30] D. Hulicova, M. Kodama, and H. Hatori, Electrochemical Performance of Nitrogen-Enriched Carbons in Aqueous and Non-Aqueous Supercapacitors. Chemistry of Materials, 18 (1-5-2006) 2318-2326.

[31] C. Delacourt, P. Ridgway, V. Srinivasan, and V. Battaglia, Measurements and Simulations of Electrochemical Impedance Spectroscopy of a Three-Electrode Coin Cell Design for Li-Ion Cell Testing. Journal of The Electrochemical Society, 161 (1-1-2014) A1253-A1260.

[32] C. Moreno-Castilla, M.B. Dawidziuk, F. Carrasco-Marín, and E. Morallón, Electrochemical performance of carbon gels with variable surface chemistry and physics. Carbon, 50 (2012) 3324-3332.

[33] K. Wang, Y. Song, R. Yan, N. Zhao, X. Tian, X. Li, Q. Guo, and Z. Liu, High capacitive performance of hollow activated carbon fibers derived from willow catkins. Applied Surface Science, 394 (1-2-2017) 569-577.

[34] E. Raymundo-Pinero and F. Béguin, Chapter 6 Application of nanotextured carbons for supercapacitors and hydrogen storage. Interface Science and Technology, 7 (2006) 293-343.

CHAPTER IX: *ELECTROCHEMICAL PERFORMANCES OF SUPERCAPACITORS FROM CARBON-ZrO_2 COMPOSITES*

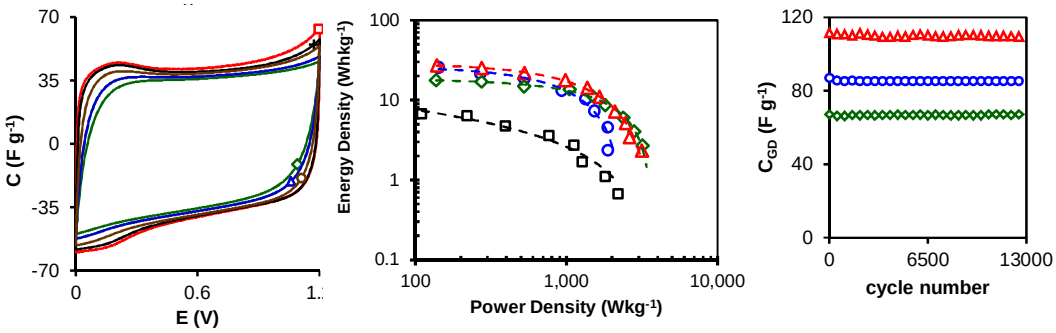

1. ABSTRACT

Carbon xerogel-ZrO_2 composites (CZrX) were successfully synthesized through a one-pot sol-gel synthesis. The XRD results confirm the presence of well dispersed (<4.5 nm) cubic ZrO_2 on the carbon support, homogeneously distributed on the carbon surface. Gas adsorption and mercury porosimetry measurement pointed out that the increase of ZrO_2 in the carbon matrix produces an increase in the mesopore volume as well as a widening of the microporosity at the expense of the narrow micropores (W_0 (CO_2)) that decreases causing simultaneously the progressive surface area decrease.

The presence of zirconium oxide in the carbon matrix improves in all case the capacitive behavior of samples in spite of the decrease of the surface area and micropore volume of the samples. It is notorious that capacitance increase with the increase of the amount of ZrO_2 up to 30 % and then decreases. That has been explained on the base of different textural properties and/or chemical characteristic of the material.

Keywords: Carbon-ZrO_2 composites; Energy storage.

2. INTRODUCTION

With the rising progress of global economy and industry, the impending energy crisis has stimulated intense research on the low cost, environmentally friendly, and renewable energy resources. Therefore, great efforts have been devoted to develop low cost electrode materials with high energy density, high power density, and excellent cycling stability. Carbon is one the best candidate for the use as electrode because of their high surface areas, large pore volume, and excellent mechanical stability [1].

Zirconium Oxide (ZrO_2) is an attractive material in various industrial applications due to its excellent textural proprieties as resistance, low cost high density. mechanical, thermal, optical and electrical characteristics [2,3]. Up to now, all those characteristics make them very good candidates to a broad range of applications and as one of the most industrially important materials has aroused interest and there have been lots of studies on the preparation of ZrO_2-carbon materials for various applications, such as catalyst supports for fuel cells [4], and transistors as advanced gate dielectrics [5].

Over the past few years, composites containing carbonaceous materials and inorganic nanoparticles have been intensively developed, and found to exhibit a range of unique and useful properties, which are attracting more and more attention from researchers [4,6,7]. This carbon composite containing carbon and inorganic metals have been intensively developed and they exhibit a properties which are different off from those of the each individual components in fact metals oxide-carbon composites present a good textural, chemical and physical proprieties which are more better than those of the each original components. For this purpose, many carbons composites are produced such as titanium composite carbon zirconium composite, ruthenium composite with well-defined structural, textural, and morphological properties. These nanostructured carbons are used extensively as electrode materials for batteries, fuel cells, and supercapacitors [1,4,8].

In the previous reports, we rarely found that zirconium carbon composite was applied in the supercapacitors [9-11]. The main reason is that the pure zirconium does not provide a high capacitance. In this work, ZrO_2–carbon composite materials with ZrO_2 particles incorporated in mesoporous carbon were prepared via hydrothermal method and the effect of the percentage of zirconium on the textural and electrochemical characteristics were studied. These composites were evaluated as a possible candidates electrode materials for supercapacitor using different techniques including cyclic voltammetry, electrochemical impedance spectroscopy and galvanostatic charge and discharge.

3. EXPERIMENTAL

3.1. Synthesis of ZrO_2-carbon xerogel composites

The ZrO_2-carbon xerogel composites were prepared using resorcinol-formaldehyde and zirconium alcoxide as precursors of carbon and zirconium oxide respectively, as described elsewhere, in details, a different amounts of zirconium propoxide was dissolved in 500 ml of n-heptane and heated at 70 °C under reflux and stirring (450 rpm). Then, a mixture containing resorcinol (R), formaldehyde (F) and water (W) was added dropwise into the above solution. The molar ratio of the mixture was R/F=1/2 and R/W=1/14. The gel formed was aged at 70 ºC for 24 h under stirring after which the suspension was filtered and the solid obtained was placed in acetone (5 days) to exchange water within the pores, in order to reduce the porosity collapse during the subsequent drying process. Then, the gel was dried by microwave heating using a Saivod MS-287W microwave oven under nitrogen atmosphere in periods of 1 minute at 384 W until constant weight.

The resulting xerogel was thermally treated at 900 ºC for 2 h at a heating rate of 1 °C min^{-1} under N_2 flow at 300 cm^3 min^{-1}. ZrO_2-Carbon xerogel composites were referred as CZrX (X correspond with the theoretical percentage of ZrO_2 present in the carbonized composite). A ZrO_2 sample was prepared by the same method but without adding R and F, Zr100.

3.2. Textural and Chemical Characterization

Textural characterization was carried out by N_2 and CO_2 adsorption at −196 ºC and 0 ºC, respectively, using Quantachrome Autosorb-1 equipment; samples were previously outgassed at 120 °C overnight at a final vacuum of 10^{-6} mbar. BET and Dubinin–Radushkevich equations were applied to determine the apparent surface area (S_{BET}) and the micropore volume (W_0) and the mean micropore width (L_0). Pore size distributions were also obtained by applying Quenched Solid Density Functional Theory (QSDFT) to the N_2 adsorption isotherms, assuming slit-shaped pores. Furthermore, the QSDFT method was used to calculate the mesopore volume of the samples (V_{mes}). The total pore volume was considered as the volume of N_2 adsorbed at $P/P_0 = 0.95$. Mercury porosimetry were used in order to determine the pore size distribution of pores larger than 6.6 nm.

The exact zirconium oxide content of samples was determined by thermogravimetric analysis (TGA). TGA was performed in air flow with a heating rate of 10 ºC min^{-1} using a Mettler-Toledo TGA/DSC1 thermobalance.

The crystallinity of the sample as well as the crystalline phase were analysed by X-ray difraction using a Bruker D8 Advance X-ray diffractometer with Cu Kα radiation at a wavelength (λ) of 1.541 Å. The 2θ angles were scanned from 20 to 70°. The average crystallite sizes (D) were estimated by the Debye-Scherer equation, $D = 0.95\lambda/\beta \cos\theta$, where θ is the diffraction angle and β is the full width at half-maximum (fwhm).

The surface chemistry of the carbon sample was studied by X-ray photoelectron spectroscopy using an Escalab 200R system (VG Scientific Co.) equipped with MgKα X-ray source ($h\upsilon$ = 1253.6 eV) and hemispherical electron analyzer. Survey and multi-region spectra were recorded at C_{1s}, O_{1s}, and Zr_{3d} photoelectron peaks. Each spectral region of photoelectron interest was scanned several times to obtain good signal-to-noise ratios. For the analysis of the XPS peaks, the C_{1s} peak position at 284.6 eV was used as reference to locate the other peaks. The fitting of the XPS peaks was done by least squares using Gaussian-Lorentzian peak shape.

3.3. Electrochemical Characterization

For the electrochemical characterization, a mixture of active material and tetrafluoethylene (PTFE) (60 % suspension in water) binder with the ratio of 90:10 was dried in oven at 120 °C overnight. For the supercapacitor preparation, 5 mg of the active material was pressed onto disc graphite paper with 9 mm in diameter. The pasted sample was impregnated with H_2SO_4 1 M for 72 h before to be used for the electrochemical measurements.

The electrochemical performances were determined using system of two electrode with a, EC-lab system from Biologic at 25 °C in H_2SO_4 1 M medium as electrolyte and glassy fibrous materials as separator. Several electrochemical techniques were used; cycling voltammetry test (CV) was carried within the range of 0 and 1.2 V; using scan rates of 0.5, 2.5, 5, 10, 20 and 30 mV s^{-1}. Galvanostatic charge-discharge was carried at different current density for 125 mA g^{-1} to 7 A g^{-1}. Gravimetric capacitance was calculated using Equation (1) [12,13]:

$$C_{GD} = \frac{I_d \times \Delta t}{m \times \Delta V} \quad \text{(Eq. 1)}$$

where I_d was the current density (A g^{-1}), Δt was the discharge time, ΔV was the voltage interval without the IR drop and m is the total mass active (g). The equivalent series resistance (ESR_{GD}) was determined from the ohmic drop at the beginning of the discharge curve [14], Equation 2;

$$R = \frac{\Delta V}{2I} \quad \text{(Eq. 2)}$$

Cyclic voltammetry (CV) and galvanostatic charge-discharge (GCD) were carried out using a Biologic VMP-300 potentiostat. CVs and GCDs were performed in the 0-0.85 V range, at a scan rate of 2.5 mV s^{-1} for CVs and current densities between 0.14 and 5 A g^{-1} for GCDs.

The EIS measurements were carried out in the frequency range of 100 kHz to 1 mHz with a sinusoidal signal amplitude of 10 mV. The capacitance value, C_{max}, was obtained by Equation 3

$$C_{max} = \frac{-Z''}{2\pi f|Z|^2} \quad \text{(Eq. 3)}$$

where f was the frequency and $|Z|^2 = |Z'^2| + |Z''^2|$, where Z' and Z" are the real and imaginary parts of the complex impedance, respectively [15].

For comparison reasons, the gravimetric capacitances in 2EC obtained from the these techniques were multiplied by 4 to obtain the capacitance per single electrode, which is the 3EC equivalent [16] being named C_{CP} and C_{EIS} respectively.

The electrical energy and power densities were calculated by using the Equations 4 and 5, respectively applied to the galvanostatic measurements [14,17]:

$$E(Wh\,kg^{-1}) = \frac{C_{GD}\,(F\,g^{-1}) \times \Delta V^2(V)}{2 \times 3.6} \quad \text{(Eq. 4)}$$

$$P(W\ kg^{-1}) = \frac{1}{2} \times \frac{I(A) \times \Delta V(V)}{m\ (kg)} \quad \text{(Eq. 5)}$$

Current charge-discharge cycling and floating tests where measured in order to determine the stability of the electrodes. Current charge-discharge cycling over 12500 cycles at current density of 4 A g^{-1} between potential range of 0 and 1.2 V were measured, the capacitance was calculated after the IR drop has been subtracted were used in order to study the stability of supercapacitors. The floating test is described as follows [14]: after every 10 h of aging, five constant current galvanostatic charge-discharge sequences at current density of 1 A g^{-1} between potential range of 0 and 1.2 V were recorded and the specific capacitance was calculated from the first and fifth discharge. These sequences were repeated 24 times, i.e. a total floating time of 240 h. The resistance (ESR_F) which is a measure

of the conductivity of the material was also estimated from the IR drop at the initial step of the discharge curve.

4. RESULTS AND DISCUSSION

4.1. Textural and chemical characterizations

The exact amount of ZrO_2 in the final CZrX carbon composites was determined by burning of the carbon phase by TGA. The final residual mass after TGA experiments was considered as the inorganic phase amount. In this way, the real % of ZrO_2 on the carbonized composites were 24.1 34.3 and 45.1 wt. % for CZr20, CZr30, and CZr40, respectively. Comparing TGA results with the theoretical ones, it is observed that the real percentages are slightly higher than the theoretical ones due to the weight loss undergoes by the samples during carbonization also slightly exceed the 50% programmed.

The ZrO_2 crystalline phase was studied by powder XRD measurements (Figure 1). In ZrO_2 pure phase (Zr100), narrower and intense diffraction peaks were observed denoting a high crystallinity. However, diffraction peaks become wider and less intense in the case of composites CZrX, independently of the ZrO_2 content. Moreover, regarding the crystalline structure, monoclinic phase is observed for the commercial ZrO_2 sample, while cubic is obtained in composites, in spite that all composites samples were obtained at 900 ºC, where the monoclinic phase should be stabilized. The assignation of these phases was carried out according to the bibliography. Thus, although is difficult to distinguish between tetragonal (t) and cubic (c) phases due to the proximity of the main diffraction peaks in both phases, it was reported [18] that the tetragonal phase is characterized by the split of the (400) diffraction peak observed at 75 º into two components. Because in CZrX composites only one peak is observed in this region, the cubic phase was suggested as the predominant crystalline structure in these samples.

It has also been reported that the stability of the different crystalline structure of ZrO_2 strongly depends on the crystal size. Jayakumar et al. [19] show the significance of particle size in stabilizing the metastable phases. They observed

that the cubic phase could be stabilised at particle size below 6 nm; the tetragonal phase is found to be stable at particle size above 6 nm and below 20 nm and the monoclinic phase is stabilized in large particles (>20nm) The mean average size of ZrO_2 particles estimated by the Debye-Scherer equation were 4.8, 4.7, 4.2, and 39.3 nm for CZr20, CZr30, CZr40 composites and bulk ZrO_2, respectively. This denotes a good dispersion of ZrO_2 nanoparticles in the carbon xerogel framework and is also in agreement with the stabilization of the cubic phase observed in composite materials and monoclinic phase in bulk zirconia. XRD therefore, confirms that the carbon phase avoid the formation of large ZrO_2 crystallites that remains in the cubic phase, avoiding the monoclinic transformation in spite of the high temperature of the treatment.

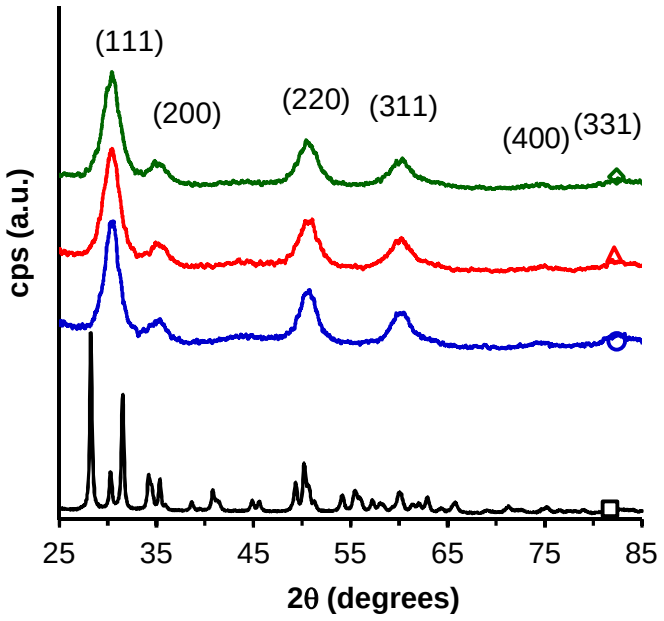

Figure 1. Powder XRD patterns of samples: Zr100, □; CZr20, ○; CZr30, △; CZr40, ◇.

Textural properties have also greatly influenced by the increase of ZrO_2 content in the composite. The pore texture of samples was studied by N_2 and CO_2 adsorption measurements, N_2 adsorption isotherms are depicted in Figure 2 and results of the application of BET and DR methods are collected in Table 1.

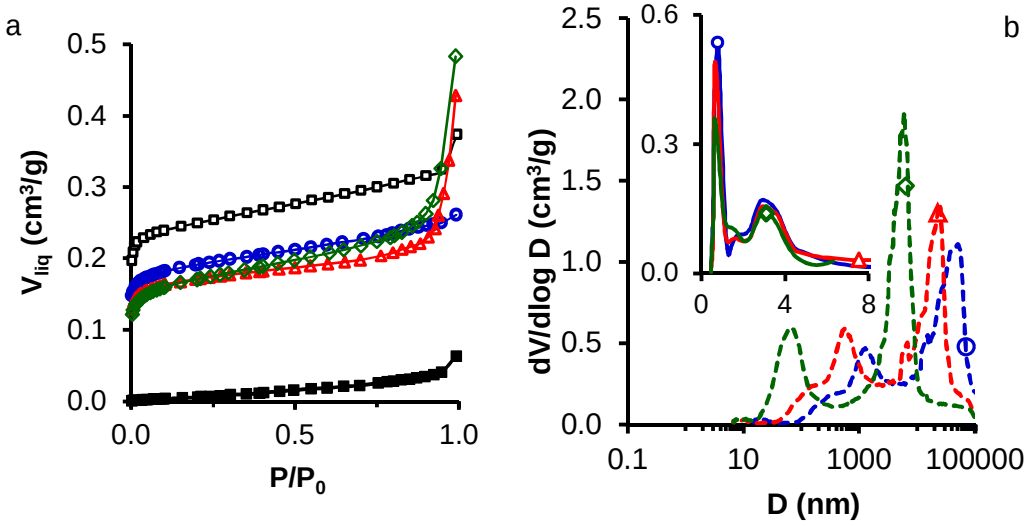

Figure 2. a) N_2 adsorption isotherms at -196 °C. b) Pore size distribution obtained by Hg porosimetry. Insert in b) Pore size distribution obtained by QSDFT applied to N_2 adsorption data. Samples: Zr100, ■; C100, □; CZr20, ○; CZr30, △; CZr40, ◇.

All isotherms exhibit a mixture of type I and IV isotherms, which is characteristic of micro-mesoporous materials. The formation of certain hysteresis cycles, but mainly, the N_2-adsorption is favored at high P/P_0 with increasing the ZrO_2 content. These facts are indicative of the progressive mesoporosity of samples in this sense as denoted the (V_{mes}) obtained. The composites become more mesoporous, V_{meso} increases with increasing the ZrO_2 fraction dispersed into the carbon xerogel matrix (Figure 3a). In this sense, the microporosity becomes also widest (L_0 (N_2) increases, Figure 3b)) at the expense of the microporosity (W_0

(CO_2)) that decreases causing simultaneously the progressive surface area decrease (Figure 3a). It is well known that the CO_2 adsorption provides information about the narrow microporosity, corresponding to micropores with diameter lower than 0.7 nm, while the total microporosity is obtained from N_2 isotherm only in absence of diffusion restrictions. In that sense, all samples show W_0 (N_2) < W_0 (CO_2) indicating diffusion restrictions of N_2 into the microporosity due to a narrower micropores and ultramicropores, but this difference is lower increasing the % ZrO_2 and as consequence, with the mesopore volume, being W_0 (N_2) = W_0 (CO_2) for CZr40 due to the opening of the porosity and reduction of narrowest micropores described above (Table 1).

Table 1. Textural properties of the carbon zirconium composites**.**

	N_2					CO_2		Hg	
Sample	S_{BET}	$W_0(N_2)$	$L_0(N_2)$	$V_{0.95}$	V_{mes}	$W_0(CO_2)$	$L_0(CO_2)$	V_2	V_3
	$m^2\ g^{-1}$	$cm^3\ g^{-1}$	nm	$cm^3\ g^{-1}$		$cm^3\ g^{-1}$	nm	$cm^3\ g^{-1}$	
C100	611	0.245	0.74	0.325	0.080	0.285	0.60	n.d.	n.d.
CZr20	465	0.182	0.97	0.250	0.068	0.213	0.56	0.015	1.150
CZr30	418	0.167	1.02	0.338	0.261	0.183	0.55	0.015	1.321
CZr40	391	0.154	1.16	0.434	0.382	0.156	0.58	0.125	1.271
ZrO_2	36	0.002	1.80	0.046	0.044	---	---	n.d.	n.d.

n.d. Not determined

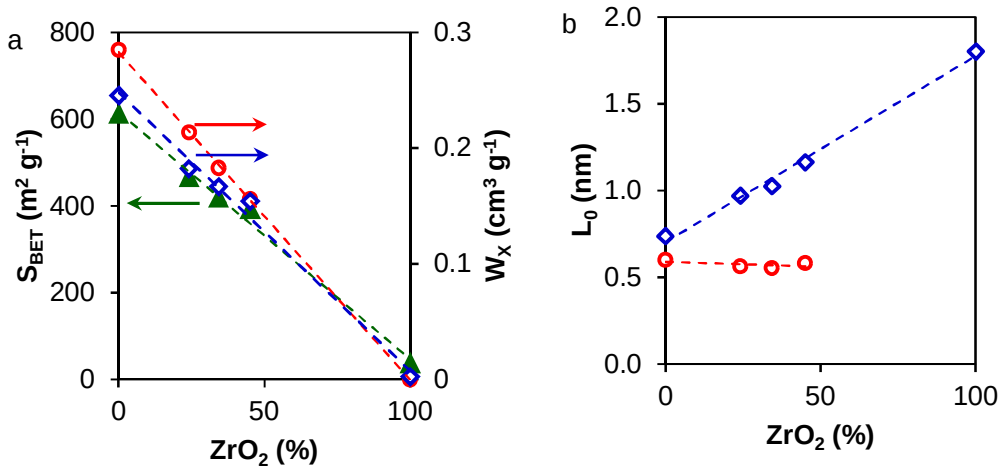

Figure 3. Dependence of textural properties with % ZrO_2. a) S_{BET}, ▲; $W_0(N_2)$, ◇; $W_0(CO_2)$, ○. b) $L_0(N_2)$, ◇; $L_0(CO_2)$, ○.

Macro and mesopore volumes are collected in Table 1 and Figure 2b despicts the pore size distributions obtained by mercury porosimetry. Although the macropore volume is more or less independent of the ZrO_2 content of the composite, their PSD change significantly, becoming progressively narrower with increasing the ZrO_2 in such a manner that the formation of mesopores is favoured. Figure 2b point out that CZr20 is a macroporous solid (without mesopores), with a monomodal macropore size distribution showing a maximum for macropores with a diameter at around 26 μm. With increasing the ZrO_2 content the macroporosity become narrowest and more heterogeneous. In the case of CZr40 the PSD presents two maxima, the first one includes the mesoporosity range, being centered in pores with a diameter of around 50-60 nm, the second maxima correspond to larger macropores, with a diameter at around 6 μm. It is noteworthy however that even these large macropores are narrower than those detected for CZr20. This bimodal PSD is also observed in the case of CZr30, with present an intermediate behavior between CZr20 and CZr40.

The morphology of the samples was analysed by scanning electron microscopy. Representative images are shown in Figure 4. In sample CZr20 the formation of large and smooth particles is observed, this fact progressively diminish with increasing the ZrO_2 content. Spherical primary particles are progressively more easily identified at the sample surface, although they are highly overlapped in all cases forming a coral-like three-dimensional structure. That morphological differences corroborates the pore size distributions obtained by mercury porosimetry.

Surface compositions of CZrX samples were analyzed by XPS technique which provided information regarding the electronic states and chemical environment of carbon (C), zirconium (Zr), and oxygen (O) atoms in the composite materials. Figure 5 shows wide-survey XP spectra in the full range of the BE, scanned from 0 to 1200 eV, which provided both a compositional overview and information about main elemental components in CZr10, CZr20, and CZr30. All CZrX samples produced three different peaks, a strong C_{1s} peak between 282 and 289 eV, one O_{1s} peak was also observed at 532 eV and finally, all the samples show the presence of Zr_{3d} and Zr_{3p} peaks. The intensity of these peaks increases with the increase of the zirconium percentage indicating an increase in Zr and O surface concentrations.

The results obtained from the deconvolution of all the XP spectra are shown in the Table 2. All the samples show six carbon components, the main carbon peak is found at 284.6 eV, which corresponds to the non-oxygenated amorphous carbon. Another peak at 285.4 eV may be assigned to graphitic carbon, and the others peaks between 286.4 and 290.6 eV may be attributed to carboxylate carbon. It is necessary to note that there is no carbon peaks associated with zirconium carbide (CZr, BE for C_{1s}, 282.9 eV) in the spectra for any of the CZrX samples, suggesting that no carbothermal reduction took place during the synthesis [20,21].

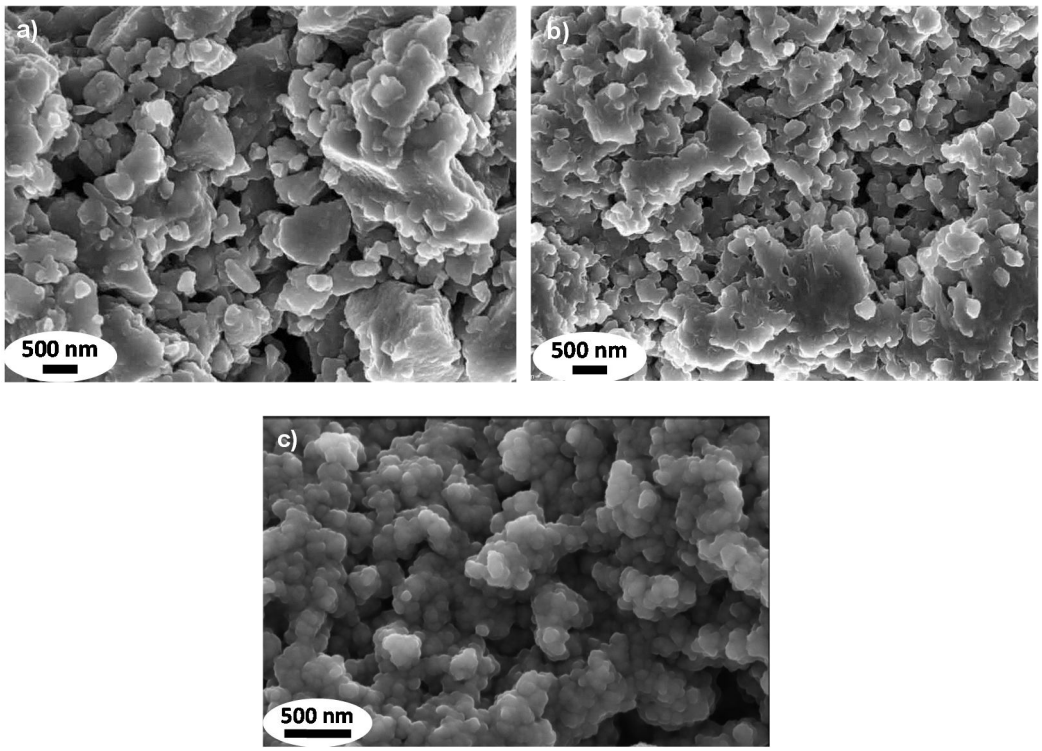

Figure 4. SEM images of a) CZr20, b) CZr30 and c) CZr40

Furthermore, the O1s spectra of CZrX composites would contain two primary contributions, one from carbon surface oxygen and the other from oxygen in ZrO_2. The O1s component associated to the Zr–O–Zr appears at 530.2 eV [22]. Additional components correspond to the formation of oxygenated surface groups like Zr–O–H (531.8 eV) or physisorbed water H-O-H (532.7 eV). For pure carbon phases, the O1s spectrum shows typically two components at 532.0 eV due to double C=O bonds from ketones and carboxylic acids, and at 533.9 eV due to single C–O bonds from alcohols, phenols and carboxylic acids [23]. In the composites, clearly the O1s of Zr-O-Zr is shifted to higher B.E. (between 0.4 - 0.5 eV higher). The second peak in this case can present also the contribution of surface groups on the inorganic phase as the C=O component of the carbon phase. Nevertheless, the last peak is clearly due to the C-O bonds. Moreover, this

assignation is confirmed by the fact that the first component increases progressively with increasing the Zr-content in the composite.

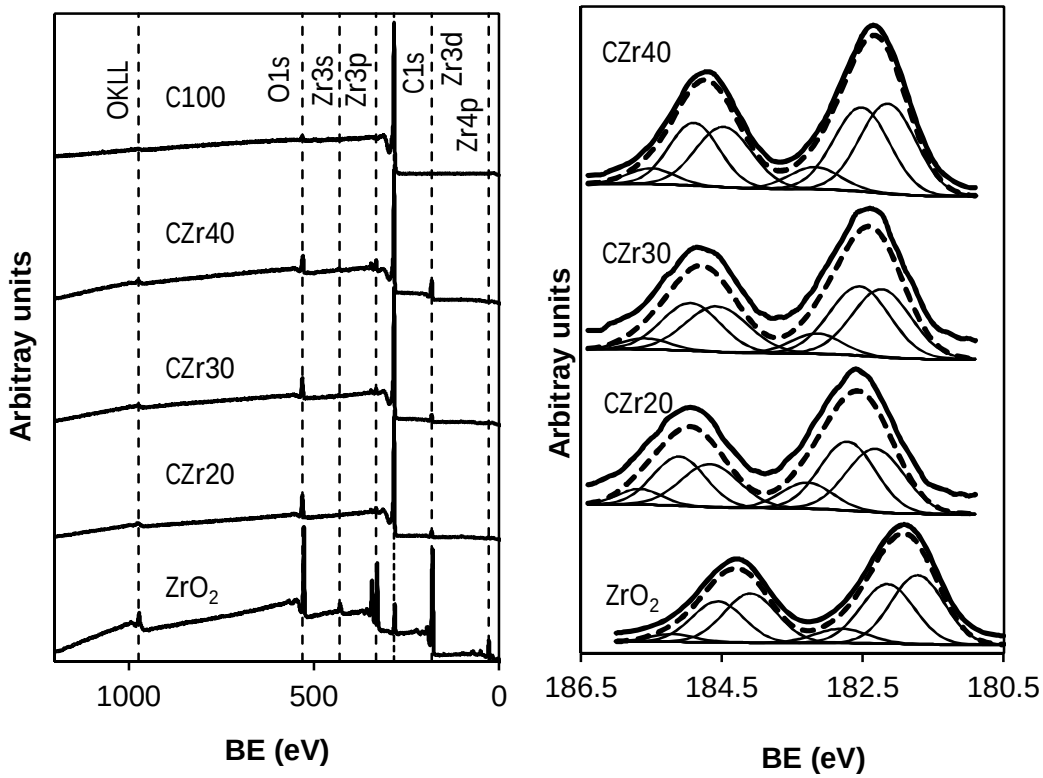

Figure 5. Survey and deconvolution of the Zr_{3d} XP spectra.

Analyzing the $Zr_{3d5/2}$ region (Figure 5 and Table 2), a peak centered at 182 eV assigned to Zr^{4+} is obtained in stoichiometric ZrO_2. However, three components are required to fit the Zr signal in the composites. For non-stoichiometric oxides (ZrO_y $0<y<2$) the Zr $3d_{5/2}$ band shifted to higher B.E. 182.8 eV [24]. This behavior is observed clearly in all the composite samples (Figure 5), with a shift of about 0.5 eV and the formation of different suboxides. The surface composition of the samples is summarized in Table 2. The Zr and O contents do not increase proportionally to the inorganic ratio in the composite. Moreover, the ZrO_2 content in surface (detected by XPS) is significantly smaller than in the bulk of the composite (detected by TG).

Table 2. Results obtained from the deconvolution of XP Spectra.

Sample	C_{1s}	Peak	O_{1s}	Peak	Zr_{3d}	Peak	C_{XPS}	O_{XPS}	Zr_{xps}
	eV	%	eV	%	eV	%	wt. %	wt. %	wt. %
C100	284.6	74	531.7	42			96.4	3.6	0.0
	285.5	14	533.1	58					
	286.5	5							
	287.4	3							
	289.1	3							
	290.6	1							
CZr20	284.6	66	530.4	17	182.3	41	88.9	7.2	3.9
	285.5	17	532.3	59	182.7	43			
	286.5	8	533.8	24	183.3	16			
	287.4	3							
	289.1	4							
	290.6	1							
CZr30	284.6	67	530.3	21	182.2	44	89.9	5.8	4.3
	285.4	18	532.3	49	182.5	45			
	286.5	6	533.9	30	183.2	11			
	287.4	4							
	289.1	4							
	290.7	2							
CZr40	284.6	68	530.2	44	182.1	46	83.3	6.0	10.7
	285.4	16	532.0	37	182.5	43			
	286.4	5	533.7	19	183.2	11			
	287.3	4							
	289.1	3							
	290.6	2							
ZrO_2	284.6	73	529.8	61	181.7	48		44.6	55.4
	286.1	17	531.4	31	182.2	42			
	288.7	10	533.8	8	182.8	10			

This fact can be consequence of the different crystal structure of pure ZrO_2 and ZrO_2 in the composites, a certain crystal growth or to the encapsulation of ZrO_2 nanoparticles by the carbon phase, which can be in agreement with the intimate interactions between the phases needed to the doping character of the carbon phase previously showed. This is also confirmed by the significant increase of suboxides proportion in the composites with the formation of a third component at 183.2 eV. Nevertheless, the proportion of the different Zr components in the different composites are quite similar between then, denoting again that in all cases the inorganic nanoparticles can present similar nature and dispersion.

4.2. Electrochemical characterization of the ZrO_2 carbon composites

CV, EIS, floating test and galvanostatic charge/discharge measurements were performed to explore the advantages of zirconium carbon composites as electrochemical supercapacitors using a 1 M H_2SO_4 electrolyte.

Figure 6a shows the cyclic voltammetries of the samples. CVs exhibit a rectangular shaped profile characteristic of an ideal capacitive behavior [25], moreover this behavior remain stable in the range of scan rate studied, Figure 6b.

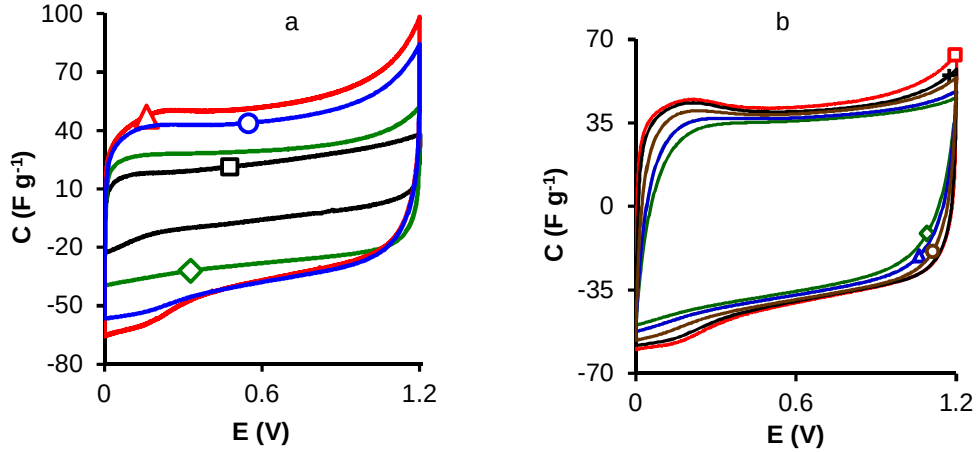

Figure 6. a) Cyclic voltammetries at 0.5 mV s^{-1} for samples: C100 (□); CZr20 (○), CZr30 (△) y CZr40 (◇). b) Cyclic voltammetries for sample CZr30 at different scan rate: 2.5 mV s^{-1}(□); 5 mV s^{-1}(+); 10 mV s^{-1} (○); 20 mV s^{-1} (△); 30mV s^{-1} (◇);

Figure 6b depicts cyclic voltammetries for sample CZr30 at different scan rate. Usually, as the scan rate increases the current versus potential relation of CV would deviate from the classical square waveform, expected for a pure capacitor due to the resistance effects down the pores [30]. The capacitance variations against the scan rate is because of the formation of the electrochemical double-layer within the micropores is slower and less complete in comparison to the rate of variation of the potential. The capacitance decreases with the increase of the scan rate because of the difficulty of the formation of the electrochemical double layer in the micropores at high scan rate. That decrease is depicted in Figure 6b, it is notorious, that the decrease is not very pronounced for CZr30 sample due to the well-developed micro and mesoporosity of the sample which improve the electrolyte diffusion into the pores.

Chronopotentiograms (CPs) obtained are depicted in Figure 7a at a current load of 125 mA g^{-1}. CPs show quasi-triangular shapes which indicates again that samples behave as an ideal electrochemical double-layer (EDL) performance with low resistance and a good diffusion of the electrolyte inside the pores.

From Fig. 6 and 7a, it is also evident that the presence of zirconium oxide in the carbon matrix improves in all case the capacitive behavior of samples in spite of the decrease of the surface area and micropore volume of the samples in comparison with the pure carbon. It is notorious that capacitance increase with the increase of the amount of ZrO_2 up to 30 % and then decreases. That could be explained on the base of different textural properties and/or chemical characteristic of the material. Comparing C100 and ZrC20 sample, they present similar pore width but the presence of 20 % of ZrO_2 induces a decrease in a 26 % the micropore volume. However the capacitance increase 130 % with the presence of ZrO_2 (Table 3).

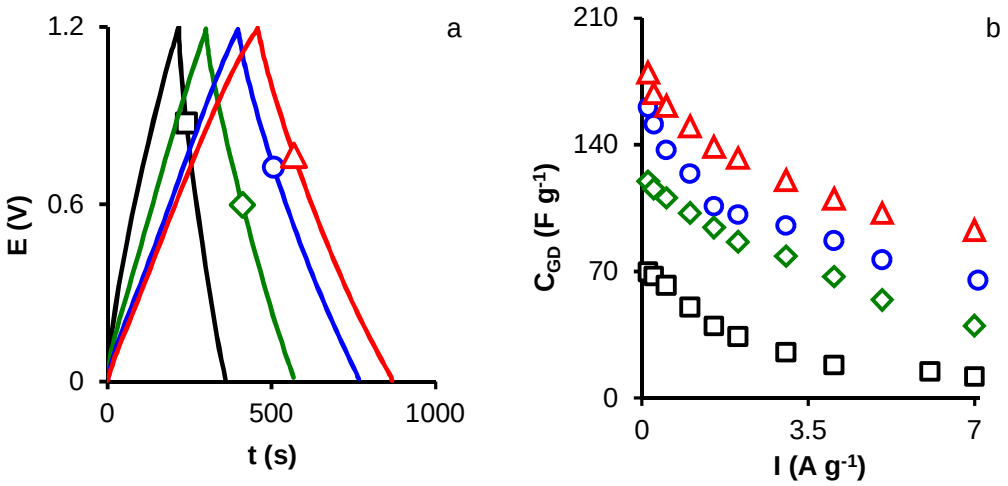

Figure 7. (a) Charge discharge curves at 0.125 A g^{-1}. (b) Variation of the capacitance with the current density, samples: C100 (□); CZr20 (○), CZr30 (△) y CZr40 (◇)

Table 3. Electrochemical performances of the composites from chronopotentiometry and impedance spectroscopy

Sample	C_{GD} 0.125 A g^{-1}	C_{GD} 7 A g^{-1}	R_{GD}	C_{EIS}	ESR	R_{CT}
	F g^{-1}	F g^{-1}	%	F g^{-1}	Ω	Ω
C100	70	12	17	65	0.60	2.76
CZr20	161	65	40	173	0.23	3.36
CZr30	180	93	52	203	0.39	2.85
CZr40	120	40	33	114	0.37	2.09

R_{GD} Retention capacitance at 7 A g^{-1} referred to 0.125 A g^{-1}

It is well know that capacitance depend on the surface area as well as the pore diameter. Many authors have found an increase in capacitance increasing the surface area of carbon materials [26-28]. In that case the opposite trend is observed. Surface area of the samples decreases as increase the ZrO_2 content and capacitances obtained present a maximum for sample CZr30 even though the

similar pore width, and mesopore volume. These variations could not be explained on the base of different diffusional restriction to the electrolyte into the pore wherefore that could be related with the presence of partially reduced species in the zirconium oxide present in the carbon matrix. These partially reduced species can act as electron transfer sites improving the electrical conductivity and enhancing the pseudocapacitance.

Regarding the ZrO_2 composite series, three factor must be taken into account to discuss the variation of capacitance: amount of ZrO_2, pore volume and pore width. Most of studies in literature suggest an increase of the specific capacitance with increasing the average pore size [29], in this study, the results show that the increase of the pore size increases the specific capacitance but when the pore size is more than 1.05 nm, the capacitance decreases in 1 M H_2SO_4 as electrolyte. An increase in ZrO_2 content from 20 to 30, increase the capacitance instead of lower surface area and micropore volume while an increase from 30 to 40 induces a decrease. That is related with the pore width and the amount of ZrO_2. In spite of the reduction of the microporous texture, the opening of the microporosity together with the presence of more ZrO_2, favors the capacitive behavior of the sample. Higher content in ZrO_2 produces a pore size higher than 1.05 nm together with the reduction of microporous texture having a more negative effect than the ZrO_2 beneficial one. Thus compromise situation must be take into account between the beneficial effect of the presence of ZrO_2, the reduction of microporous texture and the opening of the porous diameter.

Figure 7b shows the variation of the specific capacitance with the increase of the current density of the carbon and the three ZrCX composites. It is know that at lower current density, samples show the highest value of capacitance but this value decrease when increase the current density. This fact can be explained by the electric resistance and diffusion restriction into the pore at high current density. Sample ZrC30 shows the best retention capacity (Table 3) which can be explained on a basis of the adequate pore diameter of the sample and the presence of ZrO_2. Thus, when the zirconium percentage increases from 20 to 30, the pore volume

decreased but the pore diameter increase and the capacitance increased as well as the retention capacity. So, one of the keys parameter for an optimal capacitance is the pore diameter. On the contrary when the zirconium percentages increases from 30 to 40, the capacitance decreases which indicate that the effect of pore volume reduction was more important than the increase of the pore diameter, as has been discussed above. Consequently, the 30 % of zirconium oxide is the optimal content of ZrO_2 to prepare carbon zirconium composite with a good electrochemical characteristics.

EIS measurements were performed to investigate the charge kinetic properties of the composites towards the capacitive behavior. Figure 8 shows the Nyquist plots, showing that all samples exhibited typical characteristics of porous carbon electrodes [31]. In the high frequency region, the first intersection point on the real axis (Z') was the ESR, which was related to three resistances: the intrinsic resistance of the active material, the electrolyte resistance, and the active material/current collector interface. Results, shown in Table 4, can be considered to reflect the resistive properties of the electrodes for comparison purposes, because the same electrolyte, collectors, and technique were used to assemble the cell [32]. ESR values were very low, ranging between 0.3-0.4 Ω for composites and 0.6 Ω for the carbon xerogel.

In the high-medium frequency region, a semicircle was observed associated with charge transfer process, which it is indicative of the presence of pseudocapacitive effects. The interfacial charge transfer resistance, R_{CT}, caused by EDL capacitance and faradic reactions was estimated from the two intercepts of the semicircle with the real axis (semicircle diameter) [31], and the values obtained are displayed in Table 4. The highest R_{CT} value was obtained for sample CZr30 which indicate that this is the sample where the pseudofaradic effects are more important.

The differences in the ESR and R_{CT} values between samples can be explained by the difference of the pore size diameter and also due to the different conductivity of the composites which depends of the content of the composites of

zirconium. These results can also explain the difference of capacitance retention of the composites with the variation of the current density. Figure 9 shows the correlation between the ESR and R_{CT} with the mean pore size diameter and, it confirms that both resistances depends on the pore diameter and consequently on the ZrO_2 content, Figure 3b.

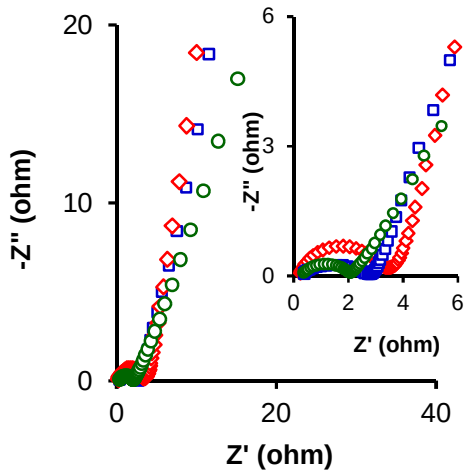

Figure 8. Nyquist plot for composites CZr20 (○), CZr30 (△) y CZr40 (◇)

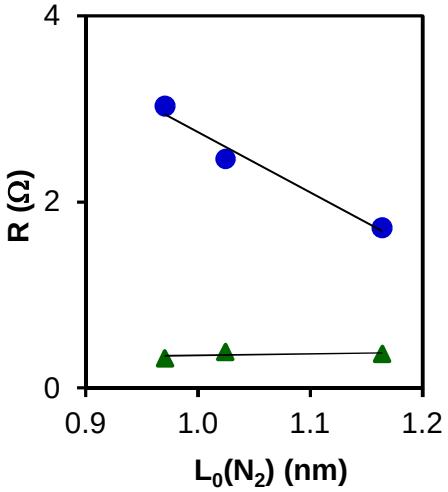

Figure 9. Variation of ESR (▲) and R_{CT} (●) with the micropore diameter $L_0(N_2)$.

The Ragone plots of the samples are shown in Figure 10. This figure shows the dependence between the energy and power density. The maximum energy density was released at the lowest power density (140 W Kg^{-1}), as shown in Table 4.

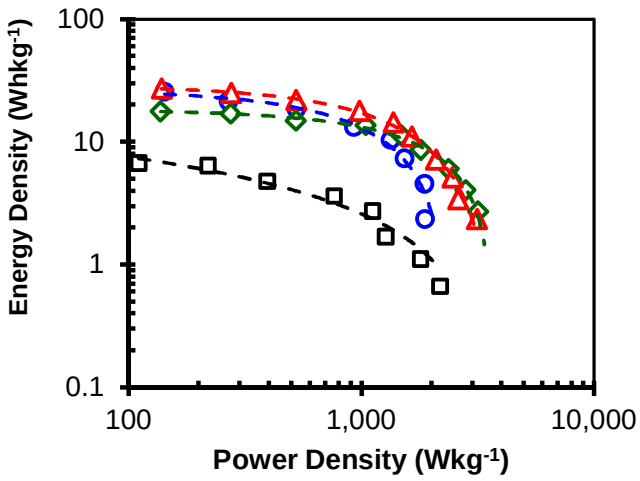

Figure 10. Ragone plots of samples samples: C100 (□); CZr20 (○), CZr30 (△) y CZr40 (◇)

Table 4. Energy density at 140 W kg^{-1}, E_{max}, and at 1800 W kg^{-1}, E_{min}, (Wh Kg^{-1}) from Ragone's plots

Sample	E_{max}	E_{min}
C100	6.6	1.1
CZr20	25.6	4.6
CZr30	27.1	9.8
CZr40	17.7	8.6

The maximum energy density increased with the presence of ZrO_2, the maximum energy density for carbon ZrO_2 composites is at least three times higher with being for times higher for sample CZr30. These results were attributed, as before, to variations in the pore structure and to the presence of the Zr oxides which improve the wettability and the mobility of the ions in the microporous

network. The energy density decreased at higher power density, E_{min}, (Table 4). Sample CZr30 showed the highest energy density of all sample that is capable of storing up a 21 % of the energy in the power density range.

The cyclic stability of supercapacitors is a crucial parameter for their practical applications. This stability was evaluated by the voltage-holding or floating test Figure 11a, which was established [14,33,34] as a reliable test alternative to the traditional method of galvanostatic charge-discharge cycles at constant current density over several thousands of cycles, Figure 11b. The floating test was carried out by applying a critical voltage cell (1.2 V) during 10 h and after that studying five charge-discharge cycles between 1.2 and 0 V at a constant current density of 1 A g^{-1}. The respective capacitance and the resistance from the IR voltage drop is determined from the first and fifth cycles. 12500 galvanostatic charge-discharge cycles were applied over at a current density of 4 A g^{-1}. Figure 11, indicates that the variation of specific capacitance of all the samples obtained by both methods, it clear that all the composites show good capacitance retention ≈ 98 %, whereas the galvanostatic resistance is practically constant during the 240 h test.

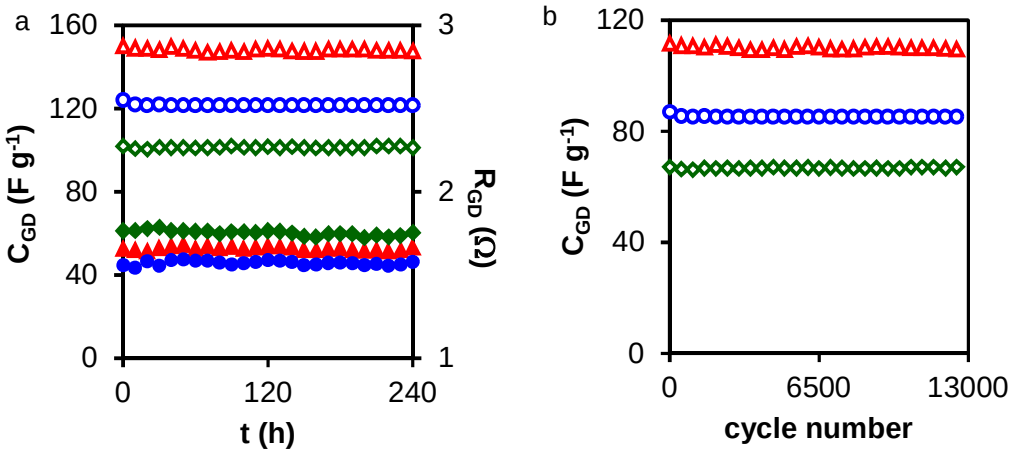

Figure 11. (a) Floating test at current density of 1 A g^{-1}, (b) Charge discharge cycles at current density of 4 A g^{-1} for composites CZr20 (○), CZr30 (△) y CZr40 (◇). Open symbols capacitance. Closed symbols resistance.

5. CONCLUSIONS

A series of a carbon xerogel doped with different percentages of ZrO_2 has been explored as a tentative via to prepare electrodes for supercapacitors. Carbon composites were obtained by an inverse emulsion method in n-heptane and after carbonization at 900 ° the metal oxide phase is well dispersed on the carbon phase, with a crystal size smaller than 4. Cubic phase is obtained in composites, in spite that all samples were obtained at 900 ºC, where the monoclinic phase should be stabilized. Gas adsorption and mercury porosimetry measurement pointed out that the increase of ZrO_2 in the carbon matrix produces an increase in the mesopore volume as well as a widening of the microporosity at the expense of the narrow micropores (W_0 (CO_2)) that decreases causing simultaneously the progressive surface area decrease. XPS results shown that non-stoichiometric oxides (ZrO_y: $0<y<2$) are present on the surface of the samples and these partially reduced species can act as electron transfer sites improving the electrical conductivity and enhancing the pseudocapacitance. A two-electrode symmetric supercapacitor based on the carbon xerogel-ZrO_2 composites exhibits a high electrochemical performance with a capacitances (up to 180 F g^{-1} at 0.125 A g^{-1} for 30 % ZrO_2 composite), a high retention capacitance and high energy density, 27.1 Wh kg^{-1}, at a power density of 140 W kg-1 in the voltage range of 0 V to 1.2 V. Sample with an optimum combination of an adequate micro-mesopore network, pore width and amount of ZrO_2 shows the best performance for energy storage. Floating test shows a very good cyclability of the synthetized materials.

6. REFERENCES

[1] A.C. Pierre and G.M. Pajonk, Chemistry of Aerogels and Their Applications, Chem. Rev., 102 (202) 4243-4266.

[2] Z. Lu, Z. Zhu, X. Zheng, Y. Qiao, J. Guo, and C.M. Li, Biocompatible fluorescence-enhanced ZrO_2-CdTe quantum dot nanocomposite for in vitro cell imaging, Nanotechnology, 22 (2011) 155604.

[3] K. Tomishige, Y. Furusawa, Y. Ikeda, M. Asadullah, and K. Fujimoto, CeO_2–ZrO_2 Solid Solution Catalyst for Selective Synthesis of Dimethyl Carbonate from Methanol and Carbon Dioxide, Catalysis Letters, 76 (2001) 71-74.

[4] D.J. Guo, X.P. Qiu, W.T. Zhu, and L.Q. Chen, Synthesis of sulfated ZrO_2/MWCNT composites as new supports of Pt catalysts for direct methanol fuel cell application, Applied Catalysis B: Environmental, 89 (2009) 597-601.

[5] G.D. Wilk, R.M. Wallace, and J.M. Anthony, High-k gate dielectrics: Current status and materials properties considerations, Journal of Applied Physics, 89 (2001) 5243-5275.

[6] P.H.C. Camargo, K.G. Satyanarayana, and F. Wypych, Nanocomposites: synthesis, structure, properties and new application opportunities, Materials Research, 12 (2009) 1-39.

[7] C.M. Perkins, B.B. Triplett, P.C. McIntyre, K.C. Saraswat, and E. Shero, Thermal stability of polycrystalline silicon electrodes on ZrO_2 gate dielectrics, Applied Physics Letters, 81 (2002) 1417-1419.

[8] P.J. Harrop and D.S. Campbell, Selection of thin film capacitor dielectrics, Thin Solid Films, 2 (1968) 273-292.

[9] M.G.H.M. Hendriks, W.E. Zyl, J.E. Elshof, and H. Verweij, Capacitance at ambient temperature and microstructure of platinum/yttria-stabilized zirconia composites, Materials Research Bulletin, 36 (2001) 2395-2406.

[10] M.G.H.M. Hendriks, J.E. Elshof, H.J.M. Bouwmeester, and H. Verweij, The electrochemical double-layer capacitance of yttria-stabilised zirconia, Solid State Ionics, 146 (2002) 211-217.

[11] M. Nasibi, M.A. Golozar, and G. Rashed, Nano zirconium oxide/carbon black as a new electrode material for electrochemical double layer capacitors, Journal of Power Sources, 206 (2012) 108-110.

[12] L.L. Zhang and X.S. Zhao, Carbon-based materials as supercapacitor electrodes, Chem. Soc. Rev., 38 (2009) 2520-2531.

[13] D. Hulicova-Jurcakova, M. Seredych, G.Q. Lu, and T.J. Bandosz, Combined Effect of Nitrogen- and Oxygen-Containing Functional Groups of Microporous Activated Carbon on its Electrochemical Performance in Supercapacitors, Adv. Funct. Mater. 19 (2009) 438-447.

[14] A. Bello, F. Barzegar, M.J. Madito, D.Y. Momodu, A.A. Khaleed, T.M. Masikhwa, J.K. Dangbegnon, and N. Manyala, Stability studies of polypyrole-derived carbon based symmetric supercapacitor via potentiostatic floating test. Electrochimica Acta, 213 (20-9-2016) 107-114.

[15] P.L. Taberna, P. Simon, and J.F. Fauvarque, Electrochemical Characteristics and Impedance Spectroscopy Studies of Carbon-Carbon Supercapacitors. Journal of The Electrochemical Society, 150 (1-3-2003) A292-A300.

[16] T.E. Rufford, D. Hulicova-Jurcakova, E. Fiset, Z. Zhu, and G.Q. Lu, Double-layer capacitance of waste coffee ground activated carbons in an organic electrolyte. Electrochemistry Communications, 11 (2009) 974-977.

[17] Y. Korenblit, M. Rose, E. Kockrick, L. Borchardt, A. Kvit, S. Kaskel, and G. Yushin, High-Rate Electrochemical Capacitors Based on Ordered Mesoporous Silicon Carbide-Derived Carbon. ACS Nano, 4 (2010) 1337-1344.

[18] K.K. Srivastava, R.N. Patil, C.B. houdhary, K.V.G.K. Gokhale, and E.C. Subbarao, Martensitic transformation in zirconia. Transactions of the British Ceramic Society, 73 (1974) 85-91.

[19] S. Jayakumar, P.V. Ananthapadmanabhan, T.K. Thiyagarajan, K. Perumal, S.C. Mishra, G. Suresh, L.T. Su, and A.I.Y. Tok, Nanosize stabilization of cubic and tetragonal phases in reactive plasma synthesized zirconia powders, Materials Chemistry and Physics, 140 (2013) 176-182.

[20] S.A. Steiner, T.F. Baumann, B.C. Bayer, R. Blume, M.A. Worsley, W.J. MoberlyChan, E.L. Shaw, R. Schlogl, A.J. Hart, S. Hofmann, and B.L. Wardle, Nanoscale Zirconia as a Nonmetallic Catalyst for Graphitization of Carbon and Growth of Single- and Multiwall Carbon Nanotubes, J. Am. Chem. Soc., 131 (2009) 12144-12154.

[21] Y.S. Won, Y.S. Kim, V.G. Varanasi, O. Kryliouk, T.J. Anderson, C.T. Sirimanne, and L. Elwee-White, Growth of ZrC thin films by aerosol-assisted MOCVD, Journal of Crystal Growth, 304 (2007) 324-332.

[22] Y. Mi, J. Wang, Z. Yang, Z. Wang, H. Wang, and S. Yang, A simple one-step solution deposition process for constructing high-performance amorphous zirconium oxide thin film, RSC Adv., 4 (2014) 6060-6067.

[23] J.F. Vivo-Vilches, E. Bailón-García, A.F. Pérez-Cadenas, F. Carrasco-Marín, and F.J. Maldonado-Hódar, Tailoring the surface chemistry and porosity of activated carbons: Evidence of reorganization and mobility of oxygenated surface groups, Carbon, 68 (2014) 520-530.

[24] J.F. Liu, C. Nistorica, I. Gory, G. Skidmore, F.M. Mantiziba, and B.E. Gnade, Layer-by-layer deposition of zirconium oxide films from aqueous solutions for friction reduction in silicon-based microelectromechanical system devices, Thin Solid Films, 492 (2005) 6-12.

[25] B. Babakhani and D.G. Ivey, Anodic deposition of manganese oxide electrodes with rod-like structures for application as electrochemical capacitors, Journal of Power Sources, 195 (2010) 2110-2117.

[26] A. Elmouwahidi, E. Bailón-García, A.n.F. Pérez-Cadenas, F.J. Maldonado-Hódar, and F. Carrasco-Marín, Activated carbons from KOH and H_3PO_4-activation of olive residues and its application as supercapacitor electrodes, Electrochimica Acta, 229 (2017) 219-228.

[27] Z. Zapata-Benabithe, C. Moreno-Castilla, and F. Carrasco-Marín, Effect of dilution ratio and drying method of resorcinol–formaldehyde carbon gels on their electrocapacitive properties in aqueous and non-aqueous electrolytes, Journal of Sol-Gel Science and Technology, 75 (2015) 407-412.

[28] K. Kierzek, E. Frackowiak, G. Lota, G. Gryglewicz, and J. Machnikowski, Electrochemical capacitors based on highly porous carbons prepared by KOH activation, Electrochimica Acta, 49 (2004) 515-523.

[29] F. Beck, M. Dolata, E. Grivei, and N. Probst, Electrochemical supercapacitors based on industrial carbon blacks in aqueous H_2SO_4, Journal of Applied Electrochemistry, 31 (2001) 845-853.

[30] W.G.P. B.E.Conway, Power limitations of supercapacitor operation associated with resistance and capacitance distribution in porous electrode devices, Journal of Power Sources. 105 (2015) 169-181.

[31] Z. Tian, M. Xiang, J. Zhou, L. Hu, and J. Cai, Nitrogen and Oxygen-Doped Hierarchical Porous Carbons from Algae Biomass: Direct Carbonization and Excellent Electrochemical Properties, Electrochimica Acta, 211 (2016) 225-233.

[32] D. Hulicova, M. Kodama, and H. Hatori, Electrochemical Performance of Nitrogen-Enriched Carbons in Aqueous and Non-Aqueous Supercapacitors, Chemistry of Materials, 18 (2006) 2318-2326.

[33] P.W. Ruch, D. Cericola, A. Foelske-Schmitz, R. Kötz, and A. Wokaun, Aging of electrochemical double layer capacitors with acetonitrile-based electrolyte at elevated voltages, Electrochimica Acta, 55 (2010) 4412-4420.

[34] D. Weingarth, A. Foelske-Schmitz, and R. Kötz, Cycle versus voltage hold-Which is the better stability test for electrochemical double layer capacitors?, Journal of Power Sources, 225 (2013) 84-88.

CHAPTER X: *DEVELOPMENT AND ELECTROCHEMICAL PERFORMANCE OF NEW VANADIUM-COATED CARBON MICROESPHERES FOR THEIR APPLICATIONS AS ELECTRODES FOR SUPERCAPACITORS*

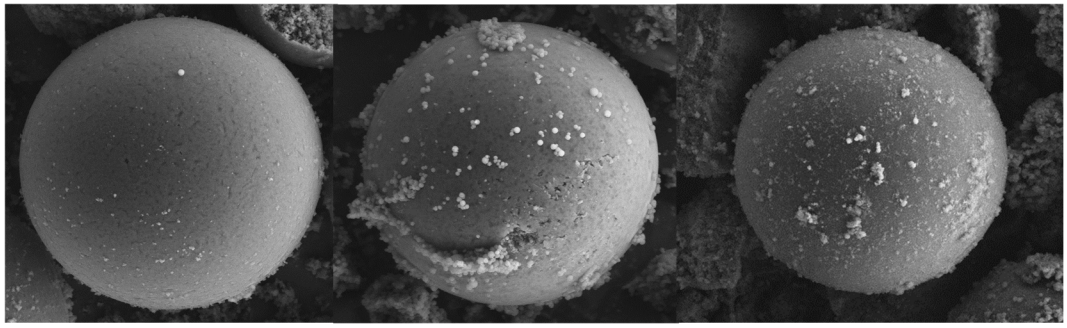

1. ABSTRACT

Vanadium-coated carbon microspheres (CSVX) were successfully prepared by a modified sol-gel method and their supercapacitor behaviour tested in a two-electrode system. Nitrogen adsorption showed that the CSVX composites present a well-developed micro and mesoporous texture, which depends on the vanadium content in the final composite. SEM images and XRD analysis manifest a high dispersion of vanadium oxide on the surface of carbon xerogels microspheres with a vanadium particle size determined by XRD of around 4.5 nm. XRD patterns, as well as XPS, point out that VO is obtained. That was also corroborated by TGA analysis, in which a weight gain is observed at around 300 ^{o}C ascribed to VO_x oxidation. The complete electrochemical characterization of the CSVX composites was carried out using several methods: cyclic voltammetry, chronopotentiometry, cycling charge-discharge and impedance spectroscopy. The results show that CSVX composites present a high capacitance with a high capacitance retention which was explained on the base of the presence of vanadium oxide and texture and chemistry surface.

Keywords: vanadium-coated carbon microspheres. Electrodes for supercapacitors. Electrochemical energy storage

2. INTRODUCTION

Recently, with the increase of power and energy demands in various applications such as hybrid vehicles, large memory back-up devices and renewable-energy power plants, many efforts have been made to develop alternatives and more efficient energy storage devices. Electrochemical capacitors [1-3] (also called supercapacitors) are investigated due to their unique characteristics such as fast charging–discharging, high power density and long cycle life time.

The selection of the material used as electrode for supercapacitor is crucial because the porous structure and surface chemistry of the material are key factors to the development of a supercapacitor with improved electrochemical performance including power density, energy density, rate capability, charging time and cyclic stability. Generally, the charge storage in electrochemical capacitors occurs by non-Faradic process and Faradic/redox process. Typically, high surface area carbon based materials reflected as non-Faradic process (also known as electrochemical double layer capacitors) while conductive polymers and metal oxides/hydroxides/sulphides have been desired as Faradic process or pseudocapacitors associated with multiple oxidation states/structures that enable rich redox reactions for pseudocapacitance generation.

In that sense, carbon materials have high specific surface area [1], high electronic conductivity and excellent stability. Therefore, activated carbons [2,3], carbon fibres [4,5], carbon aerogels [6,7] and carbon spheres [8,9] have been usually used as supercapacitor electrodes. However, these carbon-based electrochemical double-layer capacitors have a low capacitance, especially at high charge/discharge rates and low energy density and limited ionic accessibility [2]. Metal oxides and hydroxides overcome these limitations of carbon and commonly exhibit high specific capacitance and high power and energy densities [3]. Many metal oxides such as RuO_2 [11-13], MnO_2 [14,15], NiO [16,17], Fe_2O_3 [4], and Vanadium oxides [5], especially V_2O_5, VO_2 and their hydroxides have been used

for supercapacitors with good results, but however, a decrease of their capacitances is observed increasing the scan rate due to their lower conductivity [6]. Among the various metal oxides, vanadium pentoxide (V_2O_5) is considered to be one of the most promising candidates due to its wide potential window, unique layered structure, variety of oxidation states (V^{2+}, V^{3+}, V^{4+} and V^{5+}) which can provide excellent pseudocapacitance.

In order to get materials with enhanced supercapacitor performance, advantages of both pure phases (surface area, conductivity and stability of carbon materials and high power and energy density of metal oxides) could be coupled using carbon-metal oxide composites.

Moreover, the morphology of material is important in the preparacion of supercapacitors. The use of carbon spheres shows many great advantages, such as the high packing density which is very important for increasing the specific energy. These materials also have excellent dispersivity and fluidity, leading to high performances in electrode manufacturing [19, 20].

With that background, in the present work carbon spheres were successfully covered by different amount of vanadium oxide and the composites obtained were deeply characterized and their electrochemical performance tested.

3. EXPERIMENTAL

3.1. Synthesis of carbon-vanadium oxide composites

Vanadium-coated carbon microspheres were prepared in an one-pot synthesis following a modified Pekala's polycondensation of resorcinol (R) with formaldehyde (F) in presence of vanadium (V) tri-isopropoxide oxide as carbon and vanadium oxide precursors, respectively. In a typical synthesis procedure, a pregelled (at 60 ºC until the gel point) mixture of RF and water (W) was added drop wise to a n-heptane solution containing Span 80 (S) at 65 ºC under refluxing and stirring (450 rpm). The molar ratio of the mixture was R/F=1/2, R/W=1/14 and

R/S=4.5. After 1 h, the proper amount of vanadium (V) tri-isopropoxide oxide 96 % from Alfa Aesar was added drop wise to the reactor.

The formed gel was aged at 65 ºC for 24 h under stirring and after that the suspension was filtered and the solid obtained was placed in acetone (5 days, changing acetone twice daily) to exchange water within the pores by acetone, in order to reduce the porosity collapse during the subsequent drying process and remove the Span 80. Then, the gel was dried by microwave heating using a Saivod MS-287W microwave oven under argon atmosphere in periods of 1 minute at 384W until constant weight. Pyrolysis of organic xerogel-vanadium oxide composite to obtain the corresponding carbon xerogel-vanadium oxide composite was carried out in N_2 flow at 300 cm^3/min, heating to 900 ºC at a heating rate of 1 ºC/min, in order to allow a soft removing of pyrolysis gases, and soaking time of 2 h. The amount of vanadium (V) tri-isopropoxide oxide needed to obtain 5, 10, 20 and 30 % of vanadium oxide on the final carbonized samples was calculated considering that V_2O_5 will be obtained after carbonization, a complete reaction between R and F and a weight loss of 50 % w.t. during the carbonization. Samples were refereed as CSVX (X corresponds with the theorical % of vanadium oxide present in the carbonized composite, e.g. CSV30 means that carbon spheres was covered by 30 % Wt. of vanadium oxide. Also, a carbon spheres sample (CS) without vanadium oxide was prepared in the same way and used as reference material

3.2. Textural and chemical characterization

The morphology of supports was studied by scanning electron microscopy (SEM) using a LEO (Carl Zeiss) GEMINI-1530 microscope. Textural characterization was carried out by N_2 and CO_2 adsorption at −196 ºC and 0º C, respectively, using Quantachrome Autosorb-1 equipment. The BET and Dubinin–Radushkevich equations were applied to determine the apparent surface area (S_{BET}) and the micropore volume (W_0), the mean micropore width (L_0) and the microporous surface (S_{mic}), respectively. Furthermore, the DFT method was used to calculate the mesopore volume of the samples (V_{mes}). Pore size distributions

were also obtained by applying the DFT method. The total pore volume was considered as the volume of N_2 adsorbed at $P/P_0 = 0.95$.

The vanadium oxide contents of samples were determinated by thermogravimetric analysis (TGA). TGA was performed in flowing air with a heating rate of 10 ºC/min using a Mettler-Toledo TGA/DSC1 thermogravimetric analyzer. The vanadium oxide phase was determined by powder X-ray diffraction (XRD) pattern using a Bruker D8 Advance X-ray diffractometer with Cu Kα radiation at a wavelength (λ) of 1.541 Å. The 2θ angles were scanned from 20 to 70°. The average crystallite sizes (D) were estimated by the Debye-Scherer equation, $D = 0.95\lambda/\beta \cos \theta$, where θ is the diffraction angle and β is the full width at half-maximum (fwhm). The fwhm was determined with an extrapolated baseline between the beginning (low angle side) and the end (high-angle side) of a diffraction peak with the highest intensity.

The chemical characterization of the samples was further analyzed by X-ray photoelectron spectroscopy (XPS). The spectra were obtained on a Kratos Axis Ultra-DLD X-ray photoelectron spectrometer equipped with a hemispherical electron analyzer connected to a detector DLD (delay-line detector).

3.3. Electrochemical Characterization

For the electrochemical characterization, a mixture of active material and tetrafluoethylene (PTFE) binder (60% suspension in water) with a ratio of 90:10 was dried in an oven at 120 ºC overnight. Then, 5mg of the active material was pressed onto a graphite paper disc with 5 mm of diameter. The pasted sample was impregnated with a 1M H_2SO_4 solution for 48h before to be used for the electrochemical measurements.

The electrochemical performances were determined using a two electrode system with EC-lab equipment at 25 ºC in H_2SO_4 1M medium as electrolyte and glassy fibrous materials as separator. Several electrochemical techniques are used for the electrochemical characterization of the composites. Cycling voltammetry test (CV) was carried within the range of 0 and 1.1 V; using scan rates

from 0.5 to 200 mvs^{-1} and the gravimetric capacitance, C_{CV} (F/g), was calculated using the Equation (1) [25,26]:

$$C_{CV} = 4\frac{\sum|I|\Delta t}{m\Delta V} \quad \text{Eq. 1}$$

where $\sum|I|\Delta t$ is the area of the current (A) against time (s) curve, m is the total active mass in both two electrode (g), and ΔV is the potential window (V), the factor 4 traduces the relation between the two electrode and three electrode systems.

The galvanostatic charging-discharging was carried out at different current density from 125 mA/g to 20 A/g. The gravimetric capacitance, C_{CP} (F/g), was calculated using the equation (2) [27,28]:

$$C_{CP} = 4\frac{I_d \Delta t}{m\Delta V} \quad \text{Eq. 2}$$

where I_d was the current density (A g^{-1}), Δt was the discharge time, ΔV was the voltage interval without the IR drop and m is the total mass active (g).

The impedance spectroscopy measurements (EIS) were carried in the frequency of 100 KHz to 0.01Hz. While the stability of the electrodes was evaluated by charge-discharge cycles at a current density of 1 A g^{-1} between potential value of 0 V and 1.1 V.

The electrical energy and the power density were calculated by using the Eq. 3 and Eq.4, respectively for two-electrode cell [29,30].

$$E(Wh\,kg^{-1}) = \frac{C_{GD}\,(F\,g^{-1}) \times (V_{max}^2 - V_{min}^2)(V)}{2 \times 3.6} \quad \text{Eq. 3}$$

$$P(W\,kg^{-1}) = \frac{1}{2} \times \frac{I(A) \times (V_{max}^2 - V_{min}^2)(V)}{m\ (kg)} \quad \text{Eq. 4}$$

4. RESULTS AND DISCUSSION

4.1. Textural and chemical characterizations

Morphology and dispersion

SEM images of carbon spheres (CS) and vanadium oxide-coated carbon spheres are shown in Figure 1. As was designed in experimental set up, isolated microspheres of around 20 μm are obtained using the pre-gelled RF solution. VO-coated carbon microspheres are shown in Figure 1b, and 1c, showing a high dispersion of vanadium oxide on the surface of carbon microspheres.

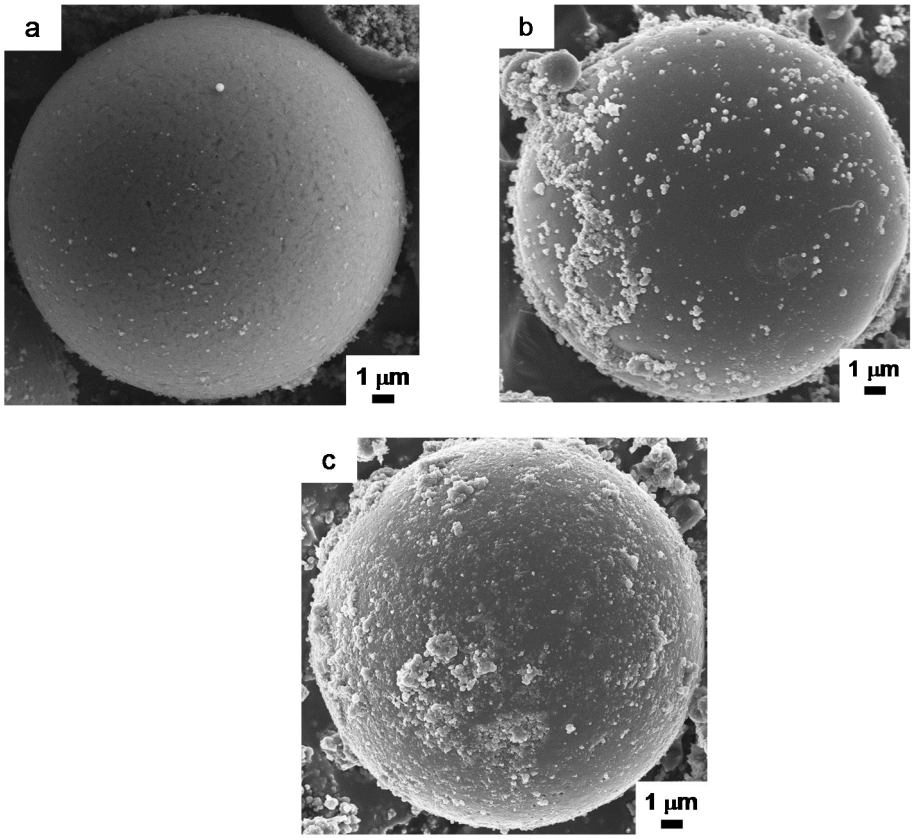

Figure 1. Scanning electron microscopy images of CS (a), CSV10 (b) and CSV30 (c).

Dispersion and crystallinity of vanadium oxide composites were analyzed by XRD. XRD patterns of CSVX composites are shown in Figure 2. Significant differences are observed between composites and pure V_2O_5. Four main diffractions peaks are obtained at values of 37.7º, 43.9º, 63.8º and 76.6º for the CSVX composites which can be attributed to cubic V^{2+} (VO) (JCPDS 75-0048) while a more complex pattern is obtained for V_2O_5 attributed to orthorhombic phase (JCPDS 01-089-0612). Moreover, narrower and intense diffraction peaks were observed in V_2O_5, denoting a high crystallinity while diffraction peaks become wider, and the intensity decreases in the case of composites CSVX. In that last case, the intensity of the peaks increases when the amount of vanadium oxide increases. The mean average size of vanadium oxide particles was estimated using the Debye-Scherer equation obtaining sizes of <4, 4.7, 4.8, 11.4 and 71.5 nm for CSV5, CSV10, CSV20, CSV30 and V_2O_5, respectively. This result denotes a good dispersion of VO nanoparticles in the carbon spheres surface but however at % higher than 20 % this dispersion decreases although a low crystal size is still obtained in comparison with pure vanadium oxide.

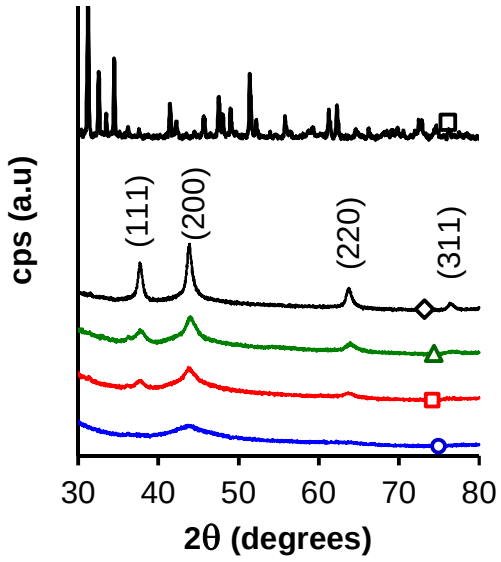

Figure 2. Powder XRD patterns of samples: CS (□), CSV5 (○), CSV10 (□), CSV20 (△), and CSV30 (◇)**.**

Note also that the vanadium oxidation state of the precursor is 5+ and during the synthesis of C/V composites, a reduction of the vanadium occurs up to the most reduced state (2+), which is preserved after the cooling and storage of the sample at room temperature. The valence of +5 is the most stable, while the stability of +4 and + 2 are the worst, in that sense, carbon matrix favour in such a way that fact.

TGA analysis

The real amount of vanadium oxide in the final CSVX carbon composites was determined by burning of the carbon phase by TGA. The final residual mass after TGA experiments was considered as the inorganic phase content. In this way, the real % of vanadium oxide on the carbonized composites was 2.95, 6.53, 14.04 and 23.11 wt. % for CSV5, CSV10, CSV20 and CSV30, respectively. Comparing TGA results with the theoretical ones, it is observed that the real percentages are slightly lower than the theoretical ones due to the weight loss undergoes by the samples during carbonization is higher than 50 %. Also note that the presence of vanadium oxide decrease the burn off temperature of the carbon matrix (around 350 ºC) comparing with pure carbon spheres which start to burn at around 500 ºC (Figure 3). Moreover, an increase of weight is observed for composites at around 220 ºC which could be ascribed to the V^{2+} oxidation.

N_2 and CO_2 isotherms adsorption

The pore structure of samples was studied by N_2 and CO_2 adsorption measurements. The results are collected in Table 1. The pure carbon xerogel is an exclusively microporous solid, while the composite materials are micro, mesoporous materials. The Vanadium oxide content greatly affects the textural characteristics of the composites. The higher is the % vanadium oxide, the higher is the volume of mesopores (V_{mes}) with a lineal relationship between both (Figure 4a). The mesoporosity increases with the percentage of vanadium oxide dispersed into the carbon xerogel matrix and also the microporosity increases and become widest ($W_0(N_2)$ and $L_0(N_2)$ increases, Figure 4b) at the expense of the ultramicroporosity ($W_0(CO_2)$) that decreases (Figure 4). It is well known that the

CO_2 adsorption provides information about the narrow microporosity, corresponding to micropores with diameter lower than 0.7 nm, while the total microporosity is obtained from N_2 isotherm only in absence of diffusion restrictions. In that sense, all samples show $W_0(N_2) < W_0(CO_2)$ indicating diffusion restrictions of N_2 into the microporosity due to the narrow ultramicropores, but this difference becomes lower with the increase of the % of vanadium oxide. Both micropores and mesopores are very important for their use as electrodes in energy storage applications because they have different roles with respect to fast charge transfer and the double layer formation of electrolyte ions in the networks of the electrode [31,32].

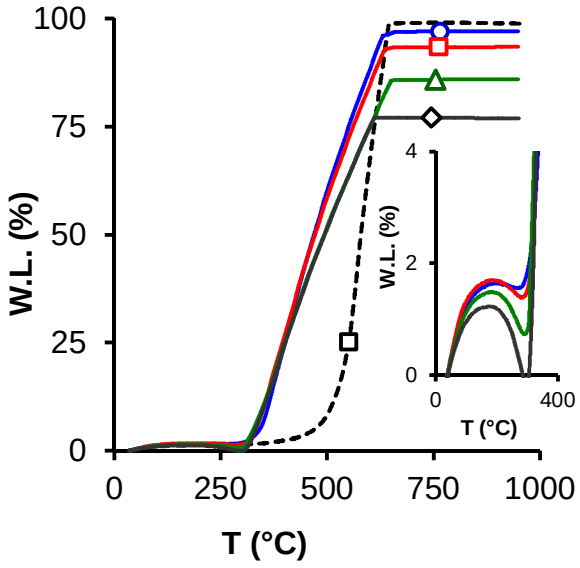

Figure 3. TGA profiles of CSVX composites and CS. CS (□) (dashed line), CSV5 (○), CSV10 (□), CSV20 (△), and CSV30 (◇)**.**

Table 1. Textural characteristics and vanadium oxide content of the carbon vanadium composites.

Sample	S_{BET}	$W_0(N_2)$	$W_0(CO_2)$	$L_0(N_2)$	$L_0(CO_2)$	$V_{0,95}$	V_{mes}	V_xO_y
	$m^2\ g^{-1}$	$cm^3\ g^{-1}$	$cm^3\ g^{-1}$	nm	nm	$cm^3\ g^{-1}$	$cm^3\ g^{-1}$	%
CS	573	0.226	0.288	0.65	0.59	0.330	0.104	0
CSV5	568	0.225	0.282	0.70	0.60	0.336	0.111	2.95
CSV10	575	0.229	0.273	0.72	0.58	0.347	0.118	6.53
CSV20	602	0.241	0.266	0.75	0.60	0.356	0.115	14.04
CSV30	566	0.228	0.245	0.79	0.59	0.352	0.124	23.11

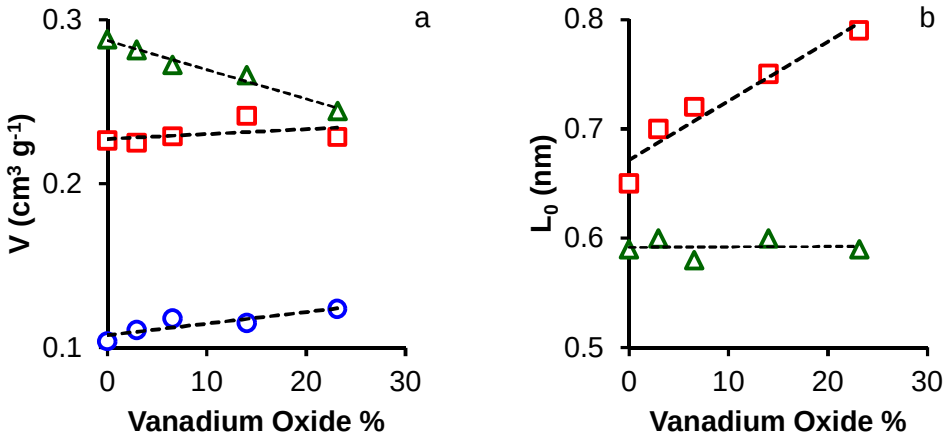

Figure 4. Dependence of textural properties of CSVX with % vanadium oxide. a) V_{meso}, ○; $W_0(N_2)$, □; $W_0(CO_2)$, △. b) $L_0(N_2)$, □; $L_0(CO_2)$, △.

Surface composition: XPS analysis

Surface compositions of samples were analyzed by XPS which provided information regarding the electronic states and chemical environment of carbon (C), vanadium (V), and oxygen (O) atoms in the composite materials. XPS data

are collected in Table 2 and vanadium and oxygen regions depicted in Figure 5. Six carbon components are needed to fix the C_{1s} spectral region in all cases; the main carbon peak is found at 284.6 eV, which corresponds to the non-oxygenated amorphous carbon. Peaks at 285.8 eV, 286.8 eV and 288.1 eV are assigned to C-O, C=O and COO^-, respectively. Note that there is no carbon peak associated with vanadium carbide (VC, BE: 282.9 eV) in CSVX samples, suggesting that no carbothermal reduction took place during the synthesis**.** No significant differences between C_{1s} region of pure carbon xerogel and CSVX composite are observed. As consequence, this fact can indicates that the presence of vanadium oxide do not affect the surface chemistry of carbon spheres.

Regarding the O_{1s} region, three different peaks were found: 530.3 eV is assigned to oxygen in a metal oxide [33,34], whereas the peak located at 532 eV is characteristic either of a hydroxyl group (–OH) bonded or oxygenated groups like ketones (C=O) on the carbon surface [35]. The third component at 533.0 eV corresponds to acids, anhydrides and lactones and also to ether groups (C–O–C) [36]. Moreover, this assignation is confirmed by the fact that the first component increases progressively with increasing the V-content in the composite while the other ones are constant.

Three components are required to fit the $V_{2p3/2}$ region; the peak at 513.9 eV corresponds to V^{2+} species whereas the peaks at 515.5 eV and 517.1 eV are ascribed to V^{3+} and V^{4+} ones, respectively [33,37]. Analyzing the % wt. of each element, as expected, a linear increase of % V_{xps} and O_{xps} is obtained increasing the vanadium oxide content on the carbon matrix (Figure 5 b).

Table 2. Relative surface concentration (%) of O, C and V functionalities from the

Sample	C_{1s} eV	Peak %	O_{1s} eV	Peak %	O_{xps} % wt	$V_{2p3/2}$ eV	Peak %	V_{xps} % wt
CS	284.6	74	531.6	18	2.65	-	-	-
	285.6	13	533.2	82				
	286.6	5						
	287.5	3						
	289.3	3						
	290.9	1						
CSV5	284.6	73	530.3	24	3.3	513.9	20	1.3
	285.8	12	531.9	32		515.6	31	
	286.8	6	533.2	45		517.2	49	
	288.1	3						
	289.6	3						
	291.0	2						
CSV10	284.6	73	530.3	41	5.0	514.0	20	4.4
	285.8	12	532.0	36		515.5	25	
	286.9	7	533.4	23		517.2	55	
	288.3	3						
	289.7	3						
	291.1	2						
CSV20	284.6	74	530.2	58	8.2	514.1	19	9.1
	285.8	12	531.9	24		515.8	23	
	286.8	6	533.3	18		517.2	58	
	288.1	3						
	289.5	3						
	290.9	2						
CSV30	284.6	73	530.2	62	9.5	513.9	17	13.5
	285.8	12	531.8	29		515.4	29	
	286.8	7	533.2	18		517.1	54	
	288.1	3						
	289.6	3						
	291.0	2						

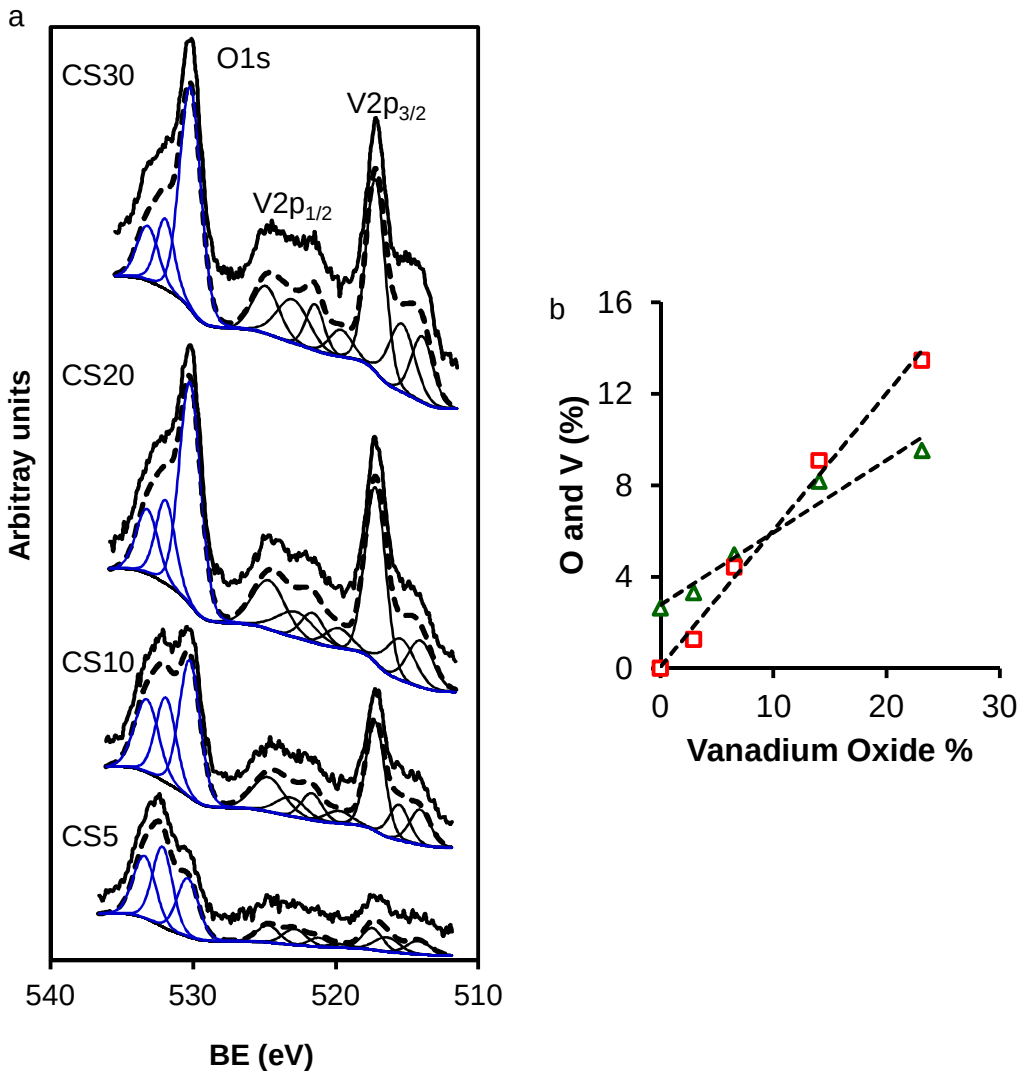

Figure 5. a) V_{2p} and O_{1s} spectral region, b) relation between surface V (□) and O (△) with % vanadium oxide in the composite.

4.2. Electrochemical characterization of vanadium-carbon composites

The electrochemical performances of the vanadium carbon composites are measured using different electrochemical techniques such as CV, EIS, and galvanostatic charge/discharge using a 1 M H_2SO_4 as electrolyte.

Figure 6a depicts the cyclic voltammograms at different scan rate for sample CSV30. It is shown the variation of the capacitance with the increasing of the scan rate, the capacitance decrease with increasing scan rate because when the scan rate is higher the formation of the electrochemical double-layer within the micropores is slower and less complete. As the scan rate increases the current versus potential is deviate from the classical rectangular waveform, expected for a pure capacitor. As discussed by some researchers this is due to the resistance effects inside the pores [38]. In addition to pore resistance, efficiency is another important parameter affecting the capacitance in high sweep rates. As the sweep rate increases, loss of energy increases and the stored charge on the electrode surface decreases causing the capacitance decrease. Figure 6b shows the results of all sample at 5 mV s^{-1}. All carbon composites showed a quasi-rectangular shape, typical voltammograms for electrochemical double-layer (EDL) capacitors with no diffusional restriction to the electrolyte [4,32] furthermore, the cyclic voltammetry are effectuated in the voltage windows from 0 to 1.1 V indicating a good stability of the electrodes due to the presence of the vanadium oxides in the composites.

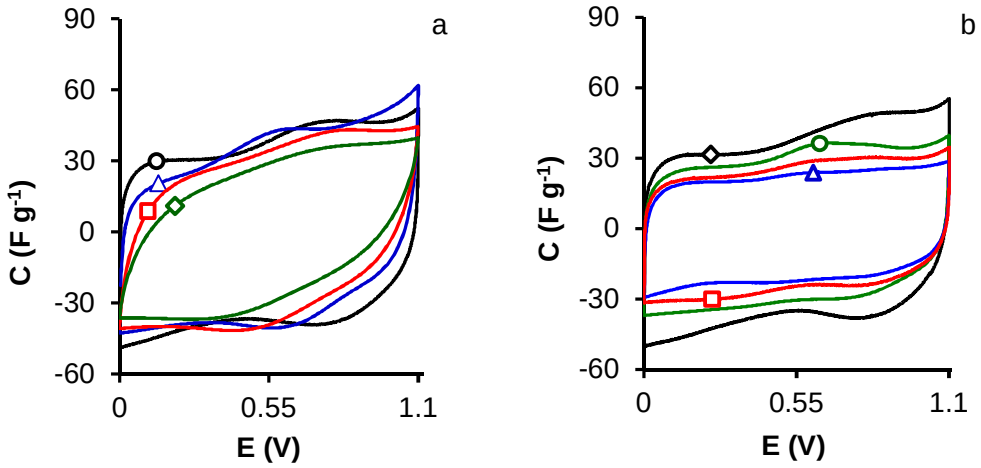

Figure 6. a) Cyclic voltammograms for sample CSV30 at different scan rate: 10 (○), 50 (△), 100 (□) and 200 (◇) mV s^{-1}. b) Cyclic voltammograms at 5 mV s^{-1} for samples: CSV5 (△), CSV10 (□) CSV20 (○) and CSV30 (◇)

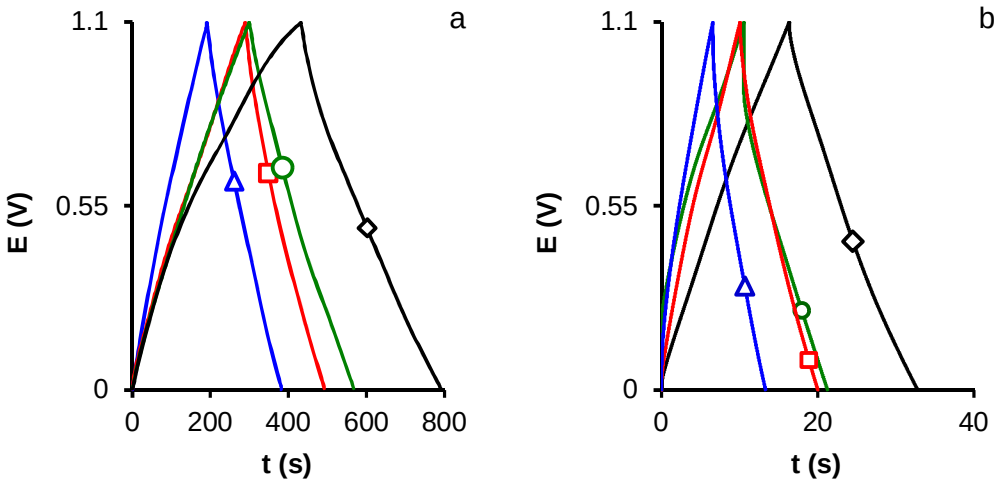

Figure 7. Chronopotentiograms for samples CSV5 (△), CSV10 (□) CSV20 (○) and CSV30 (◇). a) 0.125 A g^{-1} and b) 2 A g^{-1}.

Chronopotentiograms (CPs) obtained are depicted in Figure 7 at a current load of a) 125 mA g^{-1} and b) 2 A g^{-1}. CPs show quasi-triangular shapes which indicates again that samples behave as an ideal electrochemical double-layer (EDL) performance with low resistance and a good diffusion of the electrolyte inside the pores.

The variation in the gravimetric capacitances measured by using both techniques (cyclic voltametry, CV, and chronoamperometry, CP) by applying Equations 1 and 2 are plotted in Figure 8 and compiled in Table 3. The pure carbon xerogel showed a lower capacitance due to its lower mesoporosity. The C_{CP} values of the composites are very high, between 105 and 224 F g^{-1}, compared with C100 sample instead their lower micropore volume. These differences can be related to their porous texture and specially the mesoporosity and the pore volume of each sample.

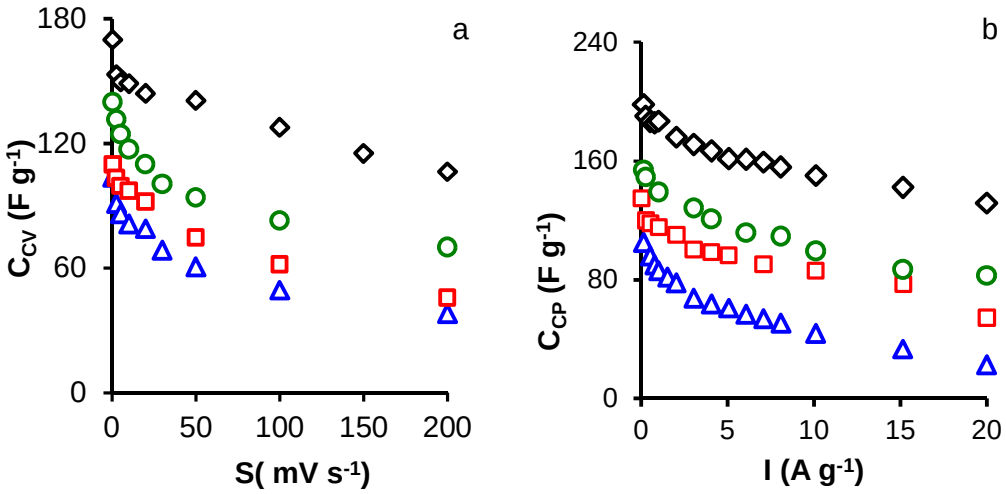

Figure 8. Variation of the gravimetric capacitance against, a) the scan rate, b) the current density, for samples: CSV5 (△), CSV10 (□) CSV20 (○) and CSV30 (◇).

Table 3. Electrochemical performances of V-C composites

Sample	C_{CV} 0.5 mV s^{-1} F g^{-1}	C_{CV} 200 mV s^{-1} F g^{-1}	C_{CP} 0.125 A g^{-1} F g^{-1}	C_{CP} 20 A g^{-1} F g^{-1}	Retention CP (%)
CS	40	-	37	-	--
CSV5	104	38	105	23	22
CSV10	110	39	135	54	40
CSV20	140	70	154	83	54
CSV30	170	106	224	132	59

At this point, two parameters must be considered to analyze the different electrochemical behavior of CSVx composites: pore size and pore volume. So,

when the vanadium percentage increases from 5 to 30, the pore volume (W_0 (N_2)) slightly decreased from 0.282 cm^3 g^{-1} to 0.245 cm^3 g^{-1} but the pore diameter increase from 0.65 to 0.79 nm with increasing the mesopores volume V_{meso} from 0.114 cm^3 g^{-1} to 0.124 cm^3 g^{-1} which is advantageous for good electrolyte accessibility and consequently a higher capacitance. There are many studies in literature suggesting that there is an increasing of the specific capacitance with increasing the average pore size [39], in this sense, increasing the volume of pores smaller than 2 nm was shown to increase the specific capacitance, the result shows that the increasing of the pore size increases the specific capacitance. Figure 8b showed that the C_{CP} decreases when the current load increases from 0.125 to 20 A g^{-1}. CSV30 shows the highest capacitance retention (Table 3), 59%, because it has a higher mesopore volume than the others samples, which favours the transport of ions through the carbon porosity at a higher current density.

Figure 9 showed the EIS characterization of the CSVx composites. It shows the electrochemical impedance spectrum in the form of Nyquist plots, where Z' and Z″ are the real and imaginary parts of the impedance, respectively. In the high frequency region, the first intersection point on the real axis (Z') was the ESR, which was related with the conductive properties of the activated carbon electrodes for comparison purposes, because the same electrolyte, collectors, and technique were used to assemble the cell [40]. The Nyquist plot contains a semi-circle at medium to high frequencies, which is due to faradic charge transfer resistance, R_{CT}, and a nearly straight line along the imaginary axis at a low-frequency component due to the mass transport limit. In the low frequency region, the imaginary part of the impedance (Z") sharply increased and the plots tended to a vertical line, which is characteristic of capacitive behavior. The maximum capacitance (C_{max}) of the composites was obtained at the lowest frequency (1 mHz), the results obtained are compiled in Table 4.

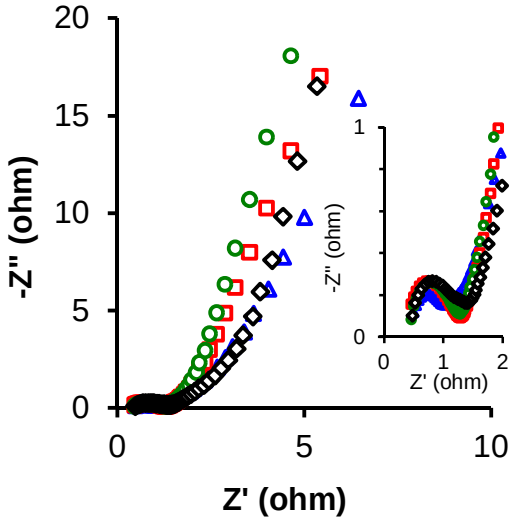

Figure 9. Nyquist plots of samples: CSV5 (△), CSV10 (□) CSV20 (○) and CSV30 (◇)

Table 4. C_{max} at 1 mHz, equivalent series resistance (ESR) and charge transfer resistance (R_{CT}) from EIS.

Sample	ESR Ω	R_{CT} Ω	C_{max} F g^{-1}
CV5	0.49	0.62	96
CV10	0.46	0.84	131
CV20	0.46	0.85	155
CV30	0.48	1.30	191

The difference of the R_{CT} for all the samples can be explained by the difference of the pore size diameter and also the conductivity of the composites which depends of the content of vanadium and carbon in the composite. Most of the samples have wide pore diameter for that reason R_{CT} have a very low values, lower in the case of the samples with low vanadium oxide content. In general, all

the sample composites show a low ESR indicating a good penetration of the electrolyte into the pore structure.

The Ragone plots of the samples are shown in Figure 10. This figure show the dependence between the energy and power density. The maximum energy density was released at the lowest power density (140 W Kg^{-1}), as shown in Table 5.

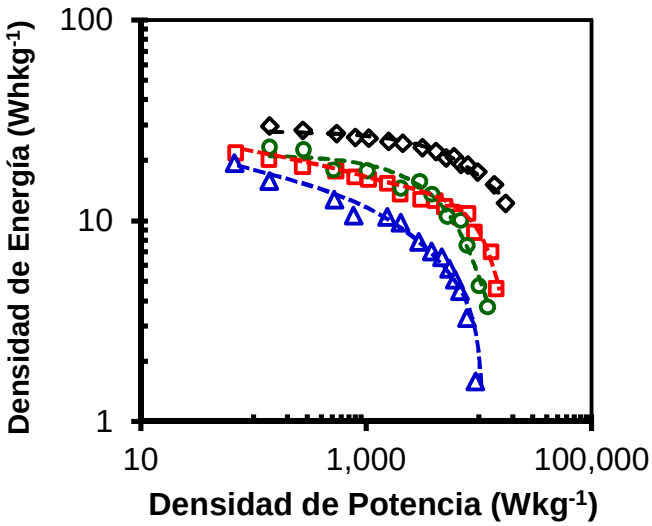

Figure 10. Ragone plots for samples: CSV5 (△), CSV10 (□) CSV20 (○) and CSV30 (◇)

Table 5. Energy density at 140 W kg^{-1}, E_{max}, and at 7800 W kg^{-1}, E_{min}, (Wh Kg^{-1}) from Ragone's plots

Sample	E_{max}	E_{min}
CV5	15.8	3.2
CV10	20.2	10.9
CV20	23.3	10.0
CV30	29.6	18.9

The energy density increased with the presence of vanadium oxide, the maximum energy densities for CSVx composites are very high for all samples and there is a significant increase with the increases in vanadium content. A gradual decrease in energy density was observed when increasing the power density. The superior performance of sample CSV30 is due to its more developed porosity, with one of the highest values of mesopore volume in addition of the presence of vanadium. It should be highlighted the very high energy density for CSV30 for both E_{max} and E_{min}, showing a retention of energy density of 69.8 % in the potential range studied and reaching a value of 18.9 Wh Kg^{-1} at a power density of 7.8 kW Kg^{-1}.

Cyclic stability of supercapacitors is one of the main factor for their practical applications. 13000 galvanostatic charge-discharge cycles were applied over at a scan rate of 1 A g^{-1}, Figure 11. Results obtained indicate that the variation of specific capacitance of all the samples is very low showing a capacitance retention ≈ 98 %.

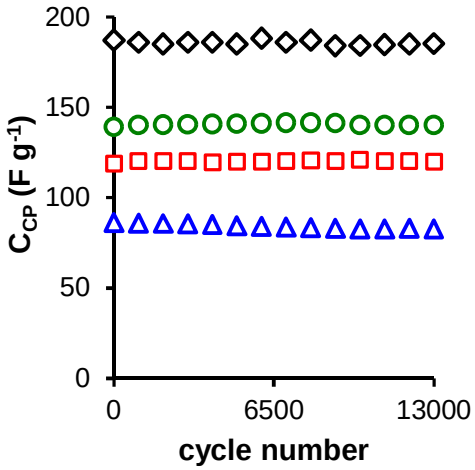

Figure 11. Charge discharge cycles at current density of 1 A g^{-1} samples: CSV5 (△), CSV10 (□) CSV20 (○) and CSV30 (◇)

5. CONCLUSIONS

Vanadium-coated carbon microspheres were, at the first time, prepared in an one-pot polimerization synthesis. SEM images and XRD analysis manifest a high dispersion of vanadium oxide on the surface of carbon. XRD also shows that V^{2+} state is stabilize in CSVX composites despite of the stability of +4 and +2 are the worst, in that sense, carbon matrix favour in such a way that reduction. XPS also reveal a reduction state of vanadium, V^{2+}, V^{3+} and V^{4+} peaks were observed while V^{5+} was not detected. This fact is also identified by TGA, where an increase of weight is observed for composites at around 220 ºC which could be ascribed to the V^{2+} oxidation. Moreover, the Vanadium oxide content greatly affects the textural characteristics of the composites, in such a way the higher is the % vanadium oxide, the higher is the mesopores (V_{mes}) and micropores ($W_0(N_2)$) volumes and micropores become widest at the expense of a decrease of the ultramicroporosity ($W_0(CO_2)$).

The complete electrochemical characterization of the CSVX composites was carried out using several methods: cyclic voltametry, chronopotentiometry, cycling charge-discharge and impedance spectroscopy. The results show that the sample CSV30 corresponding to the composite with 30% of vanadium oxide has a good specific capacitance of 224 F g^{-1} at current density of 125 mA g^{-1} in H_2SO_4, 1M as electrolyte, furthermore this sample was able to keep 58.8% of the capacitance at a high current density of 20 A g^{-1} and keep 100% of the capacitance over 13000 charge discharge cycles at 1 Ag^{-1}. Moreover, this sample keeps the rectangular form of the voltammogram at high scan rate of 200 mVs^{-1} indicating a good conductivity and stability of the electrode.

6. REFERENCES

[1] J. Chmiola and Y. Gogotsi, Supercapacitors as advanced energy storage devices, Nanotechnol. Law Bus., 4 (2007) 577-584.

[2] B.E. Conway, Electrochemical Supercapacitors: Scientific Fundamentals and Technological Applications. (1999).

[3] M. Sevilla and R. Mokaya, Energy storage applications of activated carbons: supercapacitors and hydrogen storage, Energy Environ. Sci., 7 (2014) 1250-1280.

[4] A. Elmouwahidi, E. Bailón-García, A.F. Pérez-Cadenas, F.J. Maldonado-Hódar, and F. Carrasco-Marín, Activated carbons from KOH and H_3PO_4-activation of olive residues and its application as supercapacitor electrodes, Electrochimica Acta, 229 (2017) 219-228.

[5] T. Chen, Carbon nanomaterials for high-performance supercapacitors, (2013).

[6] C. Portet, G. Yushin, and Y. Gogotsi, Electrochemical performance of carbon onions, nanodiamonds, carbon black and multiwalled nanotubes in electrical double layer capacitors, Carbon, 45 (2007) 2511-2518.

[7] Q. Xie, Core-shell N-doped active carbon fiber@graphene composites for aqueous symmetric supercapacitors with high-energy and high-power density, (2016).

[8] Z. Zapata-Benabithe, F. Carrasco-Marín, and C. Moreno-Castilla, Preparation, surface characteristics, and electrochemical double-layer capacitance of KOH-activated carbon aerogels and their O- and N-doped derivatives, Journal of Power Sources, 219 (2012) 80-88.

[9] C. Moreno-Castilla, M.B. Dawidziuk, F. Carrasco-Marín, and E. Morallón, Electrochemical performance of carbon gels with variable surface chemistry and physics. Carbon, 50 (2012) 3324-3332.

[10] B. Chang, Convenient and large-scale synthesis of nitrogen-rich hierarchical porous carbon spheres for supercapacitors and CO2 capture, (2017).

[11] G. Wang, Synthesis of hollow mesoporous carbon spheres via Friedel-Crafts reaction strategy for supercapacitor, (2017).

[12] X. Xiao, Preparation and electrochemical performances of carbon spheres ZnO core-shell nanocomposites for supercapacitor applications, (2017).

[13] T. Chen and L. Dai, Carbon nanomaterials for high-performance supercapacitors, Materials Today, 16 (2013) 272-280.

[14] Y. Wang, J. Guo, T. Wang, J. Shao, D. Wang, and Y.W. Yang, Mesoporous Transition Metal Oxides for Supercapacitors, Nanomaterials, 5 (2015) 1667-1689.

[15] J.P. Zheng, P.J. Cygan, and T.R. Jow, Hydrous Ruthenium Oxide as an Electrode Material for Electrochemical Capacitors, Journal of the Electrochemical Society, 142 (1995) 2699-2703.

[16] D. Rochefort, P. Dabo, D. Guay, and P.M.A. Sherwood, XPS investigations of thermally prepared RuO2 electrodes in reductive conditions, Electrochimica Acta, 48 (2003) 4245-4252.

[17] A.E. Fischer, K.A. Pettigrew, D.R. Rolison, R.M. Stroud, and J.W. Long, Incorporation of homogeneous, nanoscale MnO2 within ultraporous carbon structures via self-limiting electroless deposition: Implications for electrochemical capacitors, Nano Lett., 7 (2007) 281-286.

[18] G.S. Gund, D.P. Dubal, N.R. Chodankar, J.Y. Cho, P. Gomez-Romero, C. Park, and C.D. Lokhande, Low-cost flexible supercapacitors with high-energy density based on nanostructured MnO(2) and Fe(2)O(3) thin films directly fabricated onto stainless steel, Scientific Reports, 5 (2015) 12454.

[19] H. Xiao, S. Yao, H. Liu, F. Qu, X. Zhang, and X. Wu, NiO nanosheet assembles for supercapacitor electrode materials, Progress in Natural Science: Materials International, 26 (2016) 271-275.

[20] U.M. Patil, R.R. Salunkhe, K.V. Gurav, and C.D. Lokhande, Chemically deposited nanocrystalline NiO thin films for supercapacitor application. Applied Surface Science, 255 (2008) 2603-2607.

[21] J.M. Li, K.H. Chang, and C.C. Hu, A novel vanadium oxide deposit for the cathode of asymmetric lithium-ion supercapacitors, Electrochemistry Communications, 12 (2010) 1800-1803.

[22] Y. Wang, J. Guo, T. Wang, J. Shao, D. Wang, and Y.W. Yang, Mesoporous Transition Metal Oxides for Supercapacitors, Nanomaterials, 5 (2015) 1667-1689.

[23] E. Umeshbabu and G. Ranga Rao, Vanadium pentoxide nanochains for high-performance electrochemical supercapacitors, Journal of Colloid and Interface Science, 472 (2016) 210-219.

[24] H.Q. Wang, Z.S. Li, Y.G. Huang, Q.Y. Li, and X.Y. Wang, A novel hybrid supercapacitor based on spherical activated carbon and spherical MnO2 in a non-aqueous electrolyte, J. Mater. Chem., 20 (2010) 3883-3889.

[25] J. Gamby, P.L. Taberna, P. Simon, J.F. Fauvarque, and M. Chesneau, Studies and characterisations of various activated carbons used for carbon/carbon supercapacitors, Journal of Power Sources, 101 (2001) 109-116.

[26] L. Bonnefoi, P. Simon, J.F. Fauvarque, C. Sarrazin, J.F. Sarrau, and A. Dugast, Electrode compositions for carbon power supercapacitors, Journal of Power Sources, 80 (1999) 149-155.

[27] L.L. Zhang and X.S. Zhao, Carbon-based materials as supercapacitor electrodes, Chem. Soc. Rev., 38 (2009) 2520-2531.

[28] D. Hulicova-Jurcakova, M. Seredych, G.Q. Lu, and T.J. Bandosz, Combined Effect of Nitrogen- and Oxygen-Containing Functional Groups of Microporous Activated Carbon on its Electrochemical Performance in Supercapacitors, Adv. Funct. Mater., 19 (2009) 438-447.

[29] A. Bello, F. Barzegar, M.J. Madito, D.Y. Momodu, A.A. Khaleed, T.M. Masikhwa, J.K. Dangbegnon, and N. Manyala, Stability studies of polypyrole-derived carbon based symmetric supercapacitor via potentiostatic floating test. Electrochimica Acta, 213 (20-9-2016) 107-114.

[30] Y. Korenblit, M. Rose, E. Kockrick, L. Borchardt, A. Kvit, S. Kaskel, and G. Yushin, High-Rate Electrochemical Capacitors Based on Ordered

Mesoporous Silicon Carbide-Derived Carbon. ACS Nano, 4 (2010) 1337-1344.

[31] P. Simon and Y. Gogotsi, Materials for electrochemical capacitors, Nat Mater, 7 (2008) 845-854.

[32] T. Chen and L. Dai, Carbon nanomaterials for high-performance supercapacitors, Materials Today, 16 (2013) 272-280.

[33] M.C. Biesinger, L.W.M. Lau, A.R. Gerson, and R.S. Smart, Resolving surface chemical states in XPS analysis of first row transition metals, oxides and hydroxides: Sc, Ti, V, Cu and Zn, Applied Surface Science, 257 (2010) 887-898.

[34] C.M. Ghimbeu, E. Raymundo-Pinero, P. Fioux, F. Beguin, and C. Vix-Guterl, Vanadium nitride/carbon nanotube nanocomposites as electrodes for supercapacitors, J. Mater. Chem., 21 (2011) 13268-13275.

[35] J.F. Vivo-Vilches, E. Bailón-García, A.F. Pérez-Cadenas, F. Carrasco-Marín, and F.J. Maldonado-Hódar, Tailoring the surface chemistry and porosity of activated carbons: Evidence of reorganization and mobility of oxygenated surface groups, Carbon, 68 (2014) 520-530.

[36] Yongjuan Mi, Jinqing Wang, Zhigang Yang, Zhaofeng Wang, Honggang Wang and Shengrong Yang, A simple one-step solution deposition process for constructing high-performance amorphous zirconium oxide thin film, RSC Adv., 4 (2014), 6060-6067.

[37] A. Dey, M.K. Nayak, A.C.M. Esther, M.S. Pradeepkumar, D. Porwal, A.K. Gupta, P. Bera, H.C. Barshilia, A.K. Mukhopadhyay, A.K. Pandey, K. Khan, M. Bhattacharya, D.R. Kumar, N. Sridhara, and A.K. Sharma, Nanocolumnar Crystalline Vanadium Oxide-Molybdenum Oxide Antireflective Smart Thin Films with Superior Nanomechanical Properties, Scientific Reports, 6 (2016) 36811.

[38] W.G.P. B.E.Conway, Power limitations of supercapacitor operation associated with resistance and capacitance distribution in porous electrode devices Journal of Power Sources. 105 (2015) 169-181.

[39] F. Beck, M. Dolata, E. Grivei, and N. Probst, Electrochemical supercapacitors based on industrial carbon blacks in aqueous H2SO4, Journal of Applied Electrochemistry, 31 (2001) 845-853.

[40] D. Hulicova, M. Kodama, and H. Hatori, Electrochemical Performance of Nitrogen-Enriched Carbons in Aqueous and Non-Aqueous Supercapacitors. Chemistry of Materials, 18 (1-5-2006) 2318-2326.

CHAPTER XI: *NEW CARBON VANADIUM COMPOSITES AS CATALYSTS FOR OXYGEN-ELECTRO- REDUCTION*

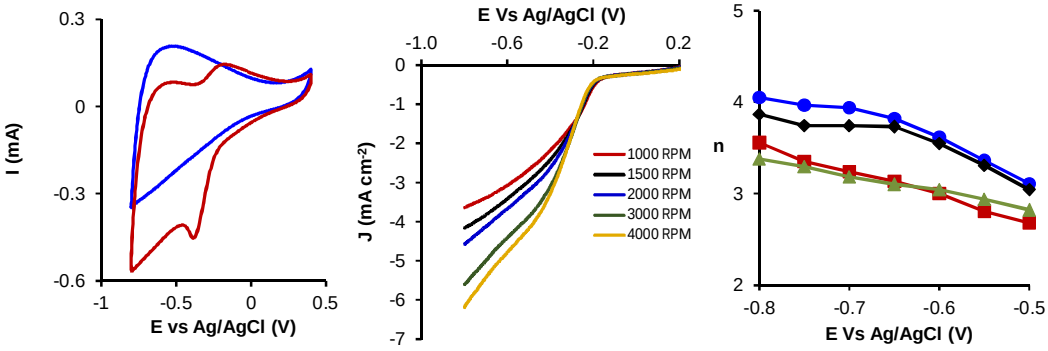

1. ABSTRACT

A creative hydrothermal synthesis method followed by calcinations for vanadium carbon composites (CsVx) is reported. Samples are exhaustively characterized to determine the textural, chemical and electrochemical properties. Those materials are tested as electro-catalysts for oxygen reduction reaction in a three electrode electrochemical set-up and in basic medium. The results show a very good electro-catalytic behaviour with larger kinetic current densities and lower activation potentials. The oxygen reduction reaction (ORR) study of the catalyst shows that CsVx possesses a comparable catalytic performance to commercial Pt/C catalyst and that those composites offer promising route for the activity enhancement of the non-precious metal catalysts.

Keywords: vanadium composite; oxygen reduction; electro-catalyst

2. INTRODUCTION

Increasing energy demands have stimulated intense research on alternative energy conversion and storage systems with high efficiency, low cost and environmental benignity. Catalysts for oxygen reduction and evolution reactions are at the heart of key renewable-energy technologies including fuel cells. Therefore, the production of electrical energy from chemical reactions by using fuel cells is a really interesting matter from both the industrial and fundamental research point of view. Oxygen Reduction Reaction (ORR) is the one that takes place on the cathode in a fuel cell and several works can be found on published literature about the synthesis and optimization of electro-catalytic materials for this reaction [1-4].

Pt or its alloys are the best known ORR catalysts. Owing to the high cost of Pt and declining activity, because of their high price, low stability, and inferior tolerance to fuel molecules. Alternative catalysts based on non-precious metals and metal-free materials have been actively pursued. Therefore, the search for cheap, highly active, and stable alternatives to the Pt catalyst can facilitate the commercialization of fuel cells. This is the reason why non precious metal electro-catalysts are more numerous and more studied in order to lower the costs of fuel cells [5-10]. To date, the most promising non precious metal catalysts (TMs, e.g., Fe, Co, Ni) studied for the ORR has attracted substantial attention due to their exceptionally high activity and stability compared to others catalysts [11-13]. Their activity and stability are still insufficient. Continued effort is still required to further explore new types of non-precious metal catalysts.

Acidic electrolytes are widely used, fuel cells based on acidic electrolytes still depend heavily on noble metal catalysts thus increasing the cost and impeding the widespread application of fuel cells. The alkaline fuel cell can adopt non precious metals. Vanadium is one of the most abundant metals on Earth. Both the pure and composite forms of vanadium are used in many chemical reactions with a wide range of applications, including steel additives, batteries, catalysts, etc. [14, 15]. Vanadium’s active sites have an important role in its catalytic activity. There

are different types of vanadium oxides, which are composed of single and mixed valence states, as well as different structures[16].

Different type of vanadium carbon material were used for electro catalytic reduction of oxygen; Taizhong Huang and al[17] study the catalytic activity of study of vanadium nitride, vanadium carbonitride, and vanadium carbide use of vanadium nitride for electro reduction of oxygen, and the results indicate a comparable catalytic performance to commercial Pt/C. Furthermore, the seam group reports[18] a new type of ORR electro-catalyst composed of Pt nanocrystals loaded on a nitrogen-doped graphene–VC hybrid support with higher catalytic performance and stability compared with commercial Pt/C.

Here, we provide the first demonstration that the vanadium carbon composites can serve as a highly active ORR electro-catalyst in alkaline media. The objective of this work was the preparation of vanadium carbon electro-catalysts with different vanadium content, from resorcinol and formaldehyde as carbon precursor using hydrothermal method. And testing the catalytic performances of all samples prepared in terms of pore structure and metal content.

3. EXPERIMENTAL

3.1. Synthesis of carbon-vanadium oxide composites

Synthesis of carbon-vanadium oxide composites has been describe in the previous Chapter

3.2. Textural and chemical characterization

Textural and chemical characterization have been describe in the previous Chapter.

3.3. Electrochemical Characterization

Cyclic Voltammetry (CV) and Linear Sweep Voltammetry (LSV) experiments were conducted on a three electrode cell controlled by a Biologic VMP multichannel potentiostat. A Rotating Disk Electrode (RDE) Metrohm AUTOLAB RDE-2, 3mm Glassy Carbon tip, was used as working electrode. 5mg of electro-catalyst were suspended on 1mL of a solution which contained Nafion (5%) and

water in a 1:9 (v: v) ratio. Subsequently, 10 µL of this suspension were loaded on RDE tip and dried under an infrared lamp. The glassy carbon electrode had been previously polished with 1, 0.3 and 0.05 µm alumina powder and sonicated in deionized water and ethanol. Ag/AgCl was chosen as reference electrode and Pt-wire as counter electrode. The three electrodes were immersed in a 0.1M KOH (electrolyte) solution in water.

CV experiments were carried out while N_2 or O_2 bubbled through the electrolyte solution during measurements. The chosen potential window ranged from -0.8to 0.4V (50mV s^{-1}). LSV curves were obtained in O_2-saturated 0.1M KOH solutions at different rotation speed and sweeping voltage, from 0.4 to -0.8V (5 mV s^{-1}). Data were fitted to the Koutecky-Levich model (Equations 1 and 2) in order to evaluate the electro-catalytic performance of samples and the transferred electron number for each of them [19-21].

$$\frac{1}{j} = \frac{1}{j_k} + \frac{1}{B\omega^{0.5}} \qquad \text{Equation 1}$$

$$B = 0.2 \times n \times F \times \left(D_{O_2}\right)^{2/3} \times \nu^{-1/6} \times C_{O_2} \qquad \text{Equation 2}$$

where j, current density; j_k, kinetic current density; ω, rotation speed; F, Faraday constant; D_{O_2}, oxygen diffusion coefficient (1.9 $10^{-5}$$cm^2$ s^{-1}); ν, viscosity (0.01 cm^2 s^{-1}); C_{O_2}, oxygen concentration (1.2 10^{-6} mol cm^{-3}).

4. RESULTS AND DISCUSSION

4.1. Textural and chemical characterizations

Textural and chemical characterizations of the samples have been described in the previous Chapter

4.2. Oxygen Reduction Reaction: CV and LSV

Cyclic Voltammetry (CV) curves were obtained while N_2 or O_2 bubbled in a 0.1 M KOH solution at a RDE rotation speed of 1000 rpm and at a scan rate of 50

mV s^{-1}. These experiments were only performed to see the difference between CV under N_2 and O_2 (no parameter was obtained). Results for CSV5, CSV10, CSV20 and CSV30 are shown in the figures 1a; 1b; 1c and 1d respectively. We can observe differences in the negative potential region (Figure 1). It is clear that the CSV20 sample is more active for ORR than others ones which will be better observed after analysing LSV experiments. Also, it can be seen that oxygen reduction takes place at around -0.18 V versus Ag/AgCl.

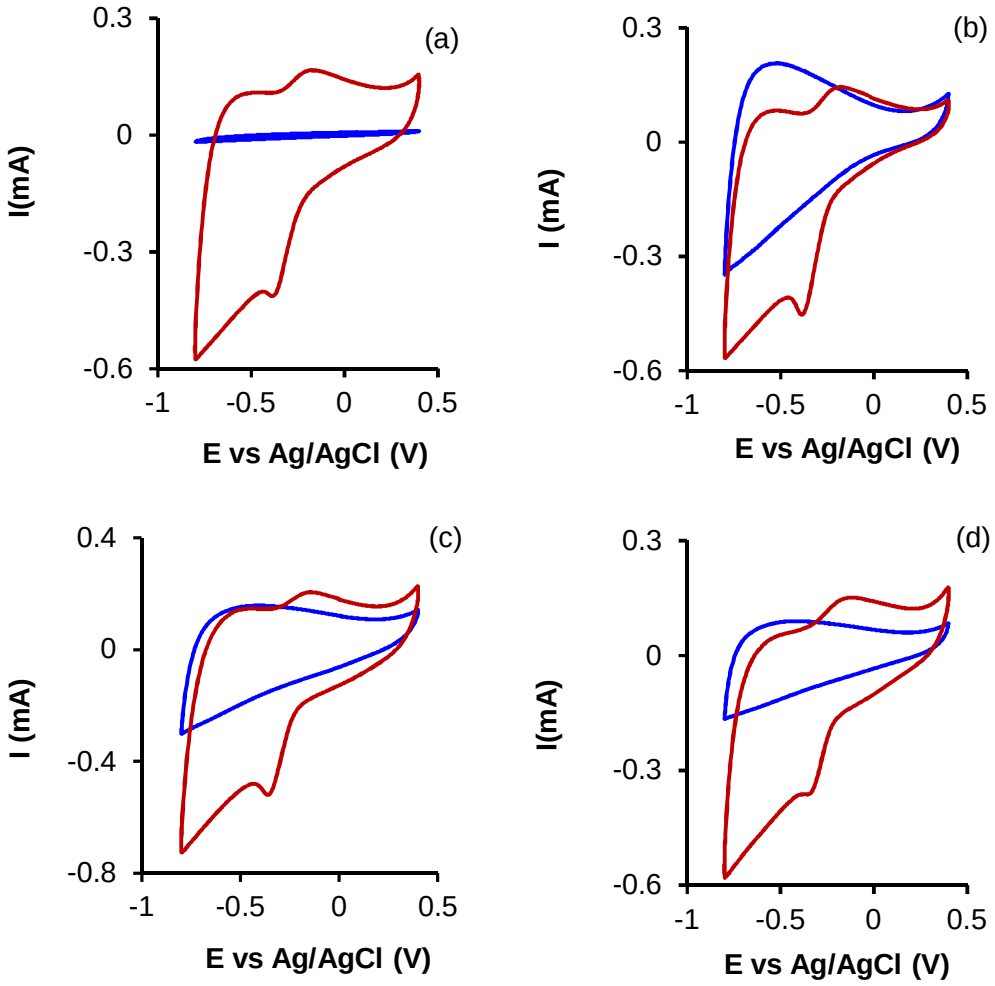

Figure 1. CV of CSV5 (a); CSV10 (b); CSV20 (c) and CSV30 (d) on N_2 (blue) and O_2 (red).

The Koutecky-Levich equation was applied to LSV curves at different rotation speeds from 1000 to 4000 rpm. It needs to be considered that ORR can take place by two different mechanisms in basic media (Equations 1 and 2) [28, 29].

$$O_2 + 2\,H_2O + 4\,e_s^- \longrightarrow 4\,OH^- \qquad \text{Equation 1}$$

$$O_2 + H_2O + 2\,e_s^- \longrightarrow HO_2^-\,OH^- \qquad \text{Equation 2}$$

It would be desirable that ORR takes place by the 4 electron pathway, rather than by the 2 electron pathway, since the former implies higher current densities on the electrochemical cell and the latter leads to the formation of peroxide species, which may deactivate [5,30] and damage the electro-catalytic layer. Therefore, it is crucial to determine whether our sample is catalysing ORR by the first or the second mechanism. In order to discern that, LSV curves were obtained at different RDE rotation speed for all the samples, Figure 2. The obtained data were fitted to K-L equation so as to get the number of electrons transferred on each sample at each potential [31,32]. This analysis was performed for all the samples and the graphic results obtained for all samples are shown in the figures 3a, 3b, 3c and 3d.

Figure 4a shows a comparison of the LSV curves at rotation speed of 3000 rpm between all the vanadium carbon composites. From this curves it is showed that the sample CSV20 present the higher current density. Figure 4b presents the variation of the number of electrons transferred with the electrochemical potential for each sample. The sample CSV20 shows the higher number of electron transferred compared to the others ones. This difference of the number of electron transferred by due in one part to the vanadium content and also to the surface area and porous structure of the vanadium carbon composites. The sample CSV20 shows the higher surface area and the microporous volume.

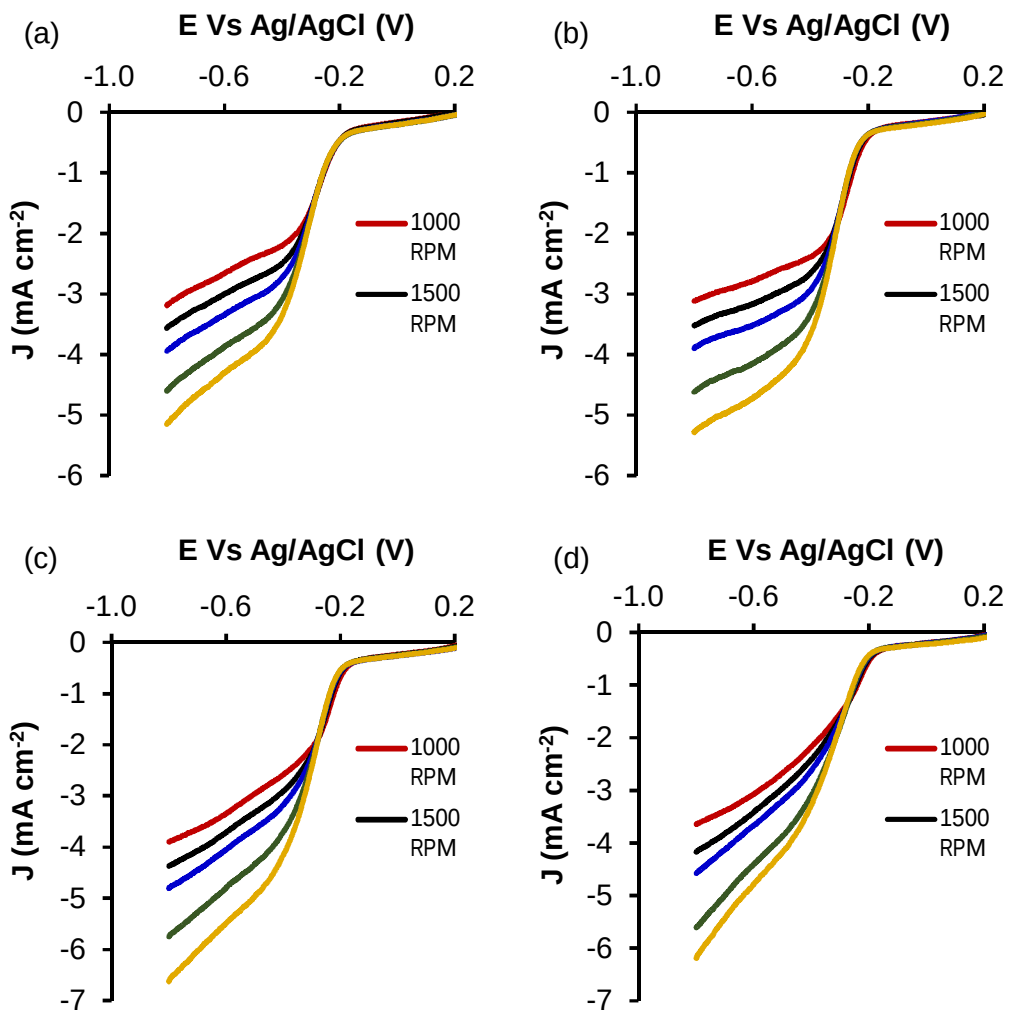

Figure 2. LSV at different rotation speed for a) CSV5; b) CSV10; c) CSV20; d) CSV30. **1000**; 1500; **2000**; **2500** and **3000** rpm

Table 1 shows the parameters obtained from the analysis of LSV curves (values of j_k and n refer to K-L fitting for data at -0.8 V). It appears that all the samples shows a four electron pathway which indicate the mechanism of the reduction of oxygen to water, furthermore the results indicate higher values of current densities at all electrochemical potentials but the sample CSV20 shows the

higher value. Also, a lower activation potential (E^0_{onset} versus Ag/AgCl) was required for the ORR to start (Table 1). However, all the samples tested show a lower activation potential, the difference of the electro-catalytic performances between all the vanadium carbon composites tested could be to the difference in the pore size and the surface area as was mentioned previously.

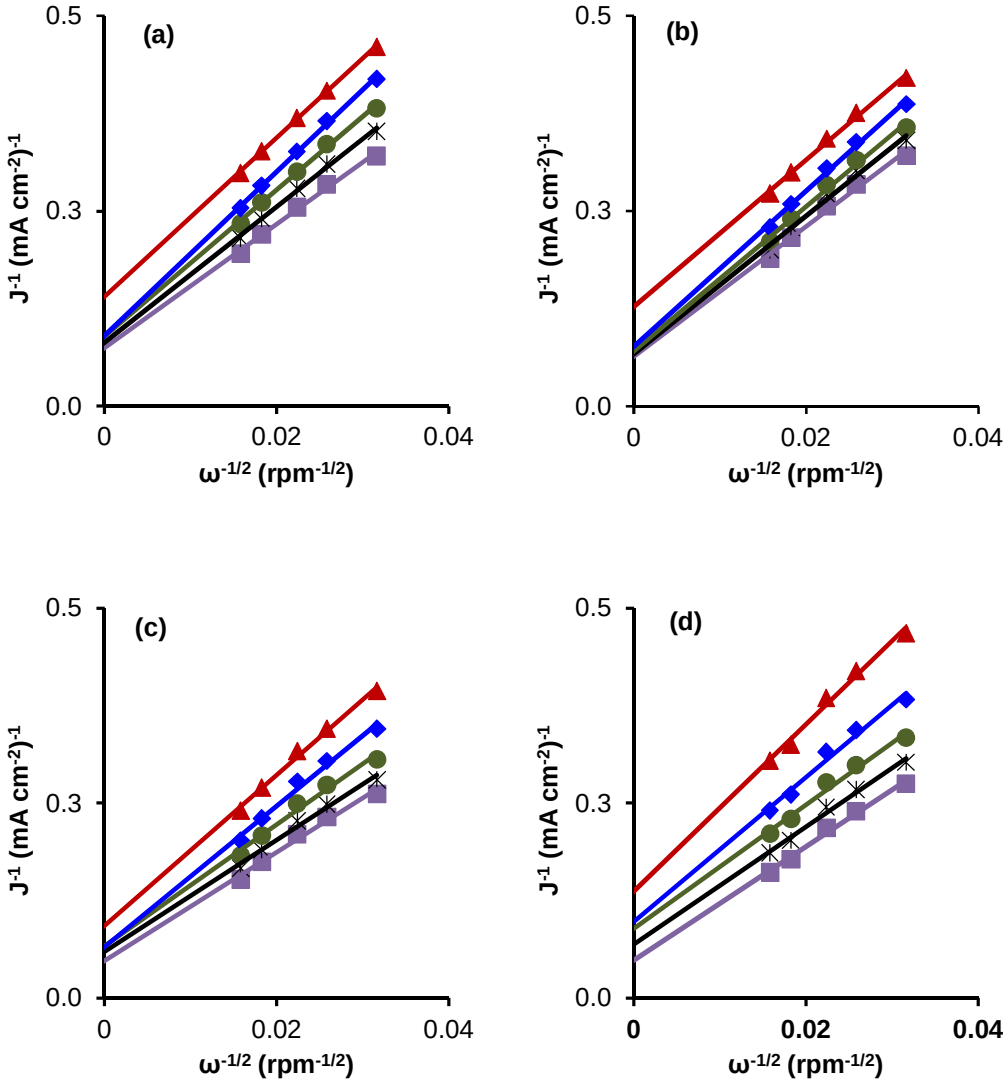

Figure 3.K-L plots for a) CSV5; b) CSV10; c) CSV20; d) CSV30 at different electrochemical potentials: from -0.4V (▲) to -0.8 V (■)

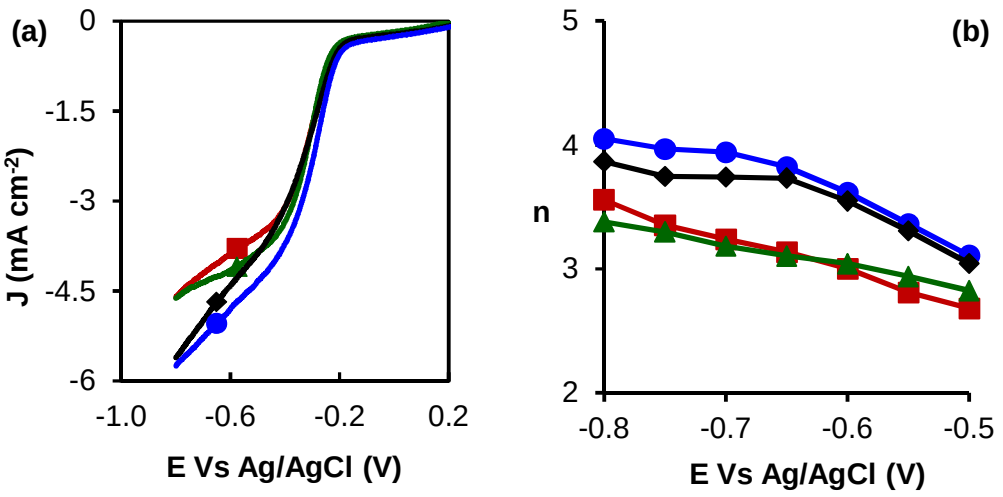

Figure 4. a) LSV curves at 3000rpm and b) variation of n with E^0vs Ag/AgCl for samples CSV5 (■), CSV10 (▲), CSV20 (●), CSV30 (♦).

Table 1. Parameters obtained from the analysis of LSV curves (values of j_k and n refer to K-L fitting for data at -0.8V).

Sample	E^0_{onset} V	j_k mA cm^{-2}	n
CsV5	-0.22	13.307	3.56
CsV10	-0.21	15.651	3.38
CsV20	-0.18	20.842	4.05
CsV30	-0.20	20.520	3.87

Figure 5 shows a good correlation of the current density and the vanadium composite contents. The correlation coefficient of R^2=0.86 which is lower than the optimal value of 1 indicates that the difference of the electro-catalytic performances depend with others parameters such as the surface area and the pore structure.

Finally, it is necessary to study the electro-catalytic performance of the vanadium composites with different amount of vanadium oxide in order to optimize the best composition for the best performance.

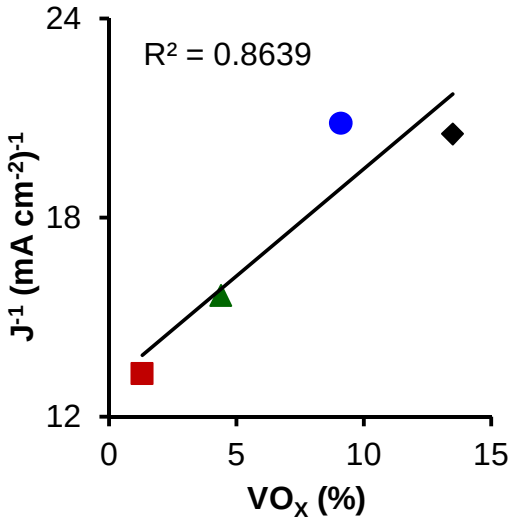

Figure 5. Correlation between the current density and the amount of vanadium oxide for samples CSV5 (■), CSV10 (▲), CSV20 (●), CSV30 (♦).

5. CONCLUSIONS

This study reports the successful synthesis of new vanadium - carbon composite by a simple hydrothermal method and their electro-chemical behaviour in ORR. High electro-catalytic activity in the oxygen reduction reaction has been achieved with all composites. Vanadium oxide content influences clearly the electro-catalytic behaviour leading it to a four electron pathway. These results show also high current densities and low electro-chemical potentials which even comparable with commercial Pt-C based electrodes. Therefore, vanadium - carbon composites are a very good candidates as electro-catalysts for ORR in basic medium.

6. REFERENCES

[1] Feng L, Yang L, Huang Z, Luo J, Li M, Wang D, Chen Y. Enhancing Electrocatalytic Oxygen Reduction on Nitrogen-Doped Graphene by Active Sites Implantation 2013;3:3306-

[2] Zhao X, Zou X, Yan X, Brown CL, Chen Z, Zhu G, Yao X. Defect-driven oxygen reduction reaction (ORR) of carbon without any element doping. Inorg. Chem. Front. 2016;3(3):417-421.

[3] Guo D, Shibuya R, Akiba C, Saji S, Kondo T, Nakamura J. Active sites of nitrogen-doped carbon materials for oxygen reduction reaction clarified using model catalysts. Science 2016;351(6271):361-

[4] Luo Y, Sreekuttan MU, Mora-Hernandez JM, Alonso-Vante N. Materials for ORR Electrocatalysis: Catalytic Center and Substrate Effects. Meeting Abstracts 2014;MA2014-02(26):1507-1507.

[5] Gong K, Du F, Xia Z, Durstock M, Dai L. Nitrogen-Doped Carbon Nanotube Arrays with High Electrocatalytic Activity for Oxygen Reduction. Science 2009;323(5915):760-

[6] Liu R, Wu D, Feng X, Müllen K. Nitrogen-Doped Ordered Mesoporous Graphitic Arrays with High Electrocatalytic Activity for Oxygen Reduction. Angewandte Chemie International Edition 2010;49(14):2565-2569.

[7] Bashyam R, Zelenay P. A class of non-precious metal composite catalysts for fuel cells. Nature 2006;443(7107):63-66.

[8] Lefèvre M, Proietti E, Jaouen Fdr, Dodelet JP. Iron-Based Catalysts with Improved Oxygen Reduction Activity in Polymer Electrolyte. Fuel Cells. Science 2009;324(5923):71-74

[9] Bezerra CWB, Zhang L, Lee K, Liu H, Marques AaLB, Marques EP, Wang H, Zhang J. A review of FeGÇôN/C and CoGÇôN/C catalysts for the oxygen reduction reaction. Electrochimica Acta 2008;53(15):4937-4951.

[10] Wang B. Recent development of non-platinum catalysts for oxygen reduction reaction. Journal of Power Sources 2005;152:1-15.

[11] Rabis A, Rodriguez P, Schmidt TJ. Electrocatalysis for Polymer Electrolyte Fuel Cells: Recent Achievements and Future Challenges. ACS Catal. 2012;2(5):864-890.

[12] Jaouen F, Proietti E, Lefevre M, Chenitz R, Dodelet JP, Wu G, Chung HT, Johnston CM, Zelenay P. Recent advances in non-precious metal catalysis for oxygen-reduction reaction in polymer electrolyte fuel cells. Energy Environ. Sci. 2011;4(1):114-130.

[13] Wang X, Ke Y, Pan H, Ma K, Xiao Q, Yin D, Wu G, Swihart MT. Cu-Deficient Plasmonic Cu2GÇôxS Nanoplate Electrocatalysts for Oxygen Reduction. ACS Catal. 2015;5(4):2534-2540.

[14] Adão P, Costa Pessoa J, Henriques RT, Kuznetsov ML, Avecilla F, Maurya MR, Kumar U, Correia I. Synthesis, Characterization, and Application of Vanadium−Salan Complexes in Oxygen Transfer Reactions. Inorg. Chem. 2009;48(8):3542-3561.

[15] Luo Q, Zhang H, Chen J, You D, Sun C, Zhang Y. Preparation and characterization of Nafion/SPEEK layered composite membrane and its application in vanadium redox flow battery. Journal of Membrane Science 2008;325(2):553-558.

[16] Rodemerck U, Kubias B, Zanthoff HW, Wolf GU, Baerns M. The reaction mechanism of the selective oxidation of butane on $(VO)_2P_2O_7$ catalysts: The influence of the valence state of vanadium. Applied Catalysis A: General 1997;153(1):217-231.

[17] Huang T, Mao S, Zhou G, Wen Z, Huang X, Ci S, Chen J. Hydrothermal synthesis of vanadium nitride and modulation of its catalytic performance for oxygen reduction reaction. Nanoscale 2014;6(16):9608-9613.

[18] Huang T, Mao S, Pu H, Wen Z, Huang X, Ci S, Chen J. Nitrogen-doped graphene-vanadium carbide hybrids as a high-performance oxygen

reduction reaction electrocatalyst support in alkaline media. J. Mater. Chem. A 2013;1(43):13404-13410.

[19] Jung DH, Bae SJ, Kim SJ, Nahm KS, Kim P. Effect of the Pt precursor On the morphology and catalytic performance of Pt-impregnated on Pd/C for the oxygen reduction reaction in polymer electrolyte fuel cells. Int. J. Hydrog. Energy 2011;36(15):9115-9122.

[20] Shervedani RK, Amini A. Carbon black/sulfur-doped graphene composite prepared by pyrolysis of graphene oxide with sodium polysulfide for oxygen reduction reaction. Electrochimica Acta 2014;142:51-60.

[21] Nie R, Bo X, Luhana C, Nsabimana A, Guo L. Simultaneous formation of nitrogen and sulfur-doped carbon nanotubes-mesoporous carbon and its electrocatalytic activity for oxygen reduction reaction. International Journal of Hydrogen Energy 2014;39(24):12597-12603.

[22] Conway, B. E. Electrochemical Supercapacitors: Scientific Fundamentals and Technological Applications. 1999. Nature Publishing Group.

[23] Miller JR, Simon P. Electrochemical capacitors for energy management. Science 2008;321:651-652.

[24] Pandolfo AG, Hollenkamp AF. Carbon properties and their role in supercapacitors. J. Power Sources 2006;157:11-27.

[25] Ghimbeu CM, Raymundo-Pinero E, Fioux P, Beguin F, Vix-Guterl C. Vanadium nitride/carbon nanotube nanocomposites as electrodes for supercapacitors. J. Mater. Chem. 2011;21(35):13268-13275.

[26] Zhao D, Cui Z, Wang S, Qin J, Cao M. VN hollow spheres assembled from porous nanosheets for high-performance lithium storage and the oxygen reduction reaction. J. Mater. Chem. A 2016;4(20):7914-7923.

[27] Mi Y, Wang J, Yang Z, Wang Z, Wang H, Yang S. A simple one-step solution deposition process for constructing high-performance amorphous zirconium oxide thin film. RSC Adv. 2014;4(12):6060-6067.

[28] Si, Fengzhan, Zhang, Yuwei, Yan, Liang, Zhu, Jianbing, Xiao, Meiling, Liu, Changpeng, Xing, Wei, and Zhang, Jiujun. Electrochemical Oxygen Reduction Reaction. Rotating Electrode Methods and Oxygen Reduction Electrocatalysts. 133-170. 2014. Amsterdam, Elsevier.

[29] Yang Z, Nie H, Chen X, Chen X, Huang S. Recent progress in doped carbon nanomaterials as effective cathode catalysts for fuel cell oxygen reduction reaction. Journal of Power Sources 2013;236:238-249.

[30] Lu J, Li Y, Li S, Jiang SP. Self-assembled platinum nanoparticles on sulfonic acid-grafted graphene as effective electrocatalysts for methanol oxidation in direct methanol fuel cells. Sci Rep 2016;6:21530-

[31] Domínguez C, Pérez-Alonso FJ, Abdel Salam M, Al-Thabaiti SA, Obaid AY, Alshehri AA, G+¦mez de la Fuente J, Fierro JLG, Rojas S. On the relationship between N content, textural properties and catalytic performance for the oxygen reduction reaction of N/CNT. Applied Catalysis B: Environmental 2015;162:420-429.

[32] Nie R, Bo X, Luhana C, Nsabimana A, Guo L. Simultaneous formation of nitrogen and sulfur-doped carbon nanotubes-mesoporous carbon and its electrocatalytic activity for oxygen reduction reaction. International Journal of Hydrogen Energy 2014;39(24):12597-12603.

CHAPTER XII: *CONCLUSIONES GENERALES*

En esta Tesis Doctoral se han preparado materiales de carbón a partir de diferentes precursores tales como residuos lignocelulósicos, maderas de olivo, higuera y chirimoyo, residuos de la industria oleícola, alpechín y alperujo y polímeros orgánicos obtenidos por reacciones de policondensación mediante emulsión inversa en presencia de alcóxidos metálicos para la obtención de materiales compuestos de carbón dopados con óxidos de Ti, Zr y V. Además se han realizado procesos de funcionalización de los carbones activados con diversos heteroátomos, O, N, P y S, mediante procesos solvotermales y/o hidrotermales.

Los materiales obtenidos se han empleado como electrodos de supercondensadores obteniéndose resultados totalmente comparables e incluso mejores a otros materiales de carbón encontrados en bibliografía y con una ciclabilidad próxima o igual al 100 %, determinada mediante estudio de ciclos de carga descarga cronopotenciométricos y análisis a voltaje constante.

Mediante la activación de alpechín con KOH se obtuvieron carbones activados con elevadas superficies, hasta 1626 m^2 g^{-1}. La activación de H_3PO_4 produce grupos funcionales que contienen P pero estos presentaron un área superficial inferior a los carbones activados con KOH. El alperujo es un excelente residuo para la preparación de carbones activados porosos con una red de poros muy desarrollada. La capacidad más alta obtenida fue 224 F g^{-1} a 250 mA g^{-1} con una capacidad de retención del 91 % después de 12500 ciclos y un τ igual 2.9 s. La muestra AP presento la mayor capacidad de retención de capacidad, prácticamente el 100 %, con 176 F g^{-1} y τ = 1.6 s debido a la presencia de grupos superficiales de fósforo y una adecuada red de micro-mesoporos.

Se puede conseguir una alta actividad electrocatalítica en la reacción de reducción de oxígeno con carbones activados, obtenidos a partir de residuos industriales de aceite de oliva dopados con azufre. Las funcionalidades de azufre se fijaron sobre la superficie porosa de los materiales de carbono por medio de un método solvotermal usando ácido tioglicólico. El contenido de azufre y las características porosas influyen en el comportamiento electro-catalítico, pero la

presencia de funciones de azufre son cruciales para el desarrollo de un mecanismo de cuatro electrones. Los electro-catalizadores de carbón activado dopados con azufre siempre trabajan a un menor potencial electroquímico y con mayores densidades de corriente que el carbón activado sin funcionalizar.

El tratamiento solvotermal con ácido tioglicólico de las muestras preparadas mediante activación química de alperujo permite la introducción de grupos superficiales de azufre. El estudio de su comportamiento como electrodos de supercondensadores indica que sus propiedades electroquímicas son mejores en medio H_2SO_4 1 M que en medio KOH 6 M.

En medio H_2SO_4 1 M, se obtuvo una alta capacidad de almacenamiento de energía, 325 F g^{-1} a una densidad de corriente de 0.125 A g^{-1}, y una alta retención de capacidad > 69 % a una densidad de corriente de 30 A g^{-1}. El contenido de azufre, la naturaleza de las funcionalidades introducidas y las características porosas de los carbones activados y funcionalizados influyen en su comportamiento electroquímico. La presencia de grupos superficiales de azufre, diferentes a sulfato o sulfónicos, aumenta la capacidad y también la estabilidad de los electrodos. Las muestras tratadas con azufre presentan una densidad de energía máxima de 37 Wh kg^{-1} a una densidad de potencia de 274 W kg^{-1}. La estabilidad de los electrodos alcanzó un 99.3 % en retención de capacidad después 12500 ciclos de carga descarga

El estudio electroquímico de los carbones activados obtenidos a partir de maderas indican que las muestra preparadas mediante activación con KOH de chirimoyo poseen unas características electroquímicas muy superiores a las de otros carbones con capacidades de hasta 240 F g^{-1} y una energía de 3.7 Wh kg^{-1} con una potencia correspondiente de 47 W kg^{-1}. Además la química superficial y la distribución de poros son los parámetros más importantes en la aplicación electroquímica de los carbones activados.

Los tratamientos realizados a los carbones activados introducen diferentes funcionalidades de nitrógeno como piridina, N-cuaternario y nitrógeno oxidado que mejoran la humectabilidad y la transferencia de iones. La alta capacidad especıfica

y el excelente rendimiento se pueden atribuir a las siguientes razones: (i) la elevada superficie proporciona una gran interfase de adsorción para que el electrólito forme la EDL, dando lugar a una gran capacitancia electroquímica. (ii) La introducción de grupos que contienen heteroátomos mejoró la humectabilidad de las muestras de carbón en electrolitos acuosos. El valor máximo de densidad de energía alcanzado fue 28.34 Wh kg^{-1} para la muestra FKC, además todas las muestras tratadas muestran un valor máximo de densidad de energía mayor que el reportado para la mayoría de los supercondensadores disponibles en el mercado (<10 Wh kg^{-1}). Después de 2500 ciclos, la capacidad de retención para todas las muestras modificadas está entre 97,0% y 100%.

Los materiales compuestos de xerogel de carbón-TiO_2 (CTiX) se sintetizaron satisfactoriamente mediante técnicas sol-gel. Los compuestos presentan una estructura mesoporosa homogénea y tridimensional, donde ambas fases están también homogéneas e íntimamente distribuidas. Todas las propiedades texturales, químicas, cristalográficas y catalíticas están condicionadas por el contenido de TiO_2 y por el efecto sinérgico entre ambas fases. Los xerogeles de carbono son eminentemente soportes microporosos, pero los materiales compuestos son materiales mesoporosos, aumentando la mesoporosidad a expensas de la microporosidad. La presencia de carbono en el material compuesto evita el crecimiento del cristal de TiO_2 y dificulta la transición anatasa a rutilo. Debido a las interacciones entre ambas fases, todos los compuestos presentan una alta dispersión de nanopartículas de TiO_2 en el soporte de carbono a pesar de que las muestras se carbonizaron a 900 °C. Estas nanopartículas están parcialmente reducidas, con una distribución de la superficie del oxígeno altamente dependiente del contenido de TiO_2.

Los materiales compuestos carbón TiO_2 presentaron un alto rendimiento electroquímico con capacidades (hasta 137 F g^{-1} a 0.250 A g^{-1} para 20 % de TiO_2), una alta capacidad de retención (66-80%) a 20 A g^{-1} y alta densidad de energía, 20.7 Wh kg^{-1}, con una densidad de potencia de 69 W kg^{-1} en el rango de tensión de 0 V a 1.1 V. Este mejor comportamiento podría estar relacionado con diferentes

propiedades de los compuestos: i) La presencia de TiO_2 mejora la hidrofilicidad de la superficie que aumenta significativamente el contacto electrolítico con la superficie favoreciendo la difusión de los iones, ii) la matriz de carbono favorece la reducción de TiO_2 y estas especies reducidas Ti^{3+} pueden actuar como centros de transferencia de electrones disminuyendo la resistencia del electrodo y iii) la presencia de TiO_2 sobre material de carbono induce una disminución en la resistencia del electrodo que mejora su rendimiento para el almacenamiento de energía debido a una optimización de la estructura de poros. La muestra con una combinación de baja hidrofobicidad y una adecuada red de micro-mesoporos mostró el mejor comportamiento para el almacenamiento de energía.

Se desarrolló una serie de un xerogel de carbono dopado con diferentes porcentajes de ZrO_2 como vía alternativa para preparar electrodos para supercondensadores. Los materiales compuestos de carbono se obtuvieron mediante un método de emulsión inversa en n-heptano. Tras una carbonización a 900 °C la fase de óxido metálico está bien dispersa sobre la fase de carbono, obteniéndose tamaño de cristal menor de 4. La adsorción de gases y la porosimetría de mercurio indicaron que el aumento de ZrO_2 en la matriz de carbono produce un aumento en el volumen de mesoporos así como un ensanchamiento de la microporosidad a expensas de los microporos estrechos ($W_0(CO_2)$). Los resultados XPS mostraron que el Zr se encuentra formando óxidos no estequiométricos (ZrO_y: $0 < y < 2$) y estas especies parcialmente reducidas pueden actuar como sitios de transferencia de electrones mejorando la conductividad eléctrica y aumentando la pseudocapacitancia. Un supercondensador simétrico de dos electrodos basado en los compuestos de xerogel de carbono-ZrO_2 presentó un alto rendimiento electroquímico con capacidades (hasta 180 F g^{-1} a 0,125 A g^{-1} para el compuesto ZrO_2 al 30 %), una alta capacidad de retención y alta energía Con una densidad de potencia de 140 W kg-1 en el rango de tensión de 0 V a 1.2 V. La muestra con una combinación óptima de una red de micro-mesoporosa adecuada, con ancho de poro y una adecuada cantidad de ZrO_2 mostró el mejor rendimiento para el almacenamiento

de energía. El ensayo a voltaje constante mostró una excelente ciclabilidad de los materiales sintetizados.

La caracterización electroquímica completa de los materiales compuestos CSVX se realizó mediante diversos métodos: voltametría cíclica, cronopotenciometría, ciclos de carga-descarga y espectroscopia de impedancia. Los resultados muestran que la muestra CSV30 correspondiente al compuesto con 30% de óxido de vanadio tiene una buena capacitancia específica de 224 F g^{-1} con una densidad de corriente de 125 mA g^{-1} en H_2SO_4, 1M como electrolito, además esta muestra fue capaz de mantener el 58.8 % de la capacidad a una densidad de corriente de 20 A g^{-1} y mantienen el 100 % de la capacidad después 13000 ciclos de descarga de carga a 1 A g^{-1}. Además, esta muestra mantiene la forma rectangular del voltamograma a una alta velocidad de barrido de 200 mV s^{-1}, indicando una buena conductividad y estabilidad del electrodo.

Los materiales compuesto de carbón con óxido de vanadio presentaron una alta actividad electrocatalítica en la reacción de reducción de oxígeno. El contenido de óxido de vanadio influye claramente en el comportamiento electro-catalítico que conduce a una vía de cuatro electrones. Estos resultados muestran también altas densidades de corriente y bajos potenciales electroquímicos que incluso son comparables con electrodos comerciales basados en Pt-C. En conclusión, los materiales compuestos óxido de vanadio – carbono presentaron un excelente comportamiento como electro - catalizadores para ORR en medio básico.